Impact of Extracellular Matrix Environment on Cardiovascular and Pancreatic Tissues

Dissertation

der Mathematisch-Naturwissenschaftlichen Fakultät

der Eberhard Karls Universität Tübingen

zur Erlangung des Grades eines

Doktors der Naturwissenschaften

(Dr. rer. nat.)

vorgelegt von

Max Nikos Urbanczyk

aus Aschaffenburg

Tübingen 2022

Gedruckt mit Genehmigung der Mathematisch-Naturwissenschaftlichen Fakultät der Eberhard Karls Universität Tübingen.

Tag der mündlichen Qualifikation:	04.04.2023
Dekan:	Prof. Dr. Thilo Stehle
1. Berichterstatter/-in	Prof. Dr. Katja Schenke-Layland
2. Berichterstatter/-in	Prof. Dr. Andreas Birkenfeld
3. Berichterstatter/-in	*Prof. Dr. Liliana Schäfer*

„Was wir wissen, ist ein Tropfen – was wir nicht wissen, ein Ozean.“

Sir Isaac Newton

Table of Contents

Abstract

The extracellular matrix (ECM) is a scaffold composed of different proteins in which the cells of living tissues reside. In healthy states, the ECM plays an important role in regulating cellular processes such as apoptosis, proliferation and differentiation, contributing to tissue homeostasis. During events of injury, such as scar tissue formation after myocardial ischemia or fibrotic capsule formation following organ transplantation, the ECM experiences pathological changes which impact the survival of cells and significantly contributes to the severity of the injury. These pathological alterations of the ECM are among the main factors that determine cellular survival in tissues and treatment efficacy. Hence, understanding the roles of the various ECM proteins and elucidating their mechanisms of action in different tissues are of growing interest in the field of tissue engineering and medicine.

In this thesis, the impact of the ECM on cardiovascular and pancreatic tissues was studied. Cardiovascular tissues experience significant impact on native ECM homeostasis during the event of myocardial infarction and reperfusion injury (MI/R). We identified the ECM protein nidogen-1 (NID1) to be highly present during cardiac development. We furthermore showed the positive effect of recombinantly produced NID1 on cellular survival, angiogenesis and prevention of pathological differentiation in vitro. The treatment of mice with NID1 post-MI/R resulted in decreased scar tissue formation, increased revascularization and increased nerval innervation in the infarcted area accompanied by overall improvement in heart function.

ECM alterations in pancreatic tissue are of special interest during the process of isolation and transplantation of hormone-secreting islets of Langerhans to treat diabetes mellitus type 1. We demonstrated that both NID1 and decorin (DCN) co-localize with insulin-producing β-cells within the islets of Langerhans. Treatment of β-cells with NID1 and DCN improved functionality and survival in vitro. Furthermore, we demonstrated that hypoxic conditions significantly impact the ECM and functionality of β-cells, which was rescued upon co-culturing β-cells with endothelial cells in a collagen type 1 gel.

The in vitro models developed in this thesis demonstrate the positive effects of ECM proteins on survival and functionality of cells from different origins and elucidate potential underlying pathways. We furthermore highlight that restoration and recapitulation of native ECM in vitro offers great potential for in vivo translation regarding cellular treatments and therapies.

Zusammenfassung

Die extrazelluläre Matrix (EZM) ist ein Gerüst aus verschieden, untereinander verbunden Proteinen, in dem sich einzelne Zellen lebenden Gewebes befinden. Im gesunden Zustand spielt die EZM eine wichtige Rolle in der Regulierung zellulärer Prozesse wie Apoptose, Proliferation und Differenzierung und trägt so zur Gewebshomöostase bei. Innerhalb der EZM kommet es nach Gewebsverletzungen und invasiven Eingriffen zu pathologischen Veränderungen, zum Beispiel zur Narbenbildung nach Herzinfarkt oder der Bildung einer fibrotischen Kapsel nach Zell- oder Organtransplantationen. Diese Veränderungen wirken sich auf den Fortbestand der Zellen im betroffenen Gewebe aus und tragen wesentlich zur Schwere der Verletzung und derer Behandlung bei. Daher ist ein besseres Verständnis der Funktionen verschiedener EZM-Proteine und deren Wirkungsmechanismen in verschiedenen Geweben von wachsendem Interesse im Bereich des Tissue Engineering sowie der Medizin.

In dieser Arbeit wurde der Einfluss der EZM auf kardiovaskuläres und pankreatisches Gewebe untersucht. Kardiovaskuläres Gewebe erfährt eine erhebliche Beeinträchtigung der natürlichen EZM-Homöostase während eines Herzinfarkts mit anschließendem Reperfusionsschaden. Wir fanden heraus, dass das EZM-Protein Nidogen-1 (NID1) speziell während der kardialen Entwicklung exprimiert wird. Darüber hinaus konnten wir die positive Wirkung von rekombinant hergestelltem NID1 in Bezug auf das zelluläre Überleben, die Angiogenese und die Verhinderung einer pathologischen Differenzierung von kardiovaskulären Zellen in vitro nachweisen. Die Behandlung von Mäusen mit NID1 nach einem Herzinfarkt führte zu einer Verringerung der Narbengewebsbildung, einer verstärkten Revaskularisation und Innervation im Infarktgebiet sowie einer allgemeinen Verbesserung der Herzfunktion.

EZM-Veränderungen im Pankreasgewebe sind von besonderem Interesse während der Isolierung und Transplantation von hormonsezernierenden Langerhans-Inseln zur Behandlung von Diabetes Mellitus Typ 1. Wir haben gezeigt, dass sowohl NID1 als auch Decorin (DCN) in insulinproduzierenden β-Zellen der Langerhans-

Inseln präsent sind. Die Behandlung von β-Zellen mit NID1 und DCN verbesserte die Funktionalität und das Überleben in vitro. Darüber hinaus konnten wir zeigen, dass hypoxische Bedingungen einen signifikanten Einfluss auf die β-zelleigene EZM und deren Funktionalität haben. Durch die Ko-Kultur von β-Zellen mit Endothelzellen in einem Kollagen-Typ-1-Gel konnte die β-Zell-EZM sowie deren Funktionalität erfolgreich wiederhergestellt werden.

Unsere in-vitro-Modelle zeigen die positiven Auswirkungen von EZM-Proteinen auf das Überleben und die Funktionalität von Zellen unterschiedlichen Ursprungs und geben Aufschluss über mögliche zugrunde liegende Mechanismen. Darüber hinaus heben wir hervor, dass die Wiederherstellung und Rekapitulation der nativen EZM in vitro ein großes Potenzial für die Translation von zellulären Behandlungen und Therapien bietet.

Abbreviations

ATP	adenosine triphosphate
BM	basement membrane
CM(s)	cardiomyocyte(s)
COL1	collagen type 1
COL3	collagen type 3
COL4	collagen type 4
CTNT	cardiac troponin T
CVDs	cardiovascular diseases
DCN	decorin
DDR(s)	discoidin domain receptor(s)
DM	diabetes mellitus
E-cadherin	epithelial cadherin
EBs	embryonic bodies
EC(s)	endothelial cell(s)
ECM	extracellular matrix
EpCAM	epithelial cell adhesion molecule
ER	endoplasmic reticulum
ERK	extracellular signaling-regulated kinase
F-actin	filamentous actin
FAK	focal adhesion kinase
FN	fibronectin
GLU	glucagon
GSIS	glucose-stimulated insulin secretion
HA	hyaluronic acid
hiPSC	human induced pluripotent stem cell
HUVEC(s)	human umbilical vein endothelial cell(s)
IL-11	interleukin-11
IL-1β	interleukin-1β

IL-6	interleukin-6
IM	interstitial matrix
INS	insulin
LAM(s)	laminin(s)
LRP1	low density lipoprotein receptor-related protein 1
MAPK	mitogen-activated protein kinase
MI	myocardial ischemia
MI/R	myocardial ischemia and reperfusion injury
MMP(s)	matrix-metalloproteinase(s)
MSCs	mesenchymal stromal cells
NF-κB	nuclear factor k-light-chain-enhancer of activated B cells
NID1	nidogen-1
NID2	nidogen-2
OxPhos	oxidative phosphorylation
PCA	principal component analysis
pFAK	phosphorylated state of focal adhesion kinase
PI	phosphatidylinositol
RRBP1	ribosome binding protein 1
SERCA	sarcoplasmic reticulum Ca^{2+} ATPase pump
SMC(s)	smooth muscle cell(s)
SR	sarcoplasmic reticulum
TAG	triacylglycerol
TCA	true component analysis
TGF-β	transforming growth factor β
TIMPs	tissue inhibitor metalloproteinases
TNF-α	tumor necrosis factor α
TUNEL	Terminal deoxynucleotidyl transferase dUTP nick end labeling
VEGF-A	vascular endothelial growth factor A
WFS1	Wolframin ER transmembrane glycoprotein
αSMA	α smooth muscle actin

List of Figures

List of Thesis-relevant Publications

[§] = authors contributed equally

1. Urbanczyk M., Layland S.L., Schenke-Layland K.; The Role of Extracellular Matrix in Biomechanics and its Impact on Bioengineering of Cells and 3D Tissues, *2020*, Matrix Biology 85, 1-14.

2. Urbanczyk M., Zbinden A., Layland S.L., Duffy G.P., Schenke-Layland K.; Controlled Heterotypic Pseudo-Islet Assembly of Human β-cells and Human Umbilical Vein Endothelial Cells Using Magnetic Levitation, *2020*, Tissue Engineering Part A 26 (7-8), 387-399.

3. Zbinden A.[§], Layland S.L.[§], **Urbanczyk M.**, Carvajal Berrio D.A., Marzi J., Zauner M., Hammerschmidt A., Brauchle E.M., Sudrow K., Fink S., Templin M., Liebscher S., Klein G., Deb A., Duffy G.P., Crooks G.M., Eble J.A., Mikkola H.K.A., Seifert M., Schenke-Layland K.; Nidogen-1 Mitigates Ischemia and Promotes Tissue Survival and Regeneration, *2021*, Advanced Science, 8(4), 2002500.

4. Urbanczyk M.[§], Zbinden A.[§], Layland S.L., Becker L., Marzi J., Bosch M., Loskill P., Duffy G.P., Schenke-Layland K.; Collagen and Endothelial Cell Coculture Improves β-cell Functionality and Rescues Pancreatic Extracellular Matrix, *2021*, Tissue Engineering Part A, 27 (13-14), 977-991.

5. Urbanczyk M., Zbinden A., Schenke-Layland K., Organ-specific Endothelial Cell Heterogenicity and its Impact on Regenerative Medicine and Biomedical Engineering Applications, *2022*, Advanced Drug Delivery Reviews, 114323.

6. Urbanczyk M.[§], Jeyagaran A.[§], Zbinden A., Lu C., Marzi J., Kuhlburger L., Nahnsen S., Layland S.L., Duffy G.P., Schenke-Layland K., Decorin Improves Pancreatic β-cell Function and Regulates Extracellular Matrix Expression in vitro, *2023*, Matrix Biology 115, 160-183.

Contribution

R. = Review

No.	1	2	3	4	5	6
Accepted for publication	yes	yes	yes	yes	yes	yes
Number of authors	3	5	21	9	3	9
Position of the candidate in the list of authors	1	1	3	1	1	1
Scientific ideas by candidate (%)	R.	50	10	30	R.	30
Data generation (%)	R.	80	20	40	R.	30
Interpretation and analysis by candidate (%)	R.	80	20	40	R.	30
Paper writing by candidate (%)	60	70	20	40	80	40

List of other Publications

1. Zbinden A., Marzi J., Schlünder K., Probst C., **Urbanczyk M.**, Black S., Brauchle E.M., Layland S.L., Kraushaar U., Duffy G.P., Schenke-Layland K., Loskill P.; Non-invasive Marker-independent High Content Raman Analysis of a Microphysiological Human Pancreas-on-a-chip Model, *2020*, Matrix Biology 85, 205-220.

2. Zbinden A.[§], Carvajal D.A.[§], **Urbanczyk M.**, Layland S.L., Bosch M., Fliri S., Lu C., Jeyagaran A., Loskill P., Duffy G.P., Schenke-Layland K.; Fluorescence Lifetime Metabolic Mapping of Hypoxia-induced Damage in Pancreatic Pseudo-islets, *2020*, Journal of Biophotonics 13 (12), e202000375.

3. Stadelmann K., Weghofer A., **Urbanczyk M.**, Maulana T.I., Loskill P., Jones P.D. Schenke-Layland K.; Development of a Bi-layered Cryogenic Electrospun Polylactic Acid Scaffold to Study Calcific Aortic Valve Disease in a 3D Co-culture Model, *2022*, Acta Biomaterialia 140, 364-378.

Chapter 1

Introduction

1 Introduction

1.1 The Extracellular Matrix

The extracellular matrix (ECM) is a scaffold composed of different crosslinked proteins which provides biomechanical and biochemical cues in organs and tissues[1,2]. ECM proteins can be divided into different subgroups depending on their characteristics: fibrous proteins, proteins with covalently attached glycosaminoglycans (proteoglycans) and free glycosaminoglycans[1,3]. These proteins are secreted by different cell types, such as smooth muscle cells (SMCs), pericytes, fibroblasts and endothelial cells (ECs) to establish a local environment for them to reside[4–6]. The combination of proteins, mechanical properties and growth factors creates an organ- and tissue-specific niche that varies between organs and also within different parts of a single organ[7]. This location-specific composition of the ECM influences cell phenotypes such as functionality, proliferation, differentiation, physiological homeostasis, protein expression and apoptosis[8–14]. The mechanical properties of the ECM, e.g., its stiffness and topography, are controlled by the amount of proteins and their degree of crosslinking[15,16]. Manipulation of the mechanical properties is influenced by the cellular secretion of degradation proteins, such as matrix-metalloproteinases (MMPs) or tissue inhibitor metalloproteinases (TIMPs), which are highly involved in tissue remodeling, wound healing and disease development upon dysregulation[17,18]. The changes in stiffness are then translated back to the cells and can impact cellular behaviour[2]. For instance, cells can deform and spread deeper into a softer matrix[19], whereas a stiffer matrix supports cellular spreading, proliferation and migration[20]. Many receptors have been identified to transmit biochemical and biomechanical cues from the ECM to the cell, including integrins, tyrosine kinases, dystroglycans and discoidin domain receptors (DDRs). Within this group, integrins are among the most important receptors due to their major role during development[21]. Integrins are heterodimeric transmembrane proteins consisting of α- and β-chains and facilitate the interaction of the ECM to the cell's actin cytoskeleton through ligand-binding[22]. Following extracellular ligand-binding, integrins cluster adaptor molecules (such as focal adhesion kinase (FAK), tensin, paxillin or

vinculin[23–25]) to the binding site within the cell resulting in actin remodeling and concomitant activation of intracellular pathways[22,26,27]. The phosphorylated state of FAK (pFAK) is especially important for integrin-mediated cellular signaling, as it can activate multiple different pathways including mitogen-activated protein kinase (MAPK) and extracellular signaling-regulated kinase (ERK)[27,28] pathways that regulate cell survival[29,30], differentiaion[31], cytoskeleton remodeling[28,32] and protein expression[33,34]. Another important group of proteins for integrin-mediated cell-ECM signaling are small GTPases of the Rho family including Rho, Rac and Cdc42[35]. Upon activation, they regulate actin polymerization, microtubule stabilization, cellular migration as well as nuclear transcription, differentiation and protein expression[36,37]. The impact of the ECM on protein expression of cells closes the feedback loop that is necessary for tissue homeostasis which is maintained by a constant building up, breaking down and remodeling of the ECM by residing cells[2,38]. Disturbances in this feedback loop due to changes in the chemical or mechanical composition of the ECM can lead to surface receptor mediated changes in cellular signaling driving the development of pathologies[2,39,40]. Pathological remodeling of ECM, for instance in the case of fibrosis post-ischemia or post-transplantation, can induce cellular death cascades, differentiation and mutations[41]. Fibrosis is defined as the differentiation of fibroblasts in myofibroblasts that excessively produce and secrete fibrous ECM proteins as an abnormal response to injuries or irritations[16,22]. The change in ECM composition and stiffness impacts the secretion of ECM proteins, MMPs and TIMPs, hindering tissue homeostasis followed by reduced cellular proliferation, migration and the activation of inflammatory processes driving pathological changes[42–46]. Diseases related to changes in the ECM are diverse and range from osteoarthritis, bone weakening, impaired wound healing, cancer development to cardiovascular diseases (CVDs) including blood vessel stiffening and atherosclerosis[47–50].

1.1.1 The Interstitial Matrix of the Extracellular Matrix

The ECM is composed of two distinct layers, the interstitial matrix (IM) and the basement membrane (BM) (Figure 1). The IM is the fibrillar part of the ECM which provides structural and mechanical stability to organs and tissues while offering biochemical cues by integrin-mediated signaling. It is mainly composed of collagen type 1 (COL1), collagen type 3 (COL3), fibronectin (FN) and proteoglycans such as decorin (DCN)[4,5,51]. COL1 governs the structural integrity of tissues and organs through its fibril-forming properties and provides stability against shear, tensile and pressure forces[52]. It is present in almost every connective tissue and is the main component of the IM[53]. The heterotrimeric collagen triple helix of COL1 is formed by two α1-chains and one α2-chain, which contain repetitions of glycine-X-Y repeats, where X and Y predominantly represent proline and hydroxyproline, or any other amino acid[54]. COL3, another fibril-forming collagen, is often associated with COL1 and is mainly present in hollow organs and blood vessels[55]. In contrast to COL1, COL3 is a homotrimer only composed of α1-chains[55]. The formation of fibrillar collagens, including COL1 and COL3, is called fibrillogenesis[56]. In the first step, monomers form a loose procollagen via self-assembly, followed by conversion from procollagen to collagen via enzymatic cleavage. Next, the collagen molecules assemble into microfibrils and ultimately to collagen fibers[57]. FN is present in vertebrates in two different forms: as soluble plasma FN in the blood and as insoluble ECM protein. Comparable to collagens, insoluble FN also forms a fibrillar matrix via fibrillogenesis to provide binding sites for cells[58]. FN is an important regulator of ECM stiffness through its diverse effects, ranging from integrin-mediated signaling to influence cell survival and functionality, to modulating the ECM by regulating the fibrillogenesis as well as fibrotic response of COL1 in wound healing[15,59,60]. DCN is a small leucine-rich proteoglycan, involved in several cellular processes, including migration, proliferation and growth[61]. It governs the process of fibrillogenesis, where the absence of DCN can lead to improper fiber formation impairing structural integrity of the IM and fibrotic response of COL1[62]. Additionally, DCN has modulatory effects on the immune response, improves angiogenesis and is involved in tumour suppression via p53 signaling[63–65].

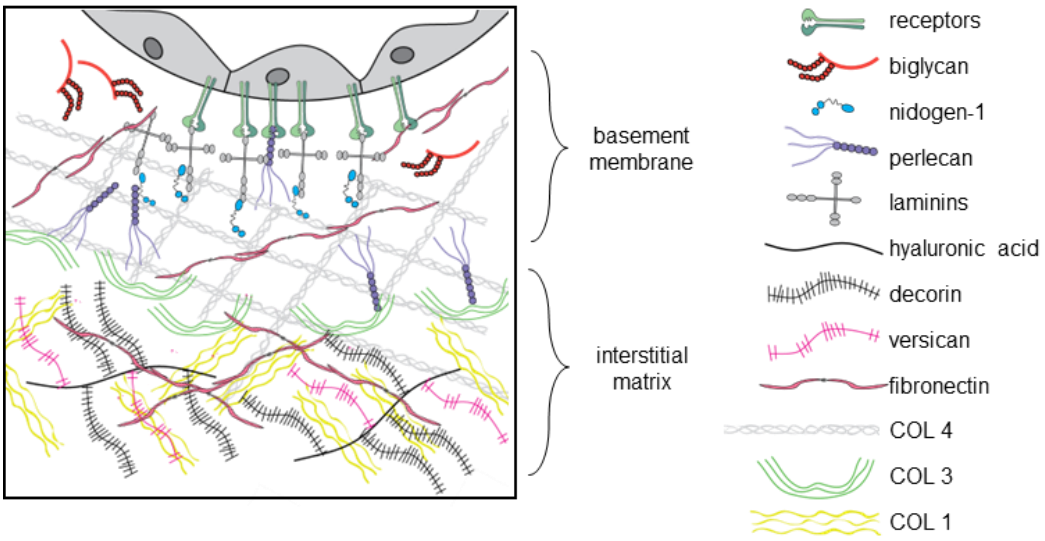

Figure 1: Schematic of the ECM composed of the basement membrane and the interstitial matrix. Adapted from[66].

1.1.2 The Basement Membrane of the Extracellular Matrix

The BM is a thin sheet of network-forming proteins which provides organ- and tissue-specific cell-matrix interactions[67]. The most abundant proteins of the BM are collagen type 4 (COL4), laminins (LAMs), FN and linker proteins, such as nidogen-1 (NID1) and nidogen-2 (NID2)[68–70]. The BM consists of two distinct parts: the lamina densa and the lamina lucida[71]. The lamina densa is composed of COL4, the major network forming protein in the BM[71]. Due to interruptions in the glycine-X-Y sequence, it is significantly more flexible than COLs of the IM[67]. Additionally, the lamina densa encompasses heparan sulfate proteoglycans, e.g., perlecan. Perlecan is a multidomain proteoglycan that interacts with different integrins to mediate adhesion and angiogenesis. Furthermore, it also has a role in mediating cell-cell paracrine signaling through its ability to sequester growth factors[67]. The lamina lucida is composed of different combinations of LAMs, a group of network forming glycoproteins that polymerize into scaffolds. The LAM family currently contains 15 different members, which are characterized by different combinations of three different chains (α, β and γ)[71]. LAMs are named after their chain composition. Hence LAM-411 contains the chains α4, β1 and γ1, where the α-chain mediates cell-matrix interaction

while the other parts are network-forming by LAM-LAM interactions[67]. Lamina lucida and lamina densa are connected via proteoglycans, namely NID1 and NID2[71]. NIDs, also known as entactins, are sulfated glycoproteins which offer binding sites for LAMs, COL4 and perlecan[67]. NIDs are therefore often referred to as linker or bridge proteins, that are also involved embryonic development, angiogenesis, hepatic regeneration as well as regenerative axon growth and guidance[72–76]. Together, the BM provides a favorable ultrastructure with varying pore-sizes and thicknesses that supports integrin-mediated cellular signaling and sequesters growth factors to stimulate intracellular processes[5] and is therefore highly involved in organogenesis, tissue development homeostasis, cell growth regulation and differentiation[77,78].

1.2 Cardiovascular Tissue

The cardiovascular system ensures the circulation of blood throughout the whole body and plays a major role in providing of nutrients, oxygen, cells and hormones for tissue and organ homeostasis as well as removal of waste products[79]. It is composed of four major parts: the heart, which pumps blood via a continuous contraction-relaxation cycle[80]; arteries, which distribute oxygen-rich blood and nutrients from the heart and lungs to peripheral tissues[81]; veins, which transport deoxygenated blood and waste from peripheral tissue back to heart and lungs for reoxygenation[81]; and capillaries, which facilitate the exchange from oxygen, nutrients, molecules and waste from the blood to the tissue[81].

1.2.1 Cardiomyocytes

The heart pumps the blood to peripheral tissues through synchronized contractions of cardiomyocytes (CMs), the main cell type in the heart[82]. The cardiac plexus, a network of nerve fibers located at the base of the heart initiates the synchronized contractions of CMs. The cardiac innervation is autonomous, yet it is additionally influenced by the vagus nerve. The sympathetic trunk of the vagus nerve increases heart rate and force, while the parasympathetic trunk decreases the heart rate[83,84]. The main purpose of CMs is the contraction and relaxation in a cyclic manner, which is supported by CM-specific sarcolemma, a structure that tightly controls molecules entering the CMs[82]. CMs contract in a synchronized manner via spatially defined Ca^{2+} in- and outflux between the cytoplasm and sarcoplasmic reticulum (SR)[80]. This in- and outflux is controlled and initiated by the electrical activity of the sarcolemma and can be classified into five phases[85] (Figure 2). The initial phase (phase 4) describes the resting phase with a membrane potential of ~ -90 mV. In phase 0, the voltage-gated Na^+ channels open to cause a rapid depolarization resulting in a positive membrane potential. In phase 1, the Na^+ channels close and the voltage-gated K^+ channels open resulting in a rapid repolarization[86]. Phase 2, the plateau phase, is characterized by Ca^{2+} entering the cell via voltage-gated L-type Ca^{2+} channels while the K^+ efflux continues[80,86]. In this phase, CM contraction takes place.

Ca^{2+} is the principal intracellular signaling ion and is not only provided from extracellular space by the surface membrane transverse tubules[87], but also via intracellular release of Ca^{2+} via ryanodine receptor 2 from the SR, where Ca^{2+} is tightly packed via calcequestrin[86,88]. The available intracellular Ca^{2+} binds to troponin-C inducing conformational changes in the troponin complex. These conformational changes provide binding spots for myosin to actin, resulting in contraction of the myofilaments[80,82,89]. Post-contraction, intracellular Ca^{2+} is removed and stored in the SR via the SR Ca^{2+} adenosine triphosphatase pump (SERCA) and through Na^{+}/Ca^{2+} exchangers in the sarcolemma[80]. In phase 3, the voltage-gated Ca^{2+} channels close and the slow voltage-gated K^{+} channels open to restore the resting membrane potential[86].

As cyclic contractility is their main purpose, the mitochondria and contractile machinery make up more than 60% of the CM's cytoplasm to meet the high energy requirements[88]. To increase the heart rate, contractile frequency changes are induced by norepinephrine released by neurons, which leads to the generation of cyclic adenosine monophosphate and activation of protein kinase A pathways. This induces increased expression of proteins involved in contractile regulation, such as SERCA, ryanodine receptor 2 and L-type Ca^{2+} channels[80,86]. The electrical coordination between CMs is coordinated by gap junctions and the cardiac conduction system[80,85]. Gap junctions are low resistance intercellular connections formed by connexins with connexin 43 being the most abundantly present followed by connexin 40 and 45. The location of these gap junctions varies between developing CMs and adult CMs: in young CMs, gap junctions are located all over the cell, while in adult CMs, post-elongation and bundling, gap junctions are only located at both tips of the cell, thus increasing the speed of signal transduction[86,90].

Further characteristics of the CMs in the adult heart are karyokinesis without cytokinesis, resulting in two nuclei per cell. Although they are growing, adult CMs are non-proliferative[80]. CMs are also active in intercellular signaling. They can secrete several proteins and growth factors, such as tumour necrosis factor α (TNF-α), transforming growth factor β (TGF-β), interleukins 1β, 6 and 11 (IL-1β, IL-6, IL-11), angiopoietin-1 and -2 as well as vascular endothelial growth factor A (VEGF-A). These

molecules play major roles survival and contractility of CMs as well as promoting of vascularization in myocardial tissue[82].

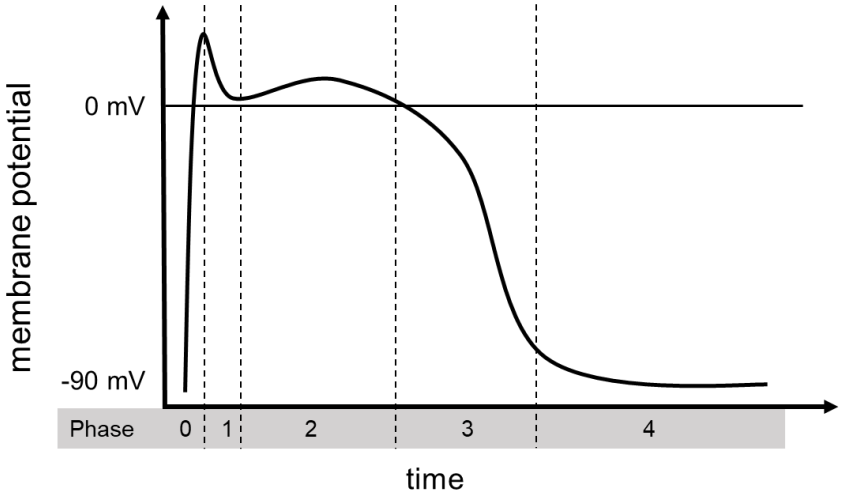

Figure 2: Membrane potential changes in CMs are distributed in five phases. 0: depolarization, 1: initial repolarization, 2: plateau, 3: rapid repolarization, 4: resting potential. Adapted from[85].

1.2.2 Endothelial Cells

ECs line the inner lumen of blood vessels and are in direct contact with molecules, nutrients, cells and toxins transported by the blood. They regulate the exchange of these molecules between blood and surrounding tissue to ensure homeostasis[66]. In addition to presenting a physical barrier between blood and tissue, ECs control vascular wall integrity and permeability, thrombosis development as well as cell differentiation and division by angiocrine signaling[91,92]. Activation of angiocrine signaling is controlled by mechanosensing via flow through VEGF receptors at the luminal side[93] and by integrin-mediated ECM-signaling at the abluminal side[94]. ECs secrete proteins to form a BM which separates the tunica intima, the innermost layer of blood vessels, from the tunica media, the middle layer of the blood vessel[6]. ECs are the main source for BM proteins, including LAM, COL4, NIDs and heparan sulfate proteoglycans[39,71]. By controlling the formation of a BM, ECs provide initial stability and spatial orientation during organogenesis[66,95]. Additionally, ECs secrete signaling molecules and various growth factors that can influence proliferation, migration and

differentiation[6,96], underlining their important role during development and homeostasis.

Vasculogenesis, the de novo formation of vessels, occurs three weeks post-gestation, when vascular plexuses are formed from multipotent mesenchymal cells[97]. Vascular maturation and branching angiogenesis leads to extension and maturation of these premature vessels[98,99]. Simultaneously, from three to eight weeks post-gestation, organogenesis occurs, where the changing local environment drives the differentiation into organ-specific ECs, which secrete growth factors pushing the differentiation of organ-specific cell types[39,100]. Hence, ECs express a significant heterogeneity between organs and even within organs, influencing phenotypes and functionality of other cell types[14].

Once matured, blood vessels are composed of three layers. The first and outermost layer is the tunica adventitia, comprised mainly of fibroblasts that secrete ECM proteins to form the IM around the vessel to provide mechanical stability. The middle layer, tunica media, contains SMCs and pericytes, while the inner layer, tunica intima, is built up by ECs[14,101]. As highlighted earlier, blood vessels are classified into three groups: arteries, veins and capillaries. Depending on their location in the cardiovascular systems, ECs express significant differences. Arterial ECs form a dense monolayer with high barrier function and have reduced proliferation and branching to maintain this phenotype[102–104]. Furthermore, arteries are characterized by a thicker and stronger BM encompassing more SMCs to provide mechanical support to withstand high arterial pressure[103–105]. In contrast, veinous ECs are more proliferative[103,104] with higher branching capabilities[103,104], leading to a more irregularly shaped vessel structure. Veinous ECs express less BM proteins, resulting in thinner BM and tunica media[103–105], which increases their elasticity.

When the blood travels along the vascular tree from the heart to peripheral tissues, it reaches capillary structures where the exchange from tissue to blood takes place[81]. The morphological appearance of capillaries is designed to facilitate the exchange of oxygen, nutrients and waste. It is important to note that not only the perivascular sheath surrounding vessels decreases traveling along the vascular tree

from macro- to microvasculature, also the thickness of ECs themselves decreases from 1 µm in macrovasculature down to 0.1 µm in capillaries[7].

1.2.3 Cardiovascular Extracellular Matrix and Pathologies

A functional vasculature that provides a healthy BM is vital for maintaining functionality in cardiac tissue. The shape and function of CMs is dictated by their cytoskeleton, which is also responding to the underlying BM[82]. CMs mainly interact with the underlying BM by integrin-signaling and dystroglycans and DDR1/2[67]. Dystroglycans are the major non-integrin receptor in the membrane of CMs. These transmembrane receptors are comprised of α-/β-domains that form adhesion complexes with proteins of the BM, such as LAMs or dystrophin to support sarcolemma stability against mechanical stress[67,106]. DDR1 and 2 are the second non-integrin receptor tyrosine kinases of the CM membrane. They have been described to interact with BM proteins such as COL4 and other fibrillar collagens[107], offering binding sites for both IM and BM. Binding of DDRs activates autophosphorylation of tyrosine to control proliferation, migration and adhesion and can further be harnessed as markers for cardiac fibroblast induced matrix remodeling after myocardial ischemia (MI) or MI and reperfusion injury (MI/R)[107].

Changes in the ECM of cardiac tissues are associated with a variety of diseases. In the native state, cardiac BM is composed of LAM and COL4 interconnected by perlecan and NIDs. The BM ensures cellular polarization, acts as reservoir for growth factors and anchors the residing cells to the IM[67,108]. Collagen types 15 and 18 are polarized to link the BM to IM. Additionally, direct interaction between COL4 and collagen type 6 creates a physical connection between the fibrils of IM and BM to strengthen their cohesion[67]. Deficiency in perlecan and NIDs, can lead to lethal cardiac abnormalities, since they are critical to maintain structural integrity of the BM under mechanical stress[109,110]. COL4 deficiency results in blood vessel dilation, cardiac hemorrhaging and abnormal development[111,112]. Similarly, LAM deficiency can lead to microvasculature rupture, resulting in the development of CVDs such as hypertrophic cardiomyopathy[67].

CVDs are the leading cause of death attributing to more than 60 million deaths per year in Europe alone[113,114]. From 1990 to 2019, the worldwide prevalence doubled to 523 million cases[67], where patients above 80 years are most affected with a prevalence rate greater than 80%[115]. CVDs include diseases of the heart itself, such as hypertrophic cardiomyopathy and MI/R, as well as diseases of the vascular system, including atherosclerosis or deep vein thrombosis[82].

A disease pattern often associated with constriction of coronary arteries is MI/R[116]. MI/R is characterized by reduced or no blood flow to the heart resulting in an imbalance between oxygen supply and demand (ischemia) resulting in damage and dysfunction of cardiac tissue[117]. Studying MI/R has shown that the reperfusion injury attributes for 50% of the final MI size[118]. The main cells suffering from reperfusion injury are CMs. The lethal reperfusion results in oxidative stress, intracellular Ca^{2+} overload and rapid changes in pH-value which causes mitochondrial permeabilization[118]. Characteristical changes in the MI/R zone include glycogen depletion, margination of nuclear chromatin, mitochondrial swelling, breaking of sarcolemma and scarring[116]. Depending on the severity of the MI/R, mitochondrial permeabilization can be rescued or results in apoptosis or necrosis[117]. Disruption of the mitochondrial membrane causes production of reactive oxygen species which activate stress pathways via IL-1β, TNF-α and nuclear factor k-light-chain-enhancer of activated B cells (NF-κB) resulting in CM death[117]. In the surrounding microvasculature, reactive oxygen species signaling can lead to impaired vasomotion, obstruction, microembolization, leukocyte adherence accompanied by infiltration and inflammation and even rupture of vessels to further worsen the pathological state[116]. Several approaches have been pursued to inhibit the activation of such stress pathways, decrease the MI/R scar size and restore native ECM composition[116]. These include the inhibition of inflammatory process by phosphoinositide 3-kinases -γ/-δ inhibitors, the use of anti-apoptotic agents (e.g., erythropoietin) or intracoronary aqueous oxygen[118]. Another strategy is ischemic preconditioning by controlled reduction of oxygen in remote tissue which activates protective nitric oxide pathways[117]; however, there are currently no effective treatments available to reduce the MI/R scar size and the one year mortality rate remains above 10%[116,118].

After pathological stimuli, such as long-term heightened blood pressure or MI/R, which result in apoptotic or necrotic CMs, the remaining CMs are exposed to increased workload. This increased stress over time and the limited proliferative capacity of the remaining CMs leads to CM growth as well as ECM remodeling termed hypertrophic cardiomyopathy[80]. Hypertrophic cardiomyopathy can activate the pathways involving protein kinase B, glycogen synthase kinase-3 β, or ERK1/2. Disruptions in these pathways can result in systolic (contractile) dysfunction, which is characterized by increased secretion of MMPs and reduction in COL network integrity, driving CM loss; or diastolic (relaxation) dysfunction induced by excessive production of fibrillar COLs in the IM as well as COL4 in the BM accompanied by impaired sarcolemma anchorage[67].

Other cardiac diseases involving changes in the ECM are myopathies. Myopathies are rooted in mutations of the CMs within the striated muscles located in the myocardium, affecting their mechanosensing. The dysregulation of integrin-mediated interaction between sarcomeres and ECM can lead to hypertrophic cardiomyopathy[119–122]. Concomitant changes in cardiac behavior can increase the deposition of COL1 by cardiac fibroblasts resulting in cardiac fibrosis[123]. Changes in the cardiac ECM composition have a negative impact on CM function, as the BM ensures separation and interaction between intracellular structure of CM with the extracellular space and provides binding sites for signaling ions including Ca^{2+} [67,87]. A functional ECM therefore plays an important role in mammalian transmembrane ion exchange and cardiac function[87]. Tissue engineered implants used to treat cardiac diseases must be designed to mimic and replace the structure and function of native tissue[124]. Approaches include the use of isolated ECM proteins or decellularized tissue to provide a structure closely mimicking native ECM to support neoformation of tissue in vivo[124,125]. Isolated ECM proteins used for cardiac tissue engineering include fibrin, elastin or COL1. Fibrin offers controlled degradation properties and improved elastogenesis compared to COL1[126] and has already been used to successfully deliver mesenchymal stromal cells (MSCs) into regions of MI/R[127]. Elastin offers comparable mechanical strength as the native tissue regarding both CMs and ECs and offers autocrine signaling for controlled SMC regulation[128–130]. COL1, as a main

component of the cardiac IM mediates cell adhesion, proliferation, migration and differentiation and is a useful tool to study myocardial contraction and electrophysiology in vitro[124,131]. A functional recapitulation of the native ECM could be achieved by mixing all three ECM gels to offer several different binding sites and mechanical characteristics to mimic the complex architecture of human cardiac tissue[125].

1.3 Pancreatic Tissue

The pancreas is part of the digestive system and consists of exocrine tissue (>95%) and endocrine tissue (<5%)[132]. The exocrine pancreas consists of acinar cells that secrete digestive enzymes, such as amylase, proteinase and lipase into the gastrointestinal tract to digest fats, proteins and carbohydrates[133]. The endocrine pancreas is built up by islets of Langerhans that secrete hormones to regulate blood glucose levels[134]. Islets of Langerhans are aggregates of different cell types with a size ranging from 50-400 µm in diameter, with a mean diameter of 150 µm[135,136]. The two main cell types in islets of Langerhans are ~30% α-cells secreting glucagon and ~60% β-cells secreting insulin[137]. Glucagon is secreted at low glucose levels in the blood and results in breakdown of stored glycogen into glucose to elevate blood glucose levels[138]. Insulin is secreted at high blood glucose levels to mediate the uptake of fatty acids, glucose and amino acids in insulin-sensitive tissues, including muscles, adipose tissue or liver; in the liver, glucose is stored as glycogen[138,139]. Other cell types present in the endocrine pancreas include δ-cells (~5%) secreting somatostatin, a local paracrine inhibition of both insulin and glucagon[140], pancreatic polypeptide cells (~1-2%) secreting pancreatic polypeptide that regulates post-prandial pancreatic secretion activites[141], and ε-cells (1-10%) secreting ghrelin[142–145], which mediates insulin, glucagon, pancreatic polypeptide and somatostatin secretion[146–150].

1.3.1 Insulin-producing β-cells

Insulin secretion by β-cells is triggered by glucose, amino acids and non-esterified fatty acids; however, glucose is the most potent regulator[151]. Once triggered, insulin is secreted in a biphasic manner where the majority of intracellularly stored insulin is secreted within 5 min (first fast phase), and the remaining insulin is slowly released in the second phase while new insulin is produced (second slow phase)[152]. Glucose is transported into human β-cells via glucose transporter 1 via facilitated diffusion[153]. After entering the cell, glucokinase controls the phosphorylation of glucose to enter glycolysis[154]. Once the process of glycolysis is finished, the endpoint

product pyruvate is transported to the mitochondria to enter the Krebs cycle to produce adenosine triphosphate (ATP)[155]. The rise in intracellular ATP levels results in K^+_{ATP} inactivation and membrane depolarization, which opens Na^+ and Ca^{2+} channels. The entry of Ca^{2+} results in fusing the intracellular insulin vesicles with the plasma membrane to release the insulin[156] (Figure 3). Post-secretion, Ca^{2+} homeostasis is maintained by the endoplasmic reticulum (ER)[157]. Along with Ca^{2+} influx, insulin trafficking requires remodeling of the cytoskeleton and actin filaments via focal adhesion complexes which can be controlled by the MAPK pathway[158,159]. As described earlier, the MAPK pathway can be triggered by external effectors, such as binding to integrin or growth factor receptors, which suggests an important role of the BM for insulin secretion and functionality of β-cells[160].

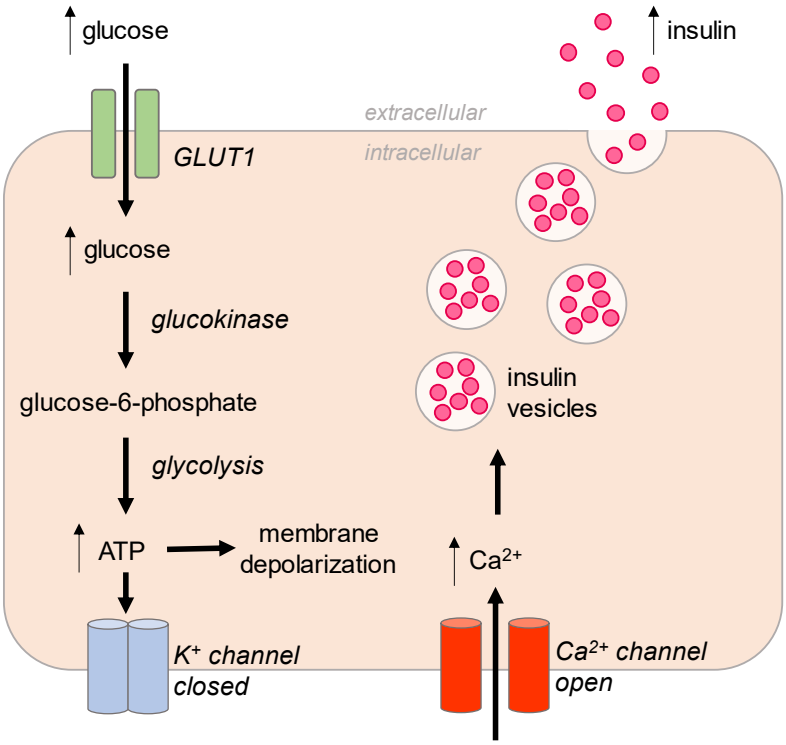

Figure 3: Schematic pathway of glucose-induced insulin secretion in β-cells. Adapted from[151].

The pancreatic ECM is mainly composed of COL4, LAM, NID1, NID2, heparan sulfate proteoglycans (e.g. perlecan)[161,162] as well as COL1 and FN[163]. Interestingly, islets of Langerhans are surrounded by two distinct BMs: the peri-islet BM that delimits the endocrine from the exocrine tissue and the vascular BM between the endocrine

tissue and the capillaries[164]. Both BM are mainly composed of LAM, COL4 and NIDs as linker proteins[165]. The BM plays an important role in developing and maintaining the function of the endocrine pancreas. LAM α5 and COL4 have been described to modulate β-cell differentiation and maturation as well stimulate β-cell functionality in vitro[166,167]. Interaction of β-cells with their environment is controlled by a large spectrum of surface proteins, including integrins, growth factor receptors, ion channels and transporters[168]. The binding of the arginylglycylaspartic acid sequence present in LAMs or FN to integrin αvβ3 is especially important for ECM related signaling[169,170]. In general, β-cells are highly susceptible to their ECM environment, where differences in composition can have a significant impact on their functionality. FN alone as well as in combination with LAMs and COL4 has been reported to have positive effects on glucose-stimulated insulin secretion (GSIS) of β-cells[171,172]; however, it was also shown that FN coating resulted in disintegration and loss of the structural integrity of islets of Langerhans[59]. COL1, which provides structural stability to the pancreas itself, plays a role in controlling β-cell survival and functionality by providing biochemical cues[15]. Immature fibrillar COL1 as a result of impaired DCN content in the ECM, can contribute to loss of β-cell glucose-responsiveness[173].

1.3.2 Endocrine Vascularization

The pancreas is a highly vascularized organ[174]. Although the endocrine pancreas only accounts for <5% of the pancreatic volume, the islets of Langerhans receive up to 20% of the pancreatic blood flow[175]. There are significant differences between the endocrine and exocrine vasculature[176]. The microvasculature of the endocrine pancreas is thinner than its exocrine counterpart, contains 5-7x more capillaries and 10x more fenestraes. It also has a thinner BM to facilitate the reciprocal exchange of glucose and secreted hormones between blood and tissue[174,177].

ECs within the pancreas are vital during development since EC signaling initiates insulin secretion and pancreatic budding, where removal of dorsal aorta precursors lead to insulin deficiency[178]. Native adult pancreatic tissue shows a capillary density of up to 400 capillaries / mm^2 [179,180], which results in a close proximity

between ECs and β-cells to ensure the quick exchange between blood and endocrine pancreatic tissue[179,181–183]. These phenotypes are tightly controlled by the secretion of VEGF-A of β-cells[179]. The VEGF-A signaling between ECs and β-cells is complex but can be summarized as follows: ECs are recruited to the endocrine pancreas by VEGF-A secretion by β-cells[179]. VEGF-A furthermore stimulates growth of vessels and fenestration to maintain the phenotype of endocrine capillaries[184–186]. The attracted ECs secrete BM proteins, especially COL4 and LAMs (namely LAM-211, LAM-322, LAM-411 and LAM-511[162,187,188]) to improve and maintain β-cell functionality, e.g. via Wnt or MAPK pathway activation and integrin-mediated interaction[38,189,190] as well as β-cell survival and therefore VEGF-A secretion, closing the feedback loop.

Additionally to VEGF signaling, thrombospondin-1 is an important glycoprotein. It is secreted by ECs and has the potential to regulate β-cell functionality via TGF-β[191–194]. It has been described to activate antioxidant defense responses within the ER via protein kinase R-like ER kinase and nuclear factor erythroid 2-related factor 2 during cellular stress. Such defense mechanisms can prolong the functionality of β-cells and ensure their survival in vivo, especially since the ER is highly involved in the Ca^{2+}-mediated sensing, production and trafficking of insulin[195].

1.3.3 Diabetes Mellitus

The disease with the highest impact on modern society associated with the pancreas is diabetes mellitus (DM). DM is a chronic disease characterized by chronic hyperglycemia due to the depletion and dysfunction of β-cells and accompanied loss of insulin for blood glucose regulation (type 1) or the defective response to the secreted insulin (type 2)[139,196]. 10% of the whole adult population suffer from either type 1 or type 2 DM, and the numbers are expected to rise from currently 537 million patients to 783 million patients by 2045[197]. The majority of DM patients suffer from type 2 DM, which is a multifactorial disease that results in dysregulation of insulin signaling and the concomitant loss of glucose regulation. Several target organs of insulin contribute to the development of type 2 DM, such as the liver, pancreas, adipose tissue and skeletal muscle by lipid accumulations within these tissues that

directly lead to insulin resistance[198]. The main causes of this lipid accumulation are high calorie diets and excessive intake of sugar, saturated fatty acids and fats[197]. Type 2 DM can be treated by physical exercise as well as dietary change. The remaining 5-10 % of patients suffer from type 1 DM. The specific cause for the autoimmune destruction of β-cells is still unknown; however there are several risk factors that trigger the pathological development such as genetic predisposition[199], an overprotective immune system with auto-reactive thymic lymphocytes[200], a general immune response dysfunction[201,202] as well as environmental influences (microbiota, dietary change or viral infections)[203]. These patients rely on lifelong medication by intake of exogenous insulin via single injections or pump systems.

1.3.4 Edmonton Protocol

Severe cases of type 1 DM can be treated with the transplantation of donor islets into the patient, known as the Edmonton protocol[204,205]. In this process, the donor human pancreas is enzymatically digested to isolate the islets of Langerhans that are then injected into the portal vein of the liver of the patient; however, long-term insulin independency fails because of impaired graft survival due to loss of ECM[70,206] and lack of vascularization following islet isolation and transplantation[181,204,207]. Up to 60% of transplanted islets fail within the first week post-transplantation due to initial ischemic conditions, leading to a maximum insulin independency of one to five years[208,209]. Long-term complications include immune response modulated fibrotic capsule formation around the graft including the transplanted islets of Langerhans, resulting in decreased vascularization concomitant with lack of oxygen and nutrient supply leading to loss of cellular mass[210,211]. During the enzymatic digestion of donor pancreases to isolate the islets of Langerhans, both vascularization and native ECM surrounding islets are removed, limiting the chances of islets survival significantly[212]. Therefore, restoring the native pancreatic ECM that surrounds the islets of Langerhans in vivo, and the BM of islets in particular to protect the functionality of insulin-secreting β-cells, is of special interest[213,214]. One promising approach is the supplementation of native ECM proteins to support the successful integration of

transplanted islets into the recipient's body and improve the survival and functionality of islets post-transplantation[215–217]. The supplementation of native BM proteins, including the use of NID1, has already been shown to improve the survival and functionality of isolated human islets ex vivo[218], highlighting the important role of islets' BM in the pancreas; however, the specific roles of the single ECM proteins during transplantation is not fully understood yet[219].

Apart from the destruction of ECM, native vascularization is highly affected by current isolation protocols resulting in decreased long-term functionality and survival[220,221]. The microvasculature, responsible for ECM-mediated signaling, and the capillary network, supplying nutrients and oxygen to the islet[222], are especially affected. Destruction of the vasculature directly affects oxygen concentration and is followed by ischemic conditions of around 1% oxygen in the islets compared to native 20% oxygen[223]. These hypoxic conditions initially affect the islets' core, represented by increase in apoptosis and necrosis in the central region of the islets[224,225]. Internal apoptosis and necrosis can be hard to identify, demanding improved isolation protocols or support of islets post-isolation.

Recreating the pancreatic niche in vitro can support islet survival by minimizing harmful conditions on the isolated cells. This can be achieved by either mimicking the ECM composition, co-culturing with other cell types, or a combination of both. Co-culturing of β-cells or islets of Langerhans with ECs has been described to improve survival of islets of Langerhans and potentially induce pre-vascularization, a process that takes up to 14 days in vivo[226–228]. Besides being the main cell type to build up vasculature, ECs are the major source of BM proteins in the pancreas[189,215,229]. Hence, co-culturing of ECs with islets might not only be beneficial on survival and functionality, but is also necessary to recreate the pancreatic niche, making them a highly potent candidate to improve islet survival ex vivo. Other cell types that are described to support islets survival and functionality are ductal epithelial cells, fibroblasts or MSCs. Ductal epithelial cells play a major role in pancreatic morphogenesis[230] and during differentiation of stem cells into pancreatic islets[231]. Since these cells also originate from foregut endoderm, they can also be used to create insulin-producing cells[231]. In the native pancreatic niche, they secrete growth factors, such as insulin-like growth

factor II, to control the β-cell population[230,232]. A COL1-matrix populated with fibroblasts has been shown to enhance survival and functionality in vitro over 30 days as well as reducing the required amount of transplanted islets by 50% in diabetic B6 mice[233]. MSCs, a self-renewing multipotent cell type with immunomodulatory properties, offers another potent cell type for co-transplantation. They have been described to improve graft survival and function in vivo[234]. Potential reasons for improved functionality due to co-culture with MSCs include their secretion of bioactive molecules and improved cell-cell contact by increased expression of N-cadherin[235]. Consequently, the co-transplantation of islets with supportive cell types resulted in enhanced functionality and reduced revascularization time post-transplantation[236–245].

1.4 In Vitro Models for Diabetes Mellitus Research

Significant advances have been made in the recent past to decipher the pathology behind the failure of islet transplantation as well as underlying mechanisms of DM itself. Scientists rely on the use of animal models to study such mechanisms in the in vivo environment, including insects, rodents, pigs and non-human primates[246]; however, the translation from animal models to humans is difficult, since there are significant differences in species-specific pathogenic pathways at gene, protein, cell and organ level[247–251]. On top of the varying biological components between single animals, growing ethical concerns and the concepts of 3R (reduce, refine, replace) in animal research have increased the importance of in vitro models for basic research.

In vitro models offer a more ethical alternative to the use of animals with the advantage of substantial control of the environmental influence on the system[252]. Furthermore, the low costs compared to in vivo studies combined with the potential of high throughput studies make them a viable alternative[253]. DM research has greatly relied on the use of rodent-derived immortalized cell lines from primary cells, such as INS-1E or MIN6[254]. Although these cell lines offer reproducible results, the translatability of results from rodent to human models is limited. Especially for β-cells, there are reported species-specific differences regarding mechanisms of glucose metabolism and insulin secretion, such as in glucose uptake by glucose transporter 4, Krebs cycle, insulin-response to glucose stimulation and other pathways involved in insulin secretion and gene expression[249–251,255]. As an alternative to rodent β-cells, cadaveric human islets from organ donors can be used for in vitro models; however, availability of donor organs is highly limited and the quality of those available for research is often poor[256]. Additionally, donor-related variations result in heterogenic experimental outcomes[257,258]. Donor variability is important to validate the efficacy, e.g., during the development of new drugs prior to in vivo studies; however, for the establishment of an experimental setup, donor variability can be hindering.

Only recently, in 2011, a human-based immortalized β-cell line was introduced that overcame the so far existing shortcoming of senescence and loss of glucose-responsiveness over time in human-based β-cell models[259]. Due to subsequent advancements, there is now a variety of subsets of functional human-based β-cell

lines available with different properties, such as conditionally immortalized, proliferative cell lines that can be turned into non-proliferating, glucose responsive β-cells or thaw-and-go, non-proliferative β-cells that highly match the insulin-secretory profile of native human islets[260–262].

The main drawback of such highly controllable in vitro systems is the lack of physiological relevance, since they do not represent the complexity of the in vivo situation[263]. To improve such systems, the use of ECM proteins and co-cultures have been established to recreate the native environment[219]. Further improvements have been made to induce physiological signals to the system by mimicking biomechanical forces through microfluidic devices, e.g., organ-on-a-chip systems[264]. These devices can combine mechanophysiological stimuli in combination with several cell types and native ECM cues to accurately recapitulate the native environment of a specific cell type of interest in a controlled manner. To study such complex systems without disturbing the intrinsic equilibrium, non-invasive imaging methods can be used[265].

A non-invasive imaging technique that is receiving more and more attention in the field of biology is Raman microspectroscopy. Raman microspectroscopy is a standard technique in material and pharmaceutical sciences to characterize the molecular structure of proteins and polymers[266,267]. The method is based on inelastic scattering where a laser is focused on the sample of interest and incoming photons interact with molecules of the sample and result in both elastic and inelastic scattering (Figure 4)[268]. In the case of inelastic scattering, where the kinetic energy of the scattered particle is either increased (Anti-Stokes-Raman) or decreased (Stokes-Raman). The scattering results in a rotation-vibrational state of the interacting molecule which can be detected by a frequency shift specific for molecular bonds[269]. Recently, researchers have applied Raman microspectroscopy to characterize biological samples to give insights on the biomolecular composition of the tissue and underlying structures, such as lipids, proteins or nucleic acids[270,271]. Raman microspectroscopy has mainly been used to identify structural changes in cancerous samples[272–278], but also to track the differentiation processes in neurons[279], cardiomyocytes[280,281] and pancreatic progenitors[282]. The non-invasive nature of

Raman microspectroscopy makes it a viable tool to monitor and control the quality of in vitro models over time.

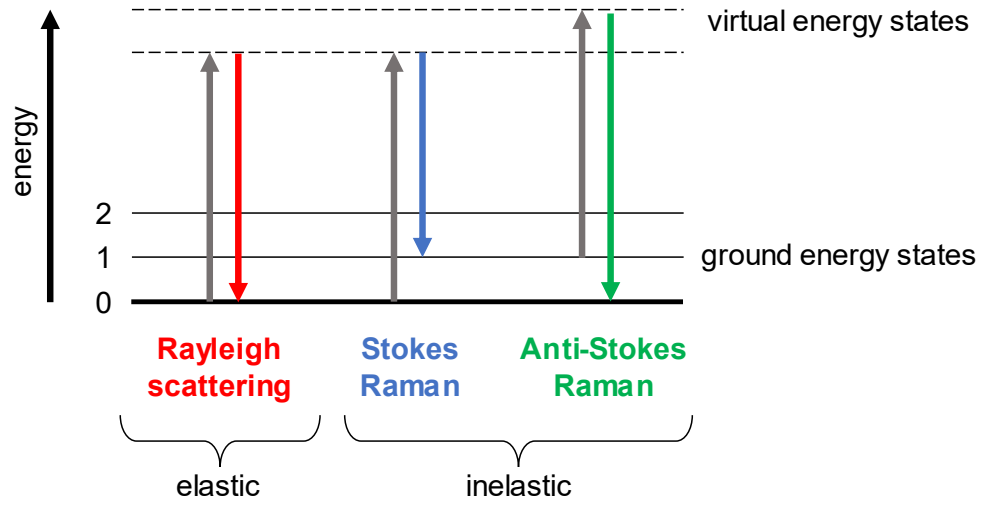

Figure 4: Interaction of incoming photons with molecular structures results in elastic and inelastic scattering. Adapted from[268].

Chapter 2

Objective of the Thesis

2 Objective of the Thesis

The aim of this study is to investigate the influence of different ECM proteins on cardiac and pancreatic tissues during periods of normoxic and ischemic environments to support functionality and survival, and understand the mechanisms of action to be harnessed during MI/R or islet transplantation.

In the first step, we investigated cardiogenesis and identified the BM protein NID1 to be cardioinductive. We hypothesized that these cardioinductive properties of NID1 could be harnessed to support the cardiovascular system during ischemic conditions in vitro and mitigate the harmful effects of ischemia on cells involved in CVDs. Apart from the impact of NID1 on the survival of CMs, we were interested in the effect of NID1 on ECs and fibroblasts, since a functional microvasculature is essential for wound healing, while transdifferentiation of fibroblasts into myofibroblasts is the main driver of fibrotic response post-ischemia[16,22]. We further performed in vivo studies in mice modeling MI/R to investigate whether the results found in vitro are translatable to the in vivo environment. Additionally, we analyzed the effect of NID1-treatment on scar size post-MI/R in mice, as pathogenic CM remodeling post-ischemia is a driving factor of MI size and therefore survival rate.

In pancreatic tissue, especially for the endocrine pancreas, the restoration of native ECM post-transplantation is vital for the successful integration into the host. We therefore investigated in vitro the role of the BM protein NID1, under normoxic and hypoxic conditions regarding survival and functionality of insulin-secreting β-cells and explored its mechanisms of action. In addition to NID1, we asked, whether the IM protein DCN, which is vital for regulation of fibrillogenesis of COL1 in vivo, can be leveraged to stimulate β-cell functionality and modulate fibrosis formation post-transplantation in vitro. These effects were investigated in suspension as well as encapsulated in a COL1 carrier material.

As ECM is mainly secreted by ECs and the pancreas is a highly vascularized organ, we aimed to improve our in vitro models by implementing a co-culture system of insulin-producing β-cells and ECs. Initially, we harnessed the approach of magnetic levitation to create stable co-culture pseudo-islets in suspension to study the

stimulatory effect in different spatial distributions. Once the co-culture was successfully established, we used the system to co-encapsulate β-cells and ECs in a COL1 carrier material in a post-transplantation setup and analyzed the impact of the co-culture on ECM expression and functionality.

Through these four studies, we aim to highlight that the incorporation of native ECM proteins, either through direct supplementation or through the use of supportive cells, is important for the survival and functionality of cells of different tissue origins. We further address that these proteins are usable in an in vivo approach through their incorporation in carrier materials towards the long-term goal of improving the outcome of MI/R and islet transplantation through recapitulation of the native ECM.

Chapter 3

Results & Discussion

The content is based on:

Urbanczyk M., Zbinden A., Layland S.L., Duffy G.P., Schenke-Layland K.; Controlled Heterotypic Pseudo-Islet Assembly of Human β-cells and Human Umbilical Vein Endothelial Cells Using Magnetic Levitation, *2020*, Tissue Engineering Part A 26 (7-8), 387-399.

Urbanczyk M.[§], Zbinden A.[§], Layland S.L., Becker L., Marzi J., Bosch M., Loskill P., Duffy G.P., Schenke-Layland K.; Collagen and Endothelial Cell Coculture Improves β-cell Functionality and Rescues Pancreatic Extracellular Matrix, *2021*, Tissue Engineering Part A, 27 (13-14), 977-991.

Zbinden A.[§], Layland S.L.[§], **Urbanczyk M.**, Carvajal Berrio D.A., Marzi J., Zauner M., Hammerschmidt A., Brauchle E.M., Sudrow K., Fink S., Templin M., Liebscher S., Klein G., Deb A., Duffy G.P., Crooks G.M., Eble J.A., Mikkola H.K.A., Seifert M., Schenke-Layland K.; Nidogen-1 Mitigates Ischemia and Promotes Tissue Survival and Regeneration, *2021*, Advanced Science, 8(4), 2002500.

Urbanczyk M.[§], Jeyagaran A.[§], Zbinden A., Lu C., Marzi J., Kuhlburger L., Nahnsen S., Layland S.L., Duffy G.P., Schenke-Layland K., Decorin Improves Pancreatic β-cell Function and Regulates Extracellular Matrix Expression in vitro, Matrix Biology, in revision.

3 Results & Discussion

3.1 Protective Effects of Nidogen-1 in Ischemic Cardiac Tissues

Ischemic conditions during MI/R result in severe tissue damage and pathological remodeling of the native ECM[283,284]. This in turn can lead to cell death, differentiation and mutations of the initially unaffected cells, worsening the clinical outcome of MI/R[41]. Due to the limited regenerative capacity of cardiac tissue, current treatments include the injection of cells, growth factors, small molecules and native ECM proteins into the damaged cardiac tissue to support cellular survival, reduce scar size and improve clinical outcome for MI/R patients[285–289].

In the first part of this work, we focused on the use of native ECM proteins present in cardiac tissue to support the survival of CMs. We investigated the expression of different ECM proteins in embryonic bodies (EBs) that underwent cardiovascular differentiation[290,291] and found a significantly higher expression of NID1 compared to FN, periostin, LAM, COL1 and COL4 in spontaneously beating EBs (Zbinden & Layland et al., **Appendix I**, Figure 1 A,B), suggesting that NID1 plays an important role in cardiac differentiation. To test this hypothesis, recombinantly produced full-length human NID1 was supplemented during differentiation into cardiac lineage, which resulted in increased expression of *TNNT2*, *ACTA2* and overall cardiac troponin T (CTNT)-positive cells in spontaneously beating EBs (Zbinden & Layland et al., **Appendix I**, Figure 1 C,F). CTNT, encoded by the gene *TNNT2*, is solely expressed in CMs as part of the sarcomeric structure that regulates their contractility, whereas *ACTA2* encodes α smooth muscle actin (αSMA), a marker for early mammalian heart development. Together, the upregulation of these genes and CTNT in EBs after NID1 treatment supports our hypothesis that NID1 drives differentiation towards the cardiac lineage[292,293]. Interestingly, we found that NID1 is also present in adult heart tissues, suggesting that NID1 not only plays a cardioinductive role during development, but also a role in cardiac tissue homeostasis over time, making NID1 a potential treatment option post-MI/R (Zbinden & Layland et al., **Appendix I**, Figure 1 G,H).

MI/R induces a variety of pathological changes in cells present in the cardiac tissue, including CMs, ECs and fibroblasts. To induce the in vivo effects of MI/R on cardiovascular cells in vitro, we exposed cells to hypoxic conditions of 1% oxygen, recapitulating the oxygen tissue concentration during ischemic invents, and investigated whether NID1 can mitigate these hypoxic effects. The supplementation of NID1 to human induced pluripotent stem cell (hiPSC)-derived CMs resulted in a significant decrease in caspase-3 expression and terminal deoxynucleotidyl transferase dUTP nick end labeling (TUNEL)-positive cells under hypoxic conditions. Caspase-3 is a downstream activator of the apoptotic pathway, while the TUNEL-assay identifies DNA fragmentation as a marker for late-stage apoptosis[294]. The combination of downregulated caspase-3 expression and TUNEL-positive cells post-NID1 treatment under hypoxic conditions showed that NID1 can reduce the impact of hypoxia-induced cell death in CMs (Figure 5 A,B). In addition to improved survival, NID1-treated CMs expressed significantly higher levels of *TNC*, *TGFB1* and *THPS1* (Figure 5 C). *TNC* is involved in the detachment process of CMs from pathological ECM for reorganizing and rebinding to the ECM, preventing anoikis[295]. Additionally, both *TNC* and *THPS1* are downstream activators of TGF-β-signaling, which is a regulator of fibrotic fiber deposition in cardiac tissue post-infarction[296].

The main cells responsible for pathological ECM remodeling post MI/R are fibroblasts that transdifferentiate into myofibroblasts following hypoxia concomitant with increased deposition of ECM proteins resulting in fibrotic scar formation[16,22]. Human dermal fibroblasts cultured under hypoxic conditions expressed significantly higher levels of *αSMA*. Upon NID1-treatment, this expression could be completely inhibited, indicating that NID1 prevents the phenotypic switch from fibroblasts to myofibroblasts, potentially minimizing the pathological ECM remodeling post-MI/R (Figure 5 D). In addition to preventing the phenotypic switch, we found that especially the expression of MMP genes, namely *MMP7*, *MMP11*, *MMP12* and *MMP13* were significantly downregulated after NID1-treatment. MMPs in general are associated with ECM remodeling, showing that NID1 has the capability to limit the remodeling response of fibroblasts during hypoxic episodes.

In addition to CMs and fibroblasts, the ECs of the microvasculature are also affected by cardiac ischemia. Angiogenesis post-ischemia is vital to support ECM remodeling. Therefore, we investigated whether NID1 has the potential to improve angiogenesis in vitro. We found that NID1-treatment significantly improved several parameters related to angiogenic potential in human umbilical vein ECs (HUVECs) in vitro (Figure 5 F). In summary, NID1-treatment shows significant impact on cells of the cardiovascular system under hypoxic conditions providing cardioprotective, antifibrotic and pro-angiogenic stimuli that could improve the outcome in of MI/R in vivo.

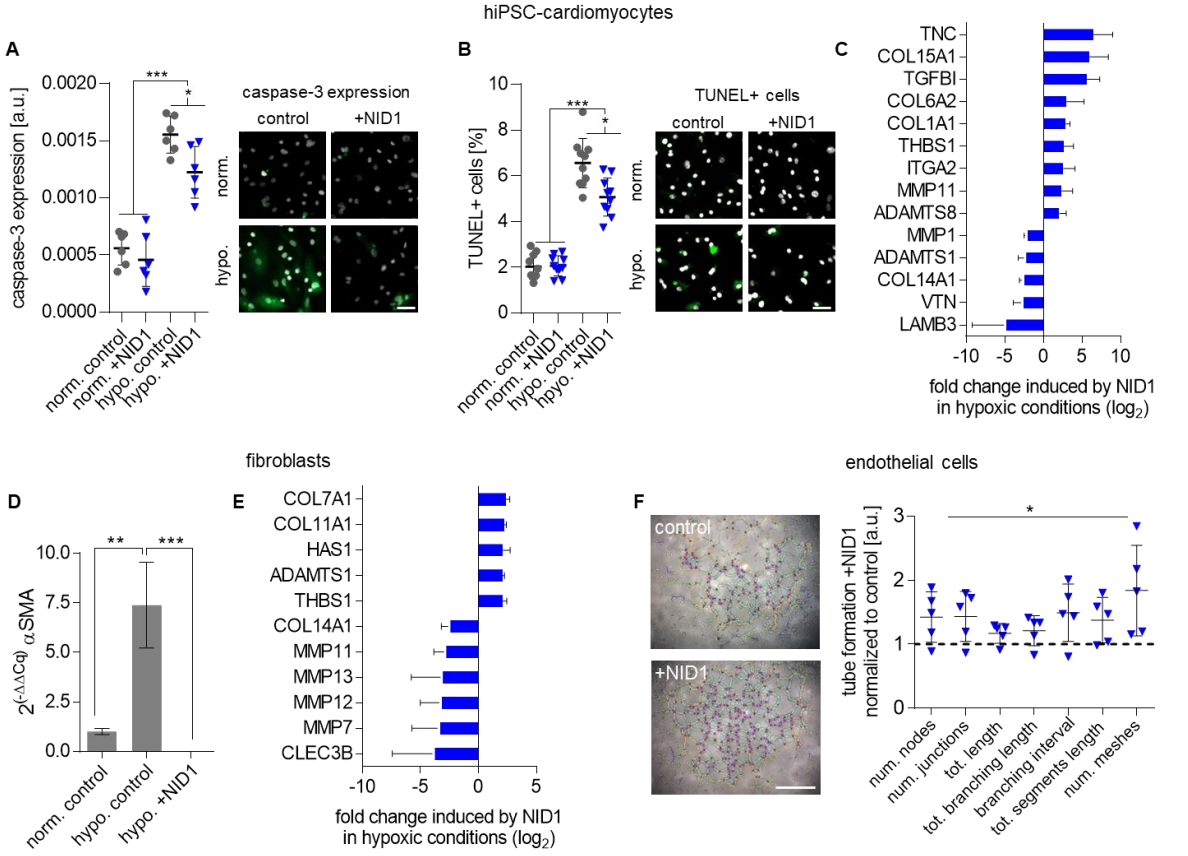

Figure 5: ***NID1 reduces the harmful effects of hypoxia treatment on cardiovascular cells. (A,B)*** *NID1 supported survival of hiPSC-CMs under hypoxic conditions shown by* ***(A)*** *reduced caspase-3 expression (n = 6) and* ***(B)*** *reduction in TUNEL-positive cells (n = 10); 1-way ANOVA with Tukey's multiple comparison.* ***(C)*** *Gene expression differences in hiPSC-CMs induced by NID1-treatment of genes related to matrix production, degradation and regulation via qPCR array (n = 3).* ***(D)*** *NID1-treatment significantly reduced αSMA expression in fibroblasts under hypoxic conditions compared to control (n = 3); 1-way ANOVA with Tukey's multiple comparison.* ***(E)*** *Gene expression differences in fibroblasts induced by NID1-treatment of genes related to matrix production, degradation and regulation via qPCR array (n = 3).* ***(F)*** *Tube formation assay of HUVECs on serum-reduced Matrigel in absence (control) and presence of NID1 showed a significant upregulation of pro-angiogenic parameters after NID1-treatment. For qPCR, only significantly differentially regulated genes with a fold change > |2| and p<0.05 are displayed. *p<0.05; **p<0.01, ***p<0.001 and ****p<0.0001. Scale bars equal 50 µm. Adapted from*[215].

To understand the mechanisms of action of NID1, we explored potential binding partners for NID1 in hiPSC-derived CMs, and identified integrin αvβ3 in cardiomyocytes[297]. We confirmed the binding of immobilized αvβ3 with soluble NID1 dose-dependently between 25 to 50 µg/ml via divalent cation-dependent interaction (Zbinden & Layland et al., **Appendix I**, Figure 3 A), which has been reported earlier[298]. Through blocking of αvβ3, we were able to inhibit the reduction in caspase-3 expression under hypoxic condition by NID1-treatment, elevating the values to PBS-controls (Figure 6 A). Accordingly, the number of TUNEL-positive cells significantly increased after blocking of αvβ3 in hiPSC-CMs, supporting that NID1 has a cardioprotective effect in CMs via binding to the integrin αvβ3 in vitro (Figure 6 B). The digital western blotting technique (DigiWest[299]) was used to decipher potential pathways activated by NID1 binding αvβ3. NID1-treated hiPSC-derived CMs showed significant upregulation of Bax, pERK1,2, SAPK, MOB1, Rac1/Cdc42 and Wnt3, whereas b-Raf, pFAK and Notch2 were significantly downregulated (Figure 6 C,D). Bax and SAPK are involved in pro-apoptotic pathways[300,301]. To investigate whether NID1-treatment and the concomitant increase in Bax and SAPK led to a shift towards pro-apoptotic conditions, the ratios between Bax and Bcl2 as well as SAPK and ERK1,2 need to be considered. These ratios depicted in Figure 6 E and F show no significant differences between NID1-treated CMs and control, which indicates an offset of Bax and SAPK expression by (non-significant) upregulation of Bcl2 and ERK1,2. The upregulation of pERK1,2 and Rac1/Cdc42 suggests the activation of the MAPK pathway which drives the protective effect of NID1 in CMs. The effectors of the MAPK pathway, such as pERK1,2 are expressed within CMs following cellular stress (hypoxia), protecting them from apoptosis[302]. Agrin, a proteoglycan associated with the BM, has been shown to support heart function by CMs and other heart cells through CM division and proliferation via activation of the MAPK pathway via Dag1[303]. Interestingly, agrin has also been described to bind the integrin αvβ1, activating downstream pathways including MAPK and Wnt signaling, highlighting the potential of different ECM proteins to induce cardioprotective effects via MAPK and Wnt signaling[304,305].

The upregulation of MOB1 is associated with inhibiting the Hippo pathway, which has been described to limit the cardiac regeneration in adults[306]. The upregulation of Wnt3 is a downstream element of αvβ3 activation, which has been associated with cell survival[307]. In addition to the activation of Wnt signaling, the activation of the β3-domain of the integrin is known to activate TNC expression[308], which we showed to be the most upregulated gene in hiPSC-derived CMs post NID1-treatment. All of the presented results suggest that NID1 acts in a cardioprotective manner through αvβ3 signaling in CMs via downstream activation of Wnt signaling and MAPK pathway as well as through inhibiting the Hippo pathway.

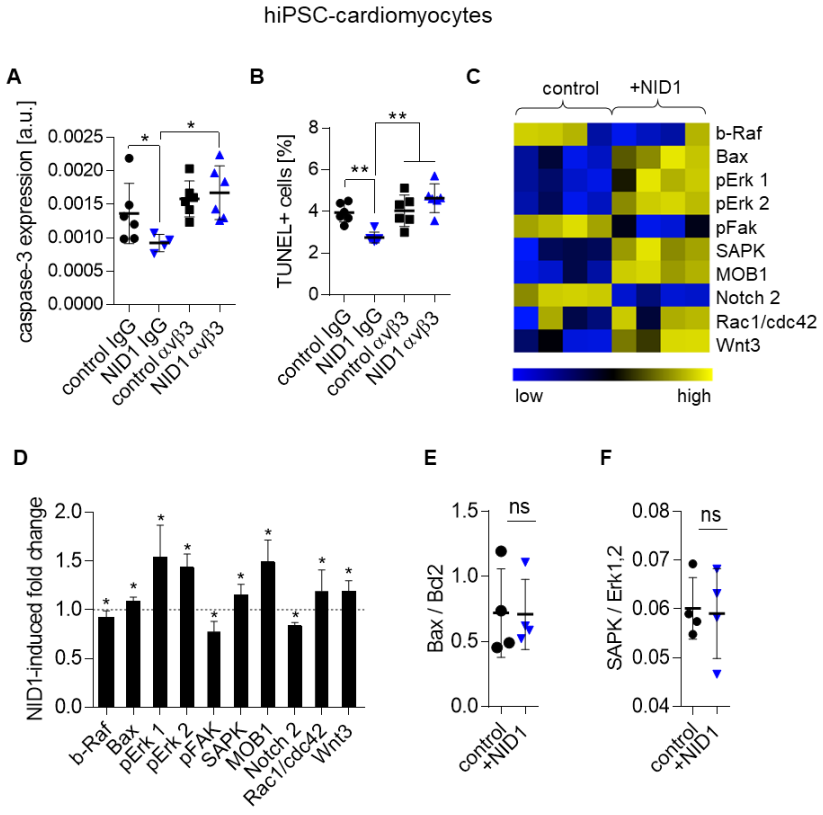

Figure 6: ***NID1 upregulates proteins of the MAPK pathway via integrin αvβ3 interaction in hiPSC-CMs.*** *Blocking of integrin αvβ3 inhibited the positive effects of NID1 on hiPSC-CMs under hypoxic conditions as shown by* ***(A)*** *increase in capase-3 expression and* ***(B)*** *increase in TUNEL-positive cells in comparison to control (n ≥ 4); 1-way ANOVA with Tukey's multiple comparisons test.* ***(C)*** *Heatmap and* ***(D)*** *column wise fold change representation of differentially expressed proteins in NID1 treated samples (n = 4); non-parametric Wilcoxon Rank sum test. Protein ratios of (****E****) Bax to Bcl2 and (****F****) SAPK to ERK1,2 showed no change after NID1-treatment (n = 4); unpaired t-test. *p<0.05; **p<0.01. Adapted from*[215].

The positive outcome of NID1-treatment on different cell types affected by MI/R injury in vitro raised the question whether these supportive and preventive effects were translatable in vivo. In C57BL/6J mice, MI/R was induced via ligation of the left anterior descending artery. Injured areas were treated post-infarction with injections of a hyaluronic acid (HA) carrier material alone or with NID1 (HA+NID1) and compared to saline-injected mice as baseline. In NID1-treated mice, echocardiographic analysis showed an overall improvement in parameters for left ventricular volume and diameter (end-systolic volume, left ventricle end-systolic diameter and left ventricular internal dimension at end-systole) compared to baseline levels 28 days after MI/R (Zbinden & Layland et al., **Appendix I**, Figure 2 A-C). Interestingly, HA-treated mice also showed an improvement, supporting previous studies that reported positive impact of HA-based hydrogels as carrier materials for cells and growth factors in cardiac tissue[309]. HA carrier materials have been used to support CM maturation with insignificant systemic immune response[310]. Muscari et al. reported an improvement in blood perfusion in combination with reduced inflammatory response after treating the infarcted area with an HA-based scaffold carrying MSCs[311]. Further, Yoon et al. highlighted the potential of pure HA to induce myocardial regeneration and function post-infarction[312]. We show that in addition to improved functionality, scar size in HA+NID1-treated mice was reduced in comparison to baseline as shown by Movat pentachrome as well as Picrosirius and Fast Green staining (Zbinden & Layland et al., **Appendix I**, Figure 2 D-L). The semi-quantification of Picrosirius and Fast Green staining showed a significant decrease in scar size by 37% throughout the heart. This finding suggests reduced transdifferentiation of fibroblasts to myofibroblasts post-infarction that results in decreased matrix deposition limiting the scar size and is in line with the previously presented in vitro data. Raman imaging was further used to identify differences between HA+NID1-treated and baseline scar tissue. HA+NID1-treated infarcted area was characterized by peaks for glycogen (497 cm^{-1}), porphyrin (1513, 1557 and 1612 cm^{-1}) and DNA (1093 cm^{-1}), which closely resembled the non-infarcted area, whereas baseline scar tissue was dominated by collagen peaks (858, 940 and 1248 cm^{-1}) (Zbinden & Layland et al., **Appendix I**, Figure S4). Hence, HA+NID1-treatment not only had an impact on the size of the scar tissue, but also

reduced overall collagen deposition, supporting the finding of reduced matrix remodeling post-MI/R in HA+NID1-treated mouse hearts.

Revascularization and reinnervation are highly important for cardiac regeneration and limitation of scar size post-MI/R[313]. IF staining for αSMA- and CD31-positive cells in the infarcted area showed a significant increase in vessel density per mm^2 in HA+NID1-treated mouse hearts compared to baseline and HA alone (Zbinden & Layland et al., **Appendix I**, Figure 2 M-Q). This finding supports the results shown in the in vitro tube formation assay indicating improved angiogenic potential after NID1-treatment. TuJ1, a marker for neuron-specific class III β-tubulin, was significantly increased in HA+NID1 treated mouse hearts compared to both HA and baseline hearts (Zbinden & Layland et al., **Appendix I**, Figure 2 R-V). This suggests that NID1 stimulates nerval reinnervation in infarcted areas, which plays an important role in successful regeneration of mammalian tissues[313].

In summary, we showed cardioprotective and pro-angiogenic effects of NID1 on different cell types of the cardiovascular system in vitro. NID1 mitigated the effects of ischemic conditions and supported survival and functionality of CMs, fibroblasts and ECs. We furthermore investigated the potential translatability for the in vivo application by treating mice with NID1 in a HA-based carrier material post-MI/R. We found that the positive results obtained in vitro could be recapitulated in vivo and resulted in improved echocardiographic results 28 days post-MI/R. Additionally, MI/R-induced scar size was significantly reduced in HA+NID1-treated mice accompanied with increased vessel density and reinnervation compared to HA-treated and baseline mice.

These findings underline the importance of recapitulating the native organ-specific environment in vitro as well as the need for ECM remodeling in vivo to support tissue regeneration after cardiac ischemic injury. Taken together, NID1 is a promising candidate to successfully reduce scar size to improve the clinical outcome and long-term survival of patients suffering from MI/R injury.

3.2 Effects of Nidogen-1 and Decorin on Pancreatic β-cells

The Edmonton protocol offers a promising long-term treatment option for patients with severe cases of type 1 DM; however, the survival rate of islets of Langerhans post-isolation and transplantation is one of the biggest limitation for this therapy[208,209]. One potential approach to support the survival and functionality post-transplantation is the restoration of the native pancreatic niche by supplementation of ECM proteins to the transplanted cells. Therefore, it is of interest to find ECM proteins that are present in native pancreas and specifically located in close proximity to islets of Langerhans.

3.2.1 Stimulatory and Protective Effects of Nidogen-1 on β-cells

In the first step, we investigated the BM proteins present in the pancreatic ECM during fetal development and adulthood. We found that the BM proteins COL4, LAM, NID1 and NID2 were present in the pancreas during both stages (Figure 7 A,B). Co-localization analysis of the co-staining with insulin (INS) revealed that NID1 had a significantly higher co-localization with INS compared to all other BM proteins (Figure 7 C). We therefore hypothesized that NID1 is a potential candidate to support islets of Langerhans post-transplantation.

In order to test our hypothesis, we supplemented human recombinantly produced NID1 to our human EndoC-βH3 β-cell pseudo-islet model. Upon supplementation with different concentrations of NID1 (20, 30 and 40 µg/ml) under normoxic conditions, insulin secretion was significantly elevated for all dosages compared to PBS controls; however, 30 µg/ml NID1 showed the highest insulin secretion at 20 mM glucose and was therefore used for future experiments (Figure 8 A). An indicator for β-cell functionality and pseudo-islet integrity is the expression of the transmembrane protein epithelial cadherin (E-cadherin), which regulates and maintains cell-cell contact through cytoskeleton remodeling and therefore functionality[314]. β-cells treated with NID1 expressed significantly higher levels of E-cadherin, which potentially contributes to the improved insulin secretion (Figure 8 B). The increase in insulin secretion cannot be attributed to more cells secreting insulin,

as cleaved caspase-3 and TUNEL-staining showed no difference between NID1-treated and control pseudo-islets (Figure 8 C). The increase in insulin secretion can therefore be associated with NID1-treatment.

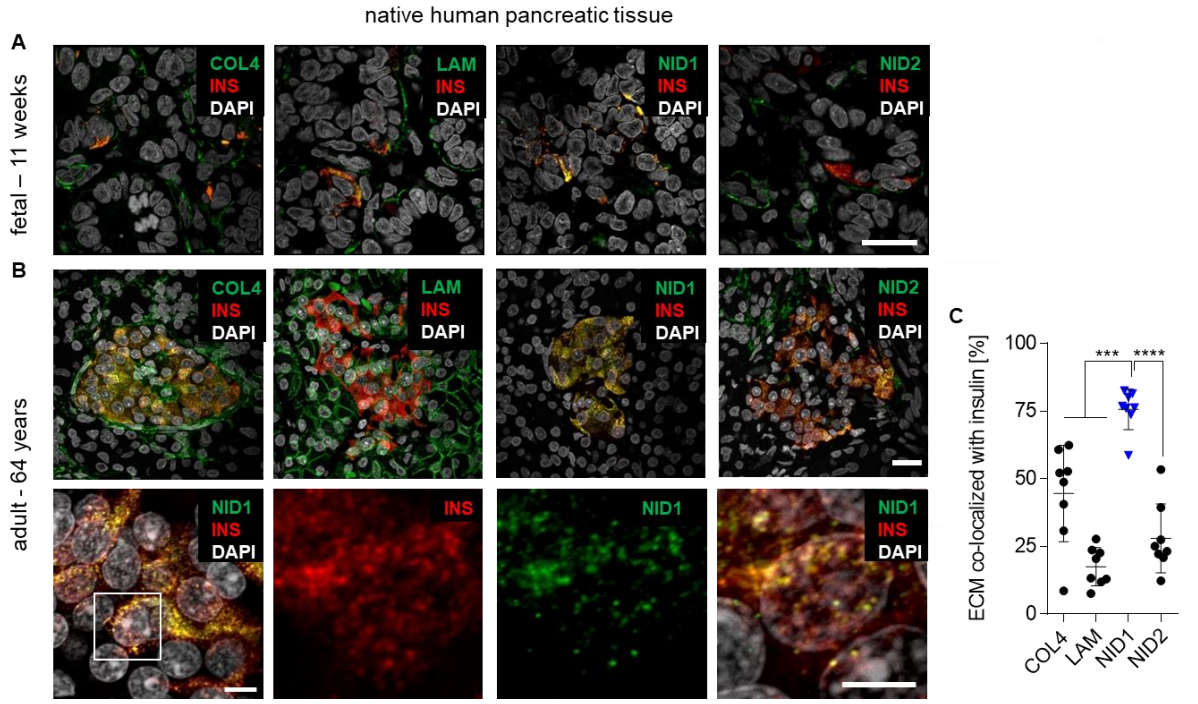

Figure 7: ***BM protein staining reveals that NID1 is highly co-localized with insulin in native pancreatic tissue.*** *Expression of BM proteins in (**A**) fetal (11 weeks) and (**B**) adult (64 years) pancreatic tissue with magnified images demonstrated a strong co-localization between NID1 and INS within the islets of Langerhans. (**C**) Co-localization quantification of the BM proteins with INS in adult pancreatic tissue (n = 10); 1-way ANOVA with Tukey's multiple comparison. Scale bars equal 20 µm for low magnification and 5 µm for high magnification images. ***p<0.001, ****p<0.0001. Adapted from*[215].

Under hypoxic conditions, NID1-treated pseudo-islets exhibited higher E-cadherin levels and were still glucose responsive in terms of increased insulin secretion at 20 mM glucose, whereas control pseudo-islets did not react to the environmental glucose (Figure 8 D,E). Concomitant with loss of glucose-responsiveness, cleaved caspase-3 and TUNEL-staining revealed significantly higher cell death in control pseudo-islets compared to NID1-treated samples (Figure 8 F).

Raman imaging of control and NID1-treated pseudo-islets under hypoxic conditions showed higher mitochondrial function as well as increases in insulin and insulin-transporting lipid vesicle expression, contributing to faster intracellular

production and release into the extracellular space (Zbinden & Layland et al., **Appendix I**, Figure S6)[315].

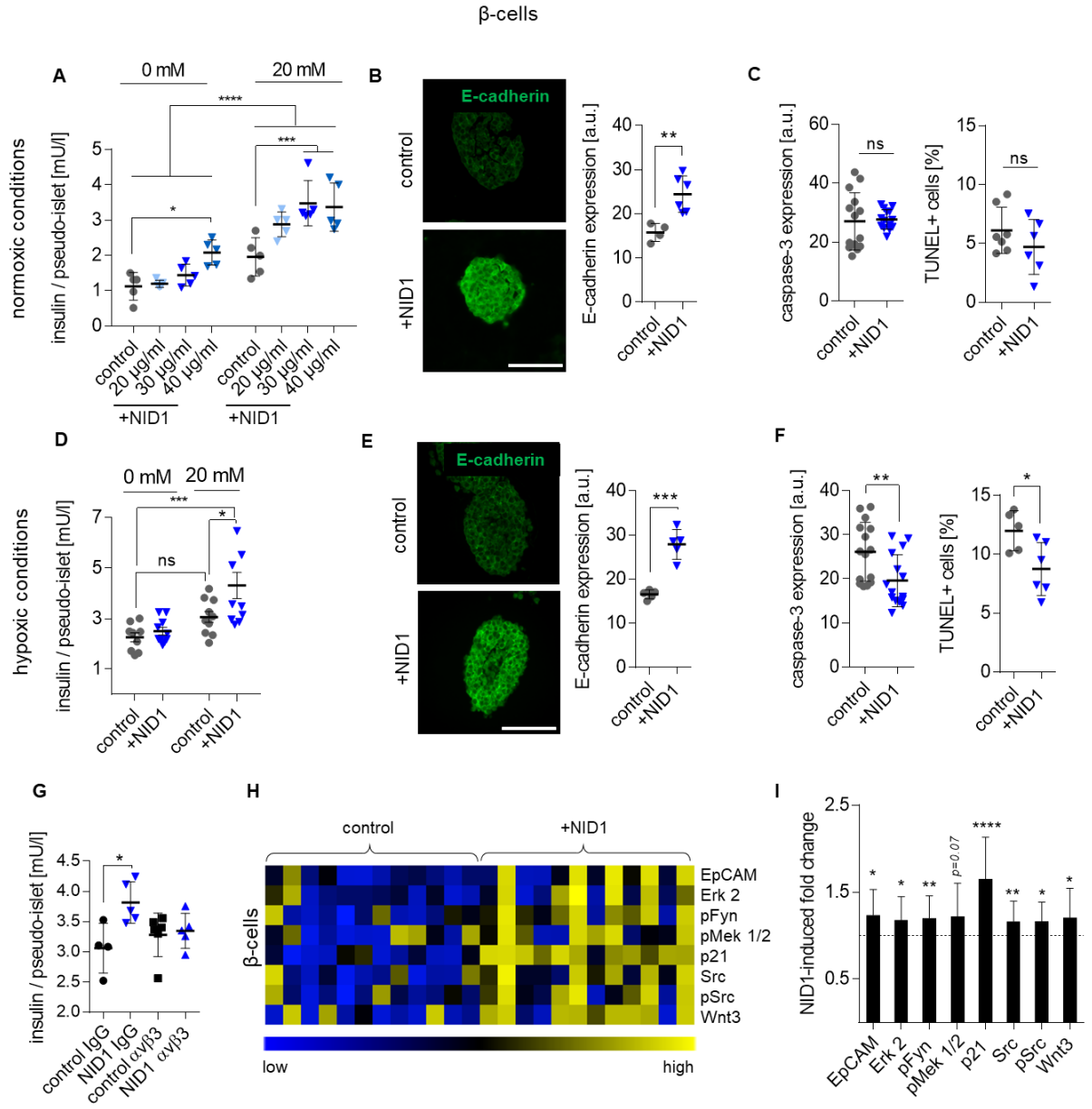

Figure 8: ***NID1 acts on human β-cell pseudo-islets via integrin αvβ3 and improves insulin secretion and survival.*** *(**A**) NID1 supplementation at 20, 30 and 40 µg/ml significantly increased the insulin secretion at all dosages compared to control (PBS) with 30 µg/ml inducing the maximum effect under normoxic conditions (n = 5); 2-way ANOVA with Tukey's multiple comparison test. (**B**) NID1-treated β-cell pseudo-islets expressed significantly more E-cadherin than control under normoxic conditions (n ≥ 5); unpaired t-test. (**C**) Immunofluorescence staining for caspase-3 (n = 14) and TUNEL (n = 7) showed no significant difference between control and NID1-treatment under normoxic conditions; unpaired t-test. (**D**) NID1-treatment at 30 µg/ml rescued glucose responsiveness of β-cell pseudo-islets under hypoxic conditions (n = 10); 2-way ANOVA with Tukey's multiple comparisons test. (**E**) NID1-treated β-cell pseudo-islets expressed significantly more E-cadherin than control under hypoxic conditions (n ≥ 5); unpaired t-test. (**F**) Immunofluorescence staining for caspase-3 (n ≥ 7) and TUNEL (n ≥ 4) showed a protective effect of NID1-treatment via a significant downregulation of both parameters; unpaired t-test. (**G**) Blocking of the integrin αvβ3 inhibited the stimulatory effect of NID1-treatment on insulin secretion of β-cell pseudo-islets at 20 mM glucose under normoxic conditions (n ≥ 4), 1-way ANOVA. (**H**) Heatmap and (**I**) column wise fold change representation of differentially expressed proteins in NID1-treated samples (n = 4); non-parametric Wilcoxon Rank sum test. *p<0.05; **p<0.01, ***p<0.001 and ****p<0.0001. Adapted from*[215].

As shown earlier, NID1 acts on CMs via αvβ3-mediated signaling. The same integrin is also expressed within the islets of Langerhans, which led us to the assumption, that NID1 acts on β-cells also through integrin αvβ3[298,316]. To validate this hypothesis, we blocked the integrin αvβ3 under normoxic conditions and showed inhibition of the positive effects of NID1-treatment on the glucose-stimulated insulin secretion (Figure 8 G). DigiWest protein analysis was used to evaluate the NID1-induced changes in protein levels under normoxic, high glucose conditions (Figure 8 H,I). We found a significant upregulation of epithelial cell adhesion molecule (EpCAM), ERK2, pFyn, p21, Src, pSrc, Wnt3 and a trend towards the upregulation of pMEK1/2. In particular, the upregulation of ERK2, pMEK1/2, Src and pSrc are strong indicators for the activation of the MAPK pathway in a comparable manner to the results found in CMs. The MAPK pathway in β-cells is involved in GSIS[158]. Furthermore, increase in Wnt3 protein expression is a result of αvβ3 downstream activation after NID1-binding, which is associated with insulin secretion and cell survival[317]. Increase in EpCAM expression might result in increased Wnt canonical signaling. This can be induced by the cooperation between the extracellular domain of EpCAM and Wnt signaling by sequestering Kremen1[318,319]. Furthermore, Wnt activation might result in a positive feedback loop with EpCAM, as EpCAM is a target of Wnt signaling itself, contributing to increased Wnt activity induced by αvβ3-ligation[320]. In summary, we suggest that NID1 acts via αvβ3-mediated integrin ligation on both CMs and β-cells to activate several downstream pathways. These pathways include MAPK signaling via upregulation of Fyn, Src and Cdc42 and crosstalk with Wnt3 signaling as well as the cell-specific regulation of EpCAM and p21 (β-cells) or Notch2 and MOB1 (CMs) (Figure 9).

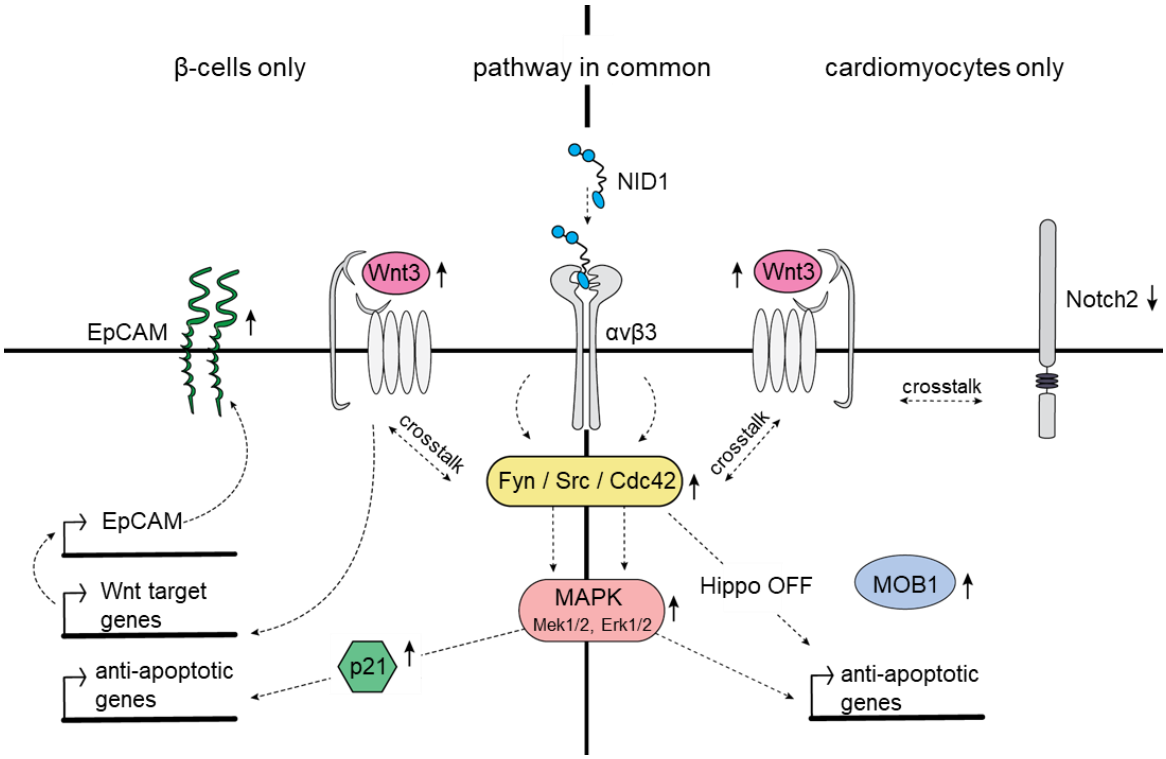

Figure 9: ***Potential mechanisms of action of NID1 on CMs and β-cells****. Center: common pathway for both cell types. NID1-αvβ3 ligation results in upregulation of Fyn/Src/Cdc42 stimulating MAPK and Wnt3 signaling. Left: β-cell-specific pathway. MAPK-induces upregulation of anti-apoptotic p21. EpCAM- and Wnt-mediated crosstalk can enhance insulin secretion. Right: CM specific pathway. Anti-apoptotic function of NID1 via Cdc42-mediated downregulation of Hippo by MOB1 upregulation. Adapted from*[215].

3.2.2 Stimulatory Effects of Decorin on β-cells

In section 3.2.1, we focused on ECM proteins of the BM within native pancreatic tissue. Here, we investigated expression patterns and co-localization of ECM proteins of both the BM (LAM, COL4) and the IM (FN, COL1, DCN) and their co-localization with INS via IF staining (Figure 10 A-E). Quantification of the co-localization showed a significantly higher correlation between INS and DCN compared to any other ECM proteins investigated in this study (Figure 10 F). To elucidate which cell type of the endocrine pancreas DCN co-localizes with, we stained islets of Langerhans for glucagon (GLU; to identify α-cells), INS (to identify β-cells) and DCN. We found that DCN is significantly more expressed in INS-positive areas compared to GLU-positive areas (Figure 10 I), suggesting a role of DCN in β-cells.

To validate our hypothesis, we treated EndoC-βH3 β-cell pseudo-islets with 50 µg/ml of recombinantly produced full-length human DCN and observed a significant increase in secreted insulin upon glucose challenge compared to the control group (Figure 11 A). This increase was also accompanied with an increase in the GSIS index, describing the fold change from low to high glucose, where a higher GSIS index indicates stronger response to the high glucose environment, highlighting improved β-cell functionality (Figure 11 A). IF staining for DCN in control and DCN-treated samples revealed the presence of a ring-like structure, showing the attachment and physical interaction of the exogenous DCN to the pseudo-islets (Figure 11 B), which occurred 24 h post-treatment (Figure 11 C). In addition to increased functionality, DCN-treatment also significantly downregulated the endogenous expression of ECM proteins FN and COL1 (Figure 11 D, E), while there was no effect on expression of E-cadherin, INS, LAM and COL4 (**Appendix II**, Figure S2). The downregulation of FN and COL1 is of special interest for graft transplantation, since they are two of the three main proteins (together with COL3) involved in immune-modulated fibrotic capsule formation[284,321,322]. The downregulation of FN and COL1 after DCN-treatment could therefore support the incorporation of the transplanted graft by reducing the fibrotic capsule formation, improving vascularization and survival of the cells. The modulatory effect of DCN has been demonstrated earlier in the context of scar tissue reduction and inhibition of inflammatory response[323–325]. The absence of DCN in mice resulted in increased inflammation by downregulation of histidase, driving inflammation, oxidative stress, insulin resistance and impaired glucose tolerance[326–329]. All results indicate a role of DCN in the regulation of inflammatory response and upholding glucose tolerance, supporting our initial hypothesis.

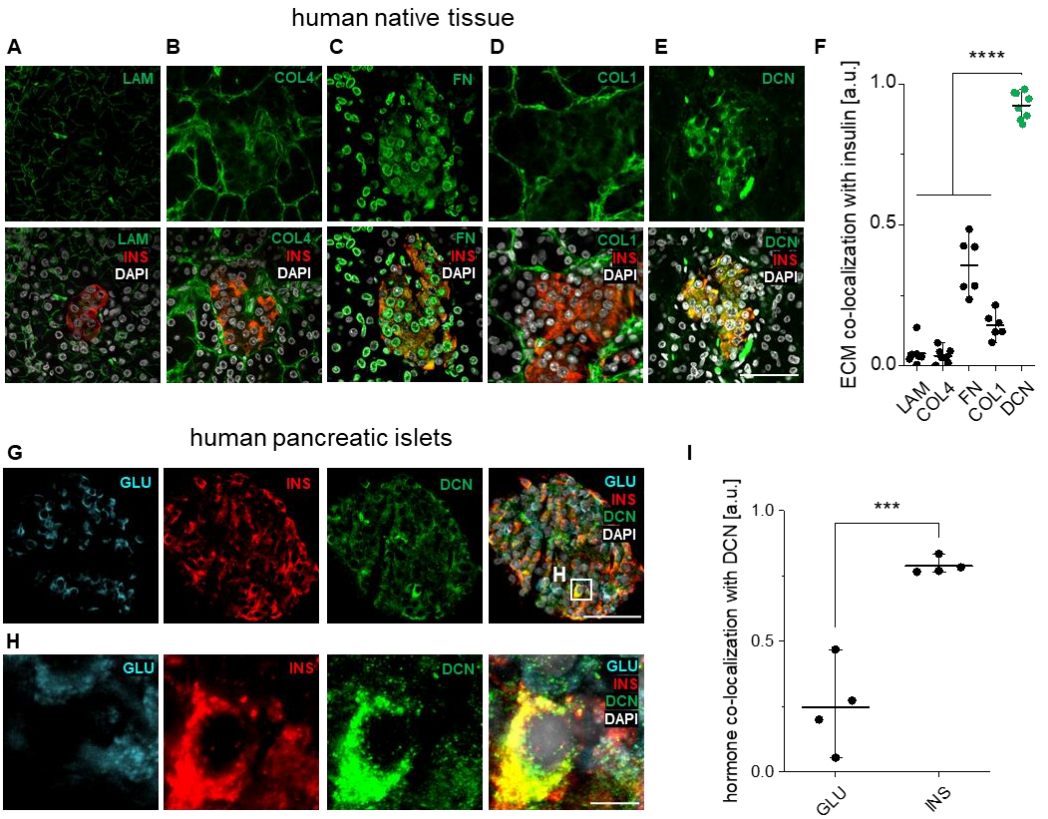

Figure 10: ***DCN co-localizes with β-cells in native pancreatic tissue***. *IF staining of native pancreatic tissue for the ECM proteins (**A**) LAM, (**B**) COL4, (**C**) FN, (**D**) COL1 and (**E**) DCN. (**F**) Co-localization quantification with INS showed significantly higher correlation between DCN and INS compared to the other ECM proteins (n ≥ 6); 1-way ANOVA with Tukey's multiple comparison test. (**G,H**) IF staining for GLU, INS and DCN in human islets of Langerhans. (**I**) Quantification of co-localization of DCN with GLU and INS showed significantly higher correlation between DCN and INS compared to DCN and GLU (n = 4); unpaired t-test. Scale bars equal (**A-E, G**) 50 µm and (**H**) 5 µm. ***p<0.001, ****p<0.0001.*

We employed next-generation sequencing to understand the underlying DCN-induced changes in gene expression that led to improved insulin secretion in β-cells. We found that a total of 348 genes were differentially expressed upon DCN-treatment. 84 of these 348 genes were mapped to specific pathways using the Kyoto Encyclopedia of Genes and Genomes (**Appendix II**, Figure 3 A). 51 of these 84 genes were involved in pathways regulating β-cell metabolism, namely ER, oxidative phosphorylation (OxPhos), cyclic guanosine monophosphate, semaphorin, MAPK and type 2 DM (**Appendix II**, Figure 3 B). Of special interest are pathways involving the OxPhos and the ER.

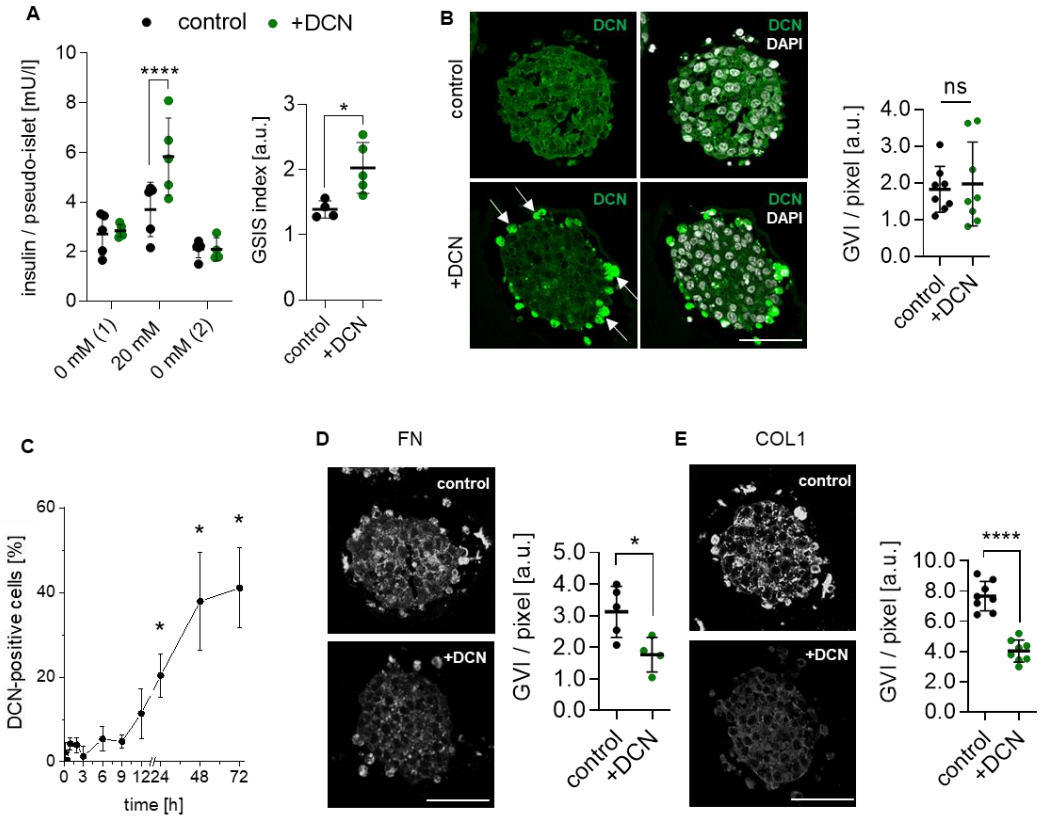

Figure 11: ***DCN improves insulin secretion and regulates ECM expression of β-cells in vitro.*** *(**A**) DCN treatment significantly increased insulin secretion concomitant with increase in GSIS index (n ≥ 4); 1-way ANOVA with Tukey's multiple comparison test, unpaired t-test. (**B**) DCN-treated β-cell pseudo-islets showed strong DCN-positive IF staining at the islet periphery (white arrows) with no overall change in staining intensity (n = 8); unpaired t-test. (**C**) DCN-positive cells occurred after 24 h of DCN-treatment (n ≥ 6); 1-way ANOVA with Tukey's multiple comparison test. DCN-treatment significantly downregulated the expression (**D**) FN (n ≥ 4) and (**E**) COL1 (n = 8) as shown by IF staining; unpaired t-tests. Scale bars equal 50 µm. *p<0.05, ****p<0.0001.*

OxPhos is a process that produces ATP within the mitochondria[330]. In our DCN-treated samples, genes related to OxPhos and to the electron transport chain were upregulated (**Appendix II**, Figure 3 C,D), indicating increased mitochondrial activity and providing ATP which is essential for insulin secretion[331,332]. β-cells that were not glucose-responsive demonstrated lower mitochondrial activity compared to glucose-responsive ones[333]. Reduced mitochondrial DNA and activity has also been described to be associated with type 2 DM[334]. The upregulation of mitochondrial activity is in line with the increased insulin secretion shown in the GSIS assay, underlining improved functionality of DCN-treated β-cells.

The ER, among other tasks, is responsible for the folding of proteins and their transportation via vesicular trafficking to their target destination. For β-cells, the folding

of pro-insulin and insulin is especially important in a high glucose environment. The upregulation of heat shock proteins in DCN-treated samples hints towards increased ER stress (**Appendix II**, Figure 3 E,F). ER stress occurs during periods of high insulin expression where more insulin and pro-insulin is produced and secreted[335–339]; however, up to 20% of pro-insulin is misfolded leading to degradation via ER associated degradation and unfolded protein response[340–342], explaining the increased ER stress. Besides protein folding and removal of misfolded proteins, vesicular trafficking is regulated by the ER. In DCN-treated samples we found an upregulation of *CANX*, *SAR1A*, *SEC62* and *SAR1B*, genes associated with vesicular trafficking. The increased secretion of insulin requires more vesicular trafficking to transport the insulin from the ER to the extracellular space. Impaired vesicular trafficking in β-cells has been described to lead to lipotoxicity, β-cell failure and ultimately DM[343–346]. MIN6 cells mutant for *Sar1A* were unable to achieve proper insulin folding resulting in β-cell failure[347,348]. This indicates that *SAR1A* upregulation in our samples not only plays a role in trafficking, but also in improved insulin folding.

We furthermore showed a downregulation of genes expressing Wolframin ER transmembrane glycoprotein (WFS1) and ribosome binding protein 1 (RRBP1). WFS1 is a Ca^{2+}-channel present on the ER in β-cells allowing the entry of Ca^{2+} into the ER[349,350]. As described earlier, Ca^{2+} is a major regulator of insulin secretion[351,352]. Reduction in WFS1 might increase cytosolic concentration of Ca^{2+} increasing the Ca^{2+} available for Ca^{2+}-mediated insulin secretion. RRBP1 is involved in the interaction between ribosomes and the ER and is associated with the unfolding protein response[353]. Reduction or knockdown of RRBP1 has been associated with ER stress; however, gene analysis of mice suggested upregulation of Rrbp1 to result in β-cell dysfunction and onset of type 2 DM[353,354].

To gain further understanding in the changes of the ER within DCN-treated samples, we used Raman microspectroscopy to investigate the ER-related spectra of control and DCN-treated pseudo-islets (Figure 12). When applying the corresponding Raman spectra of the ER component to the Raman images, we found no difference in distribution and expression of ER-positive pixels via true component analysis (TCA) (Figure 12 A,B, **Appendix II**, Figure S4); however, when performing principal

component analysis (PCA) of the ER component, we found a separation via PC-2, which was significant when comparing the mean loading scores between control and DCN-treated pseudo-islets (Figure 12 C,D). The loading plot of PC-2 can be used to identify peaks and therefore biochemical structures and fingerprints that are responsible for the separation between both groups (Figure 12 E). DCN-treated samples were characterized by peaks for phosphatidylinositol (PI) (415, 516 and 770 cm^{-1}), whereas control samples showed peaks for cholesterol (1444 and 1659 cm^{-1}) and triacylglycerol (TAG) (1252 and 1300 cm^{-1}). Quantification of these peaks' intensity showed a significant higher presence of PI in DCN-treated samples (Figure 12 F), while TAG and cholesterol were significantly downregulated post-DCN treatment (Figure 12 G,H). PI is associated with intracellular processes including vesicular trafficking, engulfment, ion channel regulation and intracellular signaling[355–357]. All these processes, especially vesicular trafficking and ion channel regulation are highly relevant for insulin secretion of β-cells. Additionally, an upregulation of PI supports the findings of our NGS data that DCN affects ER-related genes. Furthermore, in a previous study we showed increased expression of PI in pseudo-islets under high glucose conditions, further strengthening our findings[315,358]. TAG was identified as potential regulator of insulin secretion. Reduced levels of TAG have been described to increase insulin secretion by increased K_{ATP}-channel expression[359]. In summary, we hypothesize that DCN-treatment acts on the vesicular trafficking system as well as the mitochondria of β-cells to improve insulin secretion. One potential mechanism of action through which DCN affects the ER and the mitochondria is through low density lipoprotein receptor-related protein 1 (LRP1)-mediated signaling. LRP1 is an endocytic receptor that has various roles in different cell types including glucose metabolism and lipid turnover[360]. It has been shown to bind ECM proteins including FN[361] and DCN[362], as well as growth factors such as platelet-derived growth factor[363] and TGF-β[364]. In murine islets, LRP1 was shown to be essential for the cell homeostasis of lipid metabolism and insulin secretion, particularly in obese mice[365]. The deletion of LRP1 resulted in reduced insulin secretion and increased lipid content, which was in line with previous studies on LRP1 deletion in adipocytes[360]. Furthermore, the activation of TGF-β pathways through LRP1[362,366], and the

stimulatory effect of this pathway on β-cells' insulin secretion and survival[192,367] make this mechanism a potential mediator of the improved glucose-response observed in our DCN-treated pseudo-islets.

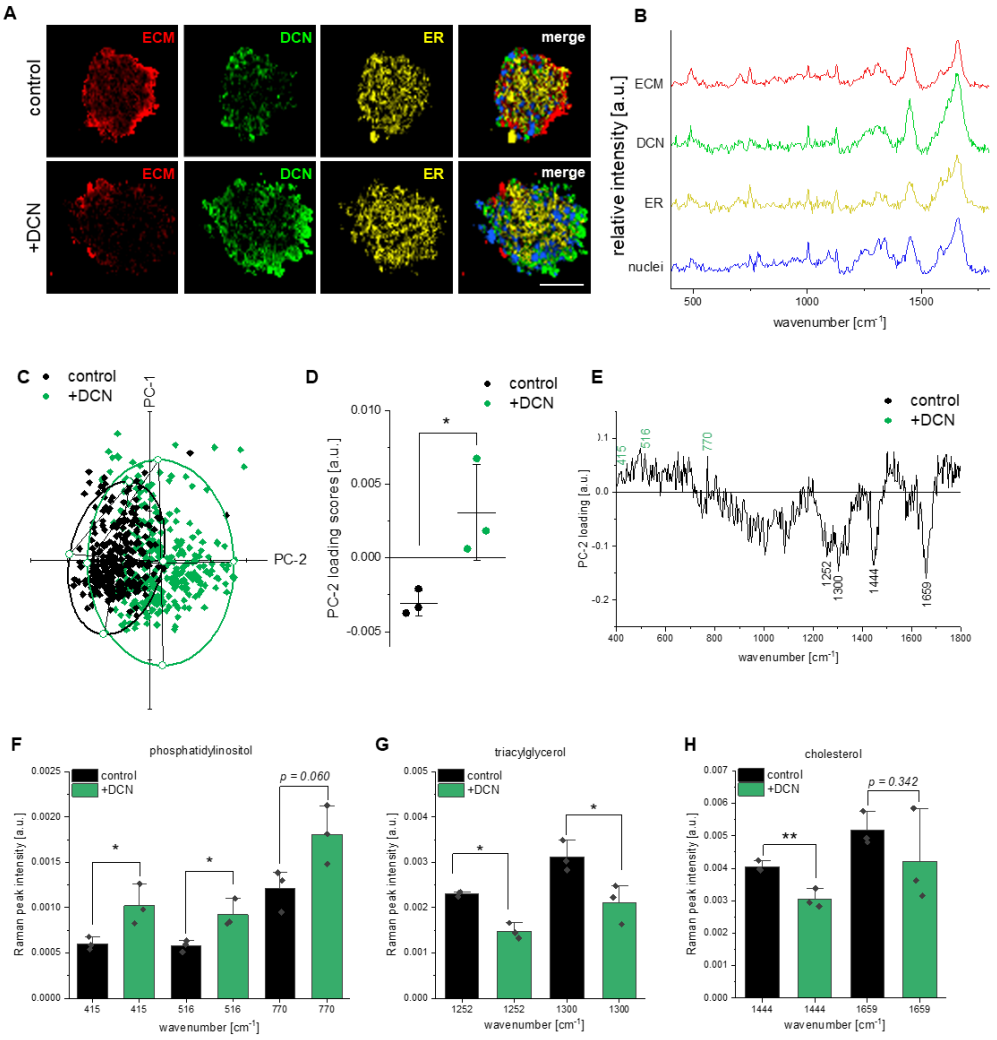

Figure 12: ***Raman imaging shows differences within ER component of DCN-treated β-cell pseudo-islets at 20 mM glucose****. (**A**) False color TCA-images of ECM, DCN and ER component in β-cell pseudo-islets identified by Raman imaging. (**B**) Corresponding Raman spectra of ECM, DCN, ER and nuclei component. (**C**) PCA of ER component showed separation via PC-2 between control and pseudo-islets +DCN. (**D**) Mean loading scores of PC-2 showed significant difference between control and pseudo-islets +DCN (n = 3); unpaired t-test. (**E**) Loading plot of PC-2 identified peaks for cholesterol (1444 and 1659 cm^{-1}) and TAG (1252 and 1300 cm^{-1}) describing control and peaks for PI (415, 516, and 770 cm^{-1}) describing the pseudo-islet +DCN. (**F**) DCN-treatment increased the levels of PI while decreasing the levels of (**G**) TAG and (**H**) cholesterol (n = 3); unpaired t-tests. Scale bar equals 50 µm. *p<0.05, **p<0.01.*

In the last step of this study, we encapsulated our pseudo-islets in a COL1 carrier material before DCN-treatment, to evaluate whether DCN has comparable

effects on encapsulated β-cells and can be made available during transplantation of islets of Langerhans. A comparative IF staining for COL1 and INS between native pancreatic tissue revealed a high resemblance between native pancreas and our COL1-embedded β-cell pseudo-islet model (**Appendix II**, Figure 5 A-D). Additionally, the COL1 gel exhibited comparable mechanical stiffness to native pancreatic tissue (**Appendix II**, Figure 5 E)[368–370], making it both a biochemically- and mechanically-valid model for studying the interaction of DCN and β-cells in a carrier material.

IF staining for DCN after DCN-treatment in the COL1 gel resulted in a comparable ring-formation and attachment of DCN to the periphery of the pseudo-islets as demonstrated in suspension (**Appendix II**, Figure 5 F), highlighting that the exogenous addition of DCN does interact with the encapsulated pseudo-islets. Correspondingly, we found that β-cells encapsulated in the COL1 gel secreted significantly more insulin upon glucose challenge after DCN-treatment compared to control (Figure 13 A). Additionally, IF staining for INS and E-cadherin showed increased expression after DCN-treatment compared to control (Figure 13 B,C). DCN also has modulatory properties on the endogenously expressed ECM proteins of β-cell pseudo-islets within the gel. While COL1 was again downregulated (Figure 13 D), FN expression was not affected in the gels (**Appendix II**, Figure S8), partly preserving the modulatory effects regarding fibrotic capsule formation within a 3D environment. Interestingly, in contrast to suspension pseudo-islets, DCN-treatment also significantly downregulated the expression of LAM, while COL4 expression was significantly increased (Figure 13 E,F). Both BM proteins LAM and COL4 have been reported to increase insulin secretion[166,167]. A decrease in LAM would therefore be contradictory to our finding of increased insulin secretion upon DCN-treatment; however, the increase in COL4 might account for the decrease in LAM, not limiting the insulin secretion after DCN-treatment.

Raman microspectroscopy in β-cell pseudo-islets in COL1 gels furthermore confirmed the results obtained in suspension: DCN-treated pseudo-islets showed significant differences in TAG and cholesterol expression within the ER component of control and DCN-treated β-cell pseudo-islets (**Appendix II**, Figure S7).

Overall, we showed that DCN significantly increased insulin secretion in vitro in suspension and in a COL1 carrier material. We present that the improved functionality can be attributed to increased mitochondrial activity as well as improved vesicular trafficking and ER stress handling. Furthermore, the modulatory effect of DCN on β-cells might contribute to a reduction in fibrotic capsule formation via suppressing the endogenous expression of fibrillar proteins. Taken together, these effects of DCN on β-cells make DCN a promising candidate to be used in islet transplantation to restore the native ECM and support integration and functionality of β-cells within islets of Langerhans in vivo.

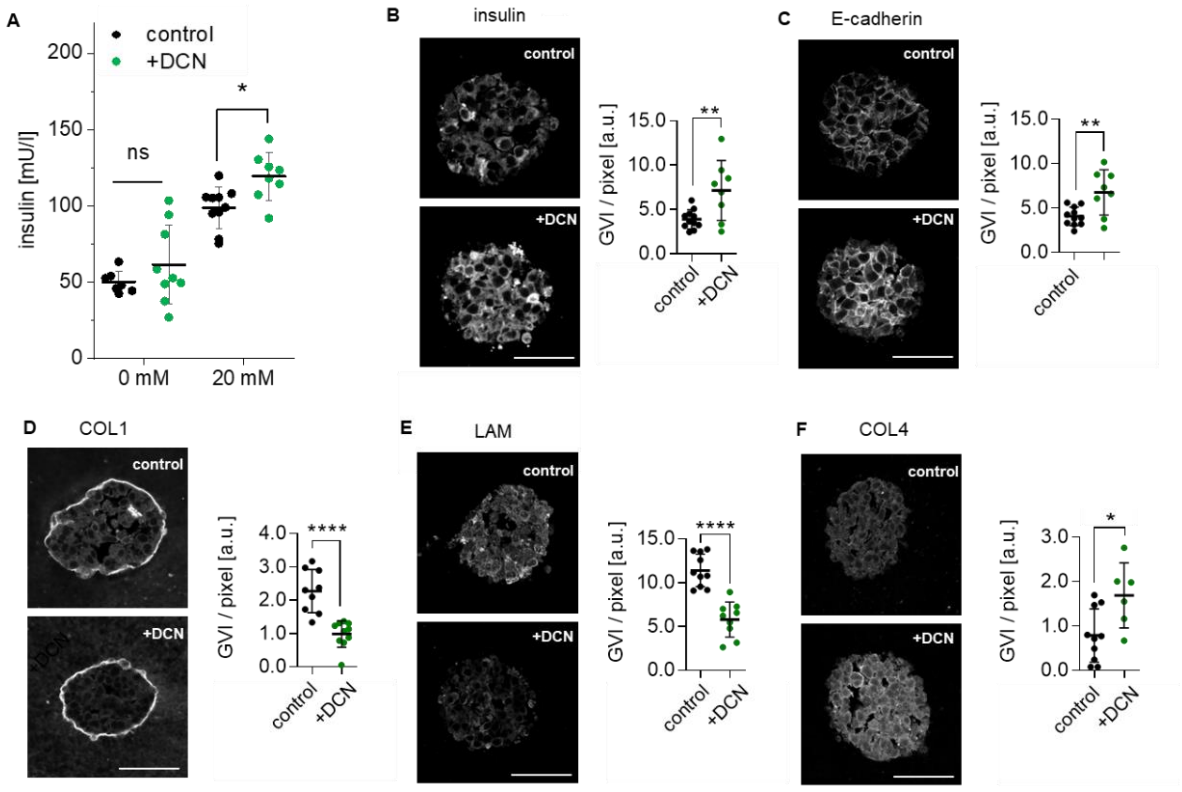

Figure 13: ***Effects of DCN are preserved when β-cell pseudo-islets are encapsulated in a COL1 carrier material.*** *(**A**) DCN-treated β-cell pseudo-islets secreted significantly more insulin at 20 mM glucose conditions (n ≥ 7); 1-way ANOVA with Fisher's multiple comparison. IF staining for (**B**) INS (n ≥ 8) and (**C**) E-cadherin (n ≥ 8) showed significantly higher values in β-cell pseudo-islets +DCN. IF staining for ECM proteins showed a significant downregulation of (**D**) COL1 (n ≥ 9) and (**E**) LAM (n ≥ 9) after DCN-treatment, while (**F**) COL4 (n ≥ 6) was significantly increased; unpaired t-tests. *p<0.05, **p<0.01, ****p<0.0001. Scale bars equal 50 µm.*

3.3 Establishing the Co-Culture of Endothelial Cells and β-cells

ECs play a critical role in islet functionality and survival, which has been reported extensively[181,182,207,240,371,372]; however, these positive effects have only been demonstrated in vitro by rodent-only co-cultures[371] or mixtures of co-cultures using rodent- and human-based cells[182,372,373]. One limitation of rodent-only and mixed cultures is that rodents exhibit significantly different ECM-distributions and mechanisms of action regarding cell-cell signaling and insulin secretion[147,374]. Additionally, rodent cells show dissimilarities upon exposure to cytotoxic reagents and cytoarchitecture, limiting the translatability of results obtained in rodent-based models to human mechanisms in vivo[147,375]. Therefore, human-based in vitro models are required. To study the mechanisms of action through which ECs stimulate β-cells in vivo, the spatial distribution between ECs and islets of Langerhans need to be met in vitro[376].

To tackle this current limitation, we employed magnetic levitation to control the aggregation process of co-culture pseudo-islets composed of HUVECs and the human β-cell line EndoC-βH3, creating the first ever reported human-based co-culture model of ECs and β-cells (Urbanczyk et al., **Appendix III**, Figure 1). Magnetic levitation uses positively charged poly-L-lysine amino acid chains to attach gold and iron-oxide particles to cells to make them susceptible to external magnetic fields[377]. This process improves the reproducibility of size of multicellular organoids, eliminating one major limitation of heterotypic spheroids[371,378].

In native pancreatic tissue, we identified three distinct spatial distributions of ECs and β-cells: random distributions (1:1) (Figure 14 A,B), ECs surrounded by β-cells (ECs inside) (Figure 14 H,I) and β-cells surrounded by ECs (β-cells inside) (Figure 14 O,P). By means of magnetic levitation, we were able to recreate stable heterotypic spheroids (Figure 14 E,F,L,M,S,T) recapitulating the three different spatial distributions, where spontaneous aggregation failed to do so. Native ratios of CD31-positive to INS-positive cells were recreated using magnetic levitation, while spontaneous aggregation showed significantly lower levels of CD31 incorporation into heterotypic spheroids (Figure 14 G,N,U). Survival was not affected by magnetic levitation as shown by TUNEL staining (Urbanczyk et al., **Appendix III**, Figure 4).

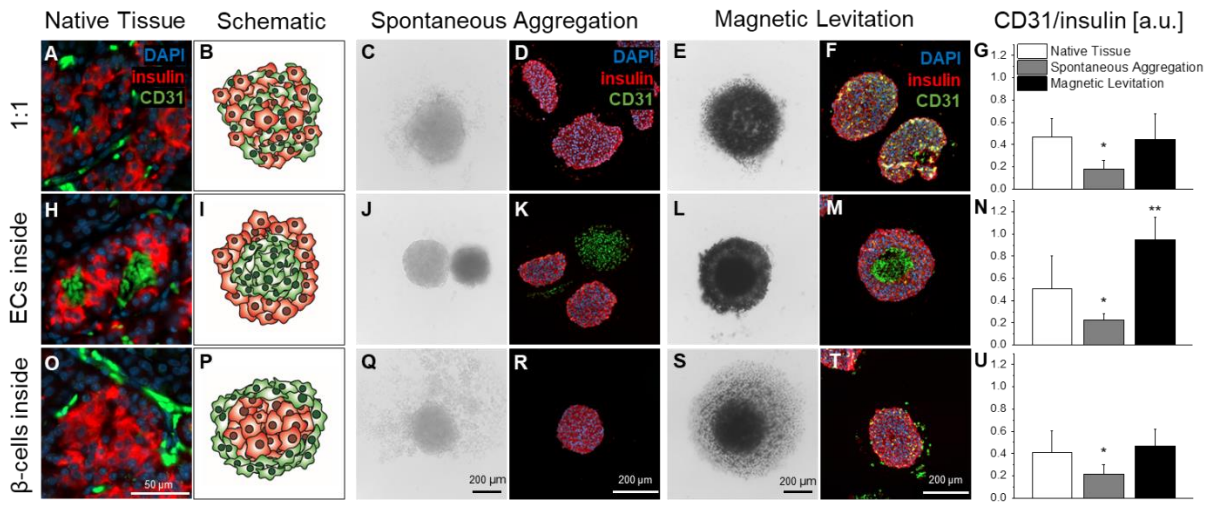

Figure 14: ***Native distribution of ECs and β-cells in the pancreas can be recreated using magnetic levitation****. ECs and β-cells show random distribution (**A,B**), β-cells surrounding ECs (**H,I**) or ECs surrounding β-cells (**O,P**). Spontaneous aggregation of HUVECs and β-cells is incapable of recreating any of these distributions (**C,D,J,K,Q,R**), whereas magnetic levitation offers controlled assembly of both cell types (**E,F,L,M,S,T**). Semi-quantification of CD31 and insulin showed recreation of native ratio of ECs to β-cells using magnetic levitation compared to spontaneous aggregation (**G,N,U**) (n = 6); unpaired t-tests. **p<0.01, ***p<0.001. Adapted from*[236].

Functionality assessment of the three spatial distributions obtained via magnetic levitation or spontaneous aggregation showed a significant increase in insulin secretion at 20 mM glucose for the β-cell inside condition (Figure 15 A). This structure was also used in other studies to result in superior insulin secretion, yet not in a comparative study between different spatial distributions[230,232,379]. Although the basal level of insulin secretion was significantly increased for β-cells inside obtained with magnetic levitation, the GSIS index was not impaired showing an overall stimulation of insulin secretion at both low and high glucose conditions (Figure 15 B). Interestingly, the spontaneously aggregated β-cells inside spheroids also showed a significant increase in insulin secretion. This hints towards a stimulation via paracrine signaling rather than direct contact, since spontaneously aggregated spheroids contained significantly fewer ECs. It has been previously described that medium conditioned with EC-secreted growth factors and other signaling molecules increased insulin secretion[181,230], which could explain the increase in insulin secretion despite the lack of integrated ECs. TUNEL staining on heterotypic spheroids obtained by magnetic levitation showed no significant difference in cell death, indicating that the higher levels of secreted insulin are not due to differences in viable cells in the

heterotypic spheroids (Figure 15 C-F). IF staining and semi-quantification of E-cadherin content in the magnetic levitation samples showed a significantly higher expression of E-cadherin in the β-cells inside condition compared to ECs inside and 1:1 (Figure 15 G-J). As described earlier, E-cadherin is a cell-cell contact marker protein and promotes insulin secretion by improving intra-islet communication[380–382]. Its binding properties to β-catenin can control actin skeleton remodelling via α-catenin[383], which regulates insulin secretion in β-cells[158]. A comparable mechanism has been described for MSCs in combination with islets of Langerhans, where co-transplantation of both cell types resulted in increased N-cadherin expression concomitant with improved functionality of islets[235].

Other potential pathways through which ECs improve β-cell functionality includes the interaction of CD31 with its counterreceptor αvβ3[172,384,385], which is also present on β-cells[316]. We already showed the involvement of this integrin on insulin secretion of β-cells in section 3.2.1. CD31 has been shown to participate in heterophilic interactions[385]. Hence, CD31 present on the surface of ECs can bind to the integrin αvβ3 to activate the ERK1/2 pathway stimulating insulin secretion, comparable to the mechanism of action of NID1[159,316,386]; however, the fact that spontaneously aggregated heterotypic spheroids also showed increased insulin secretion suggests a paracrine signaling-induced stimulation. It is possible that the ECs present in the heterotypic spheroids secreted different ECM proteins that stimulated β-cell functionality; however, this was not evaluated in the frame of this work.

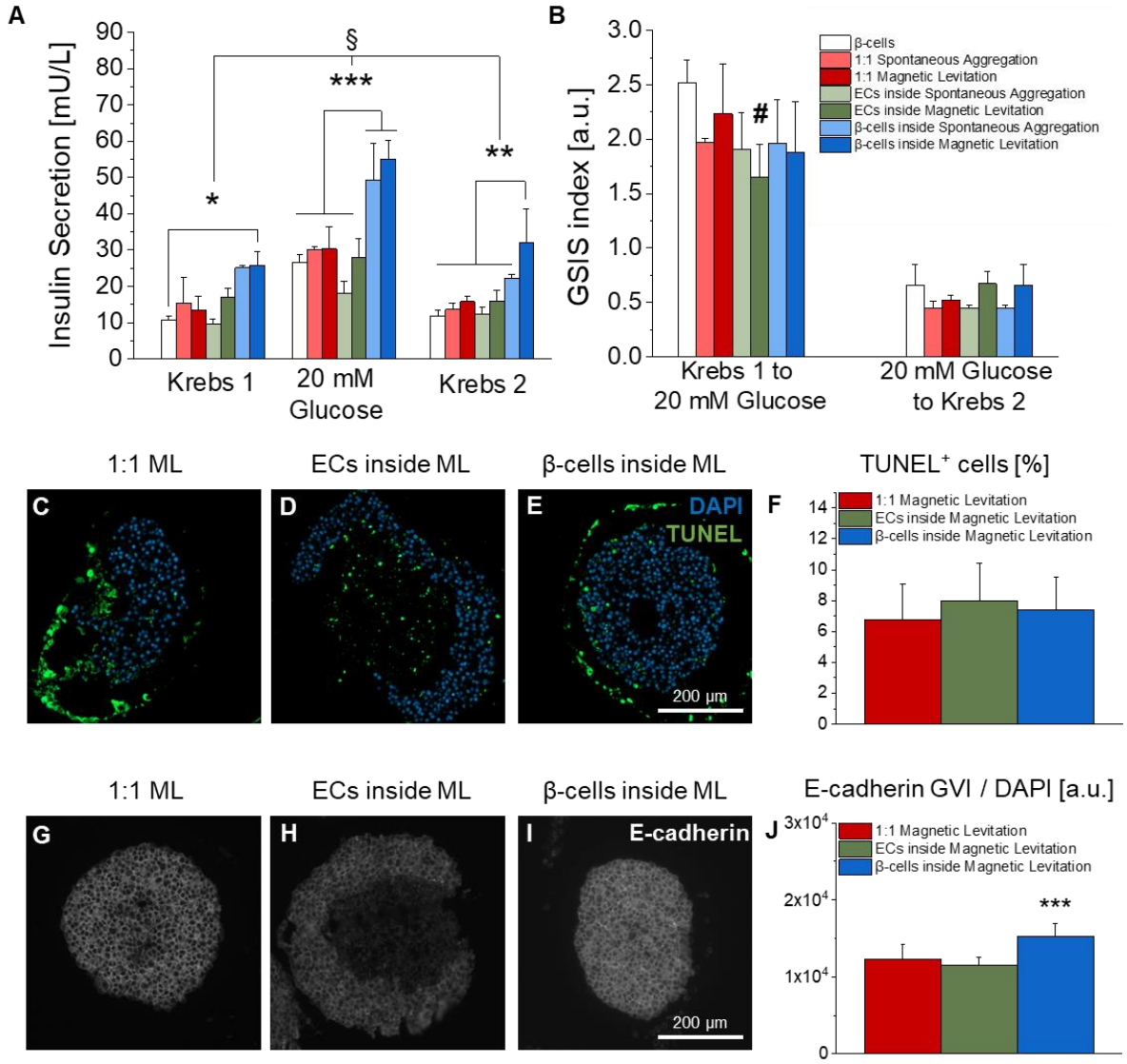

Figure 15: ***Co-culture of ECs and β-cells significantly increases glucose-stimulated insulin secretion.*** *(**A,B**) β-cells inside secreted significantly more insulin than any other co-culture distribution and control without change in GSIS index (n ≥ 3); 2-way ANOVA with Tukey's multiple comparison test (**A**), 1-way ANOVA with Tukey's multiple comparison test (**B**). (**C-F**) TUNEL-staining showed no significant difference in cell death between different culture conditions (n = 10); 1-way ANOVA with Tukey's multiple comparison test. (**G-J**) IF staining for E-cadherin showed significant increase in E-cadherin expression for β-cells inside compared to the other co-culture conditions (n = 20); 1-way ANOVA with Tukey's multiple comparison test. §p<0.001, #p<0.01, *p<0.05, **p<0.01 ***p<0.001. Adapted from*[387].

3.4 Effects of Hypoxia on the Extracellular Matrix of β-cells

ECs are a strong candidate to be co-transplanted with islets of Langerhans to reduce the time until revascularization occurs while supporting islet survival and functionality. A functional vasculature requires a surrounding 3D matrix in which the ECs can anchor, grow and sprout. Such matrices can be composed of a variety of materials, including Matrigel, electrospun scaffolds as well as natural or synthetic polymers. In chapter 3.2.2, we showed that COL1 can be used as such carrier material to encapsulate the islets of Langerhans as well as supportive cells[190,388–390]. In addition to its potential to be functionalized and support transplant function in vivo[171,391–396], COL1 has been used to support β-cell functionality under normoxic conditions[171,397]. We therefore asked the question, whether COL1 also has supportive effects on β-cells under hypoxic conditions.

In the first step, we optimized an INS1E pseudo-islet in vitro model under normoxic conditions (Zbinden & Urbanczyk et al., **Appendix IV**, Figure 1). After ensuring reliable functionality, we exposed the pseudo-islets to hypoxia for 48 h prior to analyzing the impact of the hypoxic environment on the β-cells. As expected, we found that hypoxia significantly increased caspase-3 expression and percentage of TUNEL-positive cells in pseudo-islets, while significantly decreasing proliferation rate as well as E-cadherin and INS expression compared to normoxia samples (Zbinden & Urbanczyk et al., **Appendix IV**, Figure 2 A-E). Pseudo-islets also lost their glucose-responsiveness after 48 h of exposure to hypoxic conditions (Zbinden & Urbanczyk et al., **Appendix IV**, Figure 2 F). These results indicate a successful modeling of hypoxic conditions that reliably induce cell death on untreated β-cell pseudo-islets.

Raman imaging to compare normoxic and hypoxic pseudo-islets showed a significant decrease in signal intensity for nuclei and ECM components, while the mitochondria component was not significantly affected (Zbinden & Urbanczyk et al., **Appendix IV**, Figure 2 G-I). The decrease in nuclei component is in line with increase in TUNEL-positive cells, since DNA fragmentation changes the biochemical composition of DNA[190]. In-depth analysis of the mitochondrial component indicated a significant separation between normoxic and hypoxic samples via PC-1 clustering (Zbinden & Urbanczyk et al., **Appendix IV**, Figure 2 J). The loading plot of PC-1

showed higher mitochondrial activity (at 715 and 1125 cm^{-1}) for normoxic samples compared to hypoxic ones, contributing to the finding of decreased functionality under hypoxic conditions (Zbinden & Urbanczyk et al., **Appendix IV**, Figure 2 K)[398,399]. The ECM component, characterized by peaks at 1173, 1310 and 1340 cm^{-1} showed significant decreases in endogenously expressed ECM proteins, contributing to the loss of pseudo-islet functionality[398,400,401]. The hypoxia-induced changes in intra-islet ECM might lead to dysregulation of proliferation, functionality and survival of β-cells[164].

To investigate changes in endogenously expressed ECM proteins within β-cell pseudo-islets, we conducted IF staining of ECM proteins representing different groups: LAM and COL4 (BM proteins), NID1 and DCN (glycoproteins) as well as COL1 and FN (fibrillar and fibril-associated proteins) (Zbinden & Urbanczyk et al., **Appendix IV**, Figure 3). We showed that hypoxia led to a significant decrease in LAM, COL4, DCN and NID1 expression, while the overall content of FN and COL1 was not affected. Loss of LAM, COL4 and NID1 are associated with reduced β-cell functionality, as their signaling directly impacts insulin secretion[166,167,215]. In general, decrease in DCN content can lead to uncontrolled collagen fiber formation, ultimately leading to fibrosis and graft failure post-transplantation[62]. Additionally, DCN has been shown to positively affect angiogenesis and modulate immune response[64,65]. Therefore, rescuing the expression of all four ECM proteins under hypoxic conditions is highly important to support islets survival post-transplantation. Interestingly, hypoxic conditions resulted in higher nuclear expression of FN without impacting the overall content. Changes in ECM compositions can induce transcriptional changes in the nucleus hinting towards cellular stress (such as hypoxia)[402]. Nuclear FN might be a first indicator of hypoxia-induced cellular damage[403], since nuclear FN is also present in cancer cells; yet its role remains unclear[404].

Carrier materials, such as COL1, are commonly used to encapsulate islets prior to transplantation. Therefore, we embedded our pseudo-islets into a COL1 gel before exposing them to hypoxic conditions for 48 h to investigate whether the negative effects of hypoxia could be dampened by the carrier material. The overall structure of our encapsulation model highly resembles the native pancreatic tissue in terms of islet distribution and size (Zbinden & Urbanczyk et al., **Appendix IV**, Figure 4).

In the first step, we investigated the effects of hypoxia on β-cells via IF staining for cell death (caspase-3, TUNEL), proliferation (Ki67) and functionality markers (E-cadherin, insulin). To be able to interpret the results from pseudo-islets in suspension to COL1-embedded pseudo-islets, we compared the hypoxia-induced fold changes in staining intensity in suspension versus COL1 gel. We found a significantly lower fold change in caspase-3 expression as well as TUNEL-positive cells (Figure 16 A,B) when pseudo-islets were encapsulated in the COL1 gel. Regarding proliferation, we found no difference in suspension and COL1 samples (Figure 16 C). In terms of functionality markers, higher levels of E-cadherin and insulin expression in COL1 samples, which was significantly different to the decrease we observed in the suspension samples (Figure 16 D,E). Additionally, we found that the pseudo-islets encapsulated in the COL1 gel remained glucose-responsive after 48 h of hypoxic conditions (Figure 16 F), confirming the IF staining results and our hypothesis of the dampening effects of a COL1 carrier material regarding functionality.

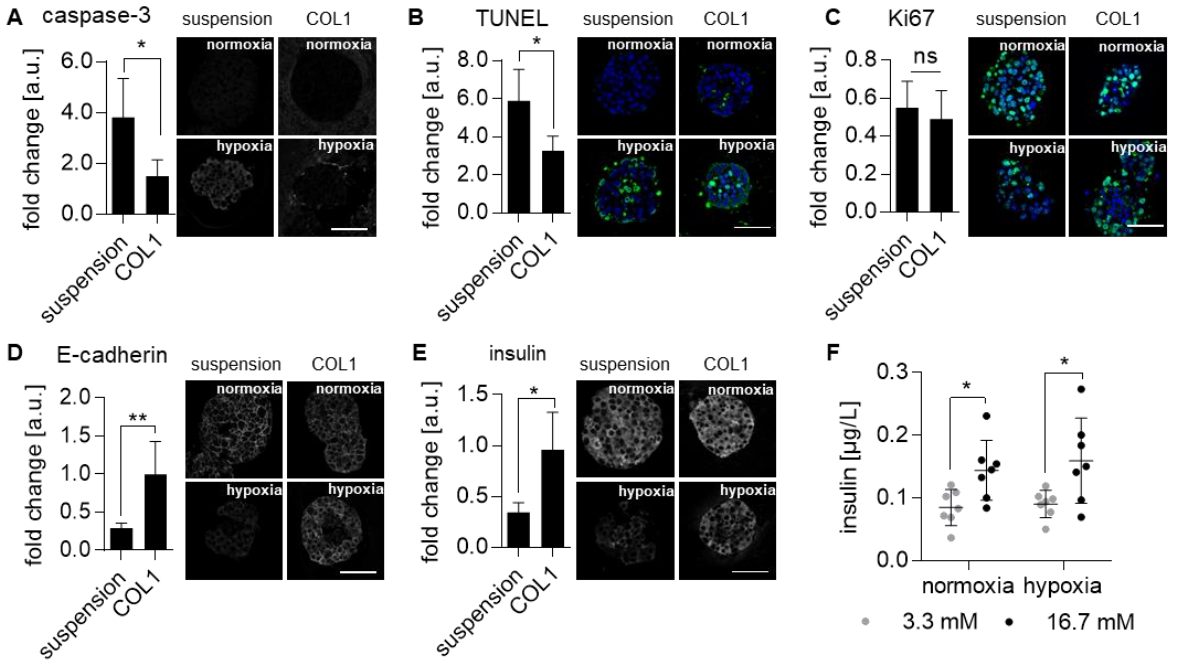

Figure 16: ***Encapsulation of β-cells into COL1 gel supports survival and rescues functionality.*** *COL1 embedded pseudo-islets showed (**A**) significant decrease in caspase-3 expression (n ≥ 3), (**B**) significant decrease in TUNEL-positive cells (n ≥ 3) compared to pseudo-islets in suspension; unpaired t-tests. (**C**) IF staining for KI67 indicated no change in proliferation (n ≥ 4); unpaired t-test. IF staining for (**D**) E-cadherin (n ≥ 5) and (**E**) INS (n ≥ 4) showed increased insulin expression for COL1 encapsulated pseudo-islets compared to suspension; unpaired t-tests. (**F**) GSIS assay shows glucose-responsiveness of pseudo-islets encapsulated in COL1 (n = 7); 2-way ANOVA with Tukey's multiple comparison. *p<0.05, **p<0.01. Scale bars equal 50 µm.*

After finding that the COL1 carrier material supports functionality after 48 h in hypoxia, we performed IF staining on the six target ECM proteins to investigate the hypoxia-induced changes of endogenous ECM protein expression of β-cells when encapsulated in COL1 (Figure 17). The BM proteins LAM and COL4 were significantly decreased, even when pseudo-islets were encapsulated (Figure 17 A,B); however, the glycoproteins NID1 and DCN showed no significant differences in staining intensity between normoxic and hypoxic conditions (Figure 17 C,D). Expression intensity of FN and COL1 remained unaffected by hypoxia (Figure 17 E,G). Interestingly, the translocation of FN from cytoplasm to nucleus was reversed and showed no difference between normoxia and hypoxia (Figure 17 F), strengthening our hypothesis of dampening effects of the COL1 carrier material.

The protective effects of encapsulation on NID1 and DCN expression might explain the successful recovery of β-cell functionality, as NID1 and DCN play significant roles in survival and functionality of β-cells as demonstrated earlier. In summary, the decrease in cell death and improved ECM expression indicate a combination of biological and mechano-physical cues provided by the COL1 gel that support β-cells[394–396].

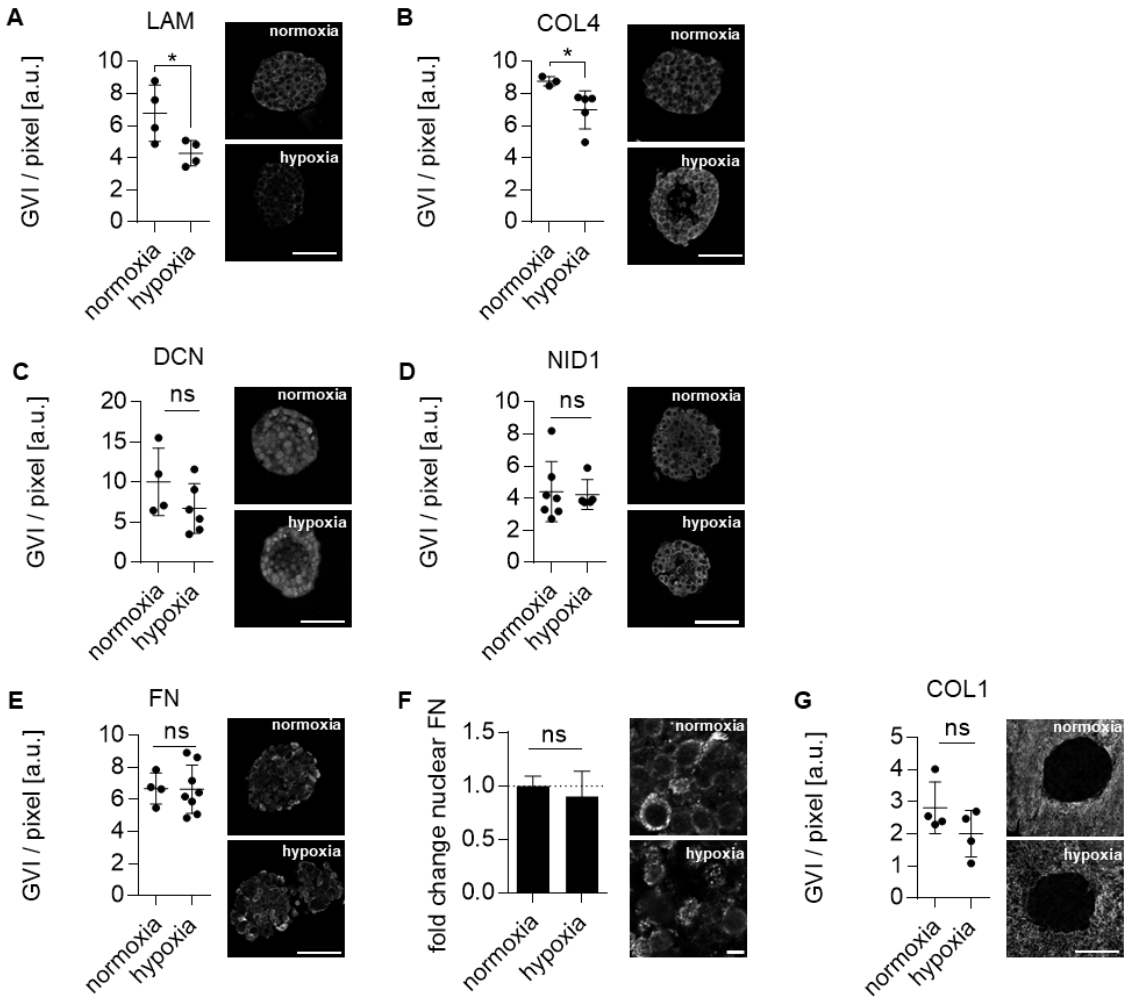

Figure 17: ***Encapsulation of β-cells into COL1 gel restores DCN and NID1 expression under hypoxic conditions.*** *IF staining and semi-quantification showed significant decrease of (**A**) LAM (n = 4) and (**B**) COL4 (n ≥ 3), while (**C**) DCN (n ≥ 3), (**D**) NID1 (n ≥ 4), (**E**) FN (n ≥ 4) and (**G**) COL1 (n = 4) showed no significant differences; unpaired t-tests. (**F**) Quantification of nuclear FN showed no significant difference between normoxia and hypoxia (n = 4). Scale bars equal (**A-E,G**) 50 µm and (**F**) 5 µm. *p<0.05.*

Although COL1 encapsulation helped restore functionality and reduce hypoxia-induced cell death, encapsulation did not support complete restoration of all endogenously expressed ECM proteins. Since the BM proteins remained significantly downregulated, we hypothesized that the co-culture of ECs with β-cell pseudo-islets within the COL1 gel might restore BM protein content. The co-culture of HUVECs and β-cell pseudo-islets were functional after hypoxia and showed significantly higher glucose-responsiveness under hypoxic conditions compared to β-cells in COL1 gel alone (Figure 18 A,B). IF staining for ECM proteins showed a significant upregulation

of both BM proteins LAM and COL4 (Figure 18 C,D) as well as their linker protein NID1 (Figure 18 F) in β-cell pseudo-islets after co-culture compared to monoculture samples. Overall FN expression was also reduced upon HUVEC co-culture accompanied by a significant decrease in nuclear FN expression (Figure 18 G,H). Both findings are positive as reduction in overall FN expression might indicate a reduced fibrotic response, while decrease in nuclear FN expression hints towards reduction in hypoxia-induced cellular stress and damage[402,403]. The co-culture did not have an effect on DCN and COL1 expression (Figure 18 E,I).

In summary, we showed that hypoxia significantly reduces the endogenous ECM expression of β-cell pseudo-islets, which might be one of the main reasons for decreased functionality and increased cell death. The encapsulation of β-cells within a COL1 gel which provides biochemical and mechano-physical support resulted in restoration of glycoproteins concomitant with increased functionality and survival. In previous studies, we showed that especially NID1 is an important regulator of β-cell survival. Hence, the COL1-induced rescue of NID1 content could be beneficial for overall survival and functionality of β-cells under hypoxic conditions. The co-culture of β-cells with ECs, which are one of the main sources for BM proteins in the pancreas[189,215,229], restored BM protein content and further enhanced functionality compared to β-cell monocultures. The presented data shows that the restoration of native ECM is essential to ensure β-cell functionality under stress conditions, e.g., post-transplantation. This can be achieved by using carrier materials in combination with supportive cell types to enhance survival and functionality of transplanted islets of Langerhans.

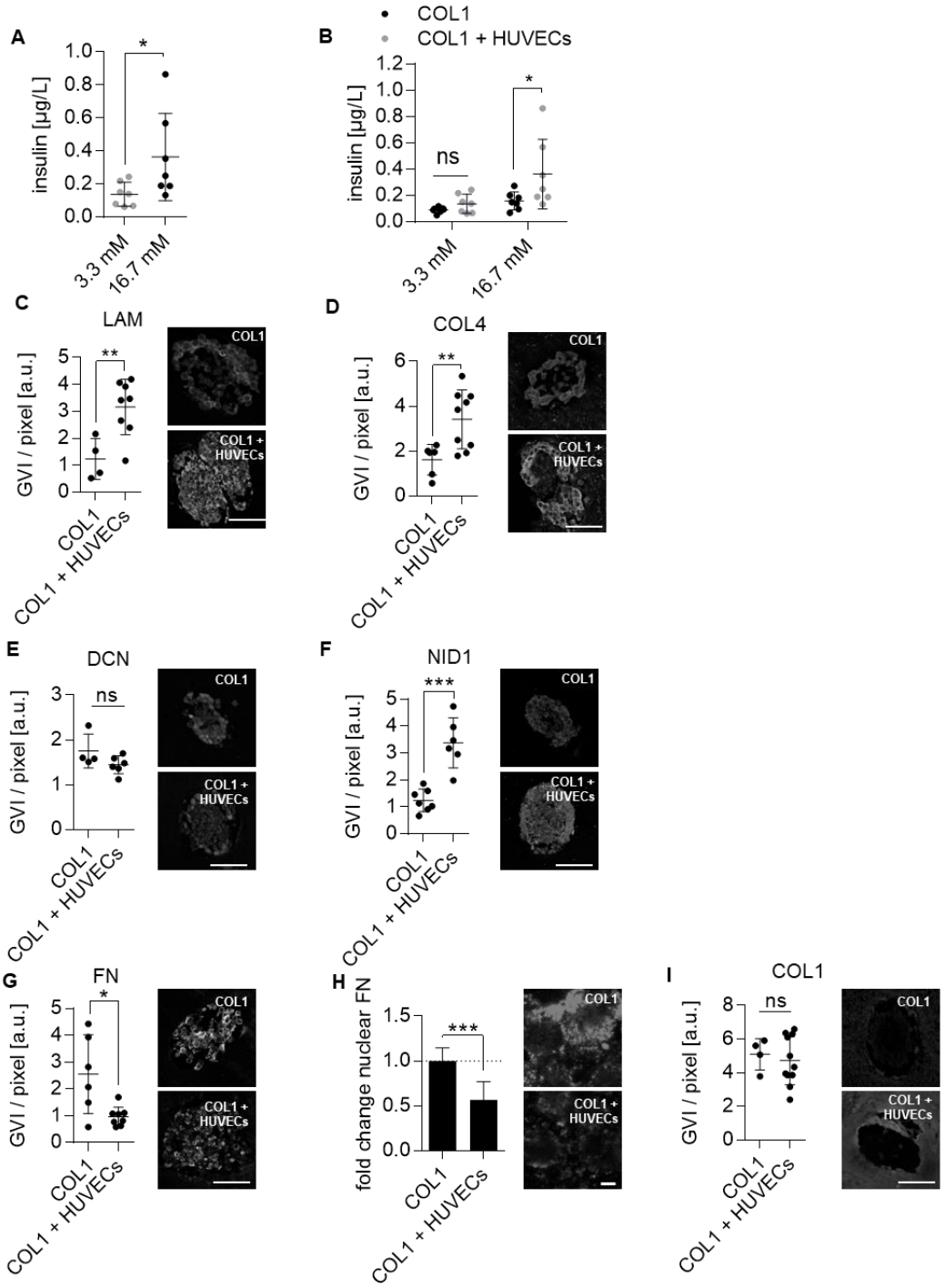

Figure 18: ***Co-encapsulation of pseudo-islets with HUVECs increases insulin secretion and restores endogenous BM protein expression of pseudo-islets.*** *(**A**) GSIS assay of pseudo-islets co-encapsulated with HUVECs were highly functional under hypoxic conditions and (**B**) secreted significantly more insulin compared to pseudo-islets encapsulated alone (n = 7); unpaired t-test, 2-way ANOVA with Sidak's multiple comparison. IF staining and semi-quantification showed significantly higher expression of (**C**) LAM (n ≥ 4), (**D**) COL4 (n ≥ 6) and (**F**) NID1 (n ≥ 6), while (**E**) DCN (n ≥ 6) and (**I**) COL1 (n ≥ 4) were not affected. (**G,H**) Overall and nuclear expression of FN was significantly decreased upon co-encapsulation of pseudo-islets with HUVECs (n ≥ 6); unpaired t-tests. *p<0.05, **p<0.01, ***p<0.001. Scale bars equal (**C-G,I**) 50 µm and (**H**) 5 µm.*

Chapter 4

Conclusion & Outlook

4 Conclusion & Outlook

The ECM is a major contributor to homeostasis in healthy tissue and plays a critical role in pathological developments and disease progression in vivo. Investigating the role of ECM in such pathophysiological processes is an important component to decipher disease development and progression. Pathological process, such as MI/R as well as invasive procedures, such as transplantations, have an immense effect on the homeostatic equilibrium and the native ECM. These changes further worsen disease progression and limit regenerative processes. Therefore, there is an urgent need to understand the roles of the different ECM proteins in their native environment and their effects on the residing cells in terms of survival, functionality and differentiation since the ECM can determine the survival of the patient and the success or failure of the intervention. This knowledge could be harnessed to restore the native composition of the ECM to minimize extents of injuries or to recapitulate the ECM ex vivo prior to transplantation to reduce recovery time and increase success rate.

In this thesis, we investigated the impact of the ECM on cardiovascular and pancreatic tissues. Regarding cardiovascular tissues, we focused on disease modeling of MI/R, since CVDs and MI/R are a major cause of death in the modern world. We found that the ECM glycoprotein NID1 plays an important role during cardiac differentiation and has positive impacts on different cell types of the cardiovascular system. More specifically, the treatment of ECs, fibroblasts and CMs in vitro resulted in increased angiogenesis, reduced transdifferentiation of fibroblasts to myofibroblasts and increased survival of CMs under hypoxic conditions. The protective effects of NID1 on CMs via integrin αvβ3-mediated signaling is of great interest, since CMs are non-proliferative in vivo. The protection of CMs under ischemic conditions is therefore of utmost importance for survival of MI/R patients. We hypothesized, that NID1-treatment of MI/R could reduce the ischemia-induced trauma in vivo. NID1-treatment showed a significant decrease in scar tissue formation, increase in nerval innervation and angiogenesis accompanied with improvement in heart function post-MI/R in mice, confirming our hypothesis; however, there are

limitations that hinder the direct extrapolation from results in mice to humans. For instance, mice hearts are 1500 times smaller than human hearts with heart rates up to ten times faster and differences in electrophysiology[85]. Nevertheless, the in vitro results obtained from human-derived cells in combination with successful in vivo data indicate that NID1 could be a potential candidate to treat MI/R patients. Its protective properties on CMs and fibroblasts as well as its stimulatory effects on neurons and ECs shows the importance of ECM in pathophysiological processes and the potential of individual proteins in disease treatment and homeostasis restoration.

The ECM also plays an important role for the successful transplantation of islets of Langerhans to treat severe cases of type 1 DM, as success relies on the integration of cells into their new environment. One key aspect, therefore, is the restoration of native ECM which is removed during the isolation process. The successful recapitulation of the pancreatic niche offers great potential to improve the integration of transplanted cells into the recipient's system. Therefore, it is of great importance to understand the role of ECM within islets of Langerhans and β-cells, especially during the initial hypoxic episode before revascularization occurs. To find potential ECM proteins that might impact the survival and functionality of the insulin-producing β-cells in vivo, we investigated the native ECM of pancreatic tissue. We found that the glycoproteins NID1 and DCN are highly co-localized with insulin-expressing cells in pancreatic tissue. β-cells showed significantly increased insulin secretion and survival under hypoxic conditions in vitro upon treatment with NID1. The stimulatory, as well as protective, effect of NID1 is mediated via αvβ3 signaling and upregulation of MAPK and Wnt signaling pathways. DCN-treatment increased functionality of β-cells in vitro by stimulating mitochondrial activity and vesicle trafficking, potentially through LRP1-signaling. Additionally, DCN-treatment significantly reduced the expression of fibrillar ECM proteins involved in fibrotic capsule formation. Besides hypoxic conditions, fibrotic capsule formation around the transplanted cells is a major reason for graft failure. The combination of anti-fibrotic and stimulatory features makes DCN a promising candidate to be used as supplement during islet transplantation. The combination of both ECM proteins, NID1 and DCN, could further support β-cells

survival and functionality, e.g., supplemented in a COL1 carrier material, recapitulating the pancreatic ECM even further.

In the next step, we wanted to validate the supportive effects of both ECM proteins in a more clinically relevant model than β-cell-only pseudo-islets. We therefore treated isolated human islets of Langerhans from donor organs with our target concentrations of NID1 or DCN and cultured them under both normoxic and hypoxic conditions (Figure 19). Under normoxic conditions, all conditions were glucose-responsive and there was no significant difference observable between control and NID1- or DCN-treated groups (Figure 19 A). Under hypoxic conditions, untreated islet of Langerhans lost their glucose-responsiveness, whereas both NID1- and DCN-treated samples were still glucose-responsive (Figure 19 B). While we previously demonstrated the protective effect of NID1-treatment on β-cells, this preliminary result also shows the potential of DCN to support cellular survival and functionality under hypoxic conditions. Potential mechanisms of action for DCN besides LRP1 include insulin growth factor 1 receptor[405], α2β1[406] and Toll-like receptor 4[407]. Future studies including next-generation sequencing will be focusing on identifying affected signaling pathways in human islets.

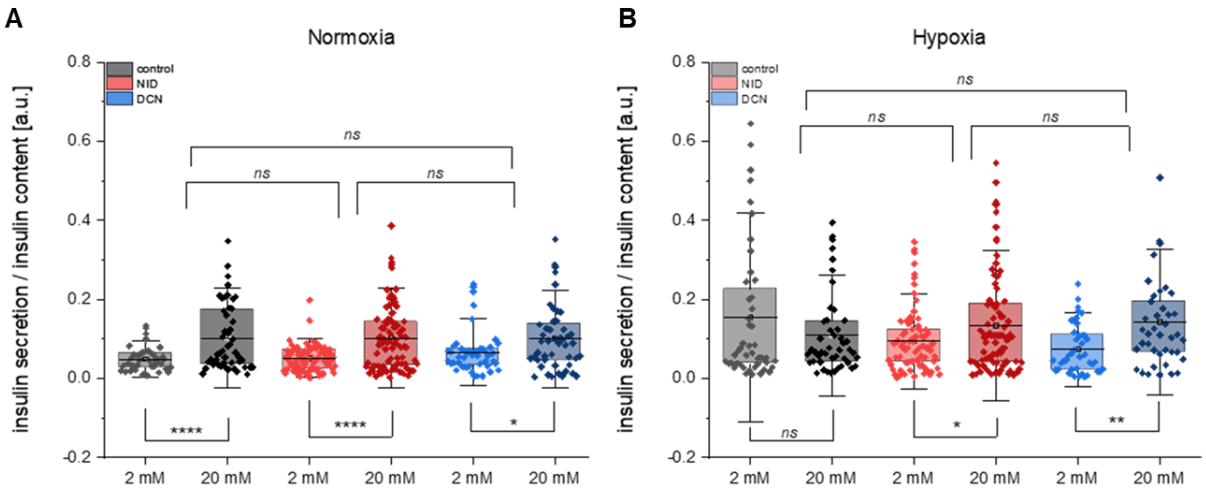

Figure 19: ***NID1 and DCN supplementation rescue functionality of human islets of Langerhans under hypoxic conditions.*** *(**A**) Human islets of Langerhans are functional under normoxic conditions independent from treatment method (n ≥ 40); unpaired t-tests, 2-way ANOVA with Tukey's multiple comparison test. (**B**) NID1 and DCN treatment rescue insulin secretion in human islets of Langerhans after 72 h of hypoxia (n ≥ 40); unpaired t-tests, 2-way ANOVA with Tukey's multiple comparison test. *p<0.05, **p<0.01, ****p<0.0001.*

External recapitulation of ECM can support survival of transplanted islet cells and increase the success rate; however, it does not overcome current limitations of long-term incorporation of grafts into the recipient's body. In order to obtain homeostasis, the restoration of ECM and its cellular composition needs to be met. A major milestone to reach homeostasis is the restoration of vascularization in the transplant area, since ECs play a major role in ECM secretion, cellular recruitment and differentiation apart from supplying oxygen and nutrients[66]. To improve the incorporation of grafts into the recipient's systems, it is necessary to gain knowledge about the interplay between ECs and organ-specific cells as well as their role in tissue homeostasis and functionality. Therefore, in vitro test systems need to be developed that closely mimic organ-specific environments in terms of biochemical and biomechanical signaling[408]. This includes creating correct ECM compositions by combining different gel types such as fibrin[240], COL1[135,190,409], matrigel[410] or decellularized pancreatic ECM as bioink[411], applying biologically relevant forces (such as stiffness, strain and shear forces[52,412413]), appropriate culture techniques (such as 3D culture using soft substrates[211,414–416]) and the use of ECs with organ-specific characteristics[66]. The development of sophisticated in vitro systems encompassing ECs is necessary to understand the feedback loop between ECs and islets of Langerhans in the pancreas to optimize vascularization pre- and post-transplantation[96,417]; however, the main EC type used in developing co-culture systems until now are HUVECs, although they do not exhibit biologically relevant EC-features[182,204,228,245,373,418–421]. Only recently, scientists are moving away from HUVECs and use other EC sources, such as microvascular fragments[422], heart microvascular ECs[240] or mouse pancreatic ECs[409].

Therefore, our next goal is to investigate the differences in ECs and their impact on β-cell functionality to improve co-culture in vitro systems and their meaningfulness. We started to analyze ECs from human umbilical vein (standard model) in comparison to ECs from human pancreatic microvasculature (hpmvECs) using Raman microspectroscopy (Figure 20). PCA of the lipid component of HUVECs and hpmvECs cultured under standard monolayer conditions showed clustering via PC-2 and PC-3 (Figure 20 A). The mean loading score of PC-2 showed a significant difference, where

peaks for TAG (1097 and 1127 cm^{-1}) characterized HUVECs, while hpmvECs were characterized by increased presence of cholesterol (1260 and 1655 cm^{-1}) and other membrane lipids (1300 and 1436 cm^{-1}) (Figure 20 B). Comparable tendencies were observable in PC-3, where TAG (1127 and 1249 cm^{-1}) was found in HUVECs, while hpmvECs were characterized by sphingolipids (1067 cm^{-1}) and cholesterol (1659 cm^{-1}) (Figure 20 C).

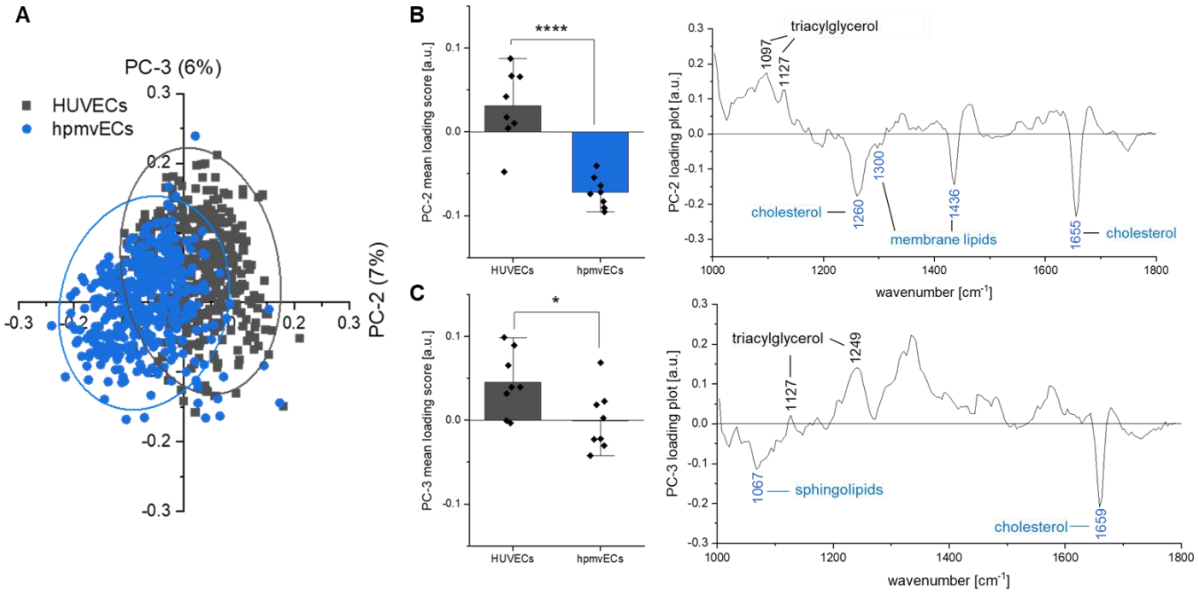

Figure 20: ***Raman imaging shows differences in biochemical composition of the lipid component between HUVECs and hpmvECs.*** *(**A**) PCA of the lipid component shows separation between HUVECs and hpmvECs for PC-2 and PC-3. (**B**) PC-2 mean loadings score and plot show separation between HUVECs (TAG at 1097 and 1127 cm^{-1}) and hpmvECs (cholesterol at 1260 and 1655 cm^{-1}; membrane lipids at 1300 and 1436 cm^{-1}) (n = 8); unpaired t-test. (**C**) PC-3 mean loadings score and plot show separation between HUVECs (TAG at 1127 and 1249 cm^{-1}) and hpmvECs (sphingolipids at 1067 cm^{-1}; cholesterol at 1659 cm^{-1}) (n = 8); unpaired t-test. *p<0.05, ****p<0.0001.*

Vesicular trafficking ensures the transport of nutrients and oxygen from the bloodstream to the surrounding tissue and is controlled by the content of fenestrae build up by membrane lipids[66]. The increased expression of membrane lipids in hpmvECs is in line with the fact that ECs from the microvasculature can be classified as fenestrated endothelium (more fenestrae to ensure exchange from blood to tissue in microvessels and capillary), while HUVECs can be classified as a continuous endothelium[423]. In particular, the expression of caveolae, a specific type of membrane rafts, is highly relevant for ECs within the pancreas. Caveolae are characterized by expression of caveolin-1, plasmalemma vesicle-associated protein and sphingolipids

and are involved in signal transduction, nitric oxide release and mediating insulin secretion[424]. The differences in membrane lipid expression already hint towards functional differences in EC signaling between HUVECs and hpmvECs when co-cultured with β-cells.

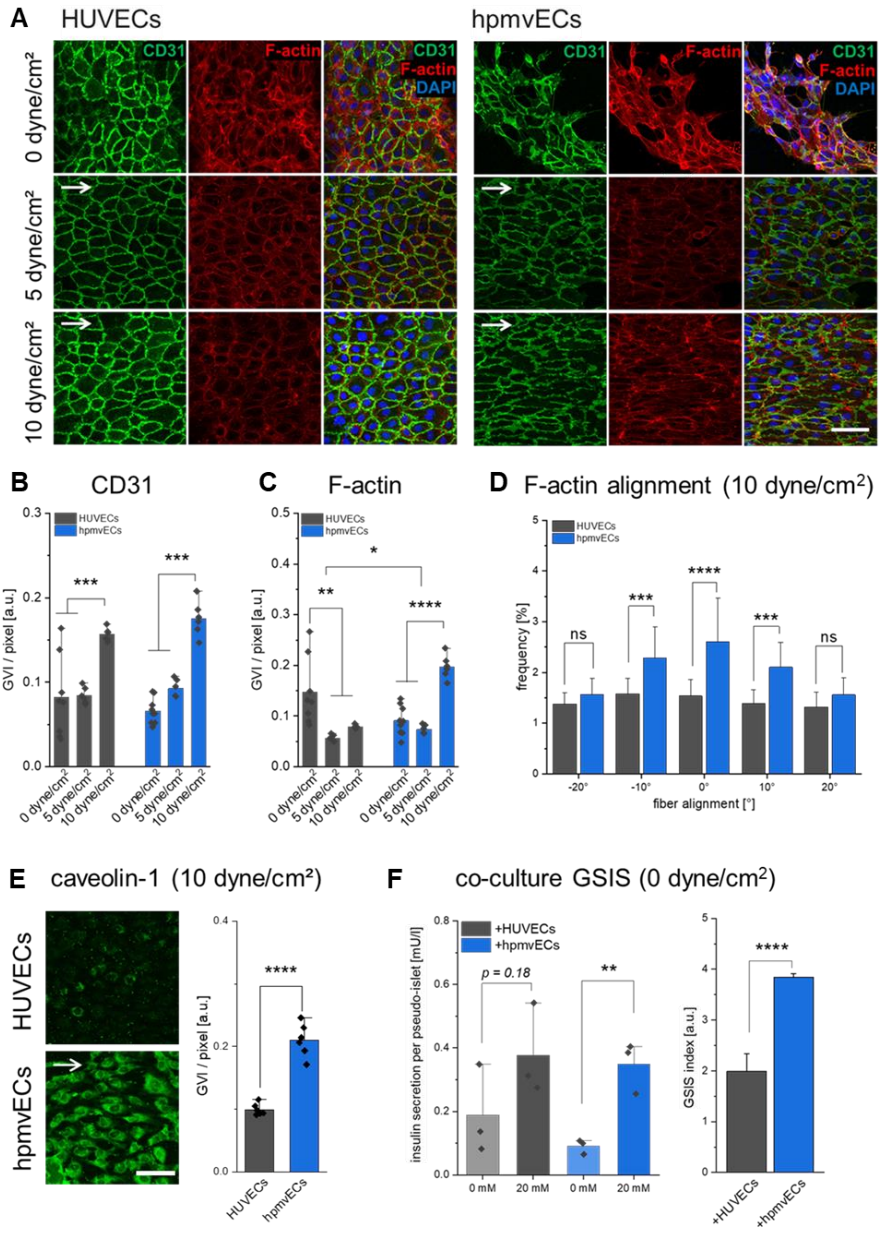

Figure 21: ***HUVECs and hpmvECs show differences in morphology and protein expression under flow and differentially impact β-cell functionality.*** *(**A**) HUVECs and hpmvECs show different patterns under static conditions (first row), 5 dyne/cm² (second row) and 10 dyne/cm² (third row). Semi-quantification of (**B**) CD31 and (**C**) F-actin of both EC types at different flow parameters (n = 18); 2-way ANOVA with Tukey's multiple comparison. (**D**) Quantification of F-actin alignment of HUVECs and hpmvECs at 10 dyne/cm² (n = 18). 2-way ANOVA with Tukey's multiple comparison. (**E**) IF staining and semi-quantification of caveolin-1 in HUVECs and hpmvECs at 10 dyne/cm² (n = 6); unpaired t-test. (**F**) Co-culture of β-cell pseudo-islets with HUVECs and hpmvECs in COL1 gel under static conditions shows functionality upon co-culture with hpmvECs accompanied with increased GSIS index (n = 3); 2-way ANOVA with Tukey's multiple comparison, unpaired t-test. *p<0.05, **p<0.01, ***p<0.001, ****p<0.0001.*

To investigate the behavior of both EC types under in vivo-like conditions, we transferred the ECs from static cultures on plastic to cultures on a COL1 gel in a commercially available chip setup with controllable application of flow and shear forces (Figure 21). After five days of culture and IF staining for CD31 and filamentous actin (F-actin), we found that HUVECs do not require the application of flow for cellular survival and the formation of a confluent monolayer in this chip setup, whereas hpmvECs did not achieve confluency under static conditions (Figure 21 A, first row). The application of 5 and 10 dyne/cm^2, respectively, differentially affected the alignment of HUVECs and hpmvECs: while HUVECs expressed the standardized cobblestone shape uniformly at 5 and 10 dyne/cm^2, hpmvECs were elongated and aligned in the direction of flow (Figure 21 A, second and third row). The different adaptations can be explained by the fact that HUVECs usually experience low shear forces between 1-6 dyne/cm^2, while shear forces in the microvasculature can range from 3-95 dyne/cm^2 [425,426].

Semi-quantification of CD31 (Figure 21 B) showed significantly higher values at 10 dyne/cm^2, indicating stronger cellular interaction with increasing shear stress for both cell types. Interestingly, F-actin expression was significantly higher in HUVECs under static conditions, while hpmvECs showed highest F-actin levels at 10 dyne/cm^2 (Figure 21 C). F-actin alignment studies showed significantly higher alignment of hpmvECs in direction of flow compared to HUVECs (Figure 21 D). These differences emerge since microvascular ECs adapt differentially to shear stresses by remodeling their cytoskeleton to the direction of flow to protect them from hydrodynamic damage and detachment[427,428]. This indicates differences in intracellular signaling pathways of ECs determined by their original location in the cardiovascular system. To examine the presence of caveolae in both EC groups, we stained for caveolin-1 in HUVECs and hpmvECs at 10 dyne/cm^2 and found significantly higher caveolin-1 expression in hpmvECs (Figure 21 E). This finding confirms the results obtained earlier from Raman microspectroscopy. In a preliminary experiment, we investigated the effect of co-cultures with different EC types with β-cell pseudo-islets on GSIS under static conditions in a COL1 gel. Our results show that β-cells co-cultured with HUVECs showed no significant differences between low and high glucose conditions, while β-

cells co-cultured with hpmvECs secreted significantly more insulin under high glucose conditions compared to low glucose, accompanied with a significant increase in GSIS index (Figure 21 F). Taken together, these preliminary data show that ECs from different locations of the cardiovascular system exhibit significant differences that impact the functionality and meaningfulness of an in vitro test system. Future studies will focus on improving the co-culture conditions under flow to better mimic in vivo conditions using in vitro test systems for DM research and elucidate the role of ECs on β-cell functionality. The obtained knowledge might offer the potential to understand the role of crosstalk between ECs and β-cells to reduce the time required for revascularization and enhance ECM restoration in vivo post-transplantation.

In summary, this dissertation highlights the importance of ECM proteins in different pathological conditions and their potential as treatment options. The combination of suitable carrier materials, supportive cell types and combinations of native ECM proteins might be the key to successfully treat ischemic trauma after events such as MI by reducing pathological scar tissue formation and improving survival of affected tissue. Additionally, carrier material with correct mechano-physical properties encompassing different native ECM proteins and supportive cells could be a way to improve the success rate of cellular therapies, such as transplantation of islets of Langerhans for type 1 DM treatment. Understanding the crosstalk between cells and the role of the ECM are important to overcome limitations en route to enabling treatments and therapies with higher success rates.

References

1. Frantz, C., Stewart, K. M. & Weaver, V. M. The extracellular matrix at a glance. *J. Cell Sci.* **123,** 4195–4200 (2010).
2. Urbanczyk, M., Layland, S. L. & Schenke-Layland, K. The role of extracellular matrix in biomechanics and its impact on bioengineering of cells and 3D tissues. *Matrix Biol.* **85–86,** 1–14 (2020).
3. Engin, A. B., Nikitovic, D., Neagu, M., Henrich-Noack, P., Docea, A. O., Shtilman, M. I., Golokhvast, K. & Tsatsakis, A. M. Mechanistic understanding of nanoparticles' interactions with extracellular matrix: the cell and immune system. *Part. Fibre Toxicol.* **14,** 22 (2017).
4. Fessler, L. I., Nelson, R. E. & Fessler, J. H. in *Methods Enzymol.* 271–294 (1994). doi:10.1016/0076-6879(94)45016-1
5. Nikolova, G., Strilic, B. & Lammert, E. The vascular niche and its basement membrane. *Trends Cell Biol.* **17,** 19–25 (2007).
6. Chelladurai, P., Seeger, W. & Pullamsetti, S. S. Matrix metalloproteinases and their inhibitors in pulmonary hypertension. *Eur. Respir. J.* **40,** 766–782 (2012).
7. Aird, W. C. Phenotypic heterogeneity of the endothelium: I. Structure, function, and mechanisms. *Circ. Res.* **100,** 158–173 (2007).
8. Schenke-Layland, K., Nsair, A., Van Handel, B., Angelis, E., Gluck, J. M., Votteler, M., Goldhaber, J. I., Mikkola, H. K., Kahn, M. & MacLellan, W. R. Recapitulation of the embryonic cardiovascular progenitor cell niche. *Biomaterials* **32,** 2748–2756 (2011).
9. Triyoso, D. H. & Good, T. A. Pulsatile shear stress leads to DNA fragmentation in human SH-SY5Y neuroblastoma cell line. *J. Physiol.* (1999). doi:10.1111/j.1469-7793.1999.355ac.x
10. Shive, M. S., Salloum, M. L. & Anderson, J. M. Shear stress-induced apoptosis of adherent neutrophils: A mechanism for persistence of cardiovascular device infections. *Proc. Natl. Acad. Sci.* (2000). doi:10.1073/pnas.110463197
11. Bjerre, L., Bünger, C. E., Kassem, M. & Mygind, T. Flow perfusion culture of human mesenchymal stem cells on silicate-substituted tricalcium phosphate scaffolds. *Biomaterials* **29,** 2616–2627 (2008).
12. Eoh, J. H., Shen, N., Burke, J. A., Hinderer, S., Xia, Z., Schenke-Layland, K. & Gerecht, S. Enhanced elastin synthesis and maturation in human vascular smooth muscle tissue derived from induced-pluripotent stem cells. *Acta Biomater.* **52,** 49–59 (2017).
13. Chen, Z., Peng, I.-C., Cui, X., Li, Y.-S., Chien, S. & Shyy, J. Y.-J. Shear stress, SIRT1, and vascular homeostasis. *Proc. Natl. Acad. Sci.* **107,** 10268–10273 (2010).
14. Nerem, R. M. Vascular Fluid Mechanics, the Arterial Wall, and Atherosclerosis. *J. Biomech. Eng.* **114,** 274–282 (1992).
15. Mouw, J. K., Ou, G. & Weaver, V. M. Extracellular matrix assembly: a multiscale deconstruction. *Nat. Rev. Mol. Cell Biol.* **15,** 771–785 (2014).
16. Cox, T. R. & Erler, J. T. Remodeling and homeostasis of the extracellular matrix: implications for fibrotic diseases and cancer. *Dis. Model. Mech.* **4,** 165–178 (2011).
17. Rodríguez, D., Morrison, C. J. & Overall, C. M. Matrix metalloproteinases: What do they not do? New substrates and biological roles identified by murine models and proteomics. *Biochim. Biophys. Acta - Mol. Cell Res.* **1803,** 39–54 (2010).
18. Apte, S. S. & Parks, W. C. Metalloproteinases: A parade of functions in matrix biology and an outlook for the future. *Matrix Biol.* **44–46,** 1–6 (2015).
19. Hanjaya-Putra, D., Yee, J., Ceci, D., Truitt, R., Yee, D. & Gerecht, S. Vascular endothelial growth factor and substrate mechanics regulate in vitro tubulogenesis of endothelial progenitor cells. *J. Cell. Mol. Med.* (2010). doi:10.1111/j.1582-4934.2009.00981.x
20. Grinnell, F. Fibroblast-collagen-matrix contraction: growth-factor signalling and mechanical loading. in *Trends Cell Biol.* (2000). doi:10.1016/S0962-8924(00)01802-X
21. Clause, K. C. & Barker, T. H. Extracellular matrix signaling in morphogenesis and repair. *Curr. Opin. Biotechnol.* **24,** 830–833 (2013).
22. Handorf, A. M., Zhou, Y., Halanski, M. A. & Li, W. J. Tissue stiffness dictates development, homeostasis, and disease progression. *Organogenesis* **11,** 1–15 (2015).
23. Liu, J., Wang, Y., Goh, W. I., Goh, H., Baird, M. A., Ruehland, S., Teo, S., Bate, N., Critchley, D. R., Davidson, M. W. & Kanchanawong, P. Talin determines the nanoscale architecture of focal adhesions. *Proc. Natl. Acad. Sci.* **112,** E4864–E4873 (2015).
24. Parsons, J. T. Focal adhesion kinase: The first ten years. *J. Cell Sci.* (2003). doi:10.1242/jcs.00373
25. Le Bœuf, F., Houle, F., Sussman, M. & Huot, J. Phosphorylation of focal adhesion kinase (FAK) on Ser732 is induced by Rho-dependent kinase and is essential for proline-rich tyrosine kinase-2-mediated phosphorylation of FAK on Tyr407 in response to vascular endothelial growth factor. *Mol. Biol. Cell* (2006). doi:10.1091/mbc.E05-12-1158
26. Kim, D.-H., Wong, P. K., Park, J., Levchenko, A. & Sun, Y. Microengineered Platforms for Cell Mechanobiology. *Annu. Rev. Biomed. Eng.* **11,** 203–233 (2009).
27. Wang, H.-B., Dembo, M., Hanks, S. K. & Wang, Y. -l. Focal adhesion kinase is involved in mechanosensing during fibroblast migration. *Proc. Natl. Acad. Sci.* (2002). doi:10.1073/pnas.201201198
28. Giancotti, F. G. & Ruoslahti, E. Integrin signaling. *Science (80-.).* **285,** 1028–1032 (1999).
29. Ilić, D., Almeida, E. A. C., Schlaepfer, D. D., Dazin, P., Aizawa, S. & Damsky, C. H. Extracellular matrix survival signals transduced by focal adhesion kinase suppress p53-mediated apoptosis. *J. Cell Biol.* (1998). doi:10.1083/jcb.143.2.547
30. Bae, Y. H., Mui, K. L., Hsu, B. Y., Liu, S. L., Cretu, A., Razinia, Z., Xu, T., Puré, E. & Assoian, R. K. A FAK-Cas-Rac-lamellipodin signaling module transduces extracellular matrix stiffness into mechanosensitive cell cycling. *Sci. Signal.* (2014). doi:10.1126/scisignal.2004838
31. Shih, Y. R. V., Tseng, K. F., Lai, H. Y., Lin, C. H. & Lee, O. K. Matrix stiffness regulation of integrin-mediated mechanotransduction during osteogenic differentiation of human mesenchymal stem cells. *J. Bone Miner. Res.* (2011). doi:10.1002/jbmr.278

32. LeGoff, L. & Lecuit, T. Mechanical forces and growth in animal tissues. *Cold Spring Harb. Perspect. Biol.* **8,** 1–18 (2016).
33. Symons, M. & Settleman, J. Rho family GTPases: More than simple switches. *Trends Cell Biol.* **10,** 415–419 (2000).
34. McCain, J. The MAPK (ERK) Pathway. *P T* **38,** 96–108 (2013).
35. Schwartz, M. Rho signalling at a glance. *J. Cell Sci.* **117,** 5457–5458 (2004).
36. Bishop, A. L. & Hall, A. Rho GTPases and their effector proteins. *Biochem. J.* **348,** 241–255 (2000).
37. Zhao, Z. & Manser, E. PAK family kinases. *Cell. Logist.* **2,** 59–68 (2012).
38. Paik, D. T., Tian, L., Williams, I. M., Rhee, S., Zhang, H., Liu, C., Mishra, R., Wu, S. M., Red-Horse, K. & Wu, J. C. Single-Cell RNA Sequencing Unveils Unique Transcriptomic Signatures of Organ-Specific Endothelial Cells. *Circulation* **142,** 1848–1862 (2020).
39. Witjas, F. M. R., van den Berg, B. M., van den Berg, C. W., Engelse, M. A. & Rabelink, T. J. Concise Review: The Endothelial Cell Extracellular Matrix Regulates Tissue Homeostasis and Repair. *Stem Cells Transl. Med.* **8,** 375–382 (2019).
40. Aird, W. C. Endothelial cell heterogeneity. *Crit Care Med* **31,** 221–230 (2003).
41. Badylak, S. F. Extracellular matrix and the immune system: friends or foes. *Nat. Rev. Urol.* **16,** 389–390 (2019).
42. Phillip, J. M., Aifuwa, I., Walston, J. & Wirtz, D. The Mechanobiology of Aging. *Annu. Rev. Biomed. Eng.* **17,** 113–141 (2015).
43. Baker, D. J., Wijshake, T., Tchkonia, T., Lebrasseur, N. K., Childs, B. G., Van De Sluis, B., Kirkland, J. L. & Van Deursen, J. M. Clearance of p16 Ink4a-positive senescent cells delays ageing-associated disorders. *Nature* (2011). doi:10.1038/nature10600
44. Pienta, K. J. & Coffey, D. S. Characterization of the subtypes of cell motility in ageing human skin fibroblasts. *Mech. Ageing Dev.* (1990). doi:10.1016/0047-6374(90)90001-V
45. Liu, L., Marti, G. P., Wei, X., Zhang, X., Zhang, H., Liu, Y. V., Nastai, M., Semenza, G. L. & Harmon, J. W. Age-dependent impairment of HIF-1α expression in diabetic mice: Correction with electroporation-facilitated gene therapy increases wound healing, angiogenesis, and circulating angiogenic cells. *J. Cell. Physiol.* (2008). doi:10.1002/jcp.21503
46. Williamson, K. A., Hamilton, A., Reynolds, J. A., Sipos, P., Crocker, I., Stringer, S. E. & Alexander, Y. M. Age-related impairment of endothelial progenitor cell migration correlates with structural alterations of heparan sulfate proteoglycans. *Aging Cell* (2013). doi:10.1111/acel.12031
47. Wood, L. K., Kayupov, E., Gumucio, J. P., Mendias, C. L., Claflin, D. R. & Brooks, S. V. Intrinsic stiffness of extracellular matrix increases with age in skeletal muscles of mice. *J. Appl. Physiol.* (2014). doi:10.1152/japplphysiol.00256.2014
48. Palombo, C. & Kozakova, M. Arterial stiffness, atherosclerosis and cardiovascular risk: Pathophysiologic mechanisms and emerging clinical indications. *Vascul. Pharmacol.* **77,** 1–7 (2016).
49. Choi, W. J., Russell, C. M., Tsai, C. M., Arzanpour, S. & Robinovitch, S. N. Age-related changes in dynamic compressive properties of trochanteric soft tissues over the hip. *J. Biomech.* (2015). doi:10.1016/j.jbiomech.2014.12.026
50. Suresh, S. Biomechanics and biophysics of cancer cells. *Acta Mater.* (2007). doi:10.1016/j.actamat.2007.04.022
51. Ignotzs, R. A. & Massague, J. Transforming Growth Factor-β Stimulates the Expression of Fibronectin and Collagen and Their Incorporation into the Extracellular Matrix. *J. Biol. Chem.* **261,** 4337–4345 (1986).
52. Bosman, F. T. & Stamenkovic, I. Functional structure and composition of the extracellular matrix. *J. Pathol.* **200,** 423–8 (2003).
53. Henriksen, K. & Karsdal, M. A. Type I Collagen. *Biochem. Collagens, Laminins Elastin Struct. Funct. Biomarkers* 1–11 (2016). doi:10.1016/B978-0-12-809847-9.00001-5
54. Jae, H. & Kwideok, C. *Novel Biomaterials for Regenerative Medicine*. **1077,** (Springer Singapore, 2018).
55. Kuivaniemi, H. & Tromp, G. Type III collagen (COL3A1): Gene and protein structure, tissue distribution, and associated diseases. *Gene* **707,** 151–171 (2019).
56. Kadler, K. E., Hill, A. & Canty-Laird, E. G. Collagen fibrillogenesis: fibronectin, integrins, and minor collagens as organizers and nucleators. *Curr. Opin. Cell Biol.* **20,** 495–501 (2008).
57. Banos, C. C., Thomas, A. H. & Kuo, C. K. Collagen fibrillogenesis in tendon development: Current models and regulation of fibril assembly. *Birth Defects Res. Part C Embryo Today Rev.* **84,** 228–244 (2008).
58. Wierzbicka-Patynowski, I. & Schwarzbauer, J. E. The ins and outs of fibronectin matrix assembly. *J. Cell Sci.* **116,** 3269–3276 (2003).
59. Navarro-Alvarez, N., Rivas-Carrillo, J. D., Soto-gutierrez, A. & Yuasa, T. Reestablishment of Microenvironment Is Necessary to Maintain In Vitro and In Vivo Human Islet Function. **17,** 111–119 (2016).
60. Leiva, O., Leon, C., Kah Ng, S., Mangin, P., Gachet, C. & Ravid, K. The role of extracellular matrix stiffness in megakaryocyte and platelet development and function. *Am. J. Hematol.* **93,** 430–441 (2018).
61. Zhang, W., Ge, Y., Cheng, Q., Zhang, Q., Fang, L. & Zheng, J. Decorin is a pivotal effector in the extracellular matrix and tumour microenvironment. *Oncotarget* **9,** 5480–5491 (2018).
62. Gubbiotti, M. A., Vallet, S. D., Ricard-blum, S. & Iozzo, R. V. Decorin interacting network : A comprehensive analysis of decorin-binding partners and their versatile functions. *Matrix Biol.* **55,** 7–21 (2016).
63. Neill, T., Schaefer, L. & Iozzo, R. V. Decorin - A Guardian from the Matrix. *Am. J. Pathol.* **181,** 380–387 (2012).
64. Järveläinen, H., Sainio, A. & Wight, T. N. Pivotal role for decorin in angiogenesis. *Matrix Biol.* **43,** 15–26 (2015).
65. Hildebrand, A., Romaris, M., Rasmussen, M., Heinegard, D., Twardzik, D. R., Border, W. A. & Ruoslahti, E. Interaction of the small interstitial proteoglycans biglycan, decorin and fibromodulin with transforming growth factor β. *Biochem. J.* (1994). doi:10.1042/bj3020527
66. Urbanczyk, M., Zbinden, A. & Schenke-Layland, K. Organ-specific endothelial cell heterogenicity and its impact on regenerative medicine and biomedical engineering applications. *Adv. Drug Deliv. Rev.* **186,** 114323 (2022).
67. Boland, E., Quondamatteo, F. & Van Agtmael, T. The role of basement membranes in cardiac biology and disease. *Biosci. Rep.* **41,** 1–21 (2021).
68. Sekiguchi, R. & Yamada, K. M. in *Physiol. Behav.* **176,** 143–191 (2018).
69. Fox, J. W., Mayer, U., Nischt, R., Aumailley, M., Reinhardt, D., Wiedemann, H., Mann, K., Timpl, R., Krieg, T. & Engel, J. Recombinant nidogen consists of three globular domains and mediates binding of laminin to collagen type IV. *EMBO J.* **10,** 3137–46 (1991).

70. Cross, S. E., Vaughan, R. H., Willcox, A. J., McBride, A. J., Abraham, A. A., Han, B., Johnson, J. D., Maillard, E., Bateman, P. A., Ramracheya, R. D., Rorsman, P., Kadler, K. E., Dunne, M. J., Hughes, S. J. & Johnson, P. R. V. Key Matrix Proteins Within the Pancreatic Islet Basement Membrane Are Differentially Digested During Human Islet Isolation. *Am. J. Transplant.* **17,** 451–461 (2017).
71. Mutgan, A. C., Jandl, K. & Kwapiszewska, G. Endothelial Basement Membrane Components and Their Products, Matrikines: Active Drivers of Pulmonary Hypertension? *Cells* **9,** 1–25 (2020).
72. Nicosia, R. F., Bonanno, E., Smith, M. & Yurchenco, P. Modulation of angiogenesis in vitro by laminin-entactin complex. *Dev. Biol.* **164,** 197–206 (1994).
73. Martinez-Hernandez, A. & Amenta, P. S. The extracellular matrix in hepatic regeneration. *FASEB J.* **9,** 1401–1410 (1995).
74. Lee, H. K., Seo, I. A., Suh, D. J. & Park, H. T. Nidogen plays a role in the regenerative axon growth of adult sensory neurons through Schwann cells. *J. Korean Med. Sci.* **24,** 654–659 (2009).
75. Wolfstetter, G., Dahlitz, I., Pfeifer, K., Töpfer, U., Alt, J. A., Pfeifer, D. C., Lakes-Harlan, R., Baumgartner, S., Palmer, R. H. & Holz, A. Characterization of *Drosophila Nidogen* / *entactin* reveals roles in basement membrane stability, barrier function and nervous system patterning. *Development* **146,** dev168948 (2019).
76. Evseenko, D., Schenke-Layland, K., Dravid, G., Zhu, Y., Hao, Q. L., Scholes, J., Wang, X. C., MacLellan, W. R. & Crooks, G. M. Identification of the critical extracellular matrix proteins that promote human embryonic stem cell assembly. *Stem Cells Dev.* (2009). doi:10.1089/scd.2008.0293
77. Liliensiek, S. J., Nealey, P. & Murphy, C. J. Characterization of endothelial basement membrane nanotopography in rhesus macaque as a guide for vessel tissue engineering. *Tissue Eng. Part A* **15,** 2643–2651 (2009).
78. Kumar, A., Placone, J. K. & Engler, A. J. Understanding the extracellular forces that determine cell fate and maintenance. *Development* **144,** 4261–4270 (2017).
79. Yang, Y., Chawla, A., Zhang, J., Esa, A., Jang, H. L. & Khademhosseini, A. Applications of Nanotechnology for Regenerative Medicine; Healing Tissues at the Nanoscale. *Princ. Regen. Med.* 485–504 (2019). doi:10.1016/b978-0-12-809880-6.00029-1
80. Woodcock, E. A. & Matkovich, S. J. Cardiomyocytes structure, function and associated pathologies. *Int. J. Biochem. Cell Biol.* **37,** 1746–1751 (2005).
81. Pugsley, M. K. & Tabrizchi, R. The vascular system. *J. Pharmacol. Toxicol. Methods* **44,** 333–340 (2000).
82. Braile, M., Marcella, S., Cristinziano, L., Galdiero, M. R., Modestino, L., Ferrara, A. L., Varricchi, G., Marone, G. & Loffredo, S. VEGF-A in Cardiomyocytes and Heart Diseases. *Int. J. Mol. Sci.* **21,** 5294 (2020).
83. Warriner, D. Davidson's Principles and Practices of Medicine (21st edn). *Br. J. Hosp. Med.* **72,** 117–117 (2011).
84. Kapa, S., DeSimone, C. V. & Asirvatham, S. J. Innervation of the heart: An invisible grid within a black box. *Trends Cardiovasc. Med.* **26,** 245–257 (2016).
85. Liu, J., Laksman, Z. & Backx, P. H. The electrophysiological development of cardiomyocytes. *Adv. Drug Deliv. Rev.* **96,** 253–273 (2016).
86. Grant, A. O. Cardiac ion channels. *Circ. Arrhythm. Electrophysiol.* **2,** 185–94 (2009).
87. Yang, H., Borg, T. K., Wang, Z., Ma, Z. & Gao, B. Z. Role of the basement membrane in regulation of cardiac electrical properties. *Ann. Biomed. Eng.* **42,** 1148–57 (2014).
88. Robertson, C., Tran, D. D. & George, S. C. Concise Review: Maturation Phases of Human Pluripotent Stem Cell-Derived Cardiomyocytes. *Stem Cells* **31,** 829–837 (2013).
89. Margulies, K. B. & Houser, S. R. Cellular Basis for Heart Failure. *Heart Fail.* 32–47 (2011). doi:10.1016/B978-1-4160-5895-3.10003-8
90. Karbassi, E., Fenix, A., Marchiano, S., Muraoka, N., Nakamura, K., Yang, X. & Murry, C. E. Cardiomyocyte maturation: advances in knowledge and implications for regenerative medicine. *Nat. Rev. Cardiol.* **17,** 341–359 (2020).
91. Vara, D. S., Salacinski, H. J., Kannan, R. Y., Bordenave, L., Hamilton, G. & Seifalian, A. M. Cardiovascular tissue engineering: State of the art. *Pathol. Biol.* **53,** 599–612 (2005).
92. Fisher, A. B., Chien, S., Barakat, A. I. & Nerem, R. M. Endothelial cellular response to altered shear stress. *Am. J. Physiol. Lung Cell. Mol. Physiol.* **281,** L529-33 (2001).
93. Chen, K.-D., Li, Y.-S., Kim, M., Li, S., Yuan, S., Chien, S. & Shyy, J. Y. J. Mechanotransduction in Response to Shear Stress. *J. Biol. Chem.* **274,** 18393–18400 (1999).
94. Jalali, S. Integrin-mediated mechanotransduction requires its dynamic interaction with specific extracellular matrix (ECM) ligands. *Proc. Natl. Acad. Sci.* **98,** 1042–1046 (2001).
95. Jin, S. W., Beis, D., Mitchell, T., Chen, J. N. & Stainier, D. Y. R. Cellular and molecular analyses of vascular tube and lumen formation in zebrafish. *Development* (2005). doi:10.1242/dev.02087
96. Nemeno-Guanzon, J. G., Lee, S., Berg, J. R., Jo, Y. H., Yeo, J. E., Nam, B. M., Koh, Y.-G. & Lee, J. I. Trends in tissue engineering for blood vessels. *J. Biomed. Biotechnol.* **2012,** 956345 (2012).
97. Demir, R., Kayisli, U. A., Cayli, S. & Huppertz, B. Sequential Steps During Vasculogenesis and Angiogenesis in the Very Early Human Placenta. *Placenta* **27,** 535–539 (2006).
98. Demir, R., Seval, Y. & Huppertz, B. Vasculogenesis and angiogenesis in the early human placenta. *Acta Histochem.* **109,** 257–265 (2007).
99. Kaufmann, P., Mayhew, T. M. & Charnock-Jones, D. S. Aspects of human fetoplacental vasculogenesis and angiogenesis. II. Changes during normal pregnancy. *Placenta* **25,** 114–126 (2004).
100. Donovan, M. F. & Cascella, M. *Embryology, Weeks 6-8*. *StatPearls* (2021). at <http://www.ncbi.nlm.nih.gov/pubmed/33085328>
101. Papaioannou, T. G. & Stefanadis, C. Vascular wall shear stress: basic principles and methods. *Hellenic J. Cardiol.* **46,** 9–15 (2005).
102. MacK, J. J. & Luisa Iruela-Arispe, M. NOTCH regulation of the endothelial cell phenotype. *Curr. Opin. Hematol.* **25,** 212–218 (2018).
103. Blose, S. H. & Chacko, S. In Vitro Behavior Of Guinea Pig Arterial And Venous Endothelial Cells. *Dev. Growth Differ.* **17,** 153–165 (1975).

104. Dyer, L. A. & Patterson, C. Development of the endothelium: An emphasis on heterogeneity. *Semin. Thromb. Hemost.* **36,** 227–235 (2010).
105. Rensen, S. S., Niessen, P. M., van Deursen, J. M., Janssen, B. J., Heijman, E., Hermeling, E., Meens, M., Lie, N., Gijbels, M. J., Strijkers, G. J., Doevendans, P. A., Hofker, M. H., De Mey, J. G. R. & van Eys, G. J. Smoothelin-B Deficiency Results in Reduced Arterial Contractility, Hypertension, and Cardiac Hypertrophy in Mice. *Circulation* **118,** 828–836 (2008).
106. Kabaeva, Z., Meekhof, K. E. & Michele, D. E. Sarcolemma instability during mechanical activity in Largemyd cardiac myocytes with loss of dystroglycan extracellular matrix receptor function. *Hum. Mol. Genet.* **20,** 3346–55 (2011).
107. Croissant, C., Tuariihionoa, A., Bacou, M., Souleyreau, W., Sala, M., Henriet, E., Bikfalvi, A., Saltel, F. & Auguste, P. DDR1 and DDR2 physical interaction leads to signaling interconnection but with possible distinct functions. *Cell Adh. Migr.* **12,** 324–334 (2018).
108. Karsdal, M. A., Nielsen, S. H., Leeming, D. J., Langholm, L. L., Nielsen, M. J., Manon-Jensen, T., Siebuhr, A., Gudmann, N. S., Rønnow, S., Sand, J. M., Daniels, S. J., Mortensen, J. H. & Schuppan, D. The good and the bad collagens of fibrosis – Their role in signaling and organ function. *Adv. Drug Deliv. Rev.* **121,** 43–56 (2017).
109. Costell, M., Gustafsson, E., Aszódi, A., Mörgelin, M., Bloch, W., Hunziker, E., Addicks, K., Timpl, R. & Fässler, R. Perlecan Maintains the Integrity of Cartilage and Some Basement Membranes. *J. Cell Biol.* **147,** 1109–1122 (1999).
110. Bader, B. L., Smyth, N., Nedbal, S., Miosge, N., Baranowsky, A., Mokkapati, S., Murshed, M. & Nischt, R. Compound genetic ablation of nidogen 1 and 2 causes basement membrane defects and perinatal lethality in mice. *Mol. Cell. Biol.* **25,** 6846–56 (2005).
111. Pöschl, E., Schlötzer-Schrehardt, U., Brachvogel, B., Saito, K., Ninomiya, Y. & Mayer, U. Collagen IV is essential for basement membrane stability but dispensable for initiation of its assembly during early development. *Development* **131,** 1619–1628 (2004).
112. Reissig, L. F., Herdina, A. N., Rose, J., Maurer-Gesek, B., Lane, J. L., Prin, F., Wilson, R., Hardman, E., Galli, A., Tudor, C., Tuck, E., Icoresi-Mazzeo, C., White, J. K., Ryder, E., Gleeson, D., Adams, D. J., Geyer, S. H., Mohun, T. J. & Weninger, W. J. The Col4a2 em1(IMPC)Wtsi mouse line – lessons from the deciphering the mechanisms of developmental disorders (DMDD) program. *Biol. Open* **8,** (2019).
113. Townsend, N., Kazakiewicz, D., Lucy Wright, F., Timmis, A., Huculeci, R., Torbica, A., Gale, C. P., Achenbach, S., Weidinger, F. & Vardas, P. Epidemiology of cardiovascular disease in Europe. *Nat. Rev. Cardiol.* (2021). doi:10.1038/s41569-021-00607-3
114. Balta, S. Endothelial Dysfunction and Inflammatory Markers of Vascular Disease. *Curr. Vasc. Pharmacol.* **19,** 243–249 (2020).
115. Fioretta, E. S., von Boehmer, L., Motta, S. E., Lintas, V., Hoerstrup, S. P. & Emmert, M. Y. Cardiovascular tissue engineering: From basic science to clinical application. *Exp. Gerontol.* **117,** 1–12 (2019).
116. Heusch, G. Myocardial ischaemia–reperfusion injury and cardioprotection in perspective. *Nat. Rev. Cardiol.* **17,** 773–789 (2020).
117. Frank, A., Bonney, M., Bonney, S., Weitzel, L., Koeppen, M. & Eckle, T. Myocardial Ischemia Reperfusion Injury. *Semin. Cardiothorac. Vasc. Anesth.* **16,** 123–132 (2012).
118. Hausenloy, D. J. & Yellon, D. M. Myocardial ischemia-reperfusion injury: a neglected therapeutic target. *J. Clin. Invest.* **123,** 92–100 (2013).
119. Martino, F., Perestrelo, A. R., Vinarský, V., Pagliari, S. & Forte, G. Cellular mechanotransduction: From tension to function. *Front. Physiol.* **9,** 1–21 (2018).
120. Worman, H. J. & Bonne, G. 'Laminopathies': A wide spectrum of human diseases. *Exp. Cell Res.* (2007). doi:10.1016/j.yexcr.2007.03.028
121. Graf, K., Neuss, M., Stawowy, P., Hsueh, W. A., Fleck, E. & Law, R. E. Angiotensin II and α(v)β3 integrin expression in rat neonatal cardiac fibroblasts. *Hypertension* (2000). doi:10.1161/01.HYP.35.4.978
122. Hinderer, S. & Schenke-Layland, K. Cardiac fibrosis – A short review of causes and therapeutic strategies. *Adv. Drug Deliv. Rev.* (2019). doi:10.1016/j.addr.2019.05.011
123. Frangogiannis, N. G. The extracellular matrix in myocardial injury, repair, and remodeling. *J. Clin. Invest.* **127,** 1600–1612 (2017).
124. Lee, A. Y., Mahler, N., Best, C., Lee, Y.-U. & Breuer, C. K. Regenerative implants for cardiovascular tissue engineering. *Transl. Res.* **163,** 321–341 (2014).
125. Badylak, S. F., Freytes, D. O. & Gilbert, T. W. Extracellular matrix as a biological scaffold material: Structure and function. *Acta Biomater.* **5,** 1–13 (2009).
126. Long, J. L. & Tranquillo, R. T. Elastic fiber production in cardiovascular tissue-equivalents. *Matrix Biol.* **22,** 339–350 (2003).
127. Ross, J. . & Tranquillo, R. . ECM gene expression correlates with in vitro tissue growth and development in fibrin gel remodeled by neonatal smooth muscle cells. *Matrix Biol.* **22,** 477–490 (2003).
128. Yao, L., Liu, J. & Andreadis, S. T. Composite Fibrin Scaffolds Increase Mechanical Strength and Preserve Contractility of Tissue Engineered Blood Vessels. *Pharm. Res.* **25,** 1212–1221 (2008).
129. Weber, M., Heta, E., Moreira, R., Gesche, V. N., Schermer, T., Frese, J., Jockenhoevel, S. & Mela, P. Tissue-Engineered Fibrin-Based Heart Valve with a Tubular Leaflet Design. *Tissue Eng. Part C Methods* **20,** 265–275 (2014).
130. Syedain, Z. H., Meier, L. A., Bjork, J. W., Lee, A. & Tranquillo, R. T. Implantable arterial grafts from human fibroblasts and fibrin using a multi-graft pulsed flow-stretch bioreactor with noninvasive strength monitoring. *Biomaterials* **32,** 714–722 (2011).
131. Souren, J. E. M., Schneijdenberg, C., Verkleij, A. J. & Wijk, R. Factors controlling the rhythmic contraction of collagen gels by neonatal heart cells. *Vitr. Cell. Dev. Biol. - Anim.* **28,** 199–204 (1992).
132. Henderson, J. R., Daniel, P. M. & Fraser, P. A. The pancreas as a single organ: the influence of the endocrine upon the exocrine part of the gland. *Gut* **22,** 158–167 (1981).
133. Keller, J. Human pancreatic exocrine response to nutrients in health and disease. *Gut* **54,** 1–28 (2005).
134. Röder, P. V., Wu, B., Liu, Y. & Han, W. Pancreatic regulation of glucose homeostasis. *Exp. Mol. Med.* **48,** e219 (2016).

135. Vlahos, A. E., Kinney, S. M., Kingston, B. R., Keshavjee, S., Won, S. Y., Martyts, A., Chan, W. W. C. & Sefton, M. V. Endothelialized collagen based pseudo-islets enables tuneable subcutaneous diabetes therapy. *Biomaterials* **232,** 119710 (2020).
136. Hellman, B. & Angervall, L. The Frequency Distribution of the Number and Volume of the Islets of Langerhans in Man. *Acta Pathol. Microbiol. Scand.* **53,** 230–236 (1961).
137. Petersen, M. C. & Shulman, G. I. Mechanisms of insulin action and insulin resistance. *Physiol. Rev.* **98,** 2133–2223 (2018).
138. Adeva-Andany, M. M., Funcasta-Calderón, R., Fernández-Fernández, C., Castro-Quintela, E. & Carneiro-Freire, N. Metabolic effects of glucagon in humans. *J. Clin. Transl. Endocrinol.* **15,** 45–53 (2019).
139. Rogal, J., Zbinden, A., Schenke-Layland, K. & Loskill, P. Stem-cell based organ-on-a-chip models for diabetes research. *Adv. Drug Deliv. Rev.* **140,** 101–128 (2019).
140. Rorsman, P. & Huising, M. O. The somatostatin-secreting pancreatic δ-cell in health and disease. *Nat. Rev. Endocrinol.* **14,** 404–414 (2018).
141. Aragón, F., Karaca, M., Novials, A., Maldonado, R., Maechler, P. & Rubí, B. Pancreatic polypeptide regulates glucagon release through PPYR1 receptors expressed in mouse and human alpha-cells. *Biochim. Biophys. Acta - Gen. Subj.* **1850,** 343–351 (2015).
142. Egido, E. M., Rodriguez-Gallardo, J., Silvestre, R. A. & Marco, J. Inhibitory effect of ghrelin on insulin and pancreatic somatostatin secretion. *Eur. J. Endocrinol.* **146,** 241–4 (2002).
143. Broglio, F., Gottero, C., Benso, A., Prodam, F., Destefanis, S., Gauna, C., Maccario, M., Deghenghi, R., van der Lely, A. J. & Ghigo, E. Effects of Ghrelin on the Insulin and Glycemic Responses to Glucose, Arginine, or Free Fatty Acids Load in Humans. *J. Clin. Endocrinol. Metab.* **88,** 4268–4272 (2003).
144. Salehi, A. Effects of ghrelin on insulin and glucagon secretion: a study of isolated pancreatic islets and intact mice. *Regul. Pept.* **118,** 143–150 (2004).
145. Arosio, M., Ronchi, C. L., Gebbia, C., Cappiello, V., Beck-Peccoz, P. & Peracchi, M. Stimulatory Effects of Ghrelin on Circulating Somatostatin and Pancreatic Polypeptide Levels. *J. Clin. Endocrinol. Metab.* **88,** 701–704 (2003).
146. Ionescu-Tirgoviste, C., Gagniuc, P. A., Gubceac, E., Mardare, L., Popescu, I., Dima, S. & Militaru, M. A 3D map of the islet routes throughout the healthy human pancreas. *Sci. Rep.* **5,** 14634 (2015).
147. Cabrera, O., Berman, D. M., Kenyon, N. S., Ricordi, C., Berggren, P. & Caicedo, A. The unique cytoarchitecture of human pancreatic islets has implications for islet cell function. *PNAS* **103,** 2334–2339 (2006).
148. Brissova, M., Fowler, M. J., Nicholson, W. E., Chu, A., Hirshberg, B., Harlan, D. M. & Powers, A. C. Assessment of Human Pancreatic Islet Architecture and Composition by Laser Scanning Confocal Microscopy. *J. Histochem. Cytochem.* **53,** 1087–1097 (2005).
149. Orci, L., Baetens, D., Ravazzola, M., Stefan, Y. & Malaisse-Lagae, F. Pancreatic polypeptide and glucagon: Non-random distribution in pancreatic islets. *Life Sci.* **19,** 1811–1816 (1976).
150. Ichii, H., Inverardi, L., Pileggi, A., Molano, R. D., Cabrera, O., Caicedo, A., Messinger, S., Kuroda, Y., Berggren, P.-O. & Ricordi, C. A Novel Method for the Assessment of Cellular Composition and Beta-Cell Viability in Human Islet Preparations. *Am. J. Transplant.* **5,** 1635–1645 (2005).
151. Fu, Z., R. Gilbert, E. & Liu, D. Regulation of Insulin Synthesis and Secretion and Pancreatic Beta-Cell Dysfunction in Diabetes. *Curr. Diabetes Rev.* **9,** 25–53 (2012).
152. Henquin, J.-C., Ishiyama, N., Nenquin, M., Ravier, M. A. & Jonas, J.-C. Signals and Pools Underlying Biphasic Insulin Secretion. *Diabetes* **51,** S60–S67 (2002).
153. McCulloch, L. J., van de Bunt, M., Braun, M., Frayn, K. N., Clark, A. & Gloyn, A. L. GLUT2 (SLC2A2) is not the principal glucose transporter in human pancreatic beta cells: Implications for understanding genetic association signals at this locus. *Mol. Genet. Metab.* **104,** 648–653 (2011).
154. Matschinsky, F. M. & Wilson, D. F. The central role of glucokinase in glucose homeostasis: A perspective 50 years after demonstrating the presence of the enzyme in islets of Langerhans. *Front. Physiol.* **10,** 148 (2019).
155. Jitrapakdee, S., Wutthisathapornchai, A., Wallace, J. C. & MacDonald, M. J. Regulation of insulin secretion: Role of mitochondrial signalling. *Diabetologia* **53,** 1019–1032 (2010).
156. Klec, C., Ziomek, G., Pichler, M., Malli, R. & Graier, W. F. Calcium signaling in ß-cell physiology and pathology: A revisit. *Int. J. Mol. Sci.* **20,** (2019).
157. Prasad, V., Okunade, G. W., Miller, M. L. & Shull, G. E. Phenotypes of SERCA and PMCA knockout mice. *Biochem. Biophys. Res. Commun.* **322,** 1192–1203 (2004).
158. Kalwat, M. A. & Thurmond, D. C. Signaling mechanisms of glucose-induced F-actin remodeling in pancreatic islet β cells. *Exp. Mol. Med.* **45,** e37-12 (2013).
159. Zhang, W., Thompson, B. J., Hietakangas, V. & Cohen, S. M. MAPK/ERK signaling regulates insulin sensitivity to control glucose metabolism in Drosophila. *PLoS Genet.* **7,** 1–10 (2011).
160. Sidarala, V. & Kowluru, A. The Regulatory Roles of Mitogen-Activated Protein Kinase (MAPK) Pathways in Health and Diabetes: Lessons Learned from the Pancreatic β-Cell. *Recent Pat. Endocr. Metab. Immune Drug Discov.* **10,** 76–84 (2017).
161. Lammert, E. & Kragl, M. in *Islets of Langerhans* **654,** 39–58 (Springer Netherlands, 2015).
162. Otonkoski, T., Banerjee, M., Korsgren, O., Thornell, L.-E. & Virtanen, I. Unique basement membrane structure of human pancreatic islets: implications for beta-cell growth and differentiation. *Diabetes. Obes. Metab.* **10 Suppl 4,** 119–27 (2008).
163. Arous, C. & Wehrle-Haller, B. Role and impact of the extracellular matrix on integrin-mediated pancreatic β-cell functions. *Biol. Cell* **109,** 223–237 (2017).
164. Townsend, S. E. & Gannon, M. Extracellular Matrix-Associated Factors Play Critical Roles in Regulating Pancreatic β-Cell Proliferation and Survival. *Endocrinology* (2019). doi:10.1210/en.2019-00206
165. Jiang, F., Naselli, G. & Harrison, L. C. Distinct Distribution of Laminin and Its Integrin Receptors in the Pancreas. **50,** 1625–1632 (2002).
166. Spenlé, C., Simon-Assmann, P., Orend, G. & Miner, J. H. Laminin α5 guides tissue patterning and organogenesis. *Cell*

Adhes. Migr. **7,** 90–100 (2013).
167. Maillard, E., Sencier, M.-C., Langlois, A., Bietiger, W., Krafft, M., Pinget, M. & Sigrist, S. Extracellular matrix proteins involved in pseudoislets formation. *Islets* **1,** 232–241 (2009).
168. Stützer, I., Esterházy, D. & Stoffel, M. The pancreatic beta cell surface proteome. *Diabetologia* **55,** 1877–89 (2012).
169. Humphries, J. D., Byron, A. & Humphries, M. J. Integrin ligands at a glance. *J. Cell Sci.* **119,** 3901–3903 (2006).
170. Takada, Y., Ye, X. & Simon, S. The integrins. *Genome Biol.* **8,** 215 (2007).
171. Daoud, J., Petropavlovskaia, M., Rosenberg, L. & Tabrizian, M. The effect of extracellular matrix components on the preservation of human islet function in vitro. *Biomaterials* **31,** 1676–1682 (2010).
172. Hadavi, E., Leijten, J., Engelse, M., de Koning, E., Jonkheijm, P., Karperien, M. & van Apeldoorn, A. Microwell Scaffolds Using Collagen-IV and Laminin-111 Lead to Improved Insulin Secretion of Human Islets. *Tissue Eng. Part C Methods* **25,** 71–81 (2019).
173. Boraschi-Diaz, I., Wang, J., Mort, J. S. & Komarova, S. V. Collagen Type I as a Ligand for Receptor-Mediated Signaling. *Front. Phys.* **5,** (2017).
174. Konstantinova, I. & Lammert, E. Microvascular development: Learning from pancreatic islets. *BioEssays* **26,** 1069–1075 (2004).
175. Jansson, L., Barbu, A., Bodin, B., Drott, C. J., Espes, D., Gao, X., Grapensparr, L., Källskog, Ö., Lau, J., Liljebäck, H., Palm, F., Quach, M., Sandberg, M., Strömberg, V., Ullsten, S. & Carlsson, P.-O. Pancreatic islet blood flow and its measurement. *Ups. J. Med. Sci.* **121,** 81–95 (2016).
176. Henderson, J. R. & Moss, M. C. A MORPHOMETRIC STUDY OF THE ENDOCRINE AND EXOCRINE CAPILLARIES OF THE PANCREAS. *Q. J. Exp. Physiol.* **70,** 347–356 (1985).
177. Nikolova, G. & Lammert, E. Interdependent development of blood vessels and organs. *Cell Tissue Res.* **314,** 33–42 (2003).
178. Lammert, E., Cleaver, O. & Melton, D. Role of endothelial cells in early pancreas and liver development. *Mech. Dev.* **120,** 59–64 (2003).
179. Olsson, R. & Carlsson, P. The pancreatic islet endothelial cell: emerging roles in islet function and disease. *Int J Biochem Cell Biol* **38,** 710–714 (2006).
180. Marcela Brissova, Alena Shostak, Corinne L. Fligner, Frank L. Revetta, Mary K. Washington, Alvin C. Powers & Rebecca L. Hull. Human Islets Have Fewer Blood Vessels than Mouse Islets and the Density of Islet Vascular Structures Is Increased in Type 2 Diabetes. *J. Histochem. Cytochem.* **63,** 637–345 (2015).
181. Johansson, Å., Lau, J., Sandberg, M., Borg, L. A. H., Magnusson, P. U. & Carlsson, P. O. Endothelial cell signalling supports pancreatic beta cell function in the rat. *Diabetologia* **52,** 2385–2394 (2009).
182. Skrzypek, K., Barrera, Y. B., Groth, T. & Stamatialis, D. Endothelial and beta cell composite aggregates for improved function of a bioartificial pancreas encapsulation device. *Int. J. Artif. Organs* **41,** 152–159 (2018).
183. Rambøl, M. H., Han, E. & Niklason, L. E. Microvessel Network Formation and Interactions with Pancreatic Islets in Three-Dimensional Chip Cultures. *Tissue Eng. Part A* **26,** 556–568 (2020).
184. Lammert, E., Gu, G., McLaughlin, M., Brown, D., Brekken, R., Murtaugh, L. C., Gerber, H.-P., Ferrara, N. & Melton, D. A. Role of VEGF-A in Vascularization of Pancreatic Islets. *Curr. Biol.* **13,** 1070–1074 (2003).
185. Brissova, M., Shostak, A., Shiota, M., Wiebe, P. O., Poffenberger, G., Kantz, J., Chen, Z., Carr, C., Gray Jerome, W., Chen, J., Scott Baldwin, H., Nicholson, W., Bader, D. M., Jetton, T., Gannon, M. & Powers, A. C. Pancreatic Islet Production of Vascular Endothelial Growth Factor-A Is Essential for Islet Vascularization, Revascularization, and Function. *Diabetes* **55,** 2974–2985 (2006).
186. Hogan, M. F. & Hull, R. L. The islet endothelial cell: a novel contributor to beta cell secretory dysfunction in diabetes. *Diabetologia* **60,** 952–959 (2018).
187. Armanet, M., Wojtusciszyn, A., Morel, P., Parnaud, G., Rousselle, P., Sinigaglia, C., Berney, T. & Bosco, D. Regulated laminin-332 expression in human islets of Langerhans. *FASEB J.* **23,** 4046–55 (2009).
188. Sigmundsson, K., Ojala, J. R. M., Öhman, M. K., Österholm, A.-M., Moreno-Moral, A., Domogatskaya, A., Chong, L. Y., Sun, Y., Chai, X., Steele, J. A. M., George, B., Patarroyo, M., Nilsson, A.-S., Rodin, S., Ghosh, S., Stevens, M. M., Petretto, E. & Tryggvason, K. Culturing functional pancreatic islets on α5-laminins and curative transplantation to diabetic mice. *Matrix Biol.* **70,** 5–19 (2018).
189. Wieland, F. C., Sthijns, M. M. J. P. E., Geuens, T., van Blitterswijk, C. A. & LaPointe, V. L. S. The Role of Alpha Cells in the Self-Assembly of Bioengineered Islets. *Tissue Eng. Part A* **00,** ten.tea.2020.0080 (2020).
190. Zbinden, A., Urbanczyk, M., Layland, S. L., Becker, L., Marzi, J., Bosch, M., Loskill, P., Duffy, G. P. & Schenke-Layland, K. Collagen and Endothelial Cell Coculture Improves β-Cell Functionality and Rescues Pancreatic Extracellular Matrix. *Tissue Eng. Part A* ten.tea.2020.0250 (2020). doi:10.1089/ten.tea.2020.0250
191. Daniel, C., Wiede, J., Krutzsch, H. C., Ribeiro, S. M. F., Roberts, D. D., Murphy-Ullrich, J. E. & Hugo, C. Thrombospondin-1 is a major activator of TGF-beta in fibrotic renal disease in the rat in vivo. *Kidney Int.* **65,** 459–68 (2004).
192. Lee, J.-H., Lee, J.-H. & Rane, S. G. TGF-β Signaling in Pancreatic Islet β Cell Development and Function. *Endocrinology* **162,** 1–10 (2021).
193. Olerud, J., Mokhtari, D., Johansson, M., Christoffersson, G., Lawler, J., Welsh, N. & Carlsson, P.-O. Thrombospondin-1: an islet endothelial cell signal of importance for β-cell function. *Diabetes* **60,** 1946–54 (2011).
194. Cunha, D. A., Cito, M., Grieco, F. A., Cosentino, C., Danilova, T., Ladrière, L., Lindahl, M., Domanskyi, A., Bugliani, M., Marchetti, P., Eizirik, D. L. & Cnop, M. Pancreatic β-cell protection from inflammatory stress by the endoplasmic reticulum proteins thrombospondin 1 and mesencephalic astrocyte-derived neutrotrophic factor (MANF). *J. Biol. Chem.* **292,** 14977–14988 (2017).
195. Cunha, D. A., Cito, M., Carlsson, P.-O., Vanderwinden, J.-M., Molkentin, J. D., Bugliani, M., Marchetti, P., Eizirik, D. L. & Cnop, M. Thrombospondin 1 protects pancreatic β-cells from lipotoxicity via the PERK–NRF2 pathway. *Cell Death Differ.* **23,** 1995–2006 (2016).
196. Diagnosis and Classification of Diabetes Mellitus. *Diabetes Care* **37,** S81–S90 (2014).
197. *IDF Diabetes Atlas*. (2021). at <https://diabetesatlas.org>

198. DeFronzo, R. A., Ferrannini, E., Groop, L., Henry, R. R., Herman, W. H., Holst, J. J., Hu, F. B., Kahn, C. R., Raz, I., Shulman, G. I., Simonson, D. C., Testa, M. A. & Weiss, R. Type 2 diabetes mellitus. *Nat. Rev. Dis. Prim.* **1,** 15019 (2015).
199. McDevitt, H. O. Characteristics of autoimmunity in type 1 diabetes and type 1.5 overlap with type 2 diabetes. *Diabetes* **54,** S4–S10 (2005).
200. Jeker, L. T., Bour-Jordan, H. & Bluestone, J. A. Breakdown in peripheral tolerance in type 1 diabetes in mice and humans. *Cold Spring Harb. Perspect. Med.* **2,** (2012).
201. Polychronakos, C. & Li, Q. Understanding type 1 diabetes through genetics: advances and prospects. *Nat. Rev. Genet.* **12,** 781–92 (2011).
202. Roep, B. O. The role of T-cells in the pathogenesis of Type 1 diabetes: From cause to cure. *Diabetologia* **46,** 305–321 (2003).
203. Rewers, M. & Ludvigsson, J. Environmental risk factors for type 1 diabetes. *Lancet* **387,** 2340–2348 (2016).
204. Vlahos, A. E., Cober, N. & Sefton, M. V. Modular tissue engineering for the vascularization of subcutaneously transplanted pancreatic islets. *Proc. Natl. Acad. Sci.* **114,** 9337–9342 (2017).
205. Cañibano-Hernández, A., Sáenz, L. & Espona-noguera, A. Current advanced therapy cell-based medicinal products for type-1-diabetes treatment. *Int. J. Pharm.* **543,** 107–120 (2018).
206. Hadavi, E., Leijten, J., Brinkmann, J., Jonkheijm, P., Karperien, M. & van Apeldoorn, A. Fibronectin and Collagen IV Microcontact Printing Improves Insulin Secretion by INS1E Cells. *Tissue Eng. Part C Methods* **24,** 628–636 (2018).
207. Shin, J.-Y., Jeong, J.-H., Han, J., Bhang, S. H., Jeong, G.-J., Haque, M. R., Al-Hilal, T. A., Noh, M., Byun, Y. & Kim, B.-S. Transplantation of Heterospheroids of Islet Cells and Mesenchymal Stem Cells for Effective Angiogenesis and Antiapoptosis. *Tissue Eng. Part A* **21,** 1024–1035 (2014).
208. Hering, B. J., Clarke, W. R., Bridges, N. D., Eggerman, T. L., Alejandro, R., Bellin, M. D., Chaloner, K., Czarniecki, C. W., Goldstein, J. S., Hunsicker, L. G., Kaufman, D. B., Korsgren, O., Larsen, C. P., Luo, X., Markmann, J. F., Naji, A., Oberholzer, J., Posselt, A. M., Rickels, M. R., Ricordi, C., Robien, M. A., Senior, P. A., James Shapiro, A. M., Stock, P. G. & Turgeon, N. A. Phase 3 trial of transplantation of human islets in type 1 diabetes complicated by severe hypoglycemia. *Diabetes Care* **39,** 1230–1240 (2016).
209. Zhou, Q. & Melton, D. A. Pancreas regeneration. *Nature* **557,** 351–358 (2018).
210. Rolfe, B., Mooney, J., Zhang, B., Jahnke, S., Le, S.-J., Chau, Y.-Q., Huang, Q., Wang, H., Campbell, G. & Campbell, J. in *Regen. Med. Tissue Eng. - Cells Biomater.* (InTech, 2011). doi:10.5772/21790
211. Nair, G. G., Liu, J. S., Russ, H. A., Tran, S., Saxton, M. S., Chen, R., Juang, C., Li, M. lan, Nguyen, V. Q., Giacometti, S., Puri, S., Xing, Y., Wang, Y., Szot, G. L., Oberholzer, J., Bhushan, A. & Hebrok, M. Recapitulating endocrine cell clustering in culture promotes maturation of human stem-cell-derived β cells. *Nat. Cell Biol.* **21,** 263–274 (2019).
212. Shapiro, J. Islet Transplantation in Seven Patients with Type 1 Diabetes Mellitus Using a Glucocorticoid-free Immunosuppressive Regimen. *N. Engl. J. Med.* **343,** 230–238 (2000).
213. Mokkapati, S., Nischt, R., Smyth, N., Ho, M. S. P. & Bo, K. Nidogens — Extracellular Matrix Linker Molecules. **395,** 387–395 (2008).
214. Kaido, T., Yebra, M., Cirulli, V. & Montgomery, A. M. Regulation of Human β-Cell Adhesion, Motility, and Insulin Secretion by Collagen IV and Its Receptor α1β1. *J. Biol. Chem.* **279,** 53762–53769 (2004).
215. Zbinden, A., Layland, S. L., Urbanczyk, M., Berrio, D. A. C., Marzi, J., Zauner, M., Hammerschmidt, A., Brauchle, E. M., Sudrow, K., Fink, S., Templin, M., Liebscher, S., Klein, G., Deb, A., Duffy, G. P., Crooks, G. M., Eble, J. A., Mikkola, H. K. A., Nsair, A. & Seifert, M. Nidogen-1 Mitigates Ischemia and Promotes Tissue Survival and Regeneration. **2002500,** 1–18 (2020).
216. Crisóstomo, J., Pereira, A. M., Bidarra, S. J., Gonçalves, A. C., Granja, P. L., Coelho, J. F. J., Barrias, C. C. & Seiça, R. ECM-enriched alginate hydrogels for bioartificial pancreas: an ideal niche to improve insulin secretion and diabetic glucose profile. *J. Appl. Biomater. Funct. Mater.* **17,** (2019).
217. Cheng, J. Y. C., Raghunath, M., Whitelock, J. & Poole-Warren, L. Matrix Components and Scaffolds for Sustained Islet Function. *Tissue Eng. Part B Rev.* **17,** 235–247 (2011).
218. Brandhorst, D., Brandhorst, H., Acreman, S., Kimura, Y., Layland, S. L., Schenke-Layland, K. & Johnson, P. R. V. Recombinant Nidogen-1 Significantly Improves Survival of Hypoxic Human Islets. *J. Nuff. Dep. Surg. Sci.* **1,** (2020).
219. Llacua, L. A., Faas, M. M. & de Vos, P. Extracellular matrix molecules and their potential contribution to the function of transplanted pancreatic islets. *Diabetologia* **61,** 1261–1272 (2018).
220. Dionne, K. E., Colton, C. K. & Yarmush, M. L. Effect of hypoxia on insulin secretion by isolated rat and canine islets of Langerhans. *Diabetes* **42,** 12–21 (1993).
221. Delaune, V., Berney, T., Lacotte, S. & Toso, C. Intraportal islet transplantation: the impact of the liver microenvironment. *Transpl. Int.* **30,** 227–238 (2017).
222. Takahashi, Y., Sekine, K., Kin, T., Takebe, T. & Taniguchi, H. Self-Condensation Culture Enables Vascularization of Tissue Fragments for Efficient Therapeutic Transplantation. *Cell Rep.* **23,** 1620–1629 (2018).
223. Wu, H., Panakanti, R., Li, F. & Mahato, R. I. XIAP Gene Expression Protects β-Cells and Human Islets from Apoptotic Cell Death. *Mol. Pharm.* **7,** 1655–1666 (2010).
224. Lehmann, R., Zuellig, R. A., Kugelmeier, P., Baenninger, P. B., Moritz, W., Perren, A., Clavien, P. A., Weber, M. & Spinas, G. A. Superiority of small islets in human islet transplantation. *Diabetes* **56,** 594–603 (2007).
225. Inoue, M., Catrina, S., Brismar, K., Zheng, X., Zheng, X., Wang, X., Ma, Z., Sunkari, V. G., Botusan, I., Takeda, T. & Bjo, A. Acute hypoxia induces apoptosis of pancreatic b -cell by activation of the unfolded protein response and upregulation of CHOP. 1–11 (2012). doi:10.1038/cddis.2012.66
226. Del Toro-Arreola, A., Robles-Murillo, A. K., Daneri-Navarro, A. & Rivas-Carrillo, J. D. The role of endothelial cells on islet function and revascularization after islet transplantation. *Organogenesis* **12,** 28–32 (2016).
227. Hillebrands, J.-L., Van Schilfgaarde, R., De Vos, P., De Haan, B. J. & Strubbe, J. H. Efficacy of a Prevascularized Expanded Polytetrafluoroethylene Solid Support System As a Transplantation Site for Pancreatic Islets1. *Transplantation* **63,** 824–830 (2003).
228. Skrzypek, K., Nibbelink, M. G., Karbaat, L. P., Karperien, M., van Apeldoorn, A. & Stamatialis, D. An important step

towards a prevascularized islet macroencapsulation device—effect of micropatterned membranes on development of endothelial cell network. *J. Mater. Sci. Mater. Med.* **29,** (2018).
229. Paik, D. T., Tian, L., Williams, I. M., Rhee, S., Zhang, H., Liu, C., Mishra, R., Wu, S. M., Red-Horse, K. & Wu, J. C. Single-Cell RNA-seq Unveils Unique Transcriptomic Signatures of Organ-Specific Endothelial Cells. *Circulation* CIRCULATIONAHA.119.041433 (2020). doi:10.1161/CIRCULATIONAHA.119.041433
230. Ilieva, A., Yuan, S., Wang, R. N., Agapitos, D., Hill, D. J. & Rosenberg, L. Pancreatic islet cell survival following islet isolation: The role of cellular interactions in the pancreas. *J. Endocrinol.* **161,** 357–364 (1999).
231. Murtaugh, L. C. Pancreas and beta-cell development: from the actual to the possible. *Development* **134,** 427–438 (2006).
232. Murray, H. E., Paget, M. B., Bailey, C. J. & Downing, R. Sustained insulin secretory response in human islets co-cultured with pancreatic duct-derived epithelial cells within a rotational cell culture system. *Diabetologia* **52,** 477–485 (2009).
233. Jalili, R. B., Moeen Rezakhanlou, A., Hosseini-Tabatabaei, A., Ao, Z., Warnock, G. L. & Ghahary, A. Fibroblast populated collagen matrix promotes islet survival and reduces the number of islets required for diabetes reversal. *J. Cell. Physiol.* **226,** 1813–1819 (2011).
234. Ben Nasr, M., Vergani, A., Avruch, J., Liu, L., Kefaloyianni, E., D'Addio, F., Tezza, S., Corradi, D., Bassi, R., Valderrama-Vasquez, A., Usuelli, V., Kim, J., Azzi, J., El Essawy, B., Markmann, J., Abdi, R. & Fiorina, P. Co-transplantation of autologous MSCs delays islet allograft rejection and generates a local immunoprivileged site. *Acta Diabetol.* **52,** 917–927 (2015).
235. Montanari, E., Meier, R. P. H., Mahou, R., Seebach, J. D., Wandrey, C., Gerber-Lemaire, S., Buhler, L. H. & Gonelle-Gispert, C. Multipotent mesenchymal stromal cells enhance insulin secretion from human islets via N-cadherin interaction and prolong function of transplanted encapsulated islets in mice. *Stem Cell Res. Ther.* **8,** 199 (2017).
236. Urbanczyk, M., Zbinden, A., Layland, S. L., Duffy, G. & Schenke-Layland, K. Controlled Heterotypic Pseudo-Islet Assembly of Human β-Cells and Human Umbilical Vein Endothelial Cells Using Magnetic Levitation. *Tissue Eng. Part A* **26,** 387–399 (2020).
237. Linn, T., Schneider, K., Hammes, H. P., Preissner, K. T., Brandhorst, H., Morgenstern, E., Kiefer, F. & Bretzel, R. G. Angiogenic capacity of endothelial cells in islets of Langerhans. *FASEB J.* **17,** 1–17 (2003).
238. Gamble, A., Pawlick, R., Pepper, A. R., Bruni, A., Adesida, A., Senior, P. A., Korbutt, G. S. & Shapiro, A. M. J. Improved islet recovery and efficacy through co-culture and co-transplantation of islets with human adipose-derived mesenchymal stem cells. *PLoS One* **13,** e0206449 (2018).
239. Perez-Basterrechea, M., Esteban, M. M., Alvarez-Viejo, M., Fontanil, T., Cal, S., Sanchez Pitiot, M., Otero, J. & Obaya, A. J. Fibroblasts accelerate islet revascularization and improve long-term graft survival in a mouse model of subcutaneous islet transplantation. *PLoS One* **12,** e0180695 (2017).
240. Hospodiuk, M., Dey, M., Ayan, B., Sosnoski, D., Moncal, K. K., Wu, Y. & Ozbolat, I. T. Sprouting angiogenesis in engineered pseudo islets. *Biofabrication* **10,** 035003 (2018).
241. Miyakoshi, J., Sakurai, T., Nagata, N., Sumi, S., Satake, A., Inoue, K. & Tabata, Y. The Efficient Prevascularization Induced by Fibroblast Growth Factor 2 With a Collagen-Coated Device Improves the Cell Survival of a Bioartificial Pancreas. *Pancreas* **28,** e70–e79 (2004).
242. Krawiec, J. T., Weinbaum, J. S., Liao, H.-T., Ramaswamy, A. K., Pezzone, D. J., Josowitz, A. D., D'Amore, A., Rubin, J. P., Wagner, W. R. & Vorp, D. A. In Vivo Functional Evaluation of Tissue-Engineered Vascular Grafts Fabricated Using Human Adipose-Derived Stem Cells from High Cardiovascular Risk Populations . *Tissue Eng. Part A* **22,** 765–775 (2016).
243. Citro, A., Moser, P. T., Dugnani, E., Rajab, K. T., Ren, X., Evangelista-Leite, D., Charest, J. M., Peloso, A., Podesser, B. K., Manenti, F., Pellegrini, S., Piemonti, L. & Ott, H. C. Biofabrication of a vascularized islet organ for type 1 diabetes. *Biomaterials* **199,** 40–51 (2019).
244. Kaufman-Francis, K., Koffler, J., Weinberg, N., Dor, Y. & Levenberg, S. Engineered vascular beds provide key signals to pancreatic hormone-producing cells. *PLoS One* **7,** 1–10 (2012).
245. Roux, B. M., Akar, B., Zhou, W., Stojkova, K., Barrera, B., Brankov, J. & Brey, E. M. Preformed Vascular Networks Survive and Enhance Vascularization in Critical Sized Cranial Defects. *Tissue Eng. Part A* **24,** 1603–1615 (2018).
246. King, A. J. F. The use of animal models in diabetes research. *Br. J. Pharmacol.* **166,** 877–894 (2012).
247. Ali, Z., Charukeshi Chandrasekera, P. & Pippin, J. J. Animal research for type 2 diabetes mellitus, its limited translation for clinical benefit, and the way forward. *ATLA Altern. to Lab. Anim.* **46,** 13–22 (2018).
248. von Herrath, M. & Nepom, G. T. Animal models of human type 1 diabetes. *Nat. Immunol.* **10,** 129–132 (2009).
249. Owerbach, D., Bell, G. I., Rutter, W. J. & Shows, T. B. The insulin gene is located on chromosome 11 in humans. *Nature* **286,** 82–84 (1980).
250. Lomedico, P., Rosenthal, N., Efstratiadis, A., Gilbert, W., Kolodner, R. & Tizard, R. The structure and evolution of the two nonallelic rat preproinsulin genes. *Cell* **18,** 545–558 (1979).
251. Wentworth, B. M., Schaefer, I. M., Villa-Komaroff, L. & Chirgwin, J. M. Characterization of the two nonallelic genes encoding mouse preproinsulin. *J. Mol. Evol.* **23,** 305–312 (1986).
252. Astashkina, A., Mann, B. & Grainger, D. W. A critical evaluation of in vitro cell culture models for high-throughput drug screening and toxicity. *Pharmacol. Ther.* **134,** 82–106 (2012).
253. Zhang, H., Whalley, R. D., Ferreira, A. M. & Dalgarno, K. High throughput physiological micro-models for in vitro pre-clinical drug testing: a review of engineering systems approaches . *Prog. Biomed. Eng.* **2,** 022001 (2020).
254. Skelin, M., Rupnik, M. & Cencic, A. Pancreatic beta cell lines and their applications in diabetes mellitus research. *ALTEX* **27,** 105–113 (2010).
255. Chandrasekera, P. C. & Pippin, J. J. Of rodents and men: Species-specific glucose regulation and type 2 diabetes research. *ALTEX* **31,** 157–176 (2014).
256. Chakradhar, S. Diabetes researchers fear worsening access to human islets. *Nat. Med.* **20,** 567 (2014).
257. Henquin, J.-C. Influence of organ donor attributes and preparation characteristics on the dynamics of insulin secretion in isolated human islets. *Physiol. Rep.* **6,** e13646 (2018).
258. Dominguez-Gutierrez, G., Xin, Y. & Gromada, J. Heterogeneity of human pancreatic β-cells. *Mol. Metab.* **27,** S7–S14

(2019).
259. Ravassard, P., Hazhouz, Y., Pechberty, S., Bricout-neveu, E., Armanet, M., Czernichow, P. & Scharfmann, R. Technical advance A genetically engineered human pancreatic β cell line exhibiting glucose-inducible insulin secretion. *J. Clin. Invest.* **121,** 3589–3597 (2011).
260. Scharfmann, R., Pechberty, S., Hazhouz, Y., Von Bülow, M., Bricout-Neveu, E., Grenier-Godard, M., Guez, F., Rachdi, L., Lohmann, M., Czernichow, P. & Ravassard, P. Development of a conditionally immortalized human pancreatic β cell line. *J. Clin. Invest.* **124,** 2087–2098 (2014).
261. Benazra, M., Lecomte, M.-J., Colace, C., Müller, A., Machado, C., Pechberty, S., Bricout-Neveu, E., Grenier-Godard, M., Solimena, M., Scharfmann, R., Czernichow, P. & Ravassard, P. A human beta cell line with drug inducible excision of immortalizing transgenes. *Mol. Metab.* **4,** 916–925 (2015).
262. Szczerbinska, I., Tessitore, A., Hansson, L. K., Agrawal, A., Ragel Lopez, A., Helenius, M., Malinowski, A. R., Gilboa, B., Ruby, M. A., Gupta, R. & Ämmälä, C. Large-Scale Functional Genomics Screen to Identify Modulators of Human β-Cell Insulin Secretion. *Biomedicines* **10,** 103 (2022).
263. Jensen, C. & Teng, Y. Is It Time to Start Transitioning From 2D to 3D Cell Culture? *Front. Mol. Biosci.* **7,** 33 (2020).
264. Low, L. A., Mummery, C., Berridge, B. R., Austin, C. P. & Tagle, D. A. Organs-on-chips: into the next decade. *Nat. Rev. Drug Discov.* 1–17 (2020). doi:10.1038/s41573-020-0079-3
265. Kilic, T., Navaee, F., Stradolini, F., Renaud, P. & Carrara, S. Organs-on-chip monitoring: sensors and other strategies. *Microphysiological Syst.* **1,** 1–1 (2018).
266. Esmonde-White, K. A., Cuellar, M., Uerpmann, C., Lenain, B. & Lewis, I. R. Raman spectroscopy as a process analytical technology for pharmaceutical manufacturing and bioprocessing. *Anal. Bioanal. Chem.* **409,** 637–649 (2017).
267. Rygula, A., Majzner, K., Marzec, K. M., Kaczor, A., Pilarczyk, M. & Baranska, M. Raman spectroscopy of proteins: a review. *J. Raman Spectrosc.* **44,** 1061–1076 (2013).
268. Mitsutake, H., Poppi, R. J. & Breitkreitz, M. C. Raman Imaging Spectroscopy: History, Fundamentals and Current Scenario of the Technique. *J. Braz. Chem. Soc* **30,** (2243).
269. Jones, R. R., Hooper, D. C., Zhang, L., Wolverson, D. & Valev, V. K. Raman Techniques: Fundamentals and Frontiers. *Nanoscale Res. Lett.* **14,** 1–34 (2019).
270. Movasaghi, Z., Rehman, S. & Rehman, I. U. Raman spectroscopy of biological tissues. *Appl. Spectrosc. Rev.* **42,** 493–541 (2007).
271. Smith, R., Wright, K. L. & Ashton, L. Raman spectroscopy: an evolving technique for live cell studies. *Analyst* **141,** 3590–3600 (2016).
272. Brauchle, E., Kasper, J., Daum, R., Schierbaum, N., Falch, C., Kirschniak, A., Schäffer, T. E. & Schenke-Layland, K. Biomechanical and biomolecular characterization of extracellular matrix structures in human colon carcinomas. *Matrix Biol.* **68–69,** 180–193 (2018).
273. Brauchle, E., Bauer, H., Fernes, P., Zuk, A., Schenke-Layland, K. & Sengle, G. Raman microspectroscopy as a diagnostic tool for the non-invasive analysis of fibrillin-1 deficiency in the skin and in the in vitro skin models. *Acta Biomater.* **52,** 41–48 (2017).
274. Sugiyama, K., Marzi, J., Brauchle, E. M., Ando, M., Yamashiro, Y., Ramkhelawon, B., Schenke-Layland, K. & Yanagisawa, H. Raman Microspectroscopy and Imaging Reveal Novel Biomarkers Specific for Thoracic Aortic Aneurysms. *SSRN Electron. J.* (2020). doi:10.2139/ssrn.3606775
275. Morais, C. L. M., Martin-Hirsch, P. L. & Martin, F. L. A three-dimensional principal component analysis approach for exploratory analysis of hyperspectral data: Identification of ovarian cancer samples based on Raman microspectroscopy imaging of blood plasma. *Analyst* **144,** 2312–2319 (2019).
276. O'Malley, J., Kumar, R., Kuzmin, A. N., Pliss, A., Yadav, N., Balachandar, S., Wang, J., Attwood, K., Prasad, P. N. & Chandra, D. Lipid quantification by Raman microspectroscopy as a potential biomarker in prostate cancer. *Cancer Lett.* **397,** 52–60 (2017).
277. Liu, W., Wang, H., Du, J. & Jing, C. Raman microspectroscopy of nucleus and cytoplasm for human colon cancer diagnosis. *Biosens. Bioelectron.* **97,** 70–74 (2017).
278. Moradi, H., Ahmad, A., Shepherdson, D., Vuong, N. H., Niedbala, G., Eapen, L., Vanderhyden, B., Nyiri, B. & Murugkar, S. Raman micro-spectroscopy applied to treatment resistant and sensitive human ovarian cancer cells. *J. Biophotonics* **10,** 1327–1334 (2017).
279. Hsu, C. C., Xu, J., Brinkhof, B., Wang, H., Cui, Z., Huang, W. E. & Ye, H. A single-cell Raman-based platform to identify developmental stages of human pluripotent stem cell-derived neurons. *Proc. Natl. Acad. Sci. U. S. A.* **117,** 18412–18423 (2020).
280. Chan, J. W., Lieu, D. K., Huser, T. & Li, R. A. Label-free separation of human embryonic stem cells and their cardiac derivatives using Raman spectroscopy. *Anal. Chem.* **81,** 1324–1331 (2009).
281. Brauchle, E., Knopf, A., Bauer, H., Shen, N., Linder, S., Monaghan, M. G., Ellwanger, K., Layland, S. L., Brucker, S. Y., Nsair, A. & Schenke-Layland, K. Non-invasive Chamber-Specific Identification of Cardiomyocytes in Differentiating Pluripotent Stem Cells. *Stem Cell Reports* **6,** 188–199 (2016).
282. Konorov, S. O., Schulze, H. G., Gage, B. K., Kieffer, T. J., Piret, J. M., Blades, M. W. & Turner, R. F. B. Process Analytical Utility of Raman Microspectroscopy in the Directed Differentiation of Human Pancreatic Insulin-Positive Cells. *Anal. Chem.* **87,** 10762–10769 (2015).
283. Eltzschig, H. K. & Eckle, T. Ischemia and reperfusion-from mechanism to translation. *Nat. Med.* **17,** 1391–1401 (2011).
284. Wynn, T. A. & Ramalingam, T. R. Mechanisms of fibrosis: therapeutic translation for fibrotic disease. *Nat. Med.* **18,** 1028–40 (2012).
285. Su, T., Huang, K., Ma, H., Liang, H., Dinh, P.-U., Chen, J., Shen, D., Allen, T. A., Qiao, L., Li, Z., Hu, S., Cores, J., Frame, B. N., Young, A. T., Yin, Q., Liu, J., Qian, L., Caranasos, T. G., Brudno, Y., Ligler, F. S. & Cheng, K. Platelet-Inspired Nanocells for Targeted Heart Repair After Ischemia/Reperfusion Injury. *Adv. Funct. Mater.* **29,** 1803567 (2019).
286. Kapnisi, M., Mansfield, C., Marijon, C., Guex, A. G., Perbellini, F., Bardi, I., Humphrey, E. J., Puetzer, J. L., Mawad, D., Koutsogeorgis, D. C., Stuckey, D. J., Terracciano, C. M., Harding, S. E. & Stevens, M. M. Auxetic Cardiac Patches with Tunable Mechanical and Conductive Properties toward Treating Myocardial Infarction. *Adv. Funct. Mater.* **28,** 1800618

(2018).
287. Seif-Naraghi, S. B., Singelyn, J. M., Salvatore, M. A., Osborn, K. G., Wang, J. J., Sampat, U., Kwan, O. L., Strachan, G. M., Wong, J., Schup-Magoffin, P. J., Braden, R. L., Bartels, K., DeQuach, J. A., Preul, M., Kinsey, A. M., DeMaria, A. N., Dib, N. & Christman, K. L. Safety and Efficacy of an Injectable Extracellular Matrix Hydrogel for Treating Myocardial Infarction. *Sci. Transl. Med.* **5,** 173ra25-173ra25 (2013).
288. Bechtel, M., Keller, M. V., Bloch, W., Sasaki, T., Boukamp, P., Zaucke, F., Paulsson, M. & Nischt, R. Different domains in nidogen-1 and nidogen-2 drive basement membrane formation in skin organotypic cocultures. *FASEB J.* **26,** 3637–3648 (2012).
289. Montgomery, M., Ahadian, S., Davenport Huyer, L., Lo Rito, M., Civitarese, R. A., Vanderlaan, R. D., Wu, J., Reis, L. A., Momen, A., Akbari, S., Pahnke, A., Li, R.-K., Caldarone, C. A. & Radisic, M. Flexible shape-memory scaffold for minimally invasive delivery of functional tissues. *Nat. Mater.* **16,** 1038–1046 (2017).
290. Yang, L., Soonpaa, M. H., Adler, E. D., Roepke, T. K., Kattman, S. J., Kennedy, M., Henckaerts, E., Bonham, K., Abbott, G. W., Linden, R. M., Field, L. J. & Keller, G. M. Human cardiovascular progenitor cells develop from a KDR+ embryonic-stem-cell-derived population. *Nature* **453,** 524–528 (2008).
291. Willems, E., Spiering, S., Davidovics, H., Lanier, M., Xia, Z., Dawson, M., Cashman, J. & Mercola, M. Small-molecule inhibitors of the Wnt pathway potently promote cardiomyocytes from human embryonic stem cell-derived mesoderm. *Circ. Res.* **109,** 360–364 (2011).
292. Potta, S. P., Liang, H., Winkler, J., Doss, M. X., Chen, S., Wagh, V., Pfannkuche, K., Hescheler, J. & Sachinidis, A. Isolation and Functional Characterization of α-Smooth Muscle Actin Expressing Cardiomyocytes from Embryonic Stem Cells. *Cell. Physiol. Biochem.* **25,** 595–604 (2010).
293. Li, B., Guo, Y., Zhan, Y., Zhou, X., Li, Y., Zhao, C., Sun, N., Xu, C. & Liang, Q. Cardiac Overexpression of XIN Prevents Dilated Cardiomyopathy Caused by TNNT2 ΔK210 Mutation. *Front. Cell Dev. Biol.* **9,** 1–10 (2021).
294. Majtnerová, P. & Roušar, T. An overview of apoptosis assays detecting DNA fragmentation. *Mol. Biol. Rep.* **45,** 1469–1478 (2018).
295. Imanaka-Yoshida, K. Tenascin-C in cardiovascular tissue remodeling. *Circ. J.* **76,** 2513–2520 (2012).
296. Frangogiannis, N. G. The role of transforming growth factor (TGF)-β in the infarcted myocardium. *J. Thorac. Dis.* **9,** S52–S63 (2017).
297. Peng, K. Y., Liu, Y. H., Li, Y. W., Yen, B. L. & Yen, M. L. Extracellular matrix protein laminin enhances mesenchymal stem cell (MSC) paracrine function through αvβ3/CD61 integrin to reduce cardiomyocyte apoptosis. *J. Cell. Mol. Med.* **21,** 1572–1583 (2017).
298. Yi, X.-Y., Wayner, E. A., Kim, Y. & FISH, A. J. Adhesion of cultured human kidney mesangial cells to native entactin: role of integrin receptors. *Cell Adhes. Commun.* **5,** 237–248 (1998).
299. Treindl, F., Ruprecht, B., Beiter, Y., Schultz, S., Döttinger, A., Staebler, A., Joos, T. O., Kling, S., Poetz, O., Fehm, T., Neubauer, H., Kuster, B. & Templin, M. F. A bead-based western for high-throughput cellular signal transduction analyses. *Nat. Commun.* **7,** 12852 (2016).
300. Misao, J., Hayakawa, Y., Ohno, M., Kato, S., Fujiwara, T. & Fujiwara, H. Expression of bcl-2 protein, an inhibitor of apoptosis, and Bax, an accelerator of apoptosis, in ventricular myocytes of human hearts with myocardial infarction. *Circulation* **94,** 1506–1512 (1996).
301. Xia, Z., Dickens, M., Raingeaud, J., Davis, R. J. & Greenberg, M. E. Opposing effects of ERK and JNK-p38 MAP kinases on apoptosis. *Science* **270,** 1326–31 (1995).
302. Adderley, S. R. & Fitzgerald, D. J. Oxidative damage of cardiomyocytes is limited by extracellular regulated kinases 1/2-mediate induction of cyclooxygenase-2. *J. Biol. Chem.* **274,** 5038–5046 (1999).
303. Bassat, E., Mutlak, Y. E., Genzelinakh, A., Shadrin, I. Y., Baruch Umansky, K., Yifa, O., Kain, D., Rajchman, D., Leach, J., Riabov Bassat, D., Udi, Y., Sarig, R., Sagi, I., Martin, J. F., Bursac, N., Cohen, S. & Tzahor, E. The extracellular matrix protein agrin promotes heart regeneration in mice. *Nature* **547,** 179–184 (2017).
304. Rimer, M. Emerging roles for MAP kinases in agrin signaling. *Commun. Integr. Biol.* **4,** 143–146 (2011).
305. Fu, W. bin, Wang, W. E. & Zeng, C. yu. Wnt signaling pathways in myocardial infarction and the therapeutic effects of Wnt pathway inhibitors. *Acta Pharmacol. Sin.* **40,** 9–12 (2019).
306. Wang, J., Liu, S., Heallen, T. & Martin, J. F. The Hippo pathway in the heart: pivotal roles in development, disease, and regeneration. *Nat. Rev. Cardiol.* **15,** 672–684 (2018).
307. Rallis, C., Pinchin, S. M. & Ish-Horowicz, D. Cell-autonomous integrin control of Wnt and Notch signalling during somitogenesis. *Development* **137,** 3591–3601 (2010).
308. Golledge, J., Clancy, P., Maguire, J., Lincz, L. & Koblar, S. The role of tenascin C in cardiovascular disease. *Cardiovasc. Res.* **92,** 19–28 (2011).
309. Hemshekhar, M., Thushara, R. M., Chandranayaka, S., Sherman, L. S., Kemparaju, K. & Girish, K. S. Emerging roles of hyaluronic acid bioscaffolds in tissue engineering and regenerative medicine. *Int. J. Biol. Macromol.* **86,** 917–928 (2016).
310. Young, J. L., Tuler, J., Braden, R., Schüp-Magoffin, P., Schaefer, J., Kretchmer, K., Christman, K. L. & Engler, A. J. In vivo response to dynamic hyaluronic acid hydrogels. *Acta Biomater.* **9,** 7151–7157 (2013).
311. Muscari, C., Bonafè, F., Martin-Suarez, S., Valgimigli, S., Valente, S., Fiumana, E., Fiorelli, F., Rubini, G., Guarnieri, C., Caldarera, C. M., Capitani, O., Arpesella, G. & Pasquinelli, G. Restored perfusion and reduced inflammation in the infarcted heart after grafting stem cells with a hyaluronan-based scaffold. *J. Cell. Mol. Med.* **17,** 518–530 (2013).
312. Yoon, S. J., Hong, S., Fang, Y. H., Song, M., Son, K. H., Son, H. S., Kim, S. K., Sun, K. & Park, Y. Differential regeneration of myocardial infarction depending on the progression of disease and the composition of biomimetic hydrogel. *J. Biosci. Bioeng.* **118,** 461–468 (2014).
313. Mahmoud, A. I., O'Meara, C. C., Gemberling, M., Zhao, L., Bryant, D. M., Zheng, R., Gannon, J. B., Cai, L., Choi, W.-Y., Egnaczyk, G. F., Burns, C. E., Burns, C. G., MacRae, C. A., Poss, K. D. & Lee, R. T. Nerves Regulate Cardiomyocyte Proliferation and Heart Regeneration. *Dev. Cell* **34,** 387–399 (2015).
314. Stendahl, J. C., Kaufman, D. B. & Stupp, S. I. Extracellular Matrix in Pancreatic Islets: Relevance to Scaffold Design and Transplantation. *Cell Transplant.* **18,** 1–12 (2009).

315. Zbinden, A., Marzi, J., Schlünder, K., Probst, C., Urbanczyk, M., Black, S., Brauchle, E. M., Layland, S. L., Kraushaar, U., Duffy, G., Schenke-Layland, K. & Loskill, P. Non-invasive marker-independent high content analysis of a microphysiological human pancreas-on-a-chip model. *Matrix Biol.* **85–86,** 205–220 (2020).
316. Riopel, M., Stuart, W. & Wang, R. Fibrin improves beta (INS-1) cell function, proliferation and survival through integrin αvβ3. *Acta Biomater.* **9,** 8140–8148 (2013).
317. Welters, H. J. & Kulkarni, R. N. Wnt signaling: relevance to β-cell biology and diabetes. *Trends Endocrinol. Metab.* **19,** 349–355 (2008).
318. Yang, Y., Liu, S., Lei, Z., Chen, G., Huang, L., Yang, F., Lei, Y., Liu, Y., Yang, L., Liu, W., Lai, L., Guo, J., Lei, Y., Lei, Y., Liu, Y., Liu, Y., Yang, L., Yang, L., Liu, W., Liu, W., Lai, L., Lai, L., Guo, J. & Guo, J. Circular RNA profile in liver tissue of EpCAM knockout mice. *Int. J. Mol. Med.* **44,** 1063–1077 (2019).
319. Lu, H., Ma, J., Yang, Y., Shi, W. & Luo, L. EpCAM Is an Endoderm-Specific Wnt Derepressor that Licenses Hepatic Development. *Dev. Cell* **24,** 543–553 (2013).
320. Yamashita, T., Budhu, A., Forgues, M. & Wang, X. W. Activation of Hepatic Stem Cell Marker EpCAM by Wnt–β-Catenin Signaling in Hepatocellular Carcinoma. *Cancer Res.* **67,** 10831–10839 (2007).
321. Ricard-Blum, S., Baffet, G. & Théret, N. Molecular and tissue alterations of collagens in fibrosis. *Matrix Biol.* **68–69,** 122–149 (2018).
322. Menke, A. & Adler, G. TGFbeta-induced Fibrogenesis of the Pancreas. *Int. J. Gastrointest. Cancer* **31,** 41–46 (2002).
323. Border, W. A., Noble, N. A., Yamamoto, T., Harper, J. R., Yamaguchi, Y. u, Pierschbacher, M. D. & Ruoslahti, E. Natural inhibitor of transforming growth factor-beta protects against scarring in experimental kidney disease. *Nature* **360,** 361–4 (1992).
324. Schaefer, L., Macakova, K., Raslik, I., Micegova, M., Gröne, H.-J., Schönherr, E., Robenek, H., Echtermeyer, F. G., Grässel, S., Bruckner, P., Schaefer, R. M., Iozzo, R. V. & Kresse, H. Absence of Decorin Adversely Influences Tubulointerstitial Fibrosis of the Obstructed Kidney by Enhanced Apoptosis and Increased Inflammatory Reaction. *Am. J. Pathol.* **160,** 1181–1191 (2002).
325. Groeneveld, T. W. L., Oroszlán, M., Owens, R. T., Faber-Krol, M. C., Bakker, A. C., Arlaud, G. J., McQuillan, D. J., Kishore, U., Daha, M. R. & Roos, A. Interactions of the Extracellular Matrix Proteoglycans Decorin and Biglycan with C1q and Collectins. *J. Immunol.* **175,** 4715–4723 (2005).
326. Svärd, J., Røst, T. H., Sommervoll, C. E. N., Haugen, C., Gudbrandsen, O. A., Mellgren, A. E., Rødahl, E., Fernø, J., Dankel, S. N., Sagen, J. V. & Mellgren, G. Absence of the proteoglycan decorin reduces glucose tolerance in overfed male mice. *Sci. Rep.* **9,** 4614 (2019).
327. Feng, R. N., Niu, Y. C., Sun, X. W., Li, Q., Zhao, C., Wang, C., Guo, F. C., Sun, C. H. & Li, Y. Histidine supplementation improves insulin resistance through suppressed inflammation in obese women with the metabolic syndrome: A randomised controlled trial. *Diabetologia* **56,** 985–994 (2013).
328. Lee, Y. T., Hsu, C. C., Lin, M. H., Liu, K. Sen & Yin, M. C. Histidine and carnosine delay diabetic deterioration in mice and protect human low density lipoprotein against oxidation and glycation. *Eur. J. Pharmacol.* **513,** 145–150 (2005).
329. Sun, X., Feng, R., Li, Y., Lin, S., Zhang, W., Li, Y., Sun, C. & Li, S. Histidine supplementation alleviates inflammation in the adipose tissue of high-fat diet-induced obese rats via the NF-κB-and PPARγ-involved pathways. *Br. J. Nutr.* **112,** 477–485 (2014).
330. Nolfi-Donegan, D., Braganza, A. & Shiva, S. Mitochondrial electron transport chain: Oxidative phosphorylation, oxidant production, and methods of measurement. *Redox Biol.* **37,** 101674 (2020).
331. Wiederkehr, A. & Wollheim, C. B. Minireview: implication of mitochondria in insulin secretion and action. *Endocrinology* **147,** 2643–2649 (2006).
332. Kaufman, B. A., Li, C. & Soleimanpour, S. A. Mitochondrial regulation of β-cell function: maintaining the momentum for insulin release. *Mol Asp. Med* **42,** 91–104 (2015).
333. Malmgreh, S., Nicholls, D. G., Taneera, J., Bacos, K., Koeck, T., Tamaddon, A., Wibom, R., Groop, L., Ling, C., Mulder, H. & Sharoyko, V. V. Tight coupling between glucose and mitochondrial metabolism in clonal β-cells is required for robust insulin secretion. *J. Biol. Chem.* **284,** 32395–32404 (2009).
334. Ritov, V. B., Menshikova, E. V., He, J., Ferrell, R. E., Goodpaster, B. H. & Kelley, D. E. Deficiency of subsarcolemmal mitochondria in obesity and type 2 diabetes. *Diabetes* **54,** 8–14 (2005).
335. Shrestha, N., Reinert, R. B. & Qi, L. Endoplasmic Reticulum Protein Quality Control in β Cells. *Semin. Cell Dev. Biol.* **103,** 59–67 (2020).
336. Yamaguchi, S., Ishihara, H., Yamada, T., Tamura, A., Usui, M., Tominaga, R., Munakata, Y., Satake, C., Katagiri, H., Tashiro, F., Aburatani, H., Tsukiyama-Kohara, K., Miyazaki, J., Sonenberg, N. & Oka, Y. ATF4-Mediated Induction of 4E-BP1 Contributes to Pancreatic β Cell Survival under Endoplasmic Reticulum Stress. *Cell Metab.* **7,** 269–276 (2008).
337. Fonseca, S. G., Gromada, J. & Urano, F. Endoplasmic reticulum stress and pancreatic β-cell death. *Trends Endocrinol. Metab.* **22,** 266–274 (2011).
338. Rabhi, N., Salas, E., Froguel, P. & Annicotte, J. S. Role of the unfolded protein response in β cell compensation and failure during diabetes. *J. Diabetes Res.* **2014,** (2014).
339. El Ouaamari, A., Zhou, J.-Y., Liew, C. W., Shirakawa, J., Dirice, E., Gedeon, N., Kahraman, S., De Jesus, D. F., Bhatt, S., Kim, J.-S., Clauss, T. R. W., Camp, D. G., Smith, R. D., Qian, W.-J. & Kulkarni, R. N. Compensatory Islet Response to Insulin Resistance Revealed by Quantitative Proteomics. *J. Proteome Res.* **14,** 3111–3122 (2015).
340. Wang, J., Chen, Y., Yuan, Q., Tang, W., Zhang, X. & Osei, K. Control of Precursor Maturation and Disposal Is an Early Regulative Mechanism in the Normal Insulin Production of Pancreatic β-Cells. *PLoS One* **6,** e19446 (2011).
341. Sun, J., Cui, J., He, Q., Chen, Z., Arvan, P. & Liu, M. Proinsulin misfolding and endoplasmic reticulum stress during the development and progression of diabetes☆. *Mol. Aspects Med.* **42,** 105–118 (2015).
342. Liu, M., Li, Y., Cavener, D. & Arvan, P. Proinsulin Disulfide Maturation and Misfolding in the Endoplasmic Reticulum. *J. Biol. Chem.* **280,** 13209–13212 (2005).
343. Bensellam, M., Maxwell, E. L., Chan, J. Y., Luzuriaga, J., West, P. K., Jonas, J. C., Gunton, J. E. & Laybutt, D. R. Hypoxia reduces ER-to-Golgi protein trafficking and increases cell death by inhibiting the adaptive unfolded protein response in mouse beta cells. *Diabetologia* **59,** 1492–1502 (2016).

344. Hwang, N., Kwon, M. Y., Cha, J. B., Chung, S. W. & Woo, J. M. Tunicamycin-induced Endoplasmic Reticulum Stress Upregulates the Expression of Pentraxin 3 in Human Retinal Pigment Epithelial Cells. *Korean J. Ophthalmol.* **30,** 468–478 (2016).
345. Guo, H., Xiong, Y., Witkowski, P., Cui, J., Wang, L. J., Sun, J., Lara-Lemus, R., Haataja, L., Hutchison, K., Shan, S. O., Arvan, P. & Liu, M. Inefficient translocation of preproinsulin contributes to pancreatic β cell failure and late-onset diabetes. *J. Biol. Chem.* **289,** 16290–16302 (2014).
346. Lee, Y. ho, Kim, J., Park, K. & Lee, M. S. β-cell autophagy: Mechanism and role in β-cell dysfunction. *Mol. Metab.* **27,** S92–S103 (2019).
347. Zhu, R., Li, X., Xu, J., Barrabi, C., Kekulandara, D., Woods, J., Chen, X. & Liu, M. Defective endoplasmic reticulum export causes proinsulin misfolding in pancreatic β cells. *Mol. Cell. Endocrinol.* **493,** 110470 (2019).
348. Fang, J., Liu, M., Zhang, X., Sakamoto, T., Taatjes, D. J., Jena, B. P., Sun, F., Woods, J., Bryson, T., Kowluru, A., Zhang, K. & Chen, X. COPII-Dependent ER Export: A Critical Component of Insulin Biogenesis and β-Cell ER Homeostasis. *Mol. Endocrinol.* **29,** 1156–69 (2015).
349. Takei, D., Ishihara, H., Yamaguchi, S., Yamada, T., Tamura, A., Katagiri, H., Maruyama, Y. & Oka, Y. WFS1 protein modulates the free Ca 2+ concentration in the endoplasmic reticulum. *FEBS Lett.* **580,** 5635–5640 (2006).
350. Ueda, K., Kawano, J., Takeda, K., Yujiri, T., Tanabe, K., Anno, T., Akiyama, M., Nozaki, J., Yoshinaga, T., Koizumi, A., Shinoda, K., Oka, Y. & Tanizawa, Y. Endoplasmic reticulum stress induces Wfs1 gene expression in pancreatic β-cells via transcriptional activation. *Eur. J. Endocrinol.* **153,** 167–176 (2005).
351. Zhang, I. X., Ren, J., Vadrevu, S., Raghavan, M. & Satin, L. S. ER stress increases store-operated Ca2+ entry (SOCE) and augments basal insulin secretion in pancreatic beta cells. *J. Biol. Chem.* **295,** 5685–5700 (2020).
352. Satin, L. S. Localized calcium influx in pancreatic β-cells: Its significance for Ca2+-dependent insulin secretion from the islets of Langerhans. *Endocrine* **13,** 251–262 (2000).
353. Tsai, H.-Y., Yang, Y.-F., Wu, A. T., Yang, C.-J., Liu, Y.-P., Jan, Y.-H., Lee, C.-H., Hsiao, Y.-W., Yeh, C.-T., Shen, C.-N., Lu, P.-J., Huang, M.-S. & Hsiao, M. Endoplasmic reticulum ribosome-binding protein 1 (RRBP1) overexpression is frequently found in lung cancer patients and alleviates intracellular stress-induced apoptosis through the enhancement of GRP78. *Oncogene* **32,** 4921–4931 (2013).
354. Lu, H., Yang, Y., Allister, E. M., Wijesekara, N. & Wheeler, M. B. The Identification of Potential Factors Associated with the Development of Type 2 Diabetes. *Mol. Cell. Proteomics* **7,** 1434–1451 (2008).
355. Cockcroft, S. & Carvou, N. Biochemical and biological functions of class I phosphatidylinositol transfer proteins. *Biochim. Biophys. Acta - Mol. Cell Biol. Lipids* **1771,** 677–691 (2007).
356. Blunsom, N. J. & Cockcroft, S. Phosphatidylinositol synthesis at the endoplasmic reticulum. *Biochim. Biophys. Acta - Mol. Cell Biol. Lipids* **1865,** 158471 (2020).
357. Mayinger, P. Phosphoinositides and vesicular membrane traffic. *Biochim. Biophys. Acta - Mol. Cell Biol. Lipids* **1821,** 1104–1113 (2012).
358. MacDonald, M. J., Ade, L., Ntambi, J. M., Ansari, I. U. H. & Stoker, S. W. Characterization of phospholipids in insulin secretory granules and mitochondria in pancreatic beta cells and their changes with glucose stimulation. *J. Biol. Chem.* **290,** 11075–11092 (2015).
359. Sánchez-Archidona, A. R., Cruciani-Guglielmacci, C., Roujeau, C., Wigger, L., Lallement, J., Denom, J., Barovic, M., Kassis, N., Mehl, F., Weitz, J., Distler, M., Klose, C., Simons, K., Ibberson, M., Solimena, M., Magnan, C. & Thorens, B. Plasma triacylglycerols are biomarkers of β-cell function in mice and humans. *Mol. Metab.* **54,** 101355 (2021).
360. Hofmann, S. M., Zhou, L., Perez-Tilve, D., Greer, T., Grant, E., Wancata, L., Thomas, A., Pfluger, P. T., Basford, J. E., Gilham, D., Herz, J., Tschöp, M. H. & Hui, D. Y. Adipocyte LDL receptor-related protein-1 expression modulates postprandial lipid transport and glucose homeostasis in mice. *J. Clin. Invest.* **117,** 3271–3282 (2007).
361. Salicioni, A. M., Mizelle, K. S., Loukinova, E., Mikhailenko, I., Strickland, D. K. & Gonias, S. L. The low density lipoprotein receptor-related protein mediates fibronectin catabolism and inhibits fibronectin accumulation on cell surfaces. *J. Biol. Chem.* **277,** 16160–16166 (2002).
362. Brandan, E., Retamal, C., Cabello-Verrugio, C. & Marzolo, M.-P. The Low Density Lipoprotein Receptor-related Protein Functions as an Endocytic Receptor for Decorin. *J. Biol. Chem.* **281,** 31562–31571 (2006).
363. Loukinova, E., Ranganathan, S., Kuznetsov, S., Gorlatova, N., Migliorini, M. M., Loukinov, D., Ulery, P. G., Mikhailenko, I., Lawrence, D. A. & Strickland, D. K. Platelet-derived growth factor (PDGF)-induced tyrosine phosphorylation of the low density lipoprotein receptor-related protein (LRP). Evidence for integrated co-receptor function between LRP and the PDGF. *J. Biol. Chem.* **277,** 15499–15506 (2002).
364. Shian Huang, S., M. Leal, S., Chen, C.-L., Liu, I.-H. & San Huang, J. Identification of insulin receptor substrate proteins as key molecules for the TβR-V/LRP-1-mediated growth inhibitory signaling cascade in epithelial and myeloid cells. *FASEB J.* **18,** 1719–1721 (2004).
365. Ye, R., Gordillo, R., Shao, M., Onodera, T., Chen, Z., Chen, S., Lin, X., SoRelle, J. A., Li, X., Tang, M., Keller, M. P., Kuliawat, R., Attie, A. D., Gupta, R. K., Holland, W. L., Beutler, B., Herz, J. & Scherer, P. E. Intracellular lipid metabolism impairs β cell compensation during diet-induced obesity. *J. Clin. Invest.* **128,** 1178–1189 (2018).
366. Cabello-Verrugio, C. & Brandan, E. A novel modulatory mechanism of transforming growth factor-beta signaling through decorin and LRP-1. *J. Biol. Chem.* **282,** 18842–50 (2007).
367. Sjoholm, A. & Hellerstrom, C. TGF-β stimulates insulin secretion and blocks mitogenic response of pancreatic β-cells to glucose. *Am. J. Physiol. - Cell Physiol.* **260,** (1991).
368. Arda, K., Ciledag, N., Aktas, E., Aribas, B. K. & Köse, K. Quantitative assessment of normal soft-tissue elasticity using shear-wave ultrasound elastography. *AJR. Am. J. Roentgenol.* **197,** 532–6 (2011).
369. Shi, Y., Liu, Y., Gao, F., Liu, Y., Tao, S., Li, Y., Glaser, K. J., Ehman, R. L. & Guo, Q. Pancreatic stiffness quantified with MR elastography: Relationship to postoperative pancreatic fistula after pancreaticoenteric anastomosis. *Radiology* **288,** 476–484 (2018).
370. Sugimoto, M., Takahashi, S., Kojima, M., Gotohda, N., Kato, Y., Kawano, S., Ochiai, A. & Konishi, M. What is the nature of pancreatic consistency? Assessment of the elastic modulus of the pancreas and comparison with tactile sensation, histology, and occurrence of postoperative pancreatic fistula after pancreaticoduodenectomy. *Surgery* **156,** 1204–11

(2014).
371. Kusamori, K., Nishikawa, M., Mizuno, N., Nishikawa, T., Masuzawa, A., Tanaka, Y., Mizukami, Y., Shimizu, K., Konishi, S., Takahashi, Y. & Takakura, Y. Increased Insulin Secretion from Insulin-Secreting Cells by Construction of Mixed Multicellular Spheroids. *Pharm. Res.* **33,** 247–256 (2016).
372. Sabra, G. & Vermette, P. A 3D cell culture system: Separation distance between INS-1 cell and endothelial cell monolayers co-cultured in fibrin influences INS-1 cells insulin secretion. *Biotechnol. Bioeng.* **110,** 619–627 (2013).
373. Paget, M. B., Murray, H. E., Bailey, C. J., Flatt, P. R. & Downing, R. Rotational co-culture of clonal β-cells with endothelial cells: Effect of PPAR-γ agonism in vitro on insulin and VEGF secretion. *Diabetes, Obes. Metab.* **13,** 662–668 (2011).
374. MacDonald, M. J., Longacre, M. J., Stoker, S. W., Kendrick, M., Thonpho, A., Brown, L. J., Hasan, N. M., Jitrapakdee, S., Fukao, T., Hanson, M. S., Fernandez, L. A. & Odorico, J. Differences between human and rodent pancreatic islets: Low pyruvate carboxylase, ATP citrate lyase, and pyruvate carboxylation and high glucose-stimulated acetoacetate in human pancreatic islets. *J. Biol. Chem.* (2011). doi:10.1074/jbc.M111.241182
375. Eizirik, D. L., Pipeleers, D. G., Ling, Z., Welsh, N., Hellerström, C. & Andersson, A. Major species differences between humans and rodents in the susceptibility to pancreatic beta-cell injury. *Proc. Natl. Acad. Sci. U. S. A.* **91,** 9253–6 (1994).
376. Narayanan, S., Loganathan, G., Dhanasekaran, M., Tucker, W., Patel, A., Subhashree, V., Mokshagundam, S., Hughes, M. G., Williams, S. K. & Balamurugan, A. N. Intra-islet endothelial cell and β-cell crosstalk: Implication for islet cell transplantation. *World J. Transplant.* **7,** 117–128 (2017).
377. Daquinag, A. C., Souza, G. R. & Kolonin, M. G. Adipose Tissue Engineering in Three-Dimensional Levitation Tissue Culture System Based on Magnetic Nanoparticles. *Tissue Eng. Part C Methods* **19,** 336–344 (2013).
378. Lin, R. Z. & Chang, H. Y. Recent advances in three-dimensional multicellular spheroid culture for biomedical research. *Biotechnol. J.* **3,** 1172–1184 (2008).
379. Ferrer, J., Solar, M., De Medts, N., Houbracken, I., Grau, V., Heimberg, H., Xu, X., Bouwens, L., Martín, M., Cardalda, C. & Maestro, M. A. Pancreatic Exocrine Duct Cells Give Rise to Insulin-Producing β Cells during Embryogenesis but Not after Birth. *Dev. Cell* **17,** 849–860 (2009).
380. Lecomte, M., Pechberty, S., Machado, C., Barroca, S. Da, Ravassard, P., Scharfmann, R., Czernichow, P. & Duvillié, B. Aggregation of Engineered Human β -Cells Into Pseudoislets : Insulin Secretion and Gene Expression Profile in Normoxic and Hypoxic Milieu. **8,** 99–112 (2016).
381. Bi, X., Pohl, N. M., Qian, Z., Yang, G. R., Gou, Y., Guzman, G., Kajdacsy-balla, A., Iozzo, R. V & Yang, W. Decorin-mediated inhibition of colorectal cancer growth and migration is associated with E-cadherin in vitro and in mice. **33,** 326–330 (2017).
382. Rogers, G. J., Hodgkin, M. N. & Squires, P. E. E-Cadherin and Cell Adhesion : a Role in Architecture and Function in the Pancreatic Islet. *Cell. Physiol. Biochem.* **19,** 987–994 (2007).
383. Nollet, F., Kools, P. & Van Roy, F. Phylogenetic analysis of the cadherin superfamily allows identification of six major subfamilies besides several solitary members. *J. Mol. Biol.* **299,** 551 (2000).
384. Newman, P. J. The biology of PECAM-1 . P J Newman Find the latest version : Perspectives Series : Cell Adhesion in Vascular Biology The Biology of PECAM-1. **99,** 3–8 (1997).
385. Piali, L., Hammel, P., Uherek, C., Bachmann, F., Gisler, R. H. & Dunon, D. CD31/PECAM-1 Is a Ligand for otv133 Integrin Involved in Adhesion of Leukocytes to Endothelium. **130,** 451–460 (1995).
386. Jun Itakura, Toshiyuki Ishiwata, Ben Shen, M. K. and M. K. Concomitant Over-Expressuin Of Vascular Endothelial Growth. *Int. J. Cancer* **34,** 27–34 (2000).
387. Urbanczyk, M., Zbinden, A., Layland, S. L., Duffy, G. & Schenke-Layland, K. Controlled heterotypic pseudo-islet assembly of human β-cells and HUVECs using magnetic levitation. *Tissue Eng. Part A* (2019). doi:10.1089/ten.TEA.2019.0158
388. Laporte, C., Tubbs, E., Pierron, M., Gallego, A., Moisan, A., Lamarche, F., Lozano, T., Hernandez, A., Cottet-Rousselle, C., Gauchez, A.-S., Persoons, V., Bottausci, F., Fontelaye, C., Boizot, F., Lablanche, S. & Rivera, F. Improved human islets' viability and functionality with mesenchymal stem cells and arg-gly-asp tripeptides supplementation of alginate micro-encapsulated islets in vitro. *Biochem. Biophys. Res. Commun.* **528,** 650–657 (2020).
389. Salvay, D. M., Rives, C. B., Zhang, X., Chen, F., Kaufman, D. B., Lowe, W. L. & Shea, L. D. Extracellular Matrix Protein-Coated Scaffolds Promote the Reversal of Diabetes After Extrahepatic Islet Transplantation. *Transplantation* **85,** 1456–1464 (2008).
390. Xiong, X., Ghosh, R., Hiller, E., Drepper, F., Knapp, B., Brunner, H. & Rupp, S. A new procedure for rapid, high yield purification of Type I collagen for tissue engineering. *Process Biochem.* **44,** 1200–1212 (2009).
391. Weber, L. M. & Anseth, K. S. Hydrogel encapsulation environments functionalized with extracellular matrix interactions increase islet insulin secretion. *Matrix Biol.* **27,** 667–673 (2008).
392. Riopel, M. & Wang, R. Collagen matrix support of pancreatic islet survival and function. (2014). doi:10.2741/4196
393. Ichihara, Y., Utoh, R., Yamada, M., Shimizu, T. & Uchigata, Y. Size effect of engineered islets prepared using microfabricated wells on islet cell function and arrangement. *Heliyon* **2,** e00129 (2016).
394. Bernhardt, A., Österreich, V. & Gelinsky, M. Three-Dimensional Co-culture of Primary Human Osteocytes and Mature Human Osteoclasts in Collagen Gels. *Tissue Eng. Part A* **26,** 647–655 (2020).
395. Schuh, C. M. A. P., Day, A. G. E., Redl, H. & Phillips, J. An Optimized Collagen-Fibrin Blend Engineered Neural Tissue Promotes Peripheral Nerve Repair. *Tissue Eng. - Part A* **24,** 1332–1340 (2018).
396. Aloy-Reverté, C., Moreno-Amador, J. L., Nacher, M., Montanya, E. & Semino, C. E. Use of RGD-Functionalized Sandwich Cultures to Promote Redifferentiation of Human Pancreatic Beta Cells After In Vitro Expansion . *Tissue Eng. Part A* **24,** 394–406 (2017).
397. Wang, Z. Z. & Sakiyama-Elbert, S. E. Matrices, scaffolds & carriers for cell delivery in nerve regeneration. *Exp. Neurol.* **319,** 1–17 (2019).
398. Dukor, R. K. in *Handb. Vib. Spectrosc.* (ed. Griffiths, P. R.) (John Wiley & Sons, Ltd, 2006). doi:10.1002/0470027320.s8107
399. Brazhe, N. A., Treiman, M., Brazhe, A. R., Find, N. L., Maksimov, G. V. & Sosnovtseva, O. V. Mapping of Redox State of Mitochondrial Cytochromes in Live Cardiomyocytes Using Raman Microspectroscopy. *PLoS One* **7,** (2012).

400. Zhang, X., Yu, F., Li, J., Song, D., Li, H., Wang, K., He, Q. & Wang, S. Investigation on the cancer invasion and metastasis of skin squamous cell carcinoma by raman spectroscopy. *Molecules* **24,** (2019).
401. Cheng, W.-T., Liu, M.-T., Liu, H.-N. & Lin, S.-Y. Micro-Raman spectroscopy used to identify and grade human skin pilomatrixoma. *Microsc. Res. Tech.* **68,** 75–79 (2005).
402. Spencer, V. A., Xu, R. & Bissell, M. J. Extracellular Matrix, Nuclear and Chromatin Structure, and Gene Expression in Normal Tissues and Malignant Tumors: A Work in Progress. *Adv. Cancer Res.* **97,** 275–294 (2007).
403. To, W. S. & Midwood, K. S. Plasma and cellular fibronectin : distinct and independent functions during tissue repair. 1–17 (2011).
404. Zerlauth, G., Wesierska-Gadek, J. & Sauermann, G. Fibronectin observed in the nuclear matrix of HeLa tumour cells. *J. Cell Sci.* **89 (Pt 3),** 415–421 (1988).
405. Iozzo, R. V., Buraschi, S., Genua, M., Xu, S.-Q., Solomides, C. C., Peiper, S. C., Gomella, L. G., Owens, R. C. & Morrione, A. Decorin Antagonizes IGF Receptor I (IGF-IR) Function by Interfering with IGF-IR Activity and Attenuating Downstream Signaling. *J. Biol. Chem.* **286,** 34712–34721 (2011).
406. Jungmann, O., Nikolovska, K., Stock, C., Schulz, J.-N., Eckes, B., Riethmüller, C., Owens, R. T., Iozzo, R. V. & Seidler, D. G. The Dermatan Sulfate Proteoglycan Decorin Modulates α2β1 Integrin and the Vimentin Intermediate Filament System during Collagen Synthesis. *PLoS One* **7,** e50809 (2012).
407. Merline, R., Moreth, K., Beckmann, J., Nastase, M. V., Zeng-Brouwers, J., Tralhão, J. G., Lemarchand, P., Pfeilschifter, J., Schaefer, R. M., Iozzo, R. V. & Schaefer, L. Signaling by the Matrix Proteoglycan Decorin Controls Inflammation and Cancer Through PDCD4 and MicroRNA-21. *Sci. Signal.* **4,** 2964–2979 (2011).
408. Zhou, Y., Horowitz, J. C., Naba, A., Ambalavanan, N., Atabai, K., Balestrini, J., Bitterman, P. B., Corley, R. A., Ding, B. Sen, Engler, A. J., Hansen, K. C., Hagood, J. S., Kheradmand, F., Lin, Q. S., Neptune, E., Niklason, L., Ortiz, L. A., Parks, W. C., Tschumperlin, D. J., White, E. S., Chapman, H. A. & Thannickal, V. J. Extracellular matrix in lung development, homeostasis and disease. *Matrix Biol.* **73,** 77–104 (2018).
409. Seo, H., Son, J. & Park, J.-K. Controlled 3D co-culture of beta cells and endothelial cells in a micropatterned collagen sheet for reproducible construction of an improved pancreatic pseudo-tissue. *APL Bioeng.* **4,** 046103 (2020).
410. Augsornworawat, P., Velazco-Cruz, L., Song, J. & Millman, J. R. A hydrogel platform for in vitro three dimensional assembly of human stem cell-derived islet cells and endothelial cells. *Acta Biomater.* **97,** 272–280 (2019).
411. Kim, J., Shim, I. K., Hwang, D. G., Lee, Y. N., Kim, M., Kim, H., Kim, S.-W., Lee, S., Kim, S. C., Cho, D.-W. & Jang, J. 3D cell printing of islet-laden pancreatic tissue-derived extracellular matrix bioink constructs for enhancing pancreatic functions. *J. Mater. Chem. B* **7,** 1773–1781 (2019).
412. Discher, D. E., Mooney, D. J. & Zandstra, P. W. Growth factors, matrices, and forces combine and control stem cells. *Science (80-.).* (2009). doi:10.1126/science.1171643
413. Tibbitt, M. W. & Anseth, K. S. Hydrogels as extracellular matrix mimics for 3D cell culture. *Biotechnol. Bioeng.* (2009). doi:10.1002/bit.22361
414. Qutub, A. A. & Popel, A. S. Elongation, proliferation and migration differentiate endothelial cell phenotypes and determine capillary sprouting. *BMC Syst. Biol.* (2009). doi:10.1186/1752-0509-3-13
415. Ayala, P., Lopez, J. I. & Desai, T. A. Microtopographical Cues in 3D Attenuate Fibrotic Phenotype and Extracellular Matrix Deposition: Implications for Tissue Regeneration. *Tissue Eng. Part A* (2010). doi:10.1089/ten.tea.2009.0815
416. Bott, K., Upton, Z., Schrobback, K., Ehrbar, M., Hubbell, J. A., Lutolf, M. P. & Rizzi, S. C. The effect of matrix characteristics on fibroblast proliferation in 3D gels. *Biomaterials* (2010). doi:10.1016/j.biomaterials.2010.07.046
417. Meijer, E. M., van Dijk, C. G. M., Kramann, R., Verhaar, M. C. & Cheng, C. Implementation of Pericytes in Vascular Regeneration Strategies. *Tissue Eng. Part B Rev.* **31,** ten.teb.2020.0229 (2021).
418. Kuehn, C., Dubiel, E. A., Sabra, G. & Vermette, P. Culturing INS-1 cells on CDPGYIGSR-, RGD- and fibronectin surfaces improves insulin secretion and cell proliferation. *Acta Biomater.* **8,** 619–626 (2012).
419. Gillies, G. T., Broaddus, W. C., Fillmore, H. L., Santos, W. Dos, Htay, A., Chen, Z. & Sholley, M. M. In vitro angiogenesis by human umbilical vein endothelial cells (HUVEC) induced by three-dimensional co-culture with glioblastoma cells. *J. Neurooncol.* **92,** 121–128 (2008).
420. Bishop, E. T., Bell, G. T., Bloor, S., Broom, I. J., Hendry, N. F. K. & Wheatley, D. N. An in vitro model of angiogenesis: Basic features. *Angiogenesis* **3,** 335–344 (1999).
421. Lam, G. C. & Sefton, M. V. Hypoxia-inducible factor drives vascularization of modularly assembled engineered tissue. *Tissue Eng. Part A* 1–39 (2018). doi:10.1089/ten.tea.2018.0294
422. Nalbach, L., Roma, L. P., Schmitt, B. M., Becker, V., Körbel, C., Wrublewsky, S., Pack, M., Später, T., Metzger, W., Menger, M. M., Frueh, F. S., Götz, C., Lin, H., Fox, J. E. M., Macdonald, P. E., Menger, M. D., Laschke, M. W. & Ampofo, E. Improvement of islet transplantation by the fusion of islet cells with functional blood vessels. 1–21 (2020). doi:10.15252/emmm.202012616
423. Tse, D. & Stan, R. Morphological Heterogeneity of Endothelium. *Semin. Thromb. Hemost.* **36,** 236–245 (2010).
424. Pilarczyk, M., Mateuszuk, L., Rygula, A., Kepczynski, M., Chlopicki, S., Baranska, M. & Kaczor, A. Endothelium in spots - High-content imaging of lipid rafts clusters in db/db mice. *PLoS One* **9,** (2014).
425. Reinhart, W. H. Shear-dependence of endothelial functions. *Experientia* **50,** 87–93 (1994).
426. Ballermann, B. J., Dardik, A., Eng, E. & Liu, A. Shear stress and the endothelium. *Kidney Int. Suppl.* **54,** 100–108 (1998).
427. Franke, R.-P., Gräfe, M., Schnittler, H., Seiffge, D., Mittermayer, C. & Drenckhahn, D. Induction of human vascular endothelial stress fibres by fluid shear stress. *Nature* **307,** 648–649 (1984).
428. Causer, A. J., Khalaf, M., Klein Rot, E., Brand, K., Smith, J., Bailey, S. J., Cummings, M. H., Shepherd, A. I., Saynor, Z. L. & Shute, J. K. CFTR limits F-actin formation and promotes morphological alignment with flow in human lung microvascular endothelial cells. *Physiol. Rep.* **9,** 1–14 (2021).

Acknowledgements

I would like to express my gratitude to my supervisor Prof. Dr. Katja Schenke-Layland for giving me the opportunity to pursue my PhD in her lab. I am grateful for the continuous support, motivation and patience throughout this journey which let me grow as a scientist and as a person.

I would like to thank Shannon Lee Layland for his everlasting input and the countless scientific and non-scientific conversations, his moral support and the help during all submission processes.

A huge thanks goes to the whole Schenke-Layland Lab that made this PhD a memorable ride with all the fun activities outside work. In particular I would like to thank Daniel Carvajal Berrio and Simone Liebscher for their patient imaging support, Dr. Julia Marzi, Chuan-En Lu and Lucas Becker for their Raman expertise, Diana Holzer for making sure everything went smoothly on the organizational side and Abiramy Jeyagaran for the unlimited creativity and sarcasm inside and outside the lab and her proofreading skills. I do not thank her for the addition of the Oxford comma and double spacing though.

A special thanks to my former colleague Dr. Aline Zbinden for the initial support and tutoring when I first joined the lab and the great collaboration during our projects. I would like to thank the students I supervised, Franziska Kern and Athar Abuhelou, for the incredible contribution their work has been to this thesis. I would also like to thank the MacDonald Lab for their cooperation and the donors and their families that made our human experiments possible.

Last but not least I would like to thank my family, friends and my partner in crime and adventure for their unconditional support and distraction during times of frustration and joyful celebrations during times of success, even though sometimes they didn’t even know what I was talking about. Most of all I would like to thank them for the impact they had on my life, which made me the person I am today and gave me the courage to pursue this degree. It wouldn’t have been possible without you. Thank you.

Declaration

Ich erkläre hiermit, dass ich die zur Promotion eingereichte Arbeit mit dem Titel *“Impact of Extracellular Matrix Environment on Cardiovascular and Pancreatic Tissues*” selbstständig verfasst, nur die angegebenen Quellen und Hilfsmittel benutzt und wörtlich oder inhaltlich übernommene Zitate also solche gekennzeichnet habe. Ich erkläre, dass die Richtlinien zur Sicherung guter wissenschaftlicher Praxis der Universität Tübingen beachtet wurden. Ich versichere an Eides statt, dass diese Angaben wahr sind und dass ich nichts verschwiegen habe. Mir ist bekannt, dass die falsche Angabe einer Versicherung an Eides statt mit Freiheitsstrafe bis zu drei Jahren oder mit Geldstrafe bestraft wird.

Tübingen, 09.11.2022

Max Nikos Urbanczyk

Appendices

Appendix I

FULL PAPER

ADVANCED SCIENCE Open Access

www.advancedscience.com

Nidogen-1 Mitigates Ischemia and Promotes Tissue Survival and Regeneration

*Aline Zbinden, Shannon L. Layland, Max Urbanczyk, Daniel A. Carvajal Berrio, Julia Marzi, Monika Zauner, Anne Hammerschmidt, Eva M. Brauchle, Katrin Sudrow, Simon Fink, Markus Templin, Simone Liebscher, Gerd Klein, Arjun Deb, Garry P. Duffy, Gay M. Crooks, Johannes A. Eble, Hanna K. A. Mikkola, Ali Nsair, Martina Seifert, and Katja Schenke-Layland**

Ischemia impacts multiple organ systems and is the major cause of morbidity and mortality in the developed world. Ischemia disrupts tissue homeostasis, driving cell death, and damages tissue structure integrity. Strategies to heal organs, like the infarcted heart, or to replace cells, as done in pancreatic islet β-cell transplantations, are often hindered by ischemic conditions. Here, it is discovered that the basement membrane glycoprotein nidogen-1 attenuates the apoptotic effect of hypoxia in cardiomyocytes and pancreatic β-cells via the $\alpha v\beta 3$ integrin and beneficially modulates immune responses in vitro. It is shown that nidogen-1 significantly increases heart function and angiogenesis, while reducing fibrosis, in a mouse postmyocardial infarction model. These results demonstrate the protective and regenerative potential of nidogen-1 in ischemic conditions.

1. Introduction

Ischemic injury due to the disruption of blood flow can lead to irreversible tissue injury precipitating to neurologic stroke, limb ischemia or myocardial infarction (MI).[1] Ischemic conditions also disrupt regenerative and protective therapies to attenuate cell death and restore organ function, particularly in applications where cell engraftment is required. Strategies to protect cells, modulate the immune response, and repair the tissue milieu within ischemic environments are therefore of critical importance.

The current clinical and preclinical stage strategies that seek to restore organ function post-ischemia include the injection of

A. Zbinden, S. L. Layland, M. Urbanczyk, D. A. Carvajal Berrio, Dr. J. Marzi, S. Liebscher, Prof. K. Schenke-Layland
Department of Bioengineering
Eberhard Karls University Tübingen
Tübingen 72076, Germany
E-mail: katja.schenke-layland@uni-tuebingen.de

A. Zbinden, S. L. Layland, M. Urbanczyk, D. A. Carvajal Berrio, Dr. J. Marzi, Dr. M. Zauner, A. Hammerschmidt, Dr. E. M. Brauchle, S. Liebscher, Prof. K. Schenke-Layland
Department of Women's Health
Research Institute for Women's Health
Eberhard Karls University Tübingen
Tübingen 72076, Germany

D. A. Carvajal Berrio, Dr. J. Marzi, Dr. E. M. Brauchle, Prof. K. Schenke-Layland
Cluster of Excellence iFIT (EXC 2180) "Image-Guided and Functionally Instructed Tumor Therapies"
Eberhard Karls University Tübingen
Tübingen 72076, Germany

The ORCID identification number(s) for the author(s) of this article can be found under https://doi.org/10.1002/advs.202002500

DOI: 10.1002/advs.202002500

Dr. J. Marzi, Dr. E. M. Brauchle, S. Fink, Dr. M. Templin, Prof. K. Schenke-Layland
NMI Natural and Medical Sciences Institute at the University of Tübingen
Reutlingen 72770, Germany

K. Sudrow, Prof. M. Seifert
Institute of Medical Immunology
Charité Universitätsmedizin Berlin
corporate member of Freie Universität Berlin
Humboldt-Universität zu Berlin
Berlin 10117, Germany

K. Sudrow, Prof. M. Seifert
Charité Universitätsmedizin
Berlin Institute of Health (BIH) Center for Regenerative Therapies Berlin (BCRT)
Berlin 10178, Germany

Prof. G. Klein
Center for Medical Research
Department of Medicine II
Eberhard Karls University Tübingen
Tübingen 72076, Germany

Prof. A. Deb, Prof. H. K. A. Mikkola
Department of Molecular
Cell and Developmental Biology
UCLA
Los Angeles CA 90095, USA

cells, growth factors, small molecules, hydrogels or decellularized extracellular matrix (ECM) proteins.[2–4] The ECM is the 3D noncellular component of tissues and organs. It consists of mostly water, proteins, and polysaccharides, and provides the biophysical scaffolding for tissues. The ECM also offers important biochemical and mechanical cues influencing cell homeostasis and differentiation.[5] Ischemia leads to pathological ECM remodeling, resulting in fibrosis due to the deposition of fibrillar proteins, such as collagens type I (COL1) and III, leading to fibrotic scarring.[6] The alteration of ECM proteins can lead to cellular mutations, transdifferentiation or apoptotic death.[7] Basement membranes (BMs) are crucial ECM structures created by networks of collagen type IV (COL4) and laminins (LAM), which are linked by nidogen-1 (NID1). Other macromolecules integrate into BMs to give them unique functions in different tissues.[8] BMs are essential for tissue development and homeostasis.[9] In previous work, we demonstrated the cardiogenic effect of COL4 and LAM in vitro,[10] as well as the role of NID1 in human embryonic stem cell (hESC) assembly.[11] Therefore, we asked whether a single BM protein could have a functional impact on tissue protection or regeneration.[12]

To address the condition of MI, we analyzed the expression of BM proteins during heart development to identify candidates that could protect cardiac tissues during ischemia and support regeneration. NID1, also known as entactin-1,[13] was selected as the lead candidate as it was the most prominent BM protein in hESC-derived cells that were differentiated to the cardiovascular lineages. In vitro and in vivo studies uncovered a novel protective function of NID1 in the cardiovascular system. We also documented a beneficial effect of NID1 on immune cells, which is an essential component of the regenerative process for therapeutic approaches.

To test if NID1 may have a similar effect on other organ systems, therefore potentially supporting a regenerative therapy that is otherwise hindered by ischemic conditions, we choose a model of pancreatic beta cell transplantation, which is a therapy for type 1 diabetes where up to 60% of beta-cell-containing islets fail to engraft due to ischemia at the transplant location and the adverse reaction of the immune system.[14] Here, we demonstrated the protective and functional effect of NID1 on pancreatic beta cells in an ischemia model. Our studies uncovered a novel protective function of NID1 in multiple organ systems in vitro and in vivo and elucidate potential integrin-driven mechanisms of action.

2. Results

2.1. NID1 Is Identified as a Candidate for Cardiovascular Regenerative Approaches

To identify potential therapeutic cardiovascular candidates, the expression of ECM BM proteins was investigated in differentiating hESC-derived embryoid bodies (EBs). We used a modified cardiovascular differentiation protocol for the formation of EBs from the H9 hESC line (Figure S1, Supporting Information).[15,16] Semiquantification of ECM immunofluorescence (IF) staining within spontaneously beating day-10 EBs showed a significantly higher expression of NID1 compared with other well-investigated ECM proteins such as fibronectin (FN), periostin (POSTN), LAM, COL4, and COL1 (**Figure 1**A).[10–18] In addition, NID1 gene expression significantly increased during cardiovascular differentiation (Figure 1B).

To assess if NID1 has a beneficial effect during cardiovascular differentiation, we produced recombinant full length human NID1, available upon request, (Figure S2, Supporting Information) and supplemented it to hESCs that were differentiating toward the cardiovascular lineages. The supplementation of NID1 increased gene expression for cardiac (cardiac troponin T (*TNNT2*)) and smooth muscle (smooth muscle α2-actin (*ACTA2*)) cell markers (Figure 1C). Image-Stream analyses revealed the presence of a significantly higher number of cardiac muscle troponin T $(CTNT)^+$ cells within the NID1-treated cultures when compared with the controls, indicating a potential cardioinductive or cardioprotective effect of NID1 (Figure 1D–F).

The presence of NID1 in native human cardiac tissue was verified both during development (9-, 12-, 17-week embryonic) and in the adult (18 and 51 years) by IF staining (Figure 1G,F; Figure S3A, Supporting Information). The positive correlation of NID1 with cardiovascular development and its presence in human cardiac tissue nominated NID1 as a potential candidate for regenerative and reparative therapies.

2.2. NID1 Improves Heart Function Post Myocardial Infarction

Regenerative and remodeling approaches for post-MI therapies, to modulate infarction size and scar formation, aim to protect

Prof. A. Deb, Prof. G. M. Crooks, Prof. H. K. A. Mikkola, Prof. A. Nsair
Eli and Edythe Broad Stem Cell Research Center
UCLA
Los Angeles CA 90095, USA
Prof. A. Deb, Prof. H. K. A. Mikkola
Molecular Biology Institute
UCLA
Los Angeles CA 90095, USA
Prof. A. Deb, Prof. G. M. Crooks, Prof. H. K. A. Mikkola
Jonsson Comprehensive Cancer Center
UCLA
Los Angeles CA 90024, USA
Prof. A. Deb, Prof. A. Nsair, Prof. K. Schenke-Layland
Department of Medicine/Cardiology
Cardiovascular Research Laboratories
David Geffen School of Medicine at UCLA
Los Angeles CA 90095, USA
Prof. G. P. Duffy
Anatomy and Regenerative Medicine Institute
School of Medicine
College of Medicine Nursing and Health Sciences
National University of Ireland Galway
Galway H91TK33, Ireland
Prof. G. M. Crooks
Department of Pathology and Laboratory Medicine, and Pediatrics
David Geffen School of Medicine at UCLA
UCLA
Los Angeles CA 90095, USA
Prof. J. A. Eble
Institute of Physiological Chemistry and Pathobiochemistry
University of Münster
Münster 48149, Germany
Prof. M. Seifert
DZHK (German Centre for Cardiovascular Research)
partner site Berlin Berlin 10117, Germany

ADVANCED SCIENCE NEWS
www.advancedsciencenews.com

ADVANCED SCIENCE Open Access
www.advancedscience.com

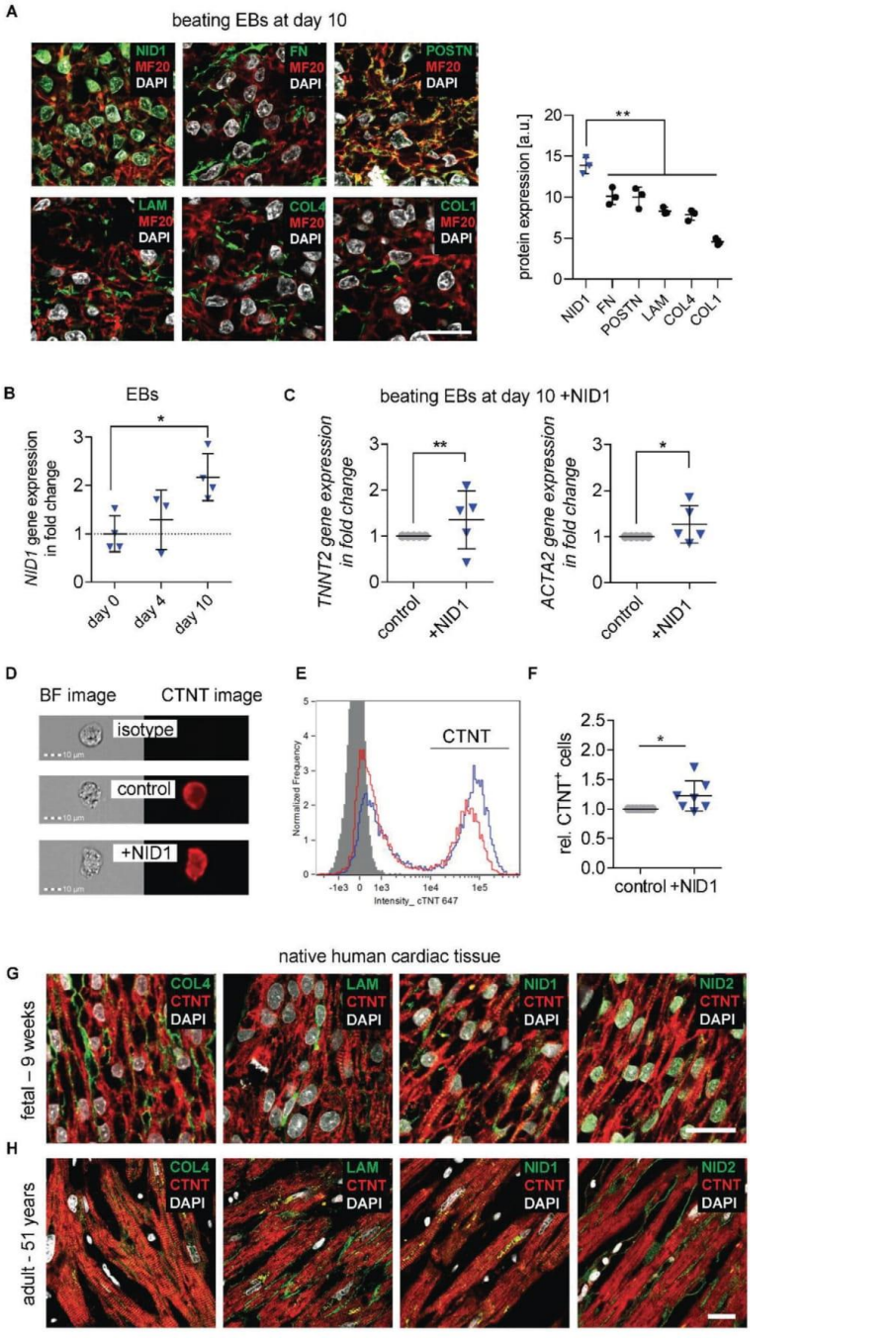

cardiovascular cells from the ischemic environment. We thus asked whether the potential remodeling properties of NID1 could improve the outcome of an MI and reperfusion (MI/R) mouse model. Ischemia/reperfusion was conducted through the ligation of the left anterior descending (LAD) artery in C57BL/6J mice as previously described.[19] Directly after reperfusion, three groups of mice received a single treatment of five injections in the infarct border zone of either saline as a procedure control, the hyaluronic acid (HA) gel carrier as a carrier control, or NID1 within the HA carrier gel (NID1 + HA).

Echocardiography 28 days post MI/R revealed a significant increase of heart ejection fraction (EF) by 19.7% (NID1 + HA 44.6% ± 1.6% versus saline 25% ± 4.8%, $p < 0.001$) (**Figure 2**A) and fractional shortening (FS) by 9.6% (NID1 + HA 21.1% ± 0.8% versus saline 11.5% ± 2.3%, $p < 0.01$) (Figure 2B). Left ventricular (LV) volume and diameter (end-systolic volume (ESV), left ventricle end-systolic diameter (LVES), and left ventricular internal dimension at end -systole (LVIDs)) were all significantly improved in the NID1 + HA-treated hearts when compared with the controls ($p < 0.0001$) (Figure 2C). Significant differences between NID1 + HA and HA treatments were found in EF and FS, as well as in LV volume and diameter. Strikingly, NID1 + HA treatment resulted in a complete recovery in end-diastolic volume (EDV), left ventricular end-diastolic diameter (LVED), and left ventricular internal dimension at end -diastole (LVIDd) when compared with the pre-MI/R baseline (Table S1, Supporting Information); however, the HA-treated hearts also showed a recovery in these values, which should be taken into consideration as the HA carrier gel may have contributed to the positive effect in these parameters.

Mouse hearts from the HA and NID1 + HA-treated groups were excised after the final echocardiography and processed. Russel–Movat pentachrome staining identified qualitative differences between the ECM-rich infarct zone and the surrounding tissue with intact cardiac muscle (Figure 2D–I). Picrosirius Red and Fast Green staining of serial sections throughout the whole heart (Figure 2J,K) were analyzed to identify and quantify scar tissue formation based on hue, saturation, and value (HSV) histograms (Figure S3B, Supporting Information). Scar tissue constituted 13.9% ± 2.6% of the HA-treated hearts and 8.8% ± 1.5% of the NID1 + HA-treated hearts, which is a 37% absolute reduction of scar tissue in the entire heart, not only the LV (Figure 2L).

IF staining of α-smooth muscle actin (αSMA) and CD31 was performed to study the effect of the NID1 + HA treatment on angiogenesis within the infarct zone (Figure 2M–P). The density of $\alpha SMA^+/CD31^+$ vessels in the scar area was significantly increased in the NID1 + HA treatment group when directly compared with the baseline and HA-treated tissues (Figure 2Q).

It has been recently demonstrated that reinnervation is critical for mammalian cardiac regeneration.[20] We used the neuronal marker β-tubulin 3 (TuJ1) to investigate the potential of NID1 + HA to increase nerve protection and innervation of infarcted tissue (Figure 2R–U). Interestingly, we identified a significant twofold increase of $TuJ1^+$ cells in the infarct area of the NID1 + HA-treated hearts compared with the baseline and HA-treated hearts (Figure 2V).

To investigate the scar tissue quality in the infarct areas, Raman microspectroscopy and Raman imaging were employed as noninvasive marker-free techniques to differentiate biochemical spectral fingerprints as previously demonstrated by our group.[21] True component analysis (TCA) and principal component analysis (PCA) identified molecular differences and spatial distribution of spectral information corresponding to myocardium, DNA, and scar tissue (Figure S4A,B, Supporting Information). Interestingly, PCA analysis of the scar fingerprint of the NID1 + HA-treated mice showed peaks associated with glycogen (497 cm^{-1}), porphyrin (1513, 1557, and 1612 cm^{-1}), and DNA (1093 cm^{-1}), while the scar fingerprint of the control mice was dominated by peaks assigned to collagens (858, 940, and 1248 cm^{-1}), which indicates that the scar tissue in the treated mice resembled the molecular fingerprint of the noninfarcted myocardium connective tissue (Extended Data in Figure S4C–G and Table S2, Supporting Information). Taken together, these data demonstrate that NID1 positively affects heart function, angiogenesis, scar size, and scar tissue quality in a therapeutic model.

2.3. NID1 Protects Cardiovascular Cells in an Ischemia In Vitro Model

To elucidate the therapeutic effect of NID1 in vitro, human induced-pluripotent stem cell-derived (hiPSC) iCell cardiomyocytes (CMs) were investigated in a hypoxia (1% oxygen) ischemia-like in vitro model. For two days, NID1-treated and control hiPSC-CMs were cultured under normoxic and hypoxic conditions and evaluated for cell death via the expression of cleaved caspase-3 and the number of $TUNEL^+$ cells (**Figure 3**A,B). NID1-treated hiPSC-CMs had a significantly lower expression of cleaved caspase-3 and a reduced the number of $TUNEL^+$ cells in hypoxic conditions when compared with nontreated controls. No changes were observed in normoxic cultures in the presence of NID1.

PCR array analysis of the expression of human ECM and adhesion molecules in NID1-treated hiPSC-CMs identified several significantly up and downregulated genes (Figure 3C). In hypoxic conditions, NID1-treated hiPSC-CMs showed significantly

Figure 1. ECM BM protein NID1 is identified as a candidate for regenerative approaches. A) IF staining and semiquantification of BM proteins NID1, FN, POSTN, LAM, COL4, and COL1, as well as DAPI and MF20 in day-10 beating EBs. Gray value intensities (GVI) of IF images were normalized to the laser intensity ($n = 3$), one-way ANOVA with Tukey's multiple comparisons test. B) qPCR analysis of *NID1* expression on day 0 (undifferentiated hESCs), and after 4 and 10 days (beating EBs) of cardiovascular differentiation. Data are normalized to the average of day 0 and shown as fold change ($n = 3$–4); one-way ANOVA with Tukey's multiple comparisons test. C) qPCR analysis of *TNNT2* and *ACTA2* gene expression within EBs at day 10 of cardiovascular differentiation without (control) and with NID1 ($n = 5$); Kolmogorov–Smirnov *t*-test. D) Bright field (BF) and CTNT IF images of single cells derived from EBs that were cultured for 10 days without (control) and with NID1 acquired with 40× magnification using imaging flow cytometry. An isotype control is provided. E) Representative histogram of cells that were cultured for 10 days with (blue) or without (red) NID1. The isotype control is shown in gray. F) Quantification of the data obtained by imaging flow cytometric analysis showing the relative amount of $CTNT^+$ cells derived from EBs that were cultured for 10 days without (control) and with NID1 ($n = 7$); Kolmogorov–Smirnov *t*-test. G,H) IF staining of BM proteins COL4, LAM, NID1, NID2, as well as DAPI and sarcomeric myosin CTNT within human (G) fetal heart sections (9 weeks postgestation) and (H) adult heart tissue (51 years). Scale bars: 20 µm. $^*p < 0.05$, $^{**}p < 0.01$, $^{***}p < 0.001$, and $^{****}p < 0.0001$.

ADVANCED SCIENCE NEWS
www.advancedsciencenews.com

ADVANCED SCIENCE Open Access
www.advancedscience.com

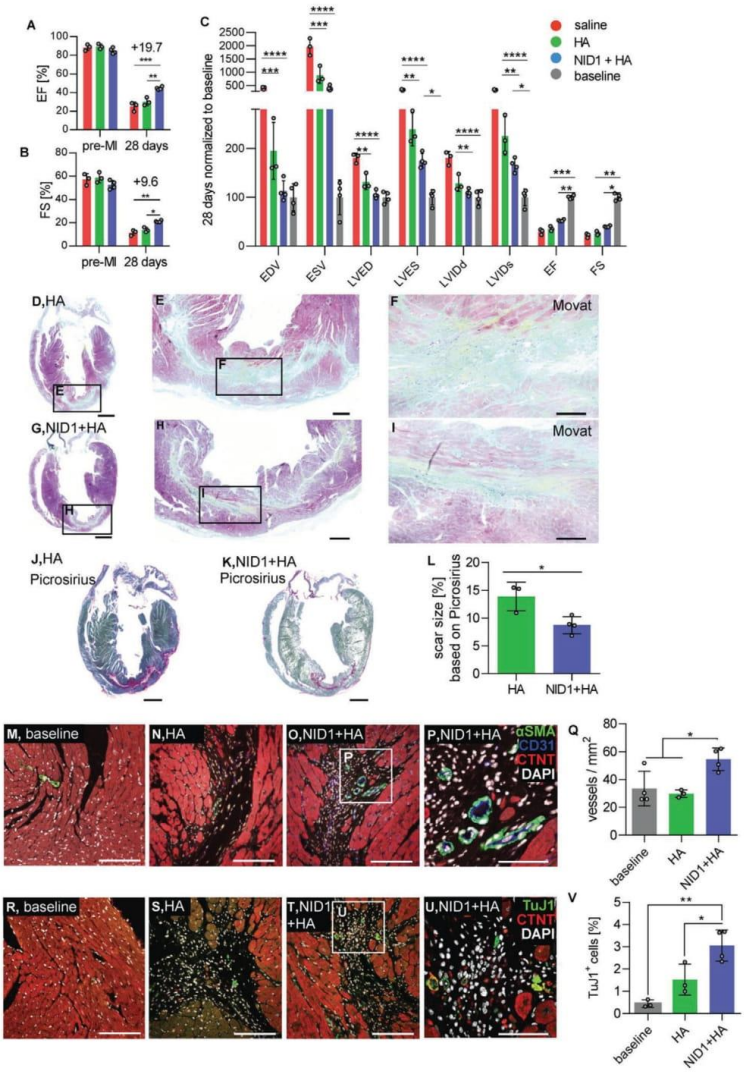

Figure 2. NID1 increases heart function post-MI. A–C) Echocardiography analysis: absolute values of (A) EF and (B) FS after intracardiac injections of saline, HA and 50 μg mL^{-1} NID1 + HA at 28 days post-MI/R, and C) parameters were normalized to the baseline at 28 days post-MI/R. Echocardiography data were analyzed by one-way ANOVA with Tukey's multiple comparisons test. D–I) Movat pentachrome staining of representative sections of (D–F) HA- and (G–I) NID1 + HA-treated hearts after 28 days post-MI/R with scar tissue stained in green and yellow. Scale bars: (D,G) 1 mm, (E,H) 200 μm, and (F,I) 100 μm. J,K) Picrosirius Red and Fast Green staining of representative (J) HA- and (K) NID1 + HA-treated heart sections with scar tissue stained in pink. Scale bars: 1 mm. L) Quantification of scar size in Picrosirius Red- and Fast Green-stained serial sections. Whole-heart scans of every tenth slide throughout the whole heart were analyzed. M–P) Confocal images of αSMA, CD31, and CTNT IF staining of representative (M) baseline, (N) HA-, and (O) NID1 + HA-treated heart sections obtained with a 25× magnification (scale bar: 100 μm), and with a P) 63× magnification (scale bar; 50 μm). Q) Quantification of vessel density within the infarct area using images obtained with a 25× magnification. R–U) Images of TuJ1 and CTNT IF staining of representative (R) baseline, (S) HA-, and (T) NID1 + HA-treated tissue sections obtained with a 25× magnification (scale bar equal 100 μm), and a (U) 63× magnification (scale bar: 50 μm). V) Quantification of TuJ1^{+} cells within the infarct area. For all MI/R studies saline mice ($n = 3$), HA mice ($n = 3$), NID1 + HA-treated mice ($n = 4$) were used, unpaired t-test. *$p < 0.05$, **$p < 0.01$, ***$p < 0.001$, ****$p < 0.0001$. LVIDd: left ventricular internal dimension at end diastole, LVIDs: left ventricular internal dimension at end-systole, LVED: left ventricle end-diastolic diameter, LVES: left ventricle end-systolic diameter, EDV: end-diastolic volume, ESV: end-systolic volume, EF: ejection fraction, FS: fractional shortening.

ADVANCED SCIENCE NEWS
www.advancedsciencenews.com

ADVANCED SCIENCE Open Access
www.advancedscience.com

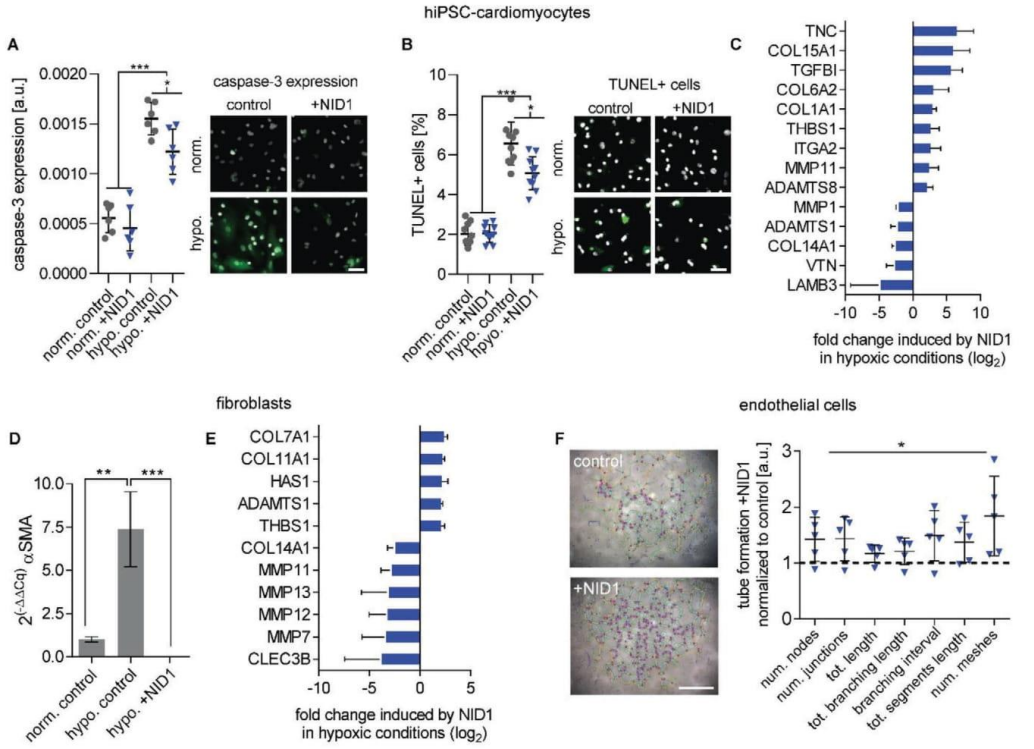

Figure 3. NID1 mitigates the effects of hypoxia on cardiovascular cells. A,B) Protective effect of NID1 on hiPSC-CMs shown by (A) cleaved caspase-3 staining and semiquantification ($n = 6$) and (B) by number of TUNEL$^+$ cells over total cell number ($n = 10$); one-way ANOVA with Tukey's multiple comparisons test. C) qPCR array analysis of NID1-treated hiPSC-CMs under hypoxic conditions with a focus on matrix production, degradation, and regulation ($n = 3$). D) qPCR analysis for the expression of αSMA in control fibroblasts under normoxic and hypoxic conditions, as well as for NID1-treated fibroblasts under hypoxic conditions ($n = 3$). One-way ANOVA with Tukey's multiple comparisons test. E) qPCR array analysis of NID1-treated fibroblasts under hypoxic conditions (identical qPCR array as in (C)) ($n = 3$). F) Tube formation assay performed using 1.5×10^4 HUVECs/0.32 cm^2 with serum-reduced Matrigel without (control) or with NID1 ($n = 4$–5). Quantification of different tube formation parameters using the angiogenesis analyzer of the ImageJ software. Data are normalized to the Matrigel control (set as 1), one-way ANOVA with Tukey's multiple comparisons test. For qPCR, gene regulation by NID1 is shown when fold-regulation > |2|, p-value < 0.05. *$p < 0.05$; **$p < 0.01$, ***$p < 0.001$, and ****$p < 0.0001$. Scale bars: 50 µm.

upregulated expression levels for *TNC, THBS1, ITGA2, ADAMTS8, MMP11,* and several collagens such as *COL1A1, COL6A2,* and *COL15A1*. Interestingly, *TGFB1* was significantly upregulated in both normoxic and hypoxic NID1-treated hiPSC-CMs (Figure S5A, Supporting Information). *LAMB3, VTN, COL14A1, ADAMTS1,* and *MMP1* were significantly downregulated in NID1-treated hiPSC-CMs under hypoxic conditions. Of the transcriptional changes in ECM-associated genes in hiPSC-CMs induced by hypoxic conditions, 28 genes out of a total of 89 genes tested were significantly differentially expressed compared to the normoxic groups. In NID1-treated hiPSC-CMs, transcriptional changes induced by hypoxia were minimal with only one differentially expressed gene (*COL14A1*) (Figure S5B, Supporting Information).

Hypoxia is known to induce a phenotypic switch from fibroblasts to myofibroblasts, which is the cell population producing the majority of the structural ECM proteins during fibrosis.[22] The phenotypic switch to myofibroblasts can be assessed by α-SMA expression and was observed in our control fibroblasts (Figure 3D). Interestingly, the expression of α-SMA was significantly reduced in NID1-treated fibroblasts. Gene expression analysis of fibroblasts showed that *MMP7, MMP11, MMP12, MMP13, COL14A1,* and *CLEC3B* were significantly downregulated by NID1; and *COL7A1, COL11A1, HAS1, ADAMTS1,* and *THBS1* were significantly upregulated by NID1 (Figure 3E). Exposure to hypoxic conditions resulted in significant up- or downregulation of 26 genes in the control group, while only 11 genes were impacted in NID1-treated fibroblasts (Figure S5C, Supporting Information).

The MI/R model data showed an increased number of αSMA$^+$/CD31$^+$ vessels in the NID1-treated infarcted hearts. To test the angiogenic potential of NID1, a human umbilical vein

endothelial cell (HUVEC) tube formation assay was performed. NID1 significantly increased a variety of angiogenesis parameters including the total segment length, number of meshes, and total mesh area, as well as number of segments (Figure 3F).

Our data shows that NID1 supports angiogenesis and cardiovascular cell homeostasis during hypoxia and provides an antifibrotic effect on fibroblasts, elucidating the cellular events underlying the positive functional effect of NID1 in the therapeutic model.

2.4. NID1 Protects Pancreatic β-Cells and Increases Insulin Secretion in an In Vitro Ischemia Model

We next asked if the protective and antifibrotic effect of NID1 during ischemia is organ-specific or would be of benefit in other noncardiac therapeutic areas, such as islet transplantation, where ischemia and the survival of transplanted islets are a major therapeutic roadblock. The presence of BM proteins COL4, LAM, NID1, and nidogen-2 (NID2) was confirmed in human 11-week fetal and 64-year adult pancreatic tissues by IF staining (**Figure 4**A,B). Interestingly, in adult tissues, NID1 was spatially confined to insulin-producing β-cells in contrast to other BM proteins, suggesting that NID1 has a specific function in β-cells (Figure 4C).

To determine if NID1 impacts β-cell functionality, we established an in vitro hypoxia model using β-cell aggregates, so-called pseudoislets, using the conditionally immortalized human EndoC-βH3 cell line (Figure S6A–I, Supporting Information). The impact of dosages of 20, 30, and 40 µg mL^{-1} NID1 on pseudoislet function was first assessed under normoxic conditions. NID1-treated pseudoislets significantly increased insulin secretion at all dosages; with 30 µg mL^{-1} reaching the maximum effect, which was the dosage chosen for all further pseudoislet experiments (Figure 4D). IF staining of NID1-treated pseudoislets cultured under normoxic conditions showed a significant increase in E-cadherin when compared with the controls (Figure 4E). NID1 had no effect on cell death under normoxic conditions, assessed by the quantification of TUNEL$^+$ cells and cleaved caspase-3 staining (Figure 4F). In hypoxic conditions, NID1 rescued the loss of insulin secretion that was lost in control cultures, preserved the significant increase in E-cadherin seen in normoxia, and significantly reduced cell death (Figure 4G–I).

Raman imaging with TCA analysis and multivariate curve resolution confirmed that NID1 enhances β-cell function in hypoxia, particularly in the pseudoislet core, by an increase in mitochondrial function, insulin, and insulin-transporting lipid vesicles (Figure S6J–P, Table S2, Supporting Information).[23] These data demonstrate the protective and stimulative effect of NID1 on pancreatic β-cells.

2.5. NID1 Modulates Immune Cell Responses toward Regeneration

Our data nominated NID1 as a potential therapeutic candidate. Therefore, its interaction with immune cells of the innate and adaptive system was evaluated in vitro utilizing a previously described human-based assay.[24] Briefly, a chemotaxis assay was performed to measure the impact of NID1 on human CD14$^+$ blood monocyte migration (**Figure 5**A). CD14$^+$ blood monocyte migration is an important process to clear the tissue of debris from apoptotic cells and disrupted ECM, thereby inducing normal tissue remodeling. Significant migration was detected for the 50 µg mL^{-1} NID1-treated CD14$^+$ monocytes compared with the negative control. Measuring the induced short-term tumor necrosis factor alpha (TNFα) release from human monocytes showed negligible TNFα levels for a NID1 dosage up to 50 µg mL^{-1} compared with the lipopolysaccharide (LPS) control (Figure 5B).

To determine the influence of NID1 on macrophage polarization, unpolarized M0 macrophages were exposed to NID1 for 24 h. The macrophages were of rounded morphology with a tendency to arrange in clusters. This appearance was qualitatively more similar to an alternatively activated/regenerative (M2) macrophage, since classically activated/proinflammatory (M1) macrophages have a more elongated cell shape (Figure 5C). Flow cytometry studies detecting the surface molecules HLA-DR, CD80, CD206, and CD163 confirmed that NID1-treated macrophages did not develop an M1 phenotype (Figure 5D). Cytokine analysis of supernatants from NID1-treated macrophages confirmed the absence of M1 macrophage induction. Rather, a profile was detected that is characteristic for M0 or M2 macrophages with low levels of IL-6 and TNFα (Figure 5E).

T cell subsets with diverse functions can also influence the inflammatory milieu and the remodeling process, for example, post-MI in heart tissue.[25] Therefore, we studied the impact of NID1 on preactivated T cells by measuring its effect on anti-CD3 (aCD3)-induced proliferation of classical T cell subsets. NID1 provided an additional trigger to CD4$^+$ T cells, but not to the cytotoxic CD8$^+$ T cell fraction (Figure 5F). The release of the proinflammatory cytokines TNFα and IFNγ was significantly reduced in 5-day cultures of NID1-treated aCD3-activated immune cells (Figure 5G). A standardized cytotoxicity test was performed according to EN ISO 10993. With this test, we assessed the metabolic activity of primary-isolated human dermal fibroblasts to determine a potential cytotoxic effect of NID1 as requested by certification bodies such as the European Medicines Agency (Figure 5H). As a complementary test, cytotoxicity of NID1 was also investigated using human primary-isolated cardiac fibroblasts (Figure 5I). We observed no cytotoxic effect due to NID1 exposure in the tested concentrations of 50, 100, and 200 µg mL^{-1}. Interestingly, we noted an increased metabolic activity of both dermal and cardiac fibroblasts in the NID1-treated groups compared with controls. These data show the regenerative immunomodulatory effect of NID1 in a human in vitro system and the safety of NID1 at dosages up to 50 µg mL^{-1}, supporting the therapeutic potential of NID1.

2.6. NID1 Signals via Integrin $\alpha v\beta 3$ and Activates the MAPK Pathway

Understanding the mechanistic function of a therapeutic biomolecule is required before entering clinical trials. Here, we sought to elucidate the mechanisms driving the function of NID1 during hypoxic events. The integrin $\alpha v\beta 3$ has been reported as a binding partner for NID1 and is expressed on the cells of human Langerhans islets and on CMs.[26–28] NID1 and $\alpha v\beta 3$

ADVANCED SCIENCE NEWS
www.advancedsciencenews.com

ADVANCED SCIENCE Open Access
www.advancedscience.com

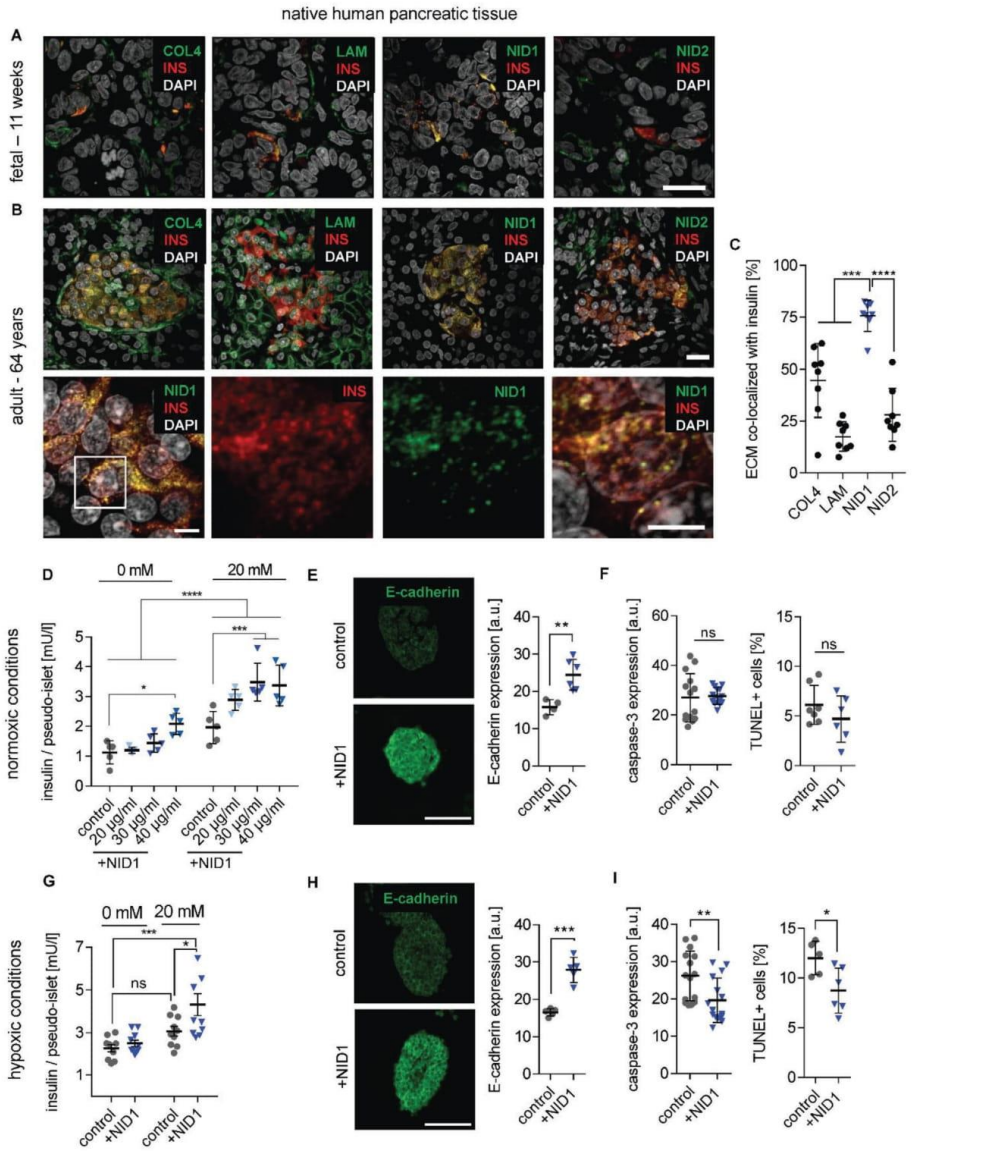

Figure 4. NID1 mitigates the effects of hypoxia on pancreatic β-cells and increases insulin secretion. A,B) Expression pattern of BM proteins, insulin (INS), and DAPI in human (A) fetal (11 weeks postgestation) and (B) adult pancreas (64 years). Scale bars: 20 µm. Highly magnified images show the colocalization of NID1 with INS in native adult pancreas. Scale bar: 5 µm. C) Quantification of the colocalization of ECM proteins with INS ($n = 10$), one-way ANOVA with Tukey's multiple comparisons test. D) GSIS response (with 0×10^{-3} and 20×10^{-3} M glucose) under normoxic conditions of human NID1-treated pseudoislets in suspension at different concentrations: 20, 30, 40 µg mL^{-1} when compared with the control (PBS) ($n = 5$); two-way ANOVA with Tukey's multiple comparisons test. E) E-cadherin expression under normoxic conditions ($n \geq 5$). F) Cell death under normoxic conditions via the detection of cleaved caspase-3 ($n = 14$) and TUNEL$^+$ cells ($n = 7$). G) GSIS response (with 0×10^{-3} and 20×10^{-3} M glucose) under hypoxic conditions of NID1-treated pseudoislets at 30 µg mL^{-1} and normalized by live cells ($n = 10$); two-way ANOVA with Tukey's multiple comparisons test. H) E-cadherin expression under hypoxic conditions ($n \geq 5$ M; unpaired t-test. I) Protective effect of NID1 assessed by cleaved caspase-3 expression ($n \geq 7$). and via detection of TUNEL$^+$ cells ($n \geq 4$); unpaired t-test. $^*p < 0.05$; $^{**}p < 0.01$, $^{***}p < 0.001$, and $^{****}p < 0.0001$.

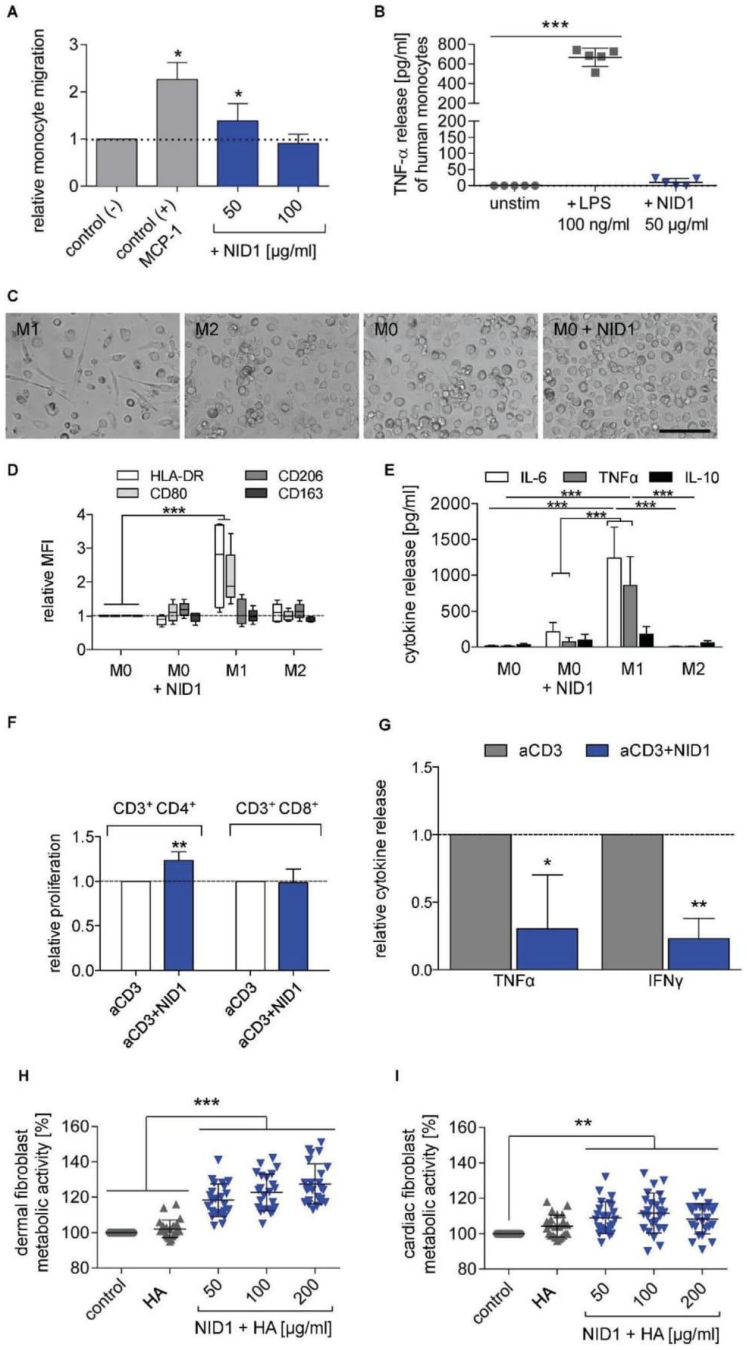

binding was confirmed at the protein level by titration of immobilized $\alpha v\beta 3$ with soluble NID1 (**Figure 6**A). No fixation was employed, as this would have altered the protein binding. Coating of 4 µg mL^{-1} of $\alpha v\beta 3$ was sufficient to have a specific ELISA signal of bound NID1 in the presence of Mn^{2+} when compared with NID1 in EDTA, indicating a divalent cation-dependent interaction of NID1 and $\alpha v\beta 3$ integrin. In addition, the binding was dose-dependent as a specific ELISA signal was detected starting between 25 and 50 µg mL^{-1} of NID1 (corresponding to $\approx 0.167 \times 10^{-6}$ M to 0.334×10^{-6} M).

Blocking of the $\alpha v\beta 3$ integrin on pseudoislets and hiPSC-CMs was performed to investigate whether the positive effect of NID1 is mediated through the activation of the $\alpha v\beta 3$ integrin (Figure 6B–D). Blocking of NID1-treated pseudoislets with an $\alpha v\beta 3$ antibody inhibited the increase in insulin secretion under normoxia (Figure 6B). Blocking $\alpha v\beta 3$ integrin in NID1-treated hiPSC-CMs under hypoxic conditions negated the decrease in apoptosis seen in nonblocked NID1-treated hiPSC-CMs in caspase-3 staining and TUNEL assay (Figure 6C,D). These data indicate that $\alpha v\beta 3$ is involved in mediating the interaction of NID1 with β-cells and CMs.

A novel high-throughput digital Western blot platform (DigiWest) was employed to investigate the specific biological pathways that are mediated by NID1 in β-cells and CMs cultured under hypoxic conditions.[29] NID1-treated β-cells showed a significantly upregulated expression of EpCAM, Erk 2, pFyn, p21, Src, pSrc, Wnt3, and a trend toward the upregulation of pMEK1/2 (Figure 6E,F). NID1 treatment of hiPSC-CMs led to an upregulation of Bax, pErk 1/2, SAPK, MOB1, Rac1/cdc42, and Wnt3 (Figure 6G,H) Downregulation was observed for b-Raf, pFAK, and Notch2. Bax and SAPK protein contents were normalized by Bcl2 and Erk1,2 in order to determine whether proapoptotic pathways have been activated. Ratios of Bax/Bcl2 and SAPK/Erk1,2 showed no significant difference between NID1-treated and control cultures (Figure 6I,J), which indicates that the increase in Bax and SAPK in the NID1-treated hiPSC-CMs had been offset by an increase in Bcl2 and Erk.[30,31] All target proteins tested and the resulting protein regulation are shown as heatmaps in Figure S7 of the Supporting Information. The hypothetical pathways associated with NID1 are proposed in Figure 6K. Here, we have shown that NID1 binds and signals through integrin $\alpha v\beta 3$ as seen by the upregulation of pFyn, Src, pSrc, and Rac1/cdc42. This leads to the activation of the mitogen-activated protein kinases (MAPK) pathway, including the kinases extracellular signal-regulated kinase 1/2 (Erk 1/2) and mitogen-activated protein kinase 1/2, which is driving the protective effects of NID1 both on β-cells and CMs.

3. Discussion

In this study, we report the protective and immune-modulatory effects of NID1 on cells and tissues of the cardiovascular, pancreatic, and immune system. We demonstrate the therapeutic efficacy of NID1 by a significant improvement in heart function post-MI/R in a preclinical mouse model and discovered a promising new avenue to improve the outcome of β-cell transplantation. We propose that the effect of NID1 is mediated by the $\alpha v\beta 3$ integrin leading to the activation of the MAPK pathway in both CMs and β-cells.

NID1 is an underinvestigated ECM BM protein that is mostly recognized as a linker protein of COL4 and LAM.[32] It has been suggested to play a role in angiogenesis, hepatic regeneration, and regenerative axon growth and guidance.[33–36] Here, the identification of NID1 as the highest expressed BM component during cardiovascular differentiation, and the important role of BM proteins in organogenesis suggested that NID1 may have a regenerative or protective effect on the ischemic heart. The heart has a highly limited capacity for regeneration; therefore, current treatment strategies seek to restore cardiac function by methods such as cell injections into the infarct border zone, and delivering growth factors and small molecules or ECM proteins to activate or modify native cardiac cells.[37,38] Despite promising results, many of these approaches have questionable or unknown safety profiles, hindering their clinical translation. We propose a simplified strategy of one ECM protein that has a potential supportive effect on immune cells, as opposed to an inflammatory effect. The therapeutic ability of NID1 was demonstrated by an improved heart function in a post-MI/R mouse model as demonstrated by elevated EF and FS, as well as the recovery of EDV, LVED, and LVIDd. Moreover, in vitro studies showed that NID1 suppresses the transdifferentiation of fibroblasts into fibrillar ECM-secreting myofibroblasts, potentially enhancing the significant reduction of fibrosis seen in vivo. The ECM protein agrin was previously shown to improve heart function post-MI through CM division and proliferation.[39] Our findings are unique as we show that NID1 improves heart function by the protection of CMs and potential regeneration of other heart cells. Interestingly, both NID1 and agrin activate the MAPK pathway in CMs; however, NID1 ligates the $\alpha v\beta 3$ integrin and agrin ligates Dag1.

Figure 5. NID1 modulates immune cells. A) CD14$^+$ monocyte migration in the presence of different NID1 concentrations (50, 100 µg mL^{-1}) and the control protein MCP-1 after 3 h. Cell migration is shown relative to the control (–) ($n = 3$ experiments with 9 single values); one-way ANOVA with Dunnett's multiple comparison test. B) Potential endotoxin contamination was tested by adding 50 µg mL^{-1} NID1 or 100 ng mL^{-1} LPS in a monocyte culture for 24 h. Released TNFα was measured by ELISA ($n = 5$); Friedman test with Dunn's multiple comparison test. C) Representative images of M1- and M2-type macrophages, unstimulated M0-type macrophages and NID1-treated M0-type macrophages. Scale bar: 100 µm. D) Expression of polarization markers (HLA-DR, CD80, CD206, CD163) was determined for M0-type macrophages cultured for 24 h with 50 µg mL^{-1} NID1, M0, M1, and M2-type macrophages. Mean fluorescence intensity (MFI) is shown relative to the untreated M0 macrophage control (set as 1) ($n = 5$); two-way ANOVA with Dunnett's multiple comparison test. E) Release of IL-6, TNFα, and IL-10 after 24 h culture of M0 macrophages with NID1 (50 µg mL^{-1}) and M0, M1 or M2 type cultures ($n = 5$); two-way ANOVA with Tukey's multiple comparison post-test. F) T cell proliferation after 5 days culture of human PBMCs with low-dose aCD3 alone or combined with NID1 (50 µg mL^{-1}) was tested in a CFSE-based assay and measured by flow cytometry. Shown is the relative proliferation level of CD3$^+$ CD4$^+$ and CD3$^+$ CD8$^+$ T cells compared to the aCD3 control. G) Relative TNFα and IFNγ release of PBMC cultures after 5 days with either aCD3 alone or combined with NID1 (50 µg mL^{-1}). Data for proliferation and cytokine release were analyzed by Kolmogorov–Smirnov *t*-test, relative to the aCD3 control ($n = 6$). H) Cytotoxicity test using human dermal fibroblasts (EN ISO 10993) or I) cardiac fibroblasts. Cell viability was measured after treatment with control medium, HA hydrogel, and HA-supplemented with NID1 (50, 100, and 200 µg mL^{-1}) for 24 h. Cell viability is shown relative to the control (set as 100% viability) ($n \geq 22$); one-way ANOVA with Tukey's multiple comparisons test: $^*p < 0.05$, $^{**}p < 0.01$, $^{***}p < 0.001$, and $^{****}p < 0.0001$.

ADVANCED SCIENCE NEWS
www.advancedsciencenews.com

ADVANCED SCIENCE Open Access
www.advancedscience.com

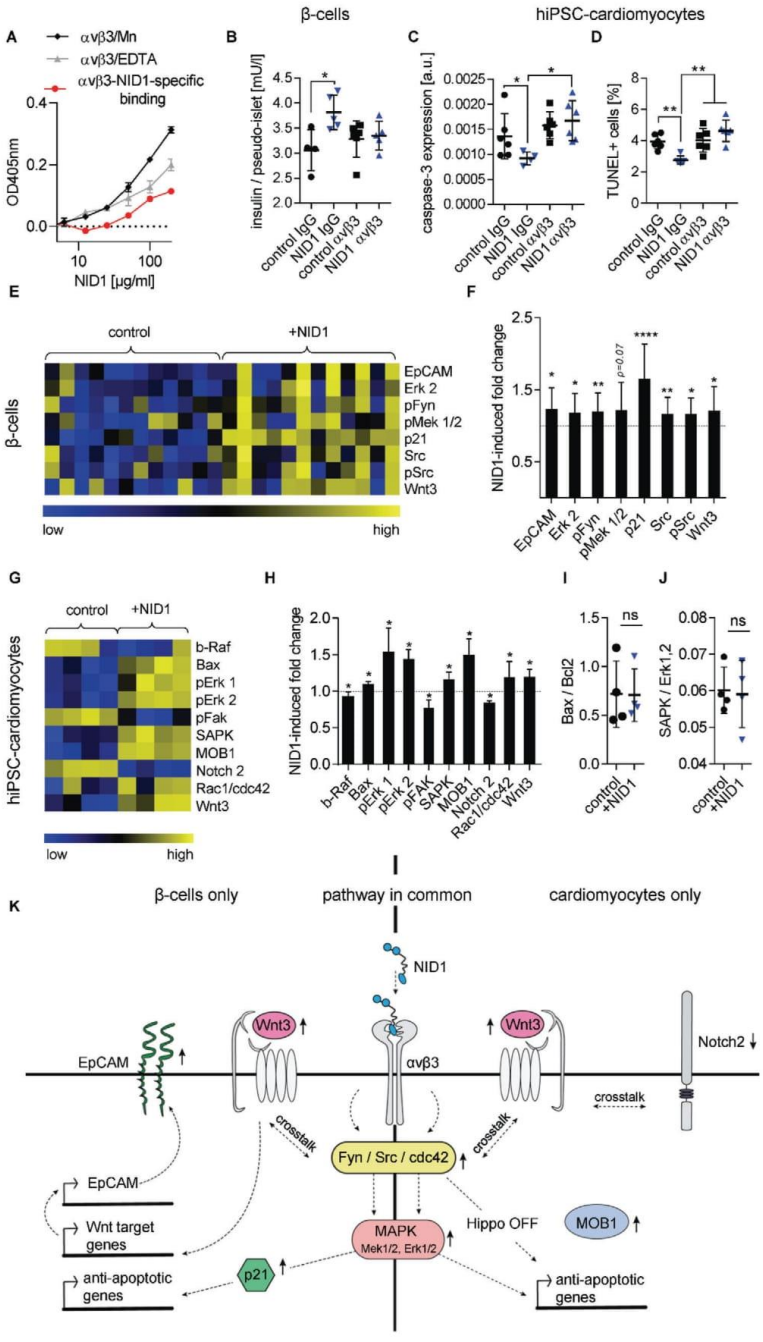

Our functional data suggest that NID1 is also applicable in other therapeutic applications where ischemia and fibrosis hinder therapeutic efficacy, such as in islet β-cell transplantation. During the first week of islet transplantation, fibrosis encapsulates the transplant delivery device, and the lack of oxygen supply causes the loss of β-cell mass, restricting the patient's insulin independency.[40] Interestingly, NID1 was the only BM protein to have a specific spatial distribution that exclusively colocalized with insulin-producing β-cells. In vitro data showed that NID1 has a protective effect on β-cells under hypoxic conditions and has a direct impact on insulin secretion in a dose-dependent manner. This suggests that NID1 could be used as a protective and functional molecule during islet transplantation as it could enhance angiogenesis and reduces fibrosis around the device while improving β-cell function and survival within.

We discovered that full length human NID1 binds to human integrin $\alpha v\beta 3$ in a divalent cation-dependent way, and that $\alpha v\beta 3$ is the primary binding ligand driving the therapeutic effect of NID1 on CMs and β-cells. The combination of gene and protein expression analysis confirmed the activation and downstream signaling of the $\alpha v\beta 3$ via the MAPK pathway in hiPSC-CMs and β-cells. MAPK effectors such as Erk 1/2 are expressed following oxidative stress in CMs, which protect them from apoptosis in vitro and in vivo.[41] In addition, the MAPK pathway is essential for glucose-stimulated insulin secretion in β-cells.[42] In CMs, an additional protective mechanism may be provided by shutting down the Hippo pathway, which has been described to inhibit adult cardiac regeneration.[43] Wnt signaling, which may arise through $\alpha v\beta 3$ downstream signaling, is involved in β-cell insulin secretion, as well as cellular survival in both cell types.[44,45] The MAPK and Wnt pathways as well as the stimulation of the $\beta 3$ integrin are known activators of *TNC* expression.[46] *TNC* is involved in CM detachment from the ECM that allows surviving CMs to reorganize and rebind to the ECM thus protecting CMs from anoikis.[47] *TNC* and *THSP1* are known activators of TGF-β signaling, which regulates the inflammatory response in the postinfarcted heart and the deposition of fibrous tissue.[48] Taken together, our data uncovered the key mechanisms of NID1 action in vitro, providing insight into the therapeutic function of NID1 seen in vivo.

It is well established that the ECM has a modulatory function on a variety of immune cells. Monocytes migrate to injured tissue and polarize to distinct macrophage phenotypes depending on the surrounding tissue milieu.[49] We identified in vitro a significant migration of CD14+ monocytes in the presence of NID1 and the influence of macrophage polarization toward a phenotype with characteristics of both the M0 and the regenerative M2 phenotype, but not the pro-inflammatory M1 phenotype. It was previously shown that NID1 binds to natural killer cells via NKp44, mediating an inhibitory effect seen by the reduction of cytokine release such as IL-2 and IFNγ.[50] We demonstrated a similar reduction of proinflammatory cytokine secretion such as TNFα and IFNγ in activated T cells by NID1, indicating the anti-inflammatory potential of NID1. Taken together with recent research showing that macrophages contribute collagen to scar formation, the NID1-mediated modulation of macrophages may play an important role in the reduction of scar tissue seen in this study.[51]

4. Conclusion

In summary, in our study, in vitro and in vivo models demonstrated that NID1 increases cardiogenesis, angiogenesis, and cell survival, while beneficially modulating immune responses and reducing fibrosis. Mechanistically, NID1 was shown to ligate the $\alpha v\beta 3$ integrin to activate the Erk 1/2-MAPK and Wnt pathways in cardiomyocytes and pancreatic β-cells. In a preclinical mouse model, a single treatment with an NID1-functionalized gel significantly increased heart function post-MI. These data demonstrate the positive effect of NID1 on ischemic cells and tissues from different organs, suggesting that it may have multiple clinical applications as an off-the-shelf product.

5. Experimental Section

hESC Cultures and Cardiovascular Differentiation: The use of hESCs (H9, passages 36–60, WiCell) was approved by the Robert Koch-Institute, Berlin, Germany (AZ: 3.04.02/0086). hESCs were maintained according to WiCell feeder-dependent Pluripotent Stem Cell Protocols, SOP-SH-001, version G, on mouse embryonic fibroblasts (AMS Biotechnology (Europe) LTD) in stem cell growth medium. For EB generation, 3×10^4 cells of an H9 single cell suspension in mTeSR1 (STEMCELL Technologies), supplemented with 10 ng mL^{-1} BMP4 and 10 ng mL^{-1} ROCK inhibitor Y-27632 (Sigma-Aldrich), were centrifuged per 96-well (nontreated, conical bottom, Thermo Fisher Scientific) at 1000 rpm for 5 min and incubated overnight. Two previously described protocols were modified for cardiovascular differentiation.[15,16] On day 1, after the overnight incubation, up to 200 EBs were transferred to one ultralow attachment 6-well well (Corning Inc.) in 3 mL of stage 1 media (StemPro 34 (Life Technologies), 3 ng mL^{-1} activin A, 5 ng mL^{-1} bFGF, 10 ng mL^{-1} BMP4). On day 4, the floating EBs were transferred to a 6-well plate, coated with 0.1% gelatin or 0.1% gelatin-supplemented with or without 50 µg mL^{-1} nidogen-1 (NID1) and cultured in 2 mL^{-1} of stage 1 media + 5×10^{-6} M inhibitor of WNT response-1 (IWR-1). The EBs were incubated for 24 h to allow attachment. The attached EBs were differentiated in stage 2 media (StemPro 34, 5 ng mL^{-1} VEGF, 10 ng mL^{-1} bFGF, 5×10^{-6} M IWR-1) from day 5 to day 10.

Figure 6. NID1 signals via $\alpha v\beta 3$ and activates the MAPK pathway in β-cells and cardiomyocytes. A) Divalent cation-dependent and dose-dependent binding of $\alpha v\beta 3$ with NID1. B) Blocking of $\alpha v\beta 3$ in NID1-treated and control pseudoislets under normoxic conditions. Functionality assessment by glucose stimulation at 20×10^{-3} M glucose ($n \geq 4$); one-way ANOVA with Tukey's multiple comparisons test. c,d) Blocking of $\alpha v\beta 3$ in NID1-treated and control hiPSC-CMs by a $\alpha v\beta 3$ antibody under hypoxic conditions. Protective effect of NID1 assessed by C) cleaved caspase-3 ($n \geq 4$) and D) TUNEL assay ($n = 6$); one-way ANOVA with Tukey's multiple comparisons test. E–H) DigiWest-based protein expression analysis of significantly regulated proteins in NID1-treated E,F) pseudoislets ($n = 12$) and G,H) hiPSC-CMs ($n = 4$) under hypoxic conditions compared with their respective controls. Data are (E,G) shown as column-wise and color-coded heatmap from the lowest (blue) to the highest (yellow) expression for each analyte; and (F,H) quantified as fold change induced by NID1. Nonparametric Wilcoxon Rank sum test. I,J) Protein ratios of (I) Bax to Bcl2 and (J) SAPK to Erk1,2 ($n = 4$); unpaired *t*-test. K) Proposed common and separate mechanisms of action of NID1 for CMs and β-cells in vitro. Middle: common pathway, NID1-$\alpha v\beta 3$ ligation upregulating Fyn/Src in β-cells and cdc42 in CMs, which stimulates Wnt3 and the MAPK pathway. Left: β-cells, Fyn/Src activates the MAPK pathway, upregulating p21, which can be antiapoptotic. Fyn/Src crosstalks with Wnt3 and EpCAM, which enhances insulin secretion. Right: CMs, cdc42 downregulates the Hippo pathway as shown by an upregulation of MOB1. Pathways specific for each cell type are shown either on the left for β-cells and on the right for CMs. $^*p < 0.05$; $^{**}p < 0.01$, $^{***}p < 0.001$, and $^{****}p < 0.0001$.

Media changes were required every two days throughout cardiovascular differentiation. Attached EBs typically started beating on day 7 and were harvested for further analysis on day 10.

Ethics Information: This study was performed in accordance with institutional guidelines and was approved by the local research ethics committees (University of California, Los Angeles IRB #05-10-093; University Tübingen IRB #356-2008BO2, #406-2011BO1, and #495-2018BO2; Landesärztekammer Baden-Württemberg, IRB #F-2012-078 and #F-2011-068; and the Charité Universitätsmedizin Berlin #EA/226/14).

Human first trimester and second trimester tissues were obtained from electively aborted fetuses following informed consent and de-identification. Normal adult heart sections were obtained from post-mortem autopsy samples (expiration due to noncardiac cases, with no history or evidence of cardiac disease on post-mortem inspection), which were provided by the department of pathology, David Geffen School of Medicine at UCLA, Los Angeles, USA.

All mouse surgeries were performed under the supervision and with approval of the UCLA Animal Review Committee (#2011-042 and #2013-057).

Histology, Histochemistry, Immunofluorescence Staining, and Quantification: Fetal tissues were freshly fixed in 4% PFA and embedded in paraffin using a Shandon Citadel 1000 (Thermo Fisher Scientific). The pseudoislets and EBs were fixed in 4% PFA, placed in Histogel (American MasterTech) and processed for paraffin embedding. All paraffin-embedded cells and tissue were sectioned (3 µm sections) using a microtome HM340E (Thermo Fisher Scientific). Sections of adult pancreas (3 µm sections) were commercially obtained (NBP2-30191, Novus Biologicals). Sections of adult human heart tissue were provided by UCLA as stated in the Ethics section.

Histological and histochemical staining was performed on deparaffinized and hydrated serial sections of explanted mouse hearts, 28 days post MI/R. Russell-Movat pentachrome staining visualized collagens (yellow), muscle tissue (red), proteoglycans/ glycosaminoglycans (blue-green), mature elastic fibers (black), and cell nuclei (dark red). Bright field (BF) images were acquired using a Zeiss Axio Observer Z1 (Carl Zeiss). Picrosirius Red and Fast Green stain visualized the collagen-rich scar (red) and the myocardium (green). In detail, deparaffinized and hydrated sections were incubated for 5 min in 0.5% acidified water (acetic acid, Carl Roth) and subsequently for 1 h in a solution of 0.1% Fast Green FCF at pH 2 (Sigma-Aldrich) and 0.1% Picrosirius Red in saturated picric acid (Morphisto) at a 1:1 ratio. The sections were cleaned twice in acidified water for 2 min, dehydrated using graded ethanol washes (70–100% v/v), and then mounted. High definition images were acquired with the glass slide scanner Opticlab H850 (Plusteck) and saved as TIFF. The glass scale bar 1972-50 peak (GWJ Co) was used to scale the collected images. A MATLAB algorithm was developed to identify and quantify the image components based on their HSV histograms. Valves and vessels of the outflow tract were stained red and cropped out of the image to determine the true scar areas. All areas calculated were normalized to the total tissue area.

For immunofluorescence staining, the paraffin sections were stained as previously described.[24–53] Briefly, antigen retrieval was performed consecutively in Tris-EDTA (pH = 9.0) and citrate buffer (pH = 6.0) in a steam cooker. For the intracellular antigens, the sections were treated with 1% Triton X-100. A goat block solution was used to block unspecific binding sites. Antibodies were diluted in antibody dilution buffer (PBS containing 1% BSA, 0.1% TritonX-100, 0.1% cold-water Fish Skin Gelatin, 0.05% Tween20) and samples were incubated overnight at 4 °C. After several washes, the secondary antibody was applied to the samples and incubated for 30 min at room temperature, and after several washes the sections were exposed to a DAPI solution (5 µg mL^{-1} in PBS, Roche). Fluorescence images were acquired using a confocal laser scanning microscope (LSM 880 with Airyscan, Carl Zeiss Microscopy GmbH, Germany). The images acquired were processed with Adobe Photoshop CS5 (Adobe System Inc.). Semiquantitative analyses of IF images were conducted by detecting the gray value intensity (GVI) using ImageJ software. All GVI data were normalized to the laser power. Quantification of E-cadherin and caspase-3 staining of pseudoislets was conducted utilizing images obtained with a 63× magnification on a Zeiss Axio Observer Z1 (Carl Zeiss). The entire pseudoislet was selected as region of interest (ROI). GVI quantification of the ROI was conducted using ImageJ, version 1.52p. TUNEL assay was performed using the Click-iT Alex Fluor Imaging Assay kit (Thermo Fisher Scientific). Sections were mounted with Prolong Gold Anti Fade solution (Thermo Fisher Scientific). TUNEL images were evaluated in a double-blinded study by two unbiased observers. Cells were identified as $TUNEL^+$ when a clear green and blue staining was exhibited. The ratio was calculated by dividing $TUNEL^+$ cells by total number of $DAPI^+$ cells per pseudoislet. Images were obtained using a 63× magnification on a Zeiss Axio Observer Z1 (Carl Zeiss). Quantification of the vessel density in αSMA/CD31/CTNT-stained mouse infarct scar area sections was conducted by counting αSMA+/CD31+ vessels utilizing images taken with a 25× objective ($n = 6$). The scar area of each image was measured using the ImageJ software. To quantify colocalization, a macro was designed using Microsoft Excel, version Office 365. Briefly, the algorithm compares GVI values of pixels of the simultaneously obtained NID1 and insulin channels. Colocalization was counted when the GVI of a specific pixel exceeded a set threshold on both channels and normalized by the total amount of pixels exceeding the threshold value in the NID1 channel. TuJ1 was used for the assessment of neuronal cells in the infarct area. 10 IF images per heart were taken with a 63× objective. $TuJ1^+$ and total cells were counted.

NID1 Production Plasmid: The inducible NID1 production plasmid was constructed from several sections of commercially available vectors. The main backbone consisted of the pcDNA3.1 vector. The inducible TRE promotor for NID1 expression was taken from the pTRE3G vector and DHFR expression was controlled by the TK promoter from the pGL4.74(hRluc/TK) vector. A codon-optimized sequence of human NID1 (GenBank accession number: BC045606.1, 5406 bp) with a histidine/asparagine tag at the C-terminus was synthesized from GeneArt (Life Technologies).

Stable NID1 Production Clone Generation and Production Induction: CHO DHFR-negative mutant cells (DSMZ no.: ACC 126) were transfected with the pCMV-Tet3G plasmid (631166, Clontech Laboratories) and selected for Geneticin (G418, Calbiochem) resistance. Selected activator clones were transfected with the NID1 production plasmid and cultured for two weeks in selection media (MEM α, 10% FBS dialyzed, 500 µg mL^{-1} of G418), which does not support the growth of DHFR-negative cells. Single cell cloning was conducted and clones were treated with 100 ng mL^{-1} doxycycline hydrochloride (Dox) (Thermo Fisher Scientific) to induce NID1 production. Secreted NID1 was measured using an ELISA (DY2570, R&D Systems). Clones with the highest measured levels of NID1 underwent selection rounds with rising levels of methotrexate (MTX) for genomic amplification. During MTX selection, ELISA, q-RT-PCR, and q-PCR were performed to measure NID1 protein levels and assess the relative levels of NID1 mRNA and the relative copy number of genome amplified NID1. The best production clones were adapted to suspension growth in Erlenmeyer flasks with serum-reduced media (DMEM/Ham's F12 basal medium, 0.5% FBS dialyzed, 2.5×10^{-6} M MTX, 2×10^{-3} M L-Glutamine, 1% penicillin–streptomycin (Pen/Strep), 250 µg mL^{-1} G418) in an incubation shaker (Minitron, Infors GmbH) at 37 °C and 5% CO_2 at 85 rpm. NID1 expression was induced with 100 ng mL^{-1} Dox and the media with secreted NID1 was harvested 4–5 days later and stored before NID1 purification at −20 °C.

NID1 Purification: The IMAC purification of the histidine/asparagine-tagged human NID1 was performed with a HisPrep FF 16/10 affinity chromatography column (GE Healthcare), controlled by the FPLC system Äkta Explorer 10 (GE Healthcare). NID1 elution was indicated by the increased absorption at the wavelengths 280 and 256 nm. Protein-containing elution fractions were pooled and desalted using a HiPrep 26/10 desalting column (GE Healthcare), controlled by the Äkta Purifier 100 (GE Healthcare). Subsequently, the protein solution was washed and concentrated with ultrafiltration units (Vivaspin 20, Sartorius), sterile filtered (SCGP00525, Millipore), and stored at −80 °C until further use.

SDS-PAGE and Western Blot: All protein samples were mixed with 4× Roti-Load (Carl Roth) and denatured at 90 °C for 5 min. The samples were run on a NuPAGE Novex 3–8% Tris-Acetate gel (EA03752BOX, Life Technologies) under denaturing conditions. The HiMark Pre-Stained Protein Standard was used for easy band identification. After SDS-PAGE, the

proteins were transferred to a nitrocellulose membrane (Whatman) in an electrical field (30 V, 60 min) in the XCell II Blot Module (Life Technologies). For an unspecific protein staining, the nitrocellulose membrane was incubated in a Ponceau-Red solution (Sigma-Aldrich) for 5 min at room temperature. Images were acquired and the membrane was discolored in a 0.1 M NaOH solution for later specific protein immunodetection. The membrane was blocked using 5% skim milk powder (Sigma-Aldrich) in TBS-T and then incubated with the primary antibodies overnight at 4 °C while shaking. After several washes with TBS-T, the membrane was incubated with the secondary antibody in TBS-T with 5% skim milk powder for 1 h at room temperature. After washing with TBS-T, SuperSignal West Dura Extended Duration Substrate (Thermo Fisher Scientific) was applied onto the membrane, drained after few seconds and the developed chemiluminescence was detected in the Luminescent Image Analyzer LAS-1000 plus (FujiFilm).

NID1 Deglycosylation: Purified NID1 was deglycosylated with an enzyme mix (P6039S, New England Biolabs) as instructed by the manufacturer. In addition to the 4 h incubation time described by the manufacturer, an identical reaction mix was incubated for 20 h. The control sample was treated accordingly, except for the addition of the deglycosylation enzymes, and incubated for 4 h. NID1 deglycosylation was analyzed by the mobility shift of the NID1 bands to a lower protein size on the SDS-PAGE gel.

Co-Immunoprecipitation (Co-IP): The protocol for Co-IP was modified from previously published studies.[54,55] The interaction partners NID1 (1 µg) and LAM 511 (0.5 µg, LN511-02, BioLamina) were mixed in 500 µL of a dilution and washing buffer (0.1 M NaCl, 0.05 M Tris/HCl pH 7.4 containing 0.04% Tween-20 and 1% BSA) and were agitated gently on a rotisserie mixer overnight. 6 µg of the antibody against LAM (ab11575, Abcam) was added to the protein mix and incubated for 24 h for Co-IP. This antibody was not added in the negative control (unspecific background control). Protein A magnetic beads (LSKMAGA02, Millipore) were added and gently agitated on the rotisserie mixer with the protein complexes ± the LAM antibody for 2.5 h at 4 °C and another 30 min at room temperature. After washing off the magnetic beads using a magnetic stand (LSKMAGS08, Millipore), the protein complexes were eluted from the beads and denatured in 30 µL of 1× Roti-Load (K929.2, Carl Roth) via heating for 10 min at 90 °C. Detection of the specific protein bands occurred after SDS-PAGE and Western blot.

qPCR and Expression Profiling Using RT2 Profiler PCR Array: RNA extraction of dermal fibroblasts was performed on lysed cells. Briefly, RNA was isolated using sequential incubation and centrifugation of the lysate with chloroform (Sigma-Aldrich), isopropanol (Carl Roth), and 75% ethanol (Applichem). RNA was resuspended in nuclease free-water and heated for 10 min at 55 °C prior to RNA quantification. RNA was reverse transcribed according to the manufacturer's instructions (RNeasy Micro Kit, Omniscript RT Kit, Qiagen). qPCR of EBs was performed on the LightCycler 480 II (Roche) with the 480 SYBR Green I Master (04887352001, Roche) for the primers NID1, p53 and β-actin for normalization and reference as listed in Extended Data in Table S4 of the Supporting Information. qPCR was performed using a Bio-Rad CFX96 system and the QuantiFast SYBR Green PCR Kit (Qiagen) for the primers *TNNT2* (QT00089782, Qiagen) and *ACTA2* (QT00088102, Qiagen).

qPCR on dermal fibroblasts was performed using ACTA2 (QT00088102, Qiagen), GAPDH (QT01192646, Qiagen) and the QuantiNova SYBR green PCR Kit (208052, Qiagen). All samples were performed as triplicates. The $2^{-\Delta\Delta Ct}$ method was applied for qPCR data quantification.

For expression profiling using RT^2 profiler PCR Array (Qiagen), RNA extraction was performed according to manufacturer's instructions (RNeasy Micro Kit, Omniscript RT Kit, Qiagen). RNA was reverse transcribed to cDNA using RT2 First Strand Kit (SABiosciences, Qiagen). The Human Extracellular Matrix & Adhesion Molecules RT^2 Profiler PCR Array (PAHS-013ZD; Qiagen) was used to measure expression levels of 84 individual genes important for cell–cell and cell–matrix interactions. For all RNA and DNA quantifications, absorbance was measured using a NanoQuant Plate in combination with Infinite 200 PRO (Tecan). If not mentioned otherwise, qPCR measurements were performed using a Bio-Rad CFX96 system and data analysis was performed using the Qiagen data analysis center online tool.

Imaging Flow Cytometry: EBs were harvested at day 10 of the cardiovascular differentiation protocol to conduct flow cytometry analyses using a standard staining protocol.[56] Briefly, cells were incubated with Zombie Red dye (BioLegend) to exclude dead cells and CD29-PE (MCA2298PE, AbD Serotec, UK) for 25 min at 4 °C protected from light. After washing, the Foxp3 Staining Buffer Kit (421403, BioLegend) was used to fix the cells for 30 min on ice, followed by washing and permeabilization for 15 min at 4 °C. After blocking with BSA for 10 min, cells were incubated with CTNT primary antibody (ab8295, Abcam) for 35 min at 4 °C, washed and blocked with 5% BSA for 10 min at room temperature to avoid unspecific binding. The secondary anitbody (rat antimouse IgG1-AF647, 406617, BioLegend) was added for 25 min at 4 °C, protected from light. For the analysis using the ImageStreamx mkII (Amnis Corporation, USA) with the INSPIRE instrument controller software with 40× magnification, 1×10^4 single cells were acquired per sample. Data were analyzed with IDEAS Image analysis software. All samples were gated on single cells that were Zombie Red-negative. The percentage of CTNT+ cells was determined and a control sample (stained with the same antibodies except the primary antibody) was used to set the background fluorescence.

In Vivo Mouse MI/R Model and NID1 Injections: A mouse MI/R model was used to identify the effect of myocardial NID1 injections post MI.[19] All surgeries were performed at UCLA. In detail, 8 weeks old female C57BL/6J mice, strain DLAMb6, were anesthetized using 2.0% isoflurane (Butler Schein), placed on a heated surgical board and given 2.5 mg kg^{-1} flunixin (Flunixin Meglumine, Schering-Plough Animal Health) subcutaneously. Under a dissecting microscope, a midline cervical incision was made to expose the trachea for intubation with a PE-90 plastic catheter (Stoelting Company). The catheter was connected to a Harvard minivent (Harvard Apparatus) supplying oxygen with a tide volume of 225–250 µL and a respiratory rate of 130 strokes per minute. Surgical plane anesthesia was subsequently maintained with 1–1.5% isoflurane. A lateral incision was made in the fourth intercostal space. The heart was exposed and the left anterior descending coronary artery (LAD) was ligated intramurally 2 mm from its origin with a 9-0 nylon suture (Ethicon). The suture was tied around a small piece of plastic tubing (PE-10) to occlude the coronary artery while allowing an easier and safer relief of the occlusion. This occlusion occurred for 45 min. During this time, a moist gauze pad was placed over the incision to maintain a sterile atmosphere. Ischemia was verified by the regional paleness of the myocardium that was no longer supplied with blood by the left coronary artery. Reperfusion was allowed by cutting the knot on the PE-10 tube and could be verified by the appearance of hyperaemia in the previously pale region. Reperfusion caused the infarcted region to change into a normal pinkish red color. This procedure was conducted on five mice for the NID + HA treatment group, five mice for the HA carrier gel group, and three mice for the saline control group. Samples sizes were determined for statistical power and in accordance to the EU 3Rs regulation for the reduction of animal studies. After confirming that there was no bleeding, the animals received injections in the MI border zone. Three animals in the control group were injected with 50 µL of saline solution. Five animals were injected with a total of 50 µL of HyStem hyaluronic acid (HA) hydrogel (Glycosan BioSystems) in PBS per animal. In the NID1 + HA group, five animals received 50 µL injections of HA in PBS with 50 µg mL^{-1} NID1. For each mouse, the 50 µL total injection volume was divided into 10 µL injections at five sites in the LV myocardial infarction border zone. The mouse chests were closed in two layers. The ribs (inner layer) were closed with 6-0 coated vicryl sutures (Ethicon) in an interrupted pattern. The skin was closed using 6-0 nylon or silk sutures (Covidien) in a subcuticular manner. The anesthesia was stopped and the mice were allowed to recover for several minutes before the endotracheal tube was removed. The mice received intraperitoneal injections of 2.5 mg kg^{-1} Banamine postsurgery for the alleviation of pain. One mouse in the NID1 + HA treatment group died of arrhythmia after surgery, which lead to the total number of four animals in this group. Two animals from the HA carrier gel group (HA controls) had to be excluded due to incomplete ischemia, giving the final number of three for this group.

Hydrogel Preparation with and Without Supplementation of NID1: All procedures for control and NID1 + HA injections were conducted under sterile conditions. The HA hydrogel was prepared according to the manufacturer's instructions (HyStem) and was further diluted to 2:13. For each mouse, a total of 50 µL HA in PBS ± 50 µg mL^{-1} NID1 was needed; therefore, due to possible residues in the preparation tube or in the syringe, 70 µL were prepared per mouse (HA: PBS ± 50 µg mL^{-1} NID1).

Echocardiography: Conscious echocardiography was conducted on three different time points. A baseline echocardiography measurement was conducted on each mouse prior to the MI/R procedure. In serial nature, further echocardiography measurements were conducted 2 days and 28 days after the MI/R and myocardial injection procedure to track cardiac function. For noninvasive echocardiographic imaging of the conscious mice in vivo, the high-frequency ultrasound imaging system Vevo 2100 (VisualSonics) was applied with the MS400 transducer 18–38 MHz. Myocardial performance was assessed via the Vevo LAB software. The mice were sacrificed after the 28-day echocardiography, and their hearts were explanted for histological and immunofluorescence assessment.

Raman Imaging of Mouse Heart Sections and Pseudoislets: Islets were prepared as previously described.[24] Briefly, hypoxic NID1-treated and control pseudoislets were placed in a microfluidic chip for noninvasive in situ Raman imaging as previously performed.[24,57] Spectral mapping was performed on a customized inverted WITec Raman system (WITec GmbH) equipped with a green laser (532 nm) and a CCD spectrograph with a grating of 600 g mm^{-1}. Images were acquired at a laser power of 50 mW, an integration time per spectrum of 0.5 s, a pixel resolution of 1 × 1 µm and at least as triplicates. Based on Movat staining, representative sections were selected from each heart and deparaffinized. The sections were kept at 4 °C in PBS until measurement. The spectra were collected with a 63× dipping objective (W Plan-apochromat; Carl Zeiss), a laser power of 60 mW and an integration time of 0.05 s (per pixel). In order to locate the scar, an overview image of 1000 × 1700 µm was collected from the apex of the heart with 1 µm image resolution. Within this scan, 3 ROIs of 200 × 200 µm were acquired with a resolution of 0.5 µm.

Multivariate Data Analysis: Raman images were processed and analyzed by TCA using the Project FIVE 5.2 software (WITec GmbH).[23] Briefly, TCA is a non-negative matrix factorization-based MVA tool that elaborates spectral components that predominantly occur in the data set and allows the identification and localization of these components by false color intensity distribution heatmaps. GVI per pixel were determined in ImageJ to semiquantify the distribution of the spectral components in both conditions. Furthermore, TCA allowed the preselection of ROIs of similar spectral information, which were extracted for further in-depth analysis of the molecular composition by PCA using Unscrambler X (Camo). Moreover, MCR analysis was applied to define the local spectral composition within the islet periphery and islet core of the pseudoislets. NID1 core, control core, NID1 periphery and control periphery were defined by the islet area and compared to determine the protective effect of NID1 on the pseudoislets.

hiPSC-Derived Cardiomyocyte Cell Culture: iCell Cardiomyocytes2 (cat: #R1057, Cellular Dynamics) culture was performed according to the manufacturer's specifications. Briefly, 96-well plates were coated with 0.1% porcine gelatin solution for 1 h. hiPSC-CMs were seeded at a density of 2 × 10^4 cells mL^{-1}. At day 9, hiPSC-CMs were treated with 50 µg mL^{-1} NID1 and placed in normoxic or hypoxic conditions for 48 h. At day 9, hiPSC-CMs were treated with 50 µg mL^{-1} NID1, or PBS as control, and placed in normoxic or hypoxic conditions for 48 h. Cells were either fixed in 4% PFA for IF staining, lysed in TRI-Reagent (Sigma-Aldrich) for RNA isolation and qPCR or prepared for DigiWest evaluation. For DigiWest evaluation, the cells were detached using TryplE (Gibco), washed five times on ice and snap frozen in liquid nitrogen.

Fibroblast Cultures: Fibroblasts were isolated from adult skin and myocardial biopsies after informed consent was given (Landesärztekammer Baden-Württemberg, IRB #F-2012-078 and #F-2011-068) as previously reported.[58,59] Fibroblasts were cultured until 90% confluency. Prior to seeding, 3.5 mm dishes (glass bottom µ-Dish, ibidi) were coated with 0.1% porcine gelatin coating (Sigma-Aldrich) for 1 h. 1 × 10^5 cells per dish were seeded in media containing 50 µg mL^{-1} NID1 and placed in normoxic or hypoxic conditions for 48 h. After incubation, cells were either fixed in 4% PFA for IF staining or lysed in TRI-Reagent (Sigma-Aldrich) for RNA isolation and qPCR.

Tube Formation Assay: HUVECs (single donor cells, C2517A, Lonza) were thawed and cultured in EGM-2 medium per manufacturer's instructions (CC-4176, Lonza) at 37 °C and 5% CO_2. One day before the tube formation assay, the cells were equilibrated in low-serum EGM2 medium (0.5% FBS and no other supplements). HUVECs were seeded in a cell density of 1.5 × 10^4 cells/96-well well (1.5 × 10^4 cells/ 0.32 cm^2) in triplicates on serum-reduced Matrigel only, or serum-reduced Matrigel supplemented with 50 µg mL^{-1} NID1. All materials for the coating were precooled and the coating was performed with 75 µL per 0.32 cm^2. Following 75 µL low serum EGM-2 medium, 100 µg mL^{-1} NID1 were added to the respective wells and allowed to equilibrate at 37 °C and 5% CO_2 for 30 min. 75 µL of the cell suspension was added per 96-well and incubated for 2 h. HUVEC tubular structure formation was assessed with a Zeiss Axio Observer Z1 (Carl Zeiss). Quantification of different tube formation parameters was performed using the angiogenesis analyzer of ImageJ Version 1.50 g, which allows for the automated visual recognition of different tube formation parameters.

EndoC-βh3 Cell Culture and Pseudoislet Formation: The conditionally immortalized human pancreatic beta cell line EndoC-ßH3 was cultured per manufacturer's instructions. After 21 days, pseudoislets were formed as previously described.[24] After 48 h in standard culture, pseudoislets were incubated for an additional 72 h under hypoxic (37 °C, 5% CO_2, and 1% O_2) or normoxic (37 °C, 5% CO_2, and 21% O_2) conditions. NID1 was supplemented in the media 72 h after seeding and for an additional 48 h at 20, 30, and 40 µg mL^{-1}. PBS was used as negative control. After 72 h, pseudoislets were either subjected to a glucose-stimulated insulin secretion (GSIS) assay, fixed in 4% PFA (Sigma-Aldrich) for IF staining or prepared for DigiWest evaluation. For DigiWest evaluation, pseudoislets were grouped and washed five times on ice, centrifuged at 700 x *g* and snap frozen in liquid nitrogen.

Pseudoislet Size Tracking: A minimum of 10 pseudoislets were imaged every 24 h with a brightfield microscope (Carl Zeiss). Images were further processed with the ImageJ software, version 1.52p, where the average area was evaluated and subsequent average diameter calculated.

GSIS Assays: Prior to all GSIS assays, pseudoislets were incubated with NID1- or PBS- OPTIβ2 (Univercell Biosolutions) medium for 24 h in normoxic or hypoxic condition. GSIS assays were performed after 5 days as previously described, except otherwise mentioned.[23,60] Pseudoislets were grouped by 6 to 8 per well and washed twice with β-Krebs (Univercell Biosolutions) and 1% BSA (Thermo Fisher Scientific). Pseudoislets were preincubated for 1 h with Krebs-BSA and the supernatant was discarded. 20 × 10^{-3} M glucose (Thermo Fisher Scientific) solution was prepared in Krebs-BSA, and pseudoislets were incubated with either Krebs-BSA or 20 × 10^{-3} M glucose solution for 1 h. The supernatant was collected and stored at −20 °C. An ultrasensitive insulin ELISA (Mercodia) was performed and the GSIS index was calculated by dividing the amount of secreted insulin during high glucose treatment by the amount of secreted insulin during basal state.

NID1 Cytotoxicity Test: A standardized cytotoxicity test according to EN ISO 10993 was performed using primary isolated human dermal fibroblasts (IRB #F-2012-078). An additional cytotoxicity test was performed utilizing primary isolated human cardiac fibroblasts (IRB #F-2011-068). 2 × 10^4 cells were seeded per 96-well well. In parallel, sterile solutions containing 50, 100, and 200 µg mL^{-1} NID1 were prepared in Dulbecco's modified Eagle medium (DMEM, Life Technologies). After 24 h, 200 µL of the NID1 solution was pipetted into each well and incubated for another 24 h. The cytotoxic substance SDS, which induces cell death, served as the positive control, and DMEM was used as the negative control. After incubation, the medium was removed and an MTS assay was performed. The cells of each well were incubated with a solution of 20 µL MTS (CellTiter 96 AQueous One Solution Cell Proliferation Assay, Promega) mixed with 100 µL DMEM. The absorbance was measured at 492 nm (Infinite 200 PRO, Tecan) after 45 min and the percentage of viable cells was calculated relative to the negative control, which was set to 100%. In all samples, cell numbers were counted.

Isolation of Human Immune Cells: Peripheral blood mononuclear cells (PBMCs) were isolated from buffy coats (DRK, Berlin, Germany, IRB #EA/226/14) as previously described.[61] Briefly, blood was diluted (1:2) with PBS (Biochrom, Germany), layered on Biocoll Separation Solution (Biochrom) and centrifuged for 30 min at 800 x *g* at room temperature. PBMCs were isolated and washed three times with PBS. PBMCs were used to isolate $CD14^+$ monocytic cells by CD14 MicroBeads (Miltenyi Biotec) according to manufacturer's instructions with MACS separation columns (Miltenyi Biotec). Labeling with CD14 PerCP/Cy5.5 (BioLegend) confirmed a purity of 95–98%.

Cultures of Human Macrophages with NID1: 1×10^6 monocytes per well or 7×10^5 M0-macrophages per well were seeded in 24-well culture plates and were treated with NID1 at 50 µg mL^{-1} in VLE-RPMI (Biochrom) containing 10% AB-Serum (Sigma-Aldrich) 1% penicillin/streptomycin (Life Technologies) and 1% glutamine (Life Technologies) at 37 °C in a 5% CO2 incubator for 7 days or 24 h, respectively. Monocytes (2×10^6 mL^{-1}) were differentiated into M0-type macrophages for 7 days in 6-well culture plates using 50 ng mL^{-1} M-CSF (Miltenyi Biotec) in complete VLE-RPMI. M0-type macrophages were polarized for 24 h either toward M1 macrophages by adding 20 ng mL^{-1} IFN-γ (Miltenyi Biotec) and 100 ng mL^{-1} LPS from *E. coli* O127:B4 (Sigma-Aldrich) or into M2 macrophages by adding 20 ng mL^{-1} IL-4 (Miltenyi Biotec) according to the recently described method.[54] Representative images were obtained using a bright-field microscope (Carl Zeiss).

Macrophage Flow Cytometry Analyses: As described above, macrophages were harvested using 1% (v/v) trypsin/EDTA (Life Technologies), washed with PBS and labeled with a master mix of fluorophore-labeled human-specific antibodies CD163-FITC, CD80-PE, HLA-DR-PE/Cy7, CD206-APC (all BioLegend), CD14-APC/Cy7 (BD Biosciences), and a Live/Dead violet fixable staining kit (Molecular Probes).[54,61] Samples were measured with FACS Canto II (BD Biosciences) and analyzed using FlowJo Version 8.8.6 (TreeStar Inc.). Surface marker expression levels were normalized to the unstimulated controls (set as 1).

Immune Cell Proliferation Assay: Modulation of NID1-treated T cell subset proliferation was analyzed with a CFSE-based proliferation assay as described previously.[24] Briefly, 96-well culture plates were coated with 0.05 µg mL^{-1} anti-CD3 antibody (OKT3, Janssen-Cillag) overnight at 4 °C. Wells were washed three times with PBS, coated with 50 µg mL^{-1} NID1 for 6 h at room temperature and washed again with PBS. Isolated PBMCs were labeled with 2.5×10^{-6} M 5.6-CFDA-SE and seeded at a cell density of 3×10^5 cells per well in complete VLE-RPMI in wells coated with anti-CD3 and NID1, anti-CD3 alone (positive control) or they were used uncoated (unstimulated control). After 5 days of culture at 37 °C and 5% CO_2, PBMCs were harvested and labeled with human-specific antibodies CD8-PE and CD4-APC (both Miltenyi Biotec) as well as CD3-APC/Cy7 (BioLegend) and Live/Dead violet fixable staining kit. Samples were processed using a FACS Canto II and data were analyzed using FlowJo Version 8.8.6. MFI of all markers were normalized to the anti-CD3 control MFI level (set to 1).

Cytokine Detection Assays: Supernatants of NID1-treated macrophage cultures (24 h or 5 days) and NID1-treated PBMC proliferation assays (5 days) were collected for detection of released cytokines IFNγ, TNFα, IL-6, and IL-10 using ELISA kits (BioLegend) according to the manufacturer's instructions. Samples were measured on a Micro-plate reader (Bio-Rad).

Monocyte Chemotaxis Assay: To analyze chemotaxis, a specific 96-well cell migration system (Neuro Probe) was applied as previously described.[54] Briefly, the chemotactic stimulus was added in a volume of 37.5 µL per well. A membrane filter with 5 µm pores was placed onto the plate. 3×10^4 cells in 40 µL diet medium consisting of VLE-RPMI (Biochrom) and 0.1% autologous serum were added on the membrane. Chemotaxis was induced by 50 or 100 µg mL^{-1} NID1 or without stimulus (negative control). MCP-1 (50 ng mL^{-1}, Miltenyi Biotec) served as positive control. After incubation for 3 h at 37 °C in a 5% CO_2 incubator, the membrane was carefully removed. Monocytes that adhered to the membrane were fixed with methanol (Merck) and labeled with Hemacolor staining kit (Merck). After microscopic documentation using ProgRes CapturePro 2.8.8 (Jenoptik), the number of migrated monocytes was determined using ImageJ Version 1.4.3.67 (National Institutes of Health). The number of migrated cells was normalized to the negative control.

Endotoxin Test: $CD14^+$ monocytes (1×10^6) were incubated alone (negative control), with 100 ng mL^{-1} LPS O127:B4 (Sigma-Aldrich, positive control) or with 50 µg mL^{-1} NID1 in 24-well plates in 1 mL^{-1} of VLE-RPMI (Biochrom). After 24 h, the supernatant was collected and tested for TNFα by ELISA (BioLegend). In addition, a Pierce Chromogenic LAL Endotoxin quantification kit (Thermo Fisher Scientific) was employed according to the manufacturer's instructions.

Integrin Binding Assays: Binding assays were performed as previously described.[62] Microtiter plates (Costar Half Area plate) were coated overnight at 4 °C with 50 µLper well and 4 µg mL^{-1} $\alpha v\beta 3$ (R&D Systems) in TBS containing 2×10^{-3} M $MgCl_2$ or TBS with 2×10^{-3} M $MgCl_2$ and 1×10^{-3} M $CaCl_2$, respectively. Plates were washed twice with the respective buffers. Blocking of nonspecific binding was performed for 1 h at room temperature with 1% BSA/TBS/$MgCl_2$ or 1% BSA/TBS/ $MgCl_2$/$CaCl_2$. Serial dilutions of NID1 were prepared on ice. For $\alpha v\beta 3$, NID1 serial dilutions were prepared in 1% BSA/TBS/$MgCl_2$ and 1×10^{-3} M $MnCl_2$, or in 1% BSA/TBS/$MgCl_2$ and 10×10^{-3} M EDTA-buffer for nonspecific binding. Reaction was stopped using 1.5 M NaOH solution. OD determination was performed at 405 nm. Three independent experiments were performed, each of them with duplicates.

Blocking of Integrin $\alpha v\beta 3$: Mouse IgG (Vector Laboratories) and $\alpha v\beta 3$ (Novus Biologicals) were used at a concentration of 10 µg mL^{-1} in PBS. Pseudoislets at 48 h and CMs at 9 days, respectively, were washed twice with PBS and incubated with the blocking antibody or control for 1 h under standard culture conditions. Pseudoislets and CMs were washed twice with PBS. The respective NID1-treated culture media or control were added to the pseudoislet or CM culture. Pseudoislets were culture for an additional 72 h and CMs for an additional 48 h before evaluation via IF staining or GSIS assay, respectively.

DigiWest: DigiWest assays (NMI Reutlingen, Germany) were performed as recently described.[30] Briefly, gel electrophoresis and blotting onto PVDF membranes was performed using the NuPAGE system as recommended by the manufacturer (Life Technologies, Carlsbad, CA, USA). Blots were washed in PBST, proteins were biotinylated on the membranes using NHS-PEG12-Biotin (50×10^{-6} M) in PBST for 1 h followed by washing in PBST and drying. Individual sample lanes were cut into 96 molecular weight fractions (0.5 mm each) and proteins were eluted in 96-well plates using 10 µL elution buffer per well (8 M urea, 1% Triton-X100 in 100×10^{-3} M Tris-HCl pH 9.5). Eluted proteins from each molecular weight fraction were loaded onto color-coded, neutravidin coated Luminex bead sets (MagPlex, Luminex, Austin, TX, USA). 384 Luminex bead sets were employed and the protein loaded beads from four different sample lanes were pooled into one bead-mix resulting in 6 bead mixes for the 24 samples. The bead-mixes were sufficient for 100 antibody incubations (see Extended Data in Table S5, Supporting Information). Aliquots of the DigiWest bead-mixes (1/100th per well) were added to 96-well plates containing 50 µL per well assay buffer (Blocking Reagent for ELISA supplemented with 0.2% milk powder, 0.05% Tween-20, and 0.02% sodium azide, Roche). Beads were briefly incubated in assay buffer and the buffer was discarded. Antibodies were diluted in an assay buffer and 30 µL were added per well. After overnight incubation at 15 °C on a shaker, the bead-mixes were washed twice with PBST and PE-labeled (Phycoerythrin) secondary antibodies (Dianova) were added and incubated for 1 h at 23 °C. Beads were washed twice prior to readout on a Luminex FlexMAP 3D. Secondary antibodies were either diluted in an assay buffer or in a polymer buffer (Blocking Reagent for ELISA supplemented with 4% PVP 360.000, 1% milk powder, 0.05% Tween-20, and 0.02% sodium azide, Roche). For quantification of the antibody specific signals the DigiWest analysis tool (version 3.8.6.1, Excel-based) was employed. This tool uses the 96 values for each initial lane obtained from the Luminex measurements on the 96 molecular weight fractions, identifies the peaks at the appropriate molecular weight, calculates a baseline using the local background and integrates the peaks. The values are based on relative fluorescence (accumulated fluorescence intensity). For analysis, data (measured signal intensity) was normalized to the total protein amount corresponding to the sample, median centered

and $\log_2$-transformed. The software package MEV 4.8.1 was used for data visualization, clustering, and nonparametric statistical analysis.

Statistical Analysis: The relevant statistical tests, sample sizes, replicate types, and *p*-values are described in the corresponding figures and tables of the Supporting Information. Each *n* represents a distinct sample. Statistical tests were two-sided if not mentioned otherwise. Data are presented as mean ± SD and as dot plots every time possible. All data sets were tested for normality. Statistical analysis was performed using Prism, version 6.07 (GraphPad Software). Statistical significance was defined at $p < 0.05$.

Supporting Information

Supporting Information is available from the Wiley Online Library or from the author.

Acknowledgements

The authors thank the flow cytometry core facility of the BCRT and Simone Pöschel from the ImageStream Core Facility at the University Tübingen for support with the cell analyses, Kristin Fröhlich for her help with the chemotaxis assays, and Maria Schneider for performing the LAL test (both BCRT), Yan Lu (UCLA, CVRL) for her support with the MI/R experiments, as well as Mariella Bosch, Madeleine Waltner, Svenja Hinderer, Peter Loskill, Germano Piccirillo (all University Tübingen), and Nam Che (UCLA, CVRL) for their technical support and scientific input. The authors thank Frank Zaucke (University Frankfurt) for providing the NID1 and NID2 antibodies. This work was financially supported by the European Union (H2020-NMP10-2014-645991-2, DRIVE, and FP7 NMP3-SME-2013-604531, AMCARE, to K.S.-L. and G.P.D.), CIRM (RB3-05086 to A.N.), the BMBF (0316059 to K.S.-L., 1315848A to M.S.), Boehringer Ingelheim Fonds (to M.Z.), the International Foundation for Ethical Research (to A.Z.), the Ministry of Science, Research and the Arts of Baden-Württemberg (33-729.55-3/214 and SI-BW 01222–91 to K.S.-L.) and the Deutsche Forschungsgemeinschaft (SCHE701/14-1, INST 2388/33-1 and Germany's Excellence Strategy-EXC 2180 to K.S.-L; SFB1009 A09 to J.A.E.).

Open access funding enabled and organized by Projekt DEAL.

Conflict of Interest

A.Z., S.L.L., G.P.D., and K.S.-L. are inventors on patent application EP19154849.4 associated with this work and owned by the University Tübingen. S.L.L., M.Z., and K.S.-L. are inventors on patents (EP3027201B1 and CN105517564A), and patent applications (US20160158314A1, CA2916614A1, JP2016530532A, and KR20160037170A) associated with this work and owned by the NMI, Reutlingen.

Author Contributions

A.Z. and S.L.L. contributed equally to this work. A.Z., S.L.L., M.U., M.Z., H.K.A.M., A.N., M.S., and K.S.-L. designed the experiments and wrote the manuscript. A.Z., S.L.L., M.U., D.A.C.B., J.M., M.Z., A.H., E.B., K.S., S.F., M.T., S.L., J.A.E., and M.S. performed experiments, collected and analyzed data. G.M.C., A.D., G.P.D., and G.K. provided reagents and gave conceptual advice.

Keywords

diabetes, ischemia, myocardial infarction, nidogen-1, pancreatic β-cells

Received: July 2, 2020
Revised: October 25, 2020
Published online:

[1] H. K. Eltzschig, T. Eckle, *Nat. Med.* **2011**, *17*, 1391.
[2] T. Su, K. Huang, H. Ma, H. Liang, P.-U. Dinh, J. Chen, D. Shen, T. A. Allen, L. Qiao, Z. Li, S. Hu, J. Cores, B. N. Frame, A. T. Young, Q. Yin, J. Liu, L. Qian, T. G. Caranasos, Y. Brudno, F. S. Ligler, K. Cheng, *Adv. Funct. Mater.* **2019**, *29*, 1803567.
[3] M. Kapnisi, C. Mansfield, C. Marijon, A. G. Guex, F. Perbellini, I. Bardi, E. J. Humphrey, J. L. Puetzer, D. Mawad, D. C. Koutsogeorgis, D. J. Stuckey, C. M. Terracciano, S. E. Harding, M. M. Stevens, *Adv. Funct. Mater.* **2018**, *28*, 1800618.
[4] S. B. Seif-Naraghi, J. M. Singelyn, M. A. Salvatore, K. G. Osborn, J. J. Wang, U. Sampat, O. L. Kwan, G. M. Strachan, J. Wong, P. J. Schup-Magoffin, R. L. Braden, K. Bartels, J. A. DeQuach, M. Preul, A. M. Kinsey, A. N. DeMaria, N. Dib, K. L. Christman, *Sci. Transl. Med.* **2013**, *5*, 173ra25.
[5] C. Frantz, K. M. Stewart, V. M. Weaver, *J. Cell Sci.* **2010**, *123*, 4195.
[6] T. A. Wynn, T. R. Ramalingam, *Nat. Med.* **2012**, *18*, 1028.
[7] S. F. Badylak, *Nat. Rev. Urol.* **2019**, *16*, 389.
[8] R. Jayadev, D. R. Sherwood, *Curr. Biol.* **2017**, *27*, R207.
[9] A. Kumar, J. K. Placone, A. J. Engler, *Development* **2017**, *144*, 4261.
[10] K. Schenke-Layland, A. Nsair, B. Van Handel, E. Angelis, J. M. Gluck, M. Votteler, J. I. Goldhaber, H. K. Mikkola, M. Kahn, W. R. MacLellan, *Biomaterials* **2011**, *32*, 2748.
[11] D. Evseenko, K. Schenke-Layland, G. Dravid, Y. Zhu, Q. L. Hao, J. Scholes, X. C. Wang, W. R. MacLellan, G. M. Crooks, *Stem Cells Dev.* **2009**, *18*, 919
[12] C. Bonnans, J. Chou, Z. Werb, *Nat. Rev. Mol. Cell Biol.* **2014**, *15*, 786.
[13] B. Carlin, R. Jaffe, B. Bender, A. E. Chung, *J. Biol. Chem.* **1981**, *256*, 5209.
[14] Q. Zhou, D. A. Melton, *Nature* **2018**, *557*, 351.
[15] L. Yang, M. H. Soonpaa, E. D. Adler, T. K. Roepke, S. J. Kattman, M. Kennedy, E. Henckaerts, K. Bonham, G. W. Abbott, R. M. Linden, L. J. Field, G. M. Keller, *Nature* **2008**, *453*, 524.
[16] E. Willems, S. Spiering, H. Davidovics, M. Lanier, Z. Xia, M. Dawson, J. Cashman, M. Mercola, *Circ. Res.* **2011**, *109*, 360.
[17] F. Monte, R. J. Hajjar, Y. Chang, D. Lebeche, S. Arab, M. T. Keating, *Nature* **2007**, *13*, 962.
[18] K. Schenke-Layland, K. E. Rhodes, E. Angelis, Y. Butylkova, S. Heydarkhan-Hagvall, C. Gekas, R. Zhang, J. I. Goldhaber, H. K. Mikkola, K. Plath, W. R. MacLellan, *Stem Cells* **2008**, *26*, 1537.
[19] J. Duan, C. Gherghe, D. Liu, E. Hamlett, L. Srikantha, L. Rodgers, J. N. Regan, M. Rojas, M. Willis, A. Leask, M. Majesky, A. Deb, *EMBO J.* **2012**, *31*, 429.
[20] A. I. Mahmoud, C. C. O'Meara, M. Gemberling, L. Zhao, D. M. Bryant, R. Zheng, J. B. Gannon, L. Cai, W.-Y. Choi, G. F. Egnaczyk, C. E. Burns, C. G. Burns, C. A. MacRae, K. D. Poss, R. T. Lee, *Dev. Cell* **2015**, *34*, 387.
[21] M. G. Monaghan, M. Holeiter, E. Brauchle, S. L. Layland, Y. Lu, A. Deb, A. Pandit, A. Nsair, K. Schenke-Layland, *Tissue Eng., Part A* **2017**, *24*, 57.
[22] N. G. Frangogiannis, *J. Clin. Invest.* **2017**, *127*, 1600.
[23] A. Zbinden, J. Marzi, K. Schlünder, C. Probst, M. Urbanczyk, S. Black, E. M. Brauchle, S. L. Layland, U. Kraushaar, G. Duffy, K. Schenke-Layland, P. Loskill, *Matrix Biol.* **2020**, *85–86*, 205.
[24] S. Hinderer, M. Schesny, A. Bayrak, B. Ibold, M. Hampel, T. Walles, U. A. Stock, M. Seifert, K. Schenke-Layland, *Biomaterials* **2012**, *33*, 5259.
[25] U. Hofmann, S. Frantz, *Eur. Hear. J.* **2016**, *37*, 873.
[26] X.-Y. Yi, E. A. Wayner, Y. Kim, A. J. Fish, *Cell Adhes. Commun.* **1998**, *5*, 237.
[27] K. Y. Peng, Y. H. Liu, Y. W. Li, B. L. Yen, M. L. Yen, *J. Cell. Mol. Med.* **2017**, *21*, 1572.
[28] M. Riopel, W. Stuart, R. Wang, *Acta Biomater.* **2013**, *9*, 8140.

[29] F. Treindl, B. Ruprecht, Y. Beiter, S. Schultz, A. Döttinger, A. Staebler, T. O. Joos, S. Kling, O. Poetz, T. Fehm, H. Neubauer, B. Kuster, M. F. Templin, *Nat. Commun.* **2016**, *7*, 12852.
[30] J. Misao, Y. Hayakawa, M. Ohno, S. Kato, T. Fujiwara, H. Fujiwara, *Circulation* **1996**, *94*, 1506.
[31] Z. Xia, M. Dickens, J. Raingeaud, R. J. Davis, M. E. Greenberg, *Science* **1995**, *270*, 1326.
[32] J. W. Fox, U. Mayer, R. Nischt, M. Aumailley, D. Reinhardt, H. Wiedemann, K. Mann, R. Timpl, T. Krieg, J. Engel, *EMBO J.* **1991**, *10*, 3137.
[33] R. F. Nicosia, E. Bonanno, M. Smith, P. Yurchenco, *Dev. Biol.* **1994**, *164*, 197.
[34] A. Martinez-Hernandez, P. S. Amenta, *FASEB J.* **1995**, *9*, 1401.
[35] H. K. Lee, I. A. Seo, D. J. Suh, H. T. Park, *J. Korean Med. Sci.* **2009**, *24*, 654.
[36] G. Wolfstetter, I. Dahlitz, K. Pfeifer, U. Töpfer, J. A. Alt, D. C. Pfeifer, R. Lakes-Harlan, S. Baumgartner, R. H. Palmer, A. Holz, *Development* **2019**, *146*, 168948.
[37] M. Bechtel, M. V. Keller, W. Bloch, T. Sasaki, P. Boukamp, F. Zaucke, M. Paulsson, R. Nischt, *FASEB J.* **2012**, *26*, 3637.
[38] M. Montgomery, S. Ahadian, L. Davenport Huyer, M. Lo Rito, R. A. Civitarese, R. D. Vanderlaan, J. Wu, L. A. Reis, A. Momen, S. Akbari, A. Pahnke, R.-K. Li, C. A. Caldarone, M. Radisic, *Nat. Mater.* **2017**, *16*, 1038.
[39] E. Bassat, Y. E. Mutlak, A. Genzelinakh, I. Y. Shadrin, K. Baruch Umansky, O. Yifa, D. Kain, D. Rajchman, J. Leach, D. Riabov Bassat, Y. Udi, R. Sarig, I. Sagi, J. F. Martin, N. Bursac, S. Cohen, E. Tzahor, *Nature* **2017**, *547*, 179.
[40] G. G. Nair, J. S. Liu, H. A. Russ, S. Tran, M. S. Saxton, R. Chen, C. Juang, M. lan Li, V. Q. Nguyen, S. Giacometti, S. Puri, Y. Xing, Y. Wang, G. L. Szot, J. Oberholzer, A. Bhushan, M. Hebrok, *Nat. Cell Biol.* **2019**, *21*, 263.
[41] S. R. Adderley, D. J. Fitzgerald, *J. Biol. Chem.* **1999**, *274*, 5038.
[42] M. A. Kalwat, D. C. Thurmond, *Exp. Mol. Med.* **2013**, *45*, 37.
[43] J. Wang, S. Liu, T. Heallen, J. F. Martin, *Nat. Rev. Cardiol.* **2018**, *15*, 672.
[44] C. Rallis, S. M. Pinchin, D. Ish-Horowicz, *Development* **2010**, *137*, 3591.
[45] H. J. Welters, R. N. Kulkarni, *Trends Endocrinol. Metab.* **2008**, *19*, 349.
[46] J. Golledge, P. Clancy, J. Maguire, L. Lincz, S. Koblar, *Cardiovasc. Res.* **2011**, *92*, 19.
[47] K. Imanaka-Yoshida, *Circ. J.* **2012**, *76*, 2513.
[48] N. G. Frangogiannis, *J. Thorac. Dis.* **2017**, *9*, S52.
[49] K. L. Spiller, T. J. Koh, *Adv. Drug Delivery Rev.* **2017**, *122*, 74.
[50] S. Gaggero, M. Bruschi, A. Petretto, M. Parodi, G. Del Zotto, C. Lavarello, C. Prato, L. Santucci, A. Barbuto, C. Bottino, G. Candiano, A. Moretta, M. Vitale, L. Moretta, C. Cantoni, *Oncoimmunology* **2018**, *7*, 1470730.
[51] F. C. Simões, T. J. Cahill, A. Kenyon, D. Gavriouchkina, J. M. Vieira, X. Sun, D. Pezzolla, C. Ravaud, E. Masmanian, M. Weinberger, S. Mayes, M. E. Lemieux, D. N. Barnette, M. Gunadasa-Rohling, R. M. Williams, D. R. Greaves, L. A. Trinh, S. E. Fraser, S. L. Dallas, R. P. Choudhury, T. Sauka-Spengler, P. R. Riley, *Nat. Commun.* **2020**, *11*, 600.
[52] M. Votteler, D. A. Carvajal Berrio, A. Horke, L. Sabatier, D. P. Reinhardt, A. Nsair, E. Aikawa, K. Schenke-Layland, *Development* **2012**, *140*, 2345.
[53] A. Zbinden, M. Urbanczyk, S. L. Layland, L. Becker, J. Marzi, M. Bosch, P. Loskill, G. Duffy, K. Schenke-Layland, *Tissue Eng., Part A* **2020**.
[54] S. Hinderer, K. Sudrow, M. Schneider, M. Holeiter, S. L. Layland, M. Seifert, K. Schenke-Layland, *Sci. Rep.* **2018**, *8*, 110.
[55] S. Puch, S. Armeanu, C. Kibler, K. R. Johnson, C. A. Müller, M. J. Wheelock, G. Klein, *J. Cell Sci.* **2001**, *114*, 1567.
[56] N. Shen, A. Knopf, C. Westendorf, U. Kraushaar, J. Riedl, H. Bauer, S. Pöschel, S. L. Layland, M. Holeiter, S. Knolle, E. Brauchle, A. Nsair, S. Hinderer, K. Schenke-Layland, *Stem Cell Rep.* **2017**, *9*, 122.
[57] A. Zbinden, D. A. Carvajal Berrio, M. Urbanczyk, S. L. Layland, M. Bosch, S. Fliri, C. Lu, A. Jeyagaran, P. Loskill, G. P. Duffy, K. Schenke-Layland, *J. Biophotonics* **2020**.
[58] G. Piccirillo, M. V. Ditaranto, N. F. S. Feuerer, D. A. Carvajal Berrio, E. M. Brauchle, A. Pepe, B. Bochicchio, K. Schenke-Layland, S. Hinderer, *J. Mater. Chem. B* **2018**, *6*, 6399.
[59] E. Brauchle, H. Johannsen, S. Nolan, S. Thude, K. Schenke-Layland, *Biomaterials* **2013**, *34*, 7401.
[60] M. Urbanczyk, A. Zbinden, S. L. Layland, G. Duffy, K. Schenke-Layland, *Tissue Eng., Part A* **2019**, *26*, 387.
[61] M. Stolk, F. Klatte-Schulz, A. Schmock, S. Minkwitz, B. Wildemann, M. Seifert, *Sci. Rep.* **2017**, *7*, 9801.
[62] J. A. Eble, K. W. Wucherpfennig, L. Gauthier, P. Dersch, E. Krukonis, R. R. Isberg, M. E. Hemler, *Biochemistry* **1998**, *37*, 10945.

WILEY-VCH

ADVANCED SCIENCE
Open Access

Supporting Information

for *Adv. Sci.*, DOI: 10.1002/advs.202002500

Nidogen-1 Mitigates Ischemia and Promotes Tissue Survival and Regeneration

*Aline Zbinden, Shannon L. Layland, Max Urbanczyk, Daniel A. Carvajal Berrio, Julia Marzi, Monika Zauner, Anne Hammerschmidt, Eva M. Brauchle, Katrin Sudrow, Simon Fink, Markus Templin, Simone Liebscher, Gerd Klein, Arjun Deb, Garry P. Duffy, Gay M. Crooks, Johannes A. Eble, Hanna K. A. Mikkola, Ali Nsair, Martina Seifert, and Katja Schenke-Layland**

Supporting Information

Nidogen-1 Mitigates Ischemia and Promotes Tissue Survival and Regeneration

Authors

*Aline Zbinden[1], Shannon L. Layland[1], Max Urbanczyk[1], Daniel A. Carvajal Berrio[1,2], Julia Marzi[1,3], Monika Zauner[1], Anne Hammerschmidt[1], Eva M. Brauchle[1,2,3], Katrin Sudrow[4,5], Simon Fink[3], Markus Templin[3], Simone Liebscher[1], Gerd Klein[6], Arjun Deb[7,8,9,10,11], Garry P. Duffy[12], Gay M. Crooks[8,10,13], Johannes A. Eble[14], Hanna K. A. Mikkola[7,8,9,10], Ali Nsair[8,11], Martina Seifert[4,5] and Katja Schenke-Layland[1,2,3,11]**

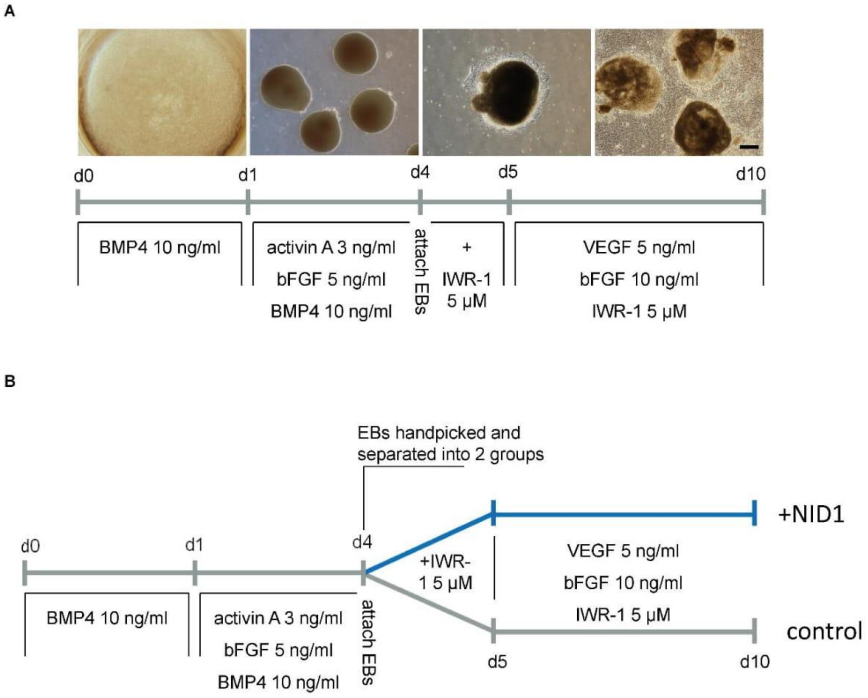

Figure S1. Schematic illustration of the modified cardiovascular differentiation protocol. EBs were derived from hESCs (line H9). **(A)** The differentiation protocol timeline is shown together with the stage-specific additives to the medium. Scale bar equals 100 µm. **(B)** The differentiation protocol using NID1 from day 4 (d4) and control are shown together with the stage-specific additives in the medium.

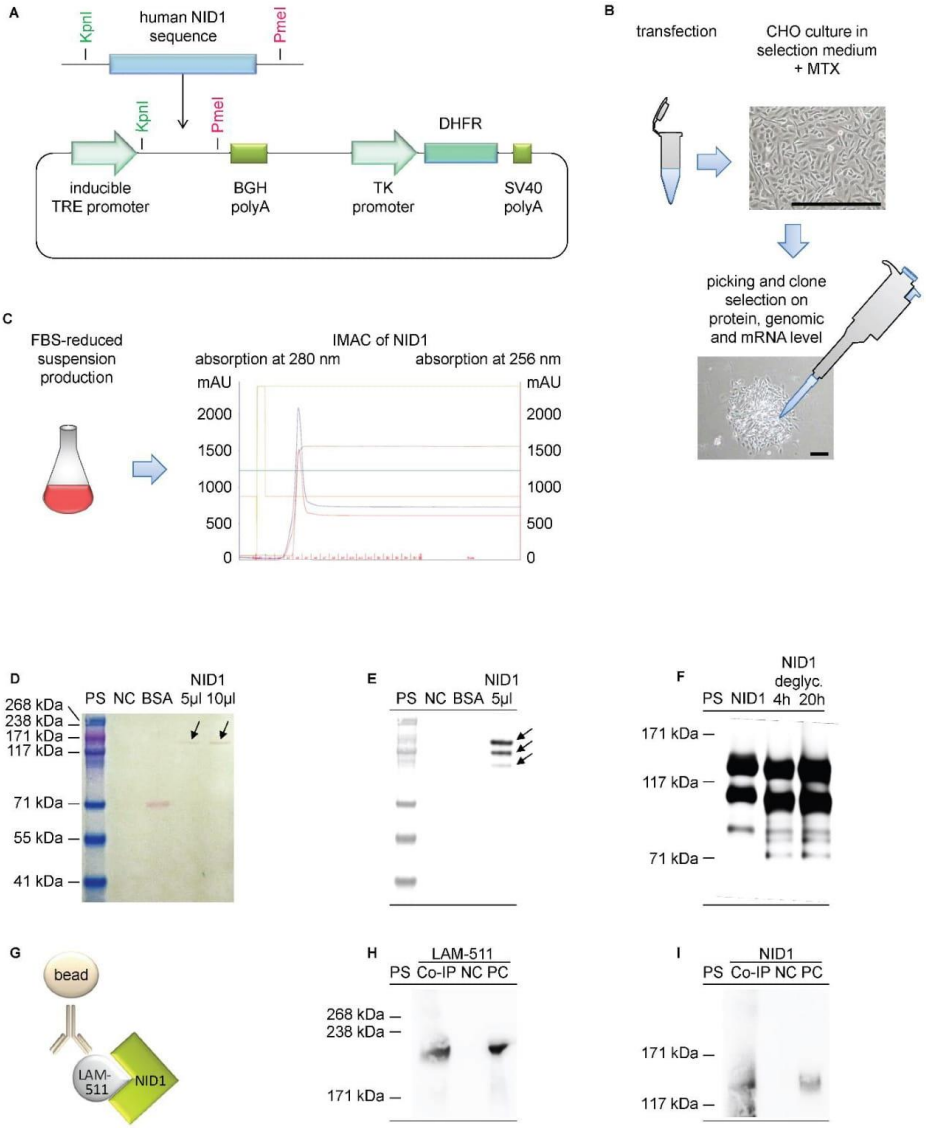

Figure S2. Recombinant NID1 production and characterization. **(A)** Schematic representation of NID1 production plasmid generation with main components for genomic amplification strategy. **(B)** Schematic depiction of CHO culture transfection with the NID1 production plasmid, MTX selection and clone analysis. Scale bars equal 200 µm. **(C)** Schematic depiction of production clone adaptation to FBS-reduced suspension culture and purification of secreted NID1 using immobilized-metal affinity chromatography (IMAC). Characteristic protein absorption is shown at 280 nm (blue line) and 256 nm (red line) in milli absorption unit (mAU). **(D)** Ponceau-Red staining of a nitrocellulose membrane with IMAC eluates: negative control (NC, 10 µl IMAC eluate of media with 1% FBS, dialyzed), BSA (10 µl IMAC eluate of media with 1% BSA) and 5

or 10 µl IMAC eluate of NID1-containing cell culture media with originally 0.5% FBS, dialyzed. **(E)** Same membrane after discoloring and specific immunodetection of NID1. Arrows indicate 3 NID1 bands at about 140 kDa, 110 kDa and 90 kDa. **(F)** Specific immunodetection of NID1 deglycosylated for 4 hours and for 20 hours shows a shift of the characteristic NID1 bands to lower molecular weight compared to a NID1 control that was not treated with the deglycosylation enzyme, proving the glycosylated state of the recombinant NID1. **(G)** Schematic of Co-IP between interaction partners NID1 and LAM-511. **(H)** Specific immunodetection of the ß1 and ɣ1 chain of LAM-511 in Co-IP, NC (Co-IP w/o LAM antibody) and positive control (PC, LAM-511). **(I)** Specific immunodetection of NID1 in Co-IP, NC (Co-IP w/o LAM antibody) and PC (NID1). The HiMark pre-stained protein standard (PS) was used in all blots.

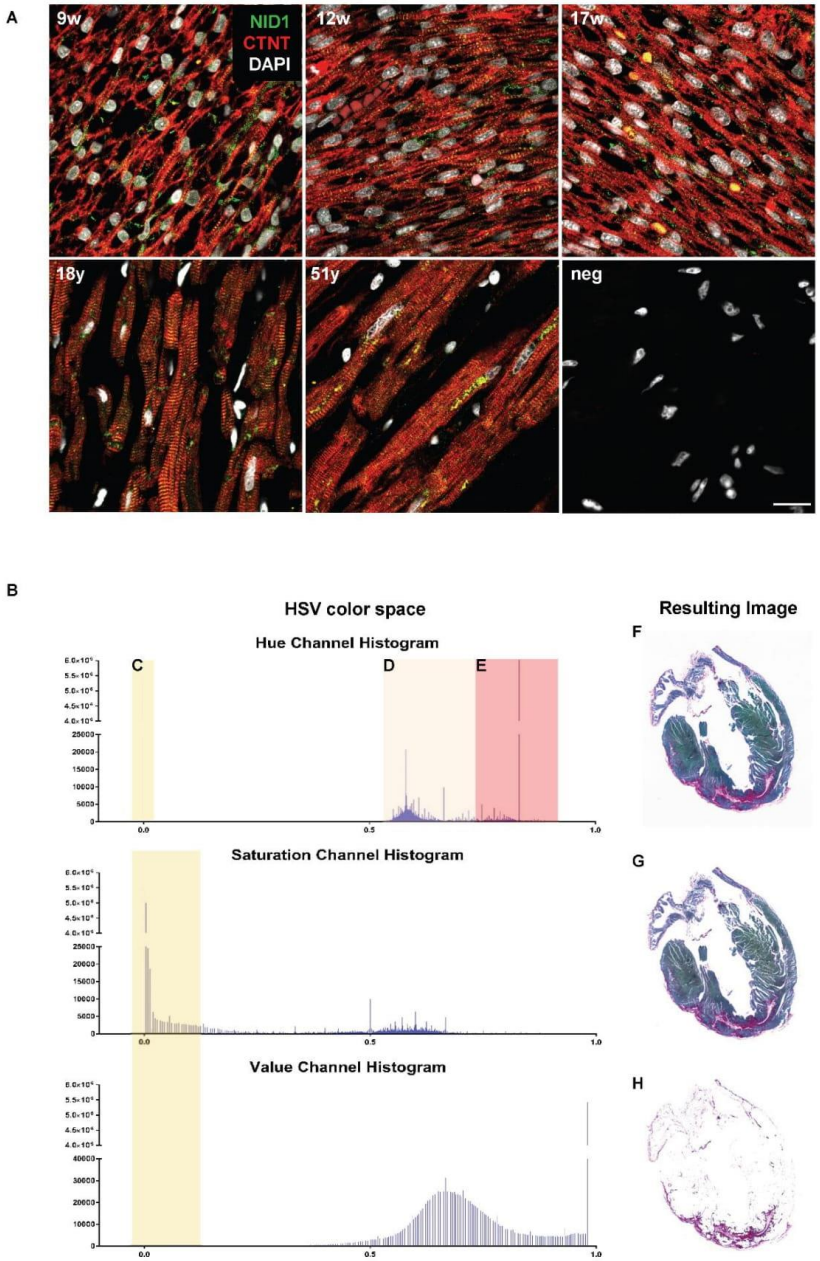

Figure S3. Identification of NID1 as crucial ECM protein in fetal and adult hearts by IF staining & Myocardial scar quantification. (A) NID1 (green) was detected in fetal heart sections 9, 12 and 17 weeks post-fertilization as well as in sections of 18 and 51 year old adult heart tissue. CTNT (red) was used to detect CMs. Cell nuclei were visualized with DAPI (white).

Scale bar equals 20 μm. **(B-H)** HSV color segmentation was performed using a customized MATLAB code. The HSV histogram bands responsible for the background are shown in **(C)**, the Fast Green-positive region labeling the myocardium is shown in **(D)** and, the Picrosirius Red-stained areas corresponding to the scar content are shown in **(E)**. By subtracting band **(C)** from an image of Picrosirius Red and Fast Green **(F)**, an image without background is generated **(G)** and, comparably, the removal of bands **(C)** and **(D)** yields an image of only the scar component **(H)**.

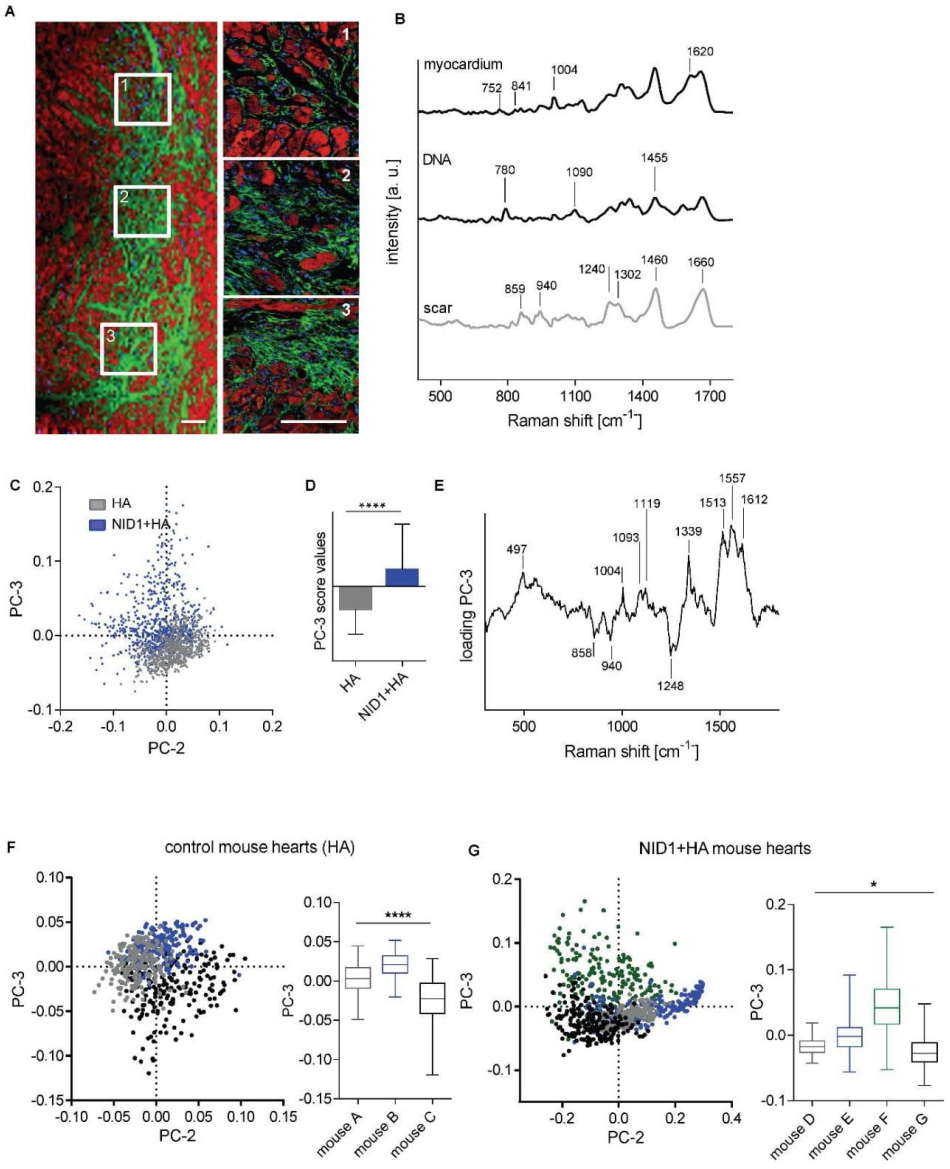

Figure S4. Raman imaging and multivariate analysis of infarcted mouse hearts and single animals. (A) Representative overview of Raman images showing DNA (blue), myocardium (red) and the scar (green). Three regions within the scar area (rectangular boxes: 1-3) were selected for high-resolution Raman images. **(B)** Spectra-associated to the color-coding shown in **(A)**. Based on the signal patterns, the specific ECM composition for the scar area was detected. Scale bar equals 100 µm**. (C,D)** PCA of Raman spectra revealed molecular and structural differences in the scar area of NID1+HA and control hearts. PC score values of spectra from NID1+HA and control

hearts were significantly different, unpaired t-test. **(E)** The loading plot displays typical porphyrin vibrations (1513, 1557, 1612 cm^{-1}) seen in the NID1+HA heart tissue. Collagen peaks (858 and 1248 cm^{-1}) were assigned to the control hearts. PCA of TCA scar component of **(F)** control (HA) and **(G)** NID1+HA mouse hearts. Significant differences between animals are detected in both groups. Kruskal-Wallis test with Dunn's multiple comparisons test. Results are shown as standard box plot diagram. *p<0.05, **p<0.01, ***p<0.001 and ****p<0.0001.

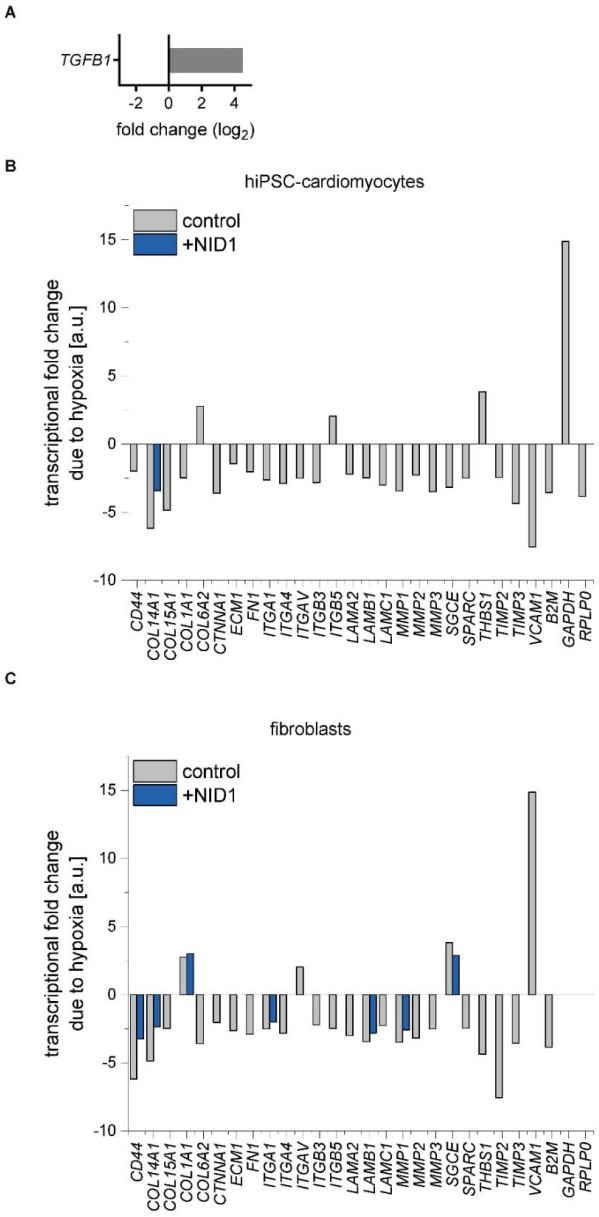

Figure S5. Translational changes in ECM production, degradation and regulation due to hypoxic conditions. **(A)** Transcriptional changes of *TGFB1* in NID1-treated hiPSC-CMs under normoxic conditions. **(B,C)** Transcriptional changes in gene expression after hypoxic conditions without (control) and with NID1 **(B)** hiPSC-CMs and **(C)** dermal fibroblasts. Gene regulation are shown when fold-regulation > |2|, p-value < 0.05.

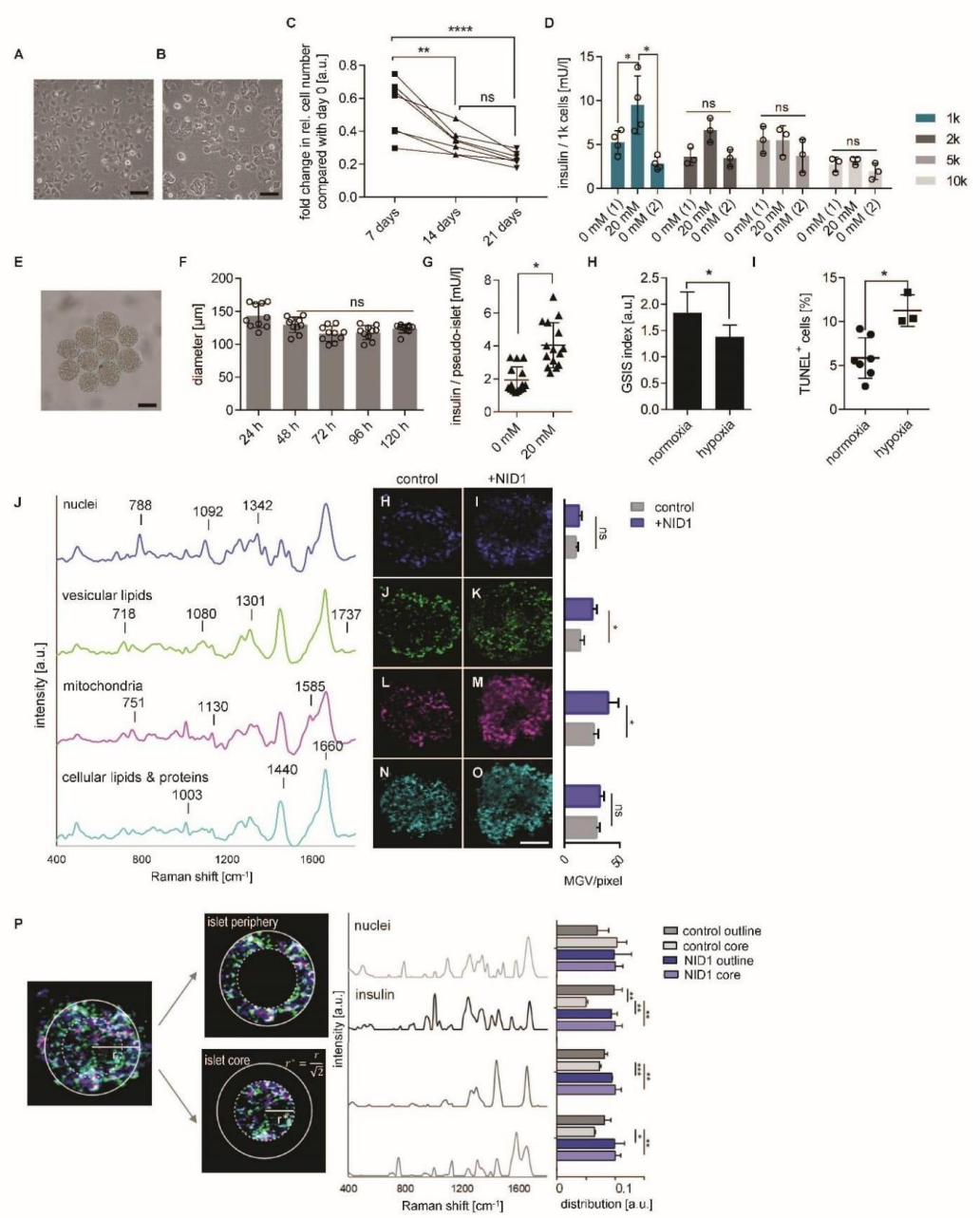

Figure S6. Human pseudo-islet functionality under hypoxic conditions and characterization by in situ Raman imaging and multivariate analysis. (A) Unexcised and **(B)** excised EndoC-βH3 morphology. Scale bars equal 100 µm. **(C)** Reduced cell number over time due to the excision of the proliferation transgene over 21 days. **(D)** GSIS assay (with 0 and 20 mM glucose) of pseudo-islets composed of 1000 (1k), 2000 (2k), 5000 (5k) and 10000 (10k) cells/ pseudo-islet

after 5 days of culture under normoxic conditions. **(E)** 1k pseudo-islet morphology. Scale bar equals 100 µm **(F)** Pseudo-islet size, described as pseudo-islet diameter, is stable from 72h until 5 days under normoxic conditions (n = 10); one-way ANOVA, *p<0.05. **(G)** GSIS assay (with 0 and 20 mM glucose) of pseudo-islets under normoxic conditions at 5 days (n = 15); unpaired t-test, *p<0.05 **(H)** Significant loss of glucose responsiveness under hypoxic conditions, described as the GSIS index (fold increase in insulin release due to the transition from Krebs buffer (0 mM glucose) to 20 mM glucose (n = 10); one-way ANOVA, *p<0.05. **(I)** DNA fragmentation under hypoxic conditions determined by the quantification of $TUNEL^+$ cells (n = 3-7); unpaired t-test. **(J)** True component analysis (TCA) identified four major spectral components assigned to nuclei (blue), insulin-transporting lipid vesicles (green), mitochondrial activity (pink) and cellular lipids and proteins (light blue). **(H-O)** False color intensity distribution images for each spectral component in (**H,J,L,N**) PBS controls and (**I,K,M,O**) NID1-treated pseudo-islets. Semi-quantitative analysis by definition of the mean gray value intensity/pixel demonstrated a significant increase in the vesicular lipids and the mitochondrial activity in NID1-treated islets. **(P)** Multivariate curve resolution (MCR) analysis was performed for in-depth analysis of the molecular composition in the periphery and core region of the hypoxic pseudo-islets. Most relevant, components related to nuclei, insulin, lipids and mitochondria were identified and their distribution within both regions were compared in PBS controls and NID1-treated pseudo-islets. The control core region showed a significant decrease in insulin, lipids and mitochondria, whereas the NID1-treated core region showed levels comparable to the peripheral regions (n = 4); *p<0.05, **p<0.01, ***p<0.001.

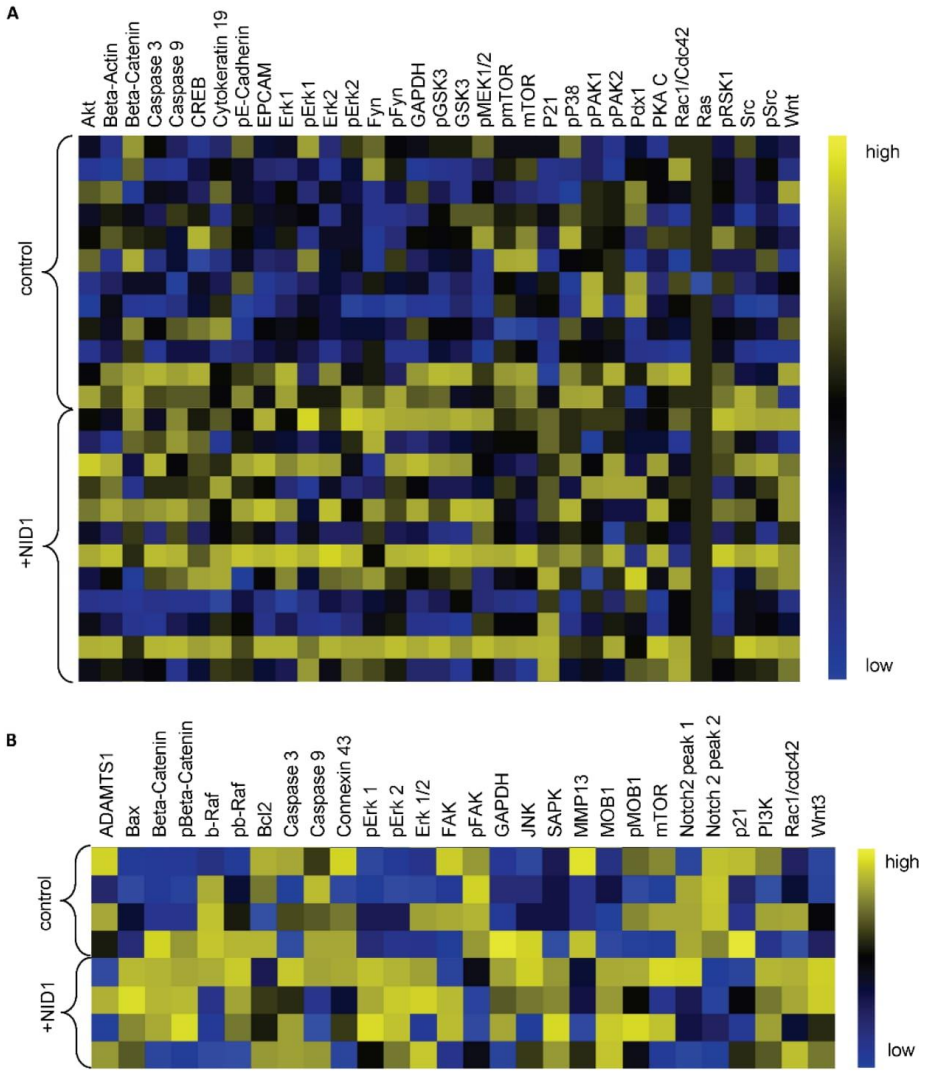

Figure S7. Change in protein expression in NID1-treated cultures. DigiWest®-based protein expression analysis of all tested proteins in (a) NID1-treated pseudo-islets (n = 12) and (b) NID1-treated hiPSC-CMs (n = 4) under hypoxic conditions compared with their respective controls. Data are shown as column-wise and color-coded heatmap from the lowest (blue) to the highest (yellow) expression for each analyte.

	baseline	saline	HA	NID1 + HA
Heart Rate^{min}	605 ± 46	675 ± 18	549 ± 46*	539 ± 45*
LVIDd^{mm}	2.65 ± 0.40	4.77 ± 0.36	3.40 ± 0.44**	2.90 ± 0.18***
LVIDs^{mm}	1.30 ± 0.22	4.29 ± 0.31	2.93 ± 0.51**	2.15 ± 0.18****,#
LVAWd^{mm}	0.73 ± 0.10	0.49 ± 0.01	0.48 ± 0.05	0.51 ± 0.06
LVAWs^{mm}	1.12 ± 0.14	0.52 ± 0.03	0.49 ± 0.04	0.60 ± 0.10
LVPWd^{mm}	0.71 ± 0.03	0.61 ± 0.17	0.53 ± 0.11	0.61 ± 0.07
LVPWs^{mm}	0.98 ± 0.03	0.79 ± 0.17	0.58 ± 0.03	0.70 ± 0.08
LVED^{mm}	2.67 ± 0.31	4.82 ± 0.26	3.52 ± 0.42**	2.82 ± 0.21****
LVES^{mm}	1.27 ± 0.20	4.26 ± 0.30	3.04 ± 0.43**	2.22 ± 0.18****,#
EDV$^{\mu L}$	26.89 ± 7.50	108.80 ± 13.57	52.39 ± 15.62***	30.30 ± 5.69****
ESV$^{\mu L}$	4.18 ± 1.49	81.83 ± 13.34	36.91 ± 13.01***	16.86 ± 3.57****
EF$^{\%}$	84.88 ± 3.08	24.96 ± 4.75	30.17 ± 4.31	44.63 ± 1.57***,##
FS$^{\%}$	52.56 ± 3.70	11.54 ± 2.34	13.80 ± 2.10	21.12 ± 0.78**,#

Table S1. Echocardiography analysis 28 days after MI/R. Baseline is the pre-MI/R measurement of the NID1+HA mice. Data are presented as means ± standard error of the mean (SEM). *p<0.05, **p<0.01, ***p<0.001, ****p<0.0001 saline vs. HA and NID1+HA, $^{\#}$p<0.05, $^{\#\#}$p<0.01 HA vs. NID1+HA; individual one-way ANOVA with Tukey's multiple comparison test, baseline (n = 4), saline (n = 3), HA (n = 3), NID1+HA (n = 4). LVIDd: left ventricular internal dimension at end diastole, LVIDs: left ventricular internal dimension at end-systole, LVAWd: left ventricular anterior wall thickness in diastole, LVAWs: left ventricular anterior wall thickness in systole, LVPWd: left ventricular posterior wall dimensions in diastole, LVPWs: left ventricular posterior wall dimensions in systole, LVED: left ventricle end-diastolic diameter, LVES: left ventricle end-systolic diameter, EDV: end-diastolic volume, ESV: end-systolic volume, EF: ejection fraction, FS: fractional shortening.

Raman shift [cm^{-1}]	Assignment
497	glycogen
718	C-N / nucleotide peak
751	mitochondrial DNA
752	porphyrin
780	DNA
788	DNA
841	Polysaccharides
858-9	proline, hydroxyproline
940	C-C backbone
1003	phenylalanine
1004	phenylalanine
1080	typical phospholipids
1090-3	phosphodioxy / DNA
1119	C-C stretch in lipids
1130	phospholipid structural changes / Mitochondrial activity
1240	lipids
1247-8	collagens, amide III
1301	lipids, fatty acids, triglycerides
1302	collagens
1339	tryptophan, CH2, CH3 wagging - bending in lipids/proteins
1342	guanine (DNA/RNA)
1440	CH2, CH3 deformation (lipids)
1455	deoxyribose
1460	CH2, CH3 deformation of lipids and collagen
1513	cytosine, porphyrin
1557	porphyrin v(C=C)
1585	mitochondria /mitochondrial activity
1612	C=C stretching (ring)
1620	porphyrin v(C=C)
1660	amide I
1737-8	lipids

Table S2. Raman-associated peaks. Raman peaks in cm^{-1} and their assigned molecular structure.

antibodies for DigiWest	species	order information
Beta-Actin	rabbit IgG	A1978, Sigma
ADAMTS1	rabbit IgG	12897, Cell Signaling
Akt	rabbit IgG	4685, Cell Signaling
Bax	rabbit IgG	2772, Cell Signaling
Bcl2	rabbit IgG	2872, Cell Signaling
Beta-Catenin	rabbit IgG	8480, Cell Signaling
Beta-Catenin	rabbit IgG	8814, Cell Signaling
Beta-Catenin - phospho Ser552	rabbit IgG	9566, Cell Signaling
b-Raf	rabbit IgG	07-583, Upstate
b-Raf - phospho Ser445	rabbit IgG	2696, Cell Signaling
Caspase 3	rabbit IgG	9662, Cell Signaling
Caspase 9	mouse IgG1	9508, Cell Signaling
Connexin 43	rabbit IgG	3512, Cell Signaling
CREB - phospho Ser133	rabbit IgG	9198, Cell Signaling
EpCAM	rabbit IgG	3599, Cell Signaling
Erk1/2 (MAPK p44/42)	rabbit IgG	4695, Cell Signaling
Erk1/2 (MAPK p44/42) - phospho Thr202/Tyr204	rabbit IgG	4370, Cell Signaling
E-cadherin	rat IgG	sc-59778, Santa Cruz
E-cadherin – phospho Ser838/Ser840	rabbit IgG	2239-1, Epitomics
FAK1	rabbit IgG	3285, Cell Signaling
FAK1 - phospho Tyr397	rabbit IgG	8556, Cell Signaling
Fyn	rabbit IgG	4023, Cell Signaling
Fyn – phospho Tyr530	rabbit IgG	orb99261, biorbyt
GAPDH	rabbit IgG	5174, Cell Signaling
GSK3 alpha/beta - phospho Ser21/Ser9	rabbit IgG	9331, Cell Signaling
GSK3 beta	rabbit IgG	9315, Cell Signaling
GSK3 beta - phospho Ser9	rabbit IgG	9336, Cell Signaling
JNK/SAPK	rabbit IgG	9252, Cell Signaling
MEK1/2 - phospho Ser217/Ser221	rabbit IgG	9154, Cell Signaling
MMP13	mouse IgG1	MAB511, R&D Systems
MOB1	rabbit IgG	3863, Cell Signaling
MOB1 - phospho Thr35	rabbit IgG	8699, Cell Signaling
mTOR (FRAP)	rabbit IgG	2983, Cell Signaling
mTOR (FRAP)- phospho Ser2448	rabbit IgG	2971, Cell Signaling
Notch 2	rabbit IgG	5732, Cell Signaling
P21	rabbit IgG	2947, Cell Signaling
P38 MAPK - phospho Thr180/Tyr182	rabbit IgG	4511, Cell Signaling
PAK 1/2 - phospho Ser144/Ser141	rabbit IgG	2606, Cell Signaling
Pdx1	rabbit IgG	5679, Cell Signaling
PI3-kinase p85 alpha	rabbit IgG	ab40755, abcam
PKA C alpha	rabbit IgG	4782, Cell Signaling
Rac1/Cdc42	rabbit IgG	4651, Cell Signaling
Ras	rabbit IgG	8955, Cell Signaling
RSK 1 (p90RSK) - phospho Thr573	rabbit IgG	ab62324, abcam
Src	rabbit IgG	2108, Cell Signaling
Src – phospho Tyr527	rabbit IgG	2105, Cell Signaling
Wnt3A	rabbit IgG	09-162, Millipore
antibodies for DigiWest	**species**	**order information**
dk-α-rb IgG (H+L) - RPE		#711-116-152, Jackson
dk-α-ms IgG (H+L) - RPE		#715-116-151, Jackson
gt-α-rt IgG (H+L) - RPE		#112-116-143, Jackson
Streptavidin - RPE		#016-110-084, Jackson

antibodies for IF staining	species	dilution	order information
NID1	rabbit IgG	1:100	Sc-33141, Santa Cruz
NID1	rabbit IgG	1:1000	kind gift from F. Zaucke
NID2	rabbit IgG	1:1000	kind gift from F. Zaucke
FN	rabbit IgG	1:500	A0245, Dako
POSTN	rabbit IgG	1:100	HPA012306, Sigma-Aldrich
LAM	rabbit IgG	1:50	ab11575, Abcam
COL4	rabbit IgG	1:250	ab6586, Abcam
COL1	rabbit IgG	1:75	R1038, Acris
αSMA-FITC	mouse IgG2a	1:500	F3777, Sigma-Aldrich
CD31	rat IgG2a	1:20	DIA-310, Dianova
MF20	mouse IgG2b	1:50	MF20, Developmental Studies Hybridoma Bank
CTNT	rabbit IgG	1:3000	HPA015774, Sigma-Aldrich
CTNT	mouse IgG1	1:600	NB200-412, Novus Biologicals
TUJ1	rabbit IgG	1:2000	802001, BioLegend
NESTIN	rabbit IgG	1:200	839801, BioLegend
MAP2	rabbit IgG	1:500	ab5622, Merck-Millipore
INS	guinea-pig IgG	1:200	A0564, Dako
E-cadherin	mouse IgG2a	1:250	ab76055, Abcam
CASP-3	rabbit IgG	1:100	ab13847, Abcam
rabbit IgG-AF488	goat	1:250	A-11034, Invitrogen
rat IgG2a-AF647	goat	1:250	A-21247, Invitrogen
mouse IgG1-AF594	goat	1:250	A-21125, Invitrogen
mouse IgG2a-AF488	goat	1:250	A-21131, Invitrogen
mouse IgG2b-AF594	goat	1:250	A-21145, Invitrogen
guinea-pig IgG-AF594	goat	1:250	A-11076, Invitrogen
antibodies for WB	**species**	**dilution**	**order information**
NID1	rabbit IgG	1:400	sc-33141, Santa Cruz
LAM	Rabbit IgG	1:500	ab11575, Abcam
anti-rabbit IgG-HRP	goat	1:4000	ab6721, Abcam

Primer		Sequence
Human NID1 5'	QhNID1-389F QhNID1-495R	CCGCTGAGTGCGTGCACAGA GTCCCGAGAAGGGCCCTGGT
Human NID1 3'	QhNID1-2015F QhNID1-2160R	CCACGGCTGCGATACCAACGCCG CC CAGGATGTGCTCTCTCTCGTGCTG G
Hamster B-Actin	QhamB-Actin-F QhamB-Actin-R	GGCGCTTTTGACTCAGGACTTTA GGGATGTTTGCTCCAACCGA
Hamster p53	Qham-p53-F Qham-p53-R	CATGCCGAATACCTGGATGACAAG GCAAATCAAACCCTGTCTTCAACC
human αSMA	Hs_ACTA2_1_SG	Qiagen, QT00088102
human GAPDH	Hs_GAPDH_2_SG	Qiagen, QT01192646
RT² Profiler PCR Arrays	Extracellular Matrix & Adhesion Molecules	Qiagen, PAHS-013Z

Table S3. List of antibodies and primer sequences.

Appendix II

Decorin improves human pancreatic β-cell function and regulates ECM expression in vitro

Max Urbanczyk[1§], Abiramy Jeyagaran[1,2§], Aline Zbinden[1,3], Chuan-en Lu[1], Julia Marzi[1,2,4], Laurence Kuhlburger[5,6], Sven Nahnsen[5,6], Shannon L. Layland[1,7], Garry Duffy[8,9], Katja Schenke-Layland[1,2,4#]

[1] Institute of Biomedical Engineering, Department for Medical Technologies and Regenerative Medicine, Eberhard Karls University Tübingen, Tübingen, Germany
[2] NMI Natural and Medical Sciences Institute at the University of Tübingen, Reutlingen, Germany
[3] Department of Immunology, Leiden University Medical Center, 2333 ZA Leiden, The Netherlands
[4] Cluster of Excellence iFIT (EXC 2180) "Image-Guided and Functionally Instructed Tumor Therapies", Eberhard Karls University Tübingen, Tübingen, Germany
[5] Quantitative Biology Center (QBiC), Eberhard Karls University of Tübingen, Tübingen, Germany
[6] Biomedical Data Science, Department of Computer Science, Eberhard Karls University Tübingen, Tübingen, Germany
[7] Department of Women's Health, Eberhard Karls University Tübingen, Tübingen, Germany
[8] Discipline of Anatomy and the Regenerative Medicine Institute, School of Medicine, College of Medicine Nursing and Health Sciences, National University of Ireland Galway, Ireland
[9] Science Foundation Ireland (SFI) Centre for Research in Advanced Materials for Biomedical Engineering (AMBER), Trinity College Dublin & National University of Ireland Galway, Galway, Ireland.

§ Authors contributed equally.
#Corresponding author:
Prof. Dr. Katja Schenke-Layland
Institute of Biomedical Engineering, Department for Medical Technologies and Regenerative Medicine, Eberhard Karls University Tübingen, Silcherstr. 7/1, 72076 Tübingen, Germany
katja.schenke-layland@uni-tuebingen.de

Abstract

Transplantation of islets of Langerhans is a promising alternative treatment strategy in severe cases of type 1 diabetes mellitus; however, the success rate is limited by the survival rate of the cells post-transplantation. Restoration of the native pancreatic niche during transplantation potentially can help to improve cell viability and function. Here, we assessed for the first time the regulatory role of the small leucine-rich proteoglycan decorin (DCN) in insulin secretion in human β-cells, and its impact on pancreatic extracellular matrix (ECM) protein expression in vitro. In depth analyses utilizing next-generation sequencing as well as Raman microspectroscopy and imaging identified pathways related to glucose metabolism to be upregulated in DCN-treated cells, including oxidative phosphorylation within the mitochondria as well as proteins and lipids of the endoplasmic reticulum. We further showed the effectiveness of DCN in a transplantation setting by treating collagen type 1-encapsulated β-cell-containing pseudo-islets with DCN. Taken together, in this study, we show the potential of DCN to improve the function of insulin-secreting β-cells while reducing the expression of ECM proteins affiliated with fibrotic capsule formation, making DCN a highly promising therapeutic agent for islet transplantation.

Keywords

decorin • β-cells • diabetes mellitus in vitro model • next-generation sequencing • Raman microspectroscopy • extracellular matrix remodeling

Abbreviations

DM – diabetes mellitus

ECM – extracellular matrix

COL1 – collagen type 1

COL3 – collagen type 3

FN - fibronectin

DCN - decorin

NGS – next-generation sequencing

ER – endoplasmic reticulum

GSIS – glucose-stimulated insulin secretion

IF – immunofluorescence

TCA – true component analysis

PCA – principal component analysis

GVI – gray value intensity

ROI – region of interest

BM – basement membrane

LAM – laminins

COL4 – collagen type 4

INS – insulin

GLU – glucagon

cGMP – cyclic guanosine monophosphate

MAPK – mitogen-activated protein kinase

OxPhos – oxidative phosphorylation

PI – phosphatidylinositol

TAG – triacylglycerol

ERAD – endoplasmic reticulum associated degradation

UPR – unfolded protein response

WFS1 – Wolframin ER transmembrane glycoprotein

RRBP1 – Ribosome Binding Protein 1

HSP – heat shock protein

Introduction

Diabetes mellitus (DM) is a metabolic disease where the internal glycemic control is disrupted by the autoimmune destruction of insulin-producing β-cells (Type 1 DM) or the inefficient use of insulin (Type 2 DM) in response to glucose. Ten percent of the adult population suffers from DM and the numbers are predicted to increase from the current 537 million patients to 783 million by 2045. Type 1 DM accounts for 5-10% of the total number of patients and they mostly rely on exogenous insulin injections to control their glucose levels [1]. The use of pancreatic organ or islets of Langerhans transplantation is an alternative treatment strategy for DM patients repeatedly suffering from severe hypoglycemia. The islets of Langerhans are the endocrine units of the pancreas responsible for controlling blood glucose levels. They contain β-cells, which are the glucose-responsive insulin-producing cells. Islet transplantation has been shown to improve glucose control and lead to insulin independency for up to 5 years [2]; however, its efficacy is limited by the loss of approximately 50% of donor islets post-transplantation, due to multiple factors such as hypoxia at the transplant site and immune system reactions [3]. During islet isolation, the human pancreas is mechanically and enzymatically digested to separate the endocrine and exocrine tissues, which results in the destruction of the vascularization and the loss of crucial extracellular matrix (ECM) proteins [4]. Following transplantation into the host's body, revascularization of the graft can take up to 14 days when no supporting intervention is used [5]. During this period, the islets are subjected to decreased oxygen and nutrient supply. The native ECM facilitates cell-cell contacts and controls several cellular processes, including cell proliferation, survival, and tissue-specific functions [6]. The removal of the essential islet ECM further diminishes the success rate of islet transplantation [7]. There are several different approaches to improve the survival rate of isolated islets post-transplantation, such as encapsulation in carrier materials [8–10], co-culture with supporting cells [7,11–13], or the supplementation of pancreatic ECM proteins [14–16], which has already been shown to improve cell survival and functionality post-isolation [17]; however, implantation still causes the formation of a fibrotic capsule composed of the fibril-forming proteins such as collagen type 1 (COL1), collagen type 3 (COL3), and fibronectin (FN) [18–20], which hinders the functional integration of the transplant in the host's system. To improve the survival of isolated islets post-transplantation, supportive strategies need to address (1) the reestablishment of the pancreatic islet niche to improve islet survival as well as (2) the reduction of fibrotic capsule formation to improve integration of the islets into the recipient's system.

The goal of this study was to identify potential ECM candidates that could improve the outcome of islet transplantation. We identified decorin (DCN) as target of interest and studied the impact of DCN on the function and endogenous ECM expression of human β-cells using the conditionally immortalized human β-cell line EndoC-βH3. We show that DCN-treatment significantly improved insulin secretion upon glucose challenge while ECM proteins affiliated with fibrosis were significantly downregulated. Utilizing Raman microspectroscopy and imaging as well as next-generation sequencing (NGS), we further monitored the impact of DCN on mitochondrial activity and the endoplasmic reticulum (ER). To evaluate its potential as a treatment option in a carrier material for β-cell or islet transplantation, we incorporated DCN in a COL1 carrier material and confirmed the improved functionality effects observed in suspension. Taken together, our results show for the first time the positive effects of DCN on improved insulin secretion in β-cells through modulation of mitochondrial activity as well as protein folding and vesicle formation processes. Additionally, we show that DCN can reduce the expression of ECM proteins affiliated with fibrotic capsule formation. Both properties make DCN a strong candidate for use in islet transplantation to support islet survival and potentially improve graft integration into the host's system.

Methods

Pseudo-islet assembly & culture

The human EndoC-βH3 β-cell line was cultured following manufacturer's instructions (Human Cell Design, Toulouse, France). Pseudo-islets were formed as previously described [21]. Briefly, aggregates of 1000 β-cells were formed in U-bottom non-adherent well plates (Greiner Bio-One, Frickenhausen, Germany) over a period of five days under standard culture conditions (37°C, 5% CO_2, 20% O_2). Culture media Optiβ1 and Optiβ2 (Human Cell Design) were supplemented with recombinantly-produced DCN [22] at 50 µg/ml, and cells were cultured in these media for two days and four days after seeding, respectively. PBS supplementation was used as control.

For COL1 gel encapsulation, 120 pseudo-islets were grouped per well. Pseudo-islets were encapsulated in COL1 with a concentration of 6.0 mg/ml as previously described and according to the manufacturer's instructions (Fraunhofer IGB, Stuttgart, Germany) [8] [23]. The encapsulated pseudo-islets were cultured in a total volume of 250 µl for three days with DCN at 50 µg/ml or PBS (control).

Pseudo-islet and pancreatic tissue preparation for histological analysis

After culture, pseudo-islets were prepared for histological analysis as previously described [8]. Briefly, pseudo-islets were washed with PBS, fixed in 4% PFA and embedded in paraffin with a Shandon Citadel 1000 (Thermo Fisher Scientific, Waltham, MA, USA) according to the manufacturer's protocol. Pseudo-islets were cut in 3 µm sections (Microtom RM2145, Leica, Nussloch, Germany), deparaffinized with xylene and graded ethanol (100%-50%) and VE-water. Adult human pancreatic tissue was purchased from Novus Biologicals (NBP2-30191, Novus Biological, Bio-Techne GmbH, Wiesbaden, Germany), which was treated by the same protocol that was used for the pseudo-islets.

Immunofluorescence (IF) staining

Antigen retrieval procedures for IF staining and primary and secondary antibodies are listed in **Suppl. Table S1**. Two different DCN antibodies were used to exclude possible staining artefacts. Sections were incubated for 10 minutes with 4',6-Daimidin-2-phenylindol solution at 2 µg/ml (DAPI, Sigma-Aldrich, Schnelldorf, Germany) and mounted with Prolong Gold Antifade Mountant (Thermo Fisher Scientific). Images were obtained using a laser scanning microscope 780 (Carl Zeiss GmbH, Jena, Germany).

COL1 gel E-modulus evaluation

Elastic modulus of the COL1 gels was tested using a BOSE Electroforce 3000 (TA Instruments, New Castle, USA). The elastic modulus was calculated by means of equation 1.

$$E = \frac{\sigma(\varepsilon)}{\varepsilon} = \frac{(F/A)}{(\Delta L/L_0)} \quad (1)$$

The gel's surface area *A* was uniformly determined as 30 mm² and the total height L_0 was measured specifically for each gel. The elastic modulus was obtained by plotting the tensile stress against strain using Microsoft Excel (Microsoft Corporation, 2021. Microsoft Excel Version 2111, retrieved from https://office.microsoft.com/excel) where the slope of the graph's regression line displayed the elastic modulus.

Glucose-Stimulated Insulin Secretion (GSIS) assays

GSIS assays were performed as previously described [7,21]. Briefly, pseudo-islets from suspension and COL1 gel cultures were starved overnight in Optiβ-2 (Univercell Biosolutions).

Afterwards, suspension pseudo-islets were grouped, washed with 0.1% BSA (A-9576, Sigma-Aldrich) in β-Krebs (KREBS-BSA, human cell design) and incubated for 1 hour in KREBS-BSA. After synchronization, pseudo-islets in suspension were subsequently incubated for 1 hour each in basal KREBS-BSA, KREBS-BSA containing 20mM glucose (A2494001, Thermo Fisher Scientific) and basal KREBS-BSA again. After each incubation, the supernatant was removed and stored at -20°C until further analysis. The insulin content was analyzed using an ultrasensitive human insulin ELISA kit (10-1132-01, Mercodia, Uppsala, Sweden). For GSIS assays in COL1 gels, all incubation times were tripled.

The GSIS index was calculated by dividing each samples' insulin secretion during high-glucose treatment at 20 mM glucose by the insulin secretion at 0 mM glucose stimulation (1). For pseudo-islets in COL1 gels, the mean ± SD of the insulin secretion during high-glucose treatment at 20 mM glucose was divided by the mean ± SD of the insulin secretion during 0 mM glucose stimulation while applying the propagation of error.

RNA isolation and NGS

To isolate RNA from pseudo-islets under glucose stimulation, pseudo-islets were washed five times using cold PBS after 30 min incubation with KREBS-BSA containing 20 mM glucose. Pseudo-islets were grouped as 180 per sample before RNA isolation was performed following the RNEasy micro kit protocol (74004, Qiagen, Hilden, Germany). Briefly, grouped pseudo-islets were lysed in 250 µl RPE buffer containing 1% β-mercaptoethanol (M7522, Sigma-Aldrich) and frozen at -80°C before further processing. On the day of the RNA isolation, vials were thawed, mixed with 250 µL of 70 % ethanol and spun down at 13'000 rpm for 15 s. Following discarding of the flowthrough, samples were washed with 350 µL RW1 and spun down at 13'000 rpm for 15 s. After discarding the flowthrough, samples were washed with 500 µL RPE buffer at 13,000 rpm for 15 s. Afterwards, samples were washed twice with 80% ethanol at 13,000 rpm for 2 min. Samples were then spun down at 13,000 rpm for 5 min with open lids to dry the membrane. The samples were resuspended in 14 µl RNAse-free water to elute the RNA and spun down for 7 min at 13,000 rpm for 15 s. The RNA content was quantified using the infinite M2000 Pro plate reader with the NanoQuant Plate (Tecan, Männedorf, Switzerland). All samples were stored at -80°C until the NGS.

RNA quality was assessed with an Agilent Fragment analyzer (Agilent) and samples with RNA integrity number > 7 were selected for library construction on the automated workstation Biomek i7 (Beckman). 100 ng of total RNA was subjected to polyA enrichment using the NEBNext Poly(A) mRNA Magnetic Isolation Module (NEB). cDNA libraries were constructed using the resulting mRNA and the NEBNext Ultra II Directional RNA Library Prep Kit (NEB). Library molarity was determined by measuring the library size (approximately 400 bp) using the Fragment Analyzer with the High NGS Fragment 1-6000bp assay (Agilent) and the library concentration (approximately 10 ng/µl) using the Infinite 200Pro (Tecan) and the Quant-iT HS Assay Kit (Thermo Fisher Scientific). The libraries were denaturated, diluted to 270 pM, and sequenced as paired-end 100bp reads on an Illumina NovaSeq6000 (Illumina, San Diego, CA, USA) with a sequencing depth of approximately 40 million clusters per sample. Library preparation and sequencing procedures were performed by the same individual at the Quantitative Biology Center (QBiC) Tübingen, and a design aimed to minimize technical batch effects was chosen. Read quality of RNA-seq data in fastq files was assessed using ngs-bits (V2020_09-39) to identify sequencing cycles with low average quality, adaptor contamination, or repetitive sequences from PCR amplification. Data management and bioinformatic analysis were performed at QBiC Tübingen, Germany. A Nextflow-based nf-core pipeline nf-core/rnaseq (version 1.4.2; https://github.com/nf-core/rnaseq, accessed on 21 January 2021) was used for the RNA-seq bioinformatic analysis. As part of this workflow, FastQC (version v0.11.8) was used to determine the quality of the FASTQ files [24]. Subsequently, adapter trimming was conducted with Trim Galore (version 0.6.4) [25]. STAR aligner (version 2.6.1, [26]) was used to map the reads that passed quality control against

GRCh37. RNA-seq data quality control was performed with RSeQC (version 3.0.1) [27] and read counting of the features (e.g., genes) with featureCounts (version 1.6.4) [28]. An aggregation of the quality control for the RNA-seq analysis was performed with MultiQC (version 1.7; http://multiqc.info/, accessed on 21 January 2021) [29]. The analysis of the differential gene expression was performed in R language (version 3.5.1) using DESeq2 (version 1.22) through the Nextflow-based workflow qbic-pipelines/rnadeseq (https://github.com/qbic-pipelines/rnadeseq, accessed on 21 January 2021, version 1.3.2). Genes were considered differentially expressed (DE) when the Benjamini–Hochberg multiple testing adjusted p-value [30] was smaller than 0.05 ($p_{adj} \leq 0.05$). Multiple testing correction helped to reduce the number of false positives (not real DE genes). In the case of a threshold of 0.05, the proportion of false discoveries in the selected group of DE genes was controlled to be less than the threshold value—in this case, 5%. Final reports were produced using the R package rmarkdown (version 2.1) with the knitr (version 1.28) and DT (version 0.13) R packages. The sample similarity heatmaps were created using the edgeR (version 3.26.5) R package. Both KEGG and REACTOME databases were used for pathway analysis [31,32]. All DE genes were included, and enrichment was calculated using Fisher's exact test ($p \leq 0.05$).

Raman microspectroscopy

A Raman microspectroscope (WiTec alpha 300 R, Ulm, Germany) with a charge-coupled device (CCD) camera (WiTec GmbH, Ulm, Germany) was utilized to analyze the pseudo-islets. A green laser (532 nm) with a grating of 600 g/mm, set to a laser power of 50 mW, and a 63x objective (W Plan-Apochromat 63x/1.0 M27, Carl Zeiss GmbH) were employed. Sections of the paraffin-embedded pseudo-islet samples were kept in PBS after deparaffinization and during the measurements. DCN reference spectra were obtained from pseudo-islets which were IF-stained for DCN. IF microscopy was used to locate DCN-positive areas before Raman measurements. The DCN spectrum was then extracted as the reference for further analyses. To obtain the reference spectrum of ER, ER-Tracker™ Green (E34251, Thermo Fisher Scientific) was used on EndoC-βH3 cells for Raman microscope navigation. The fluorescence signal from the ER was detected on the Raman heatmap (**Suppl. Fig. S3**). The ER spectrum was acquired by averaging the spectra of the fluorescence areas for the use of further TCA assessments. Unstained sections of pseudo-islets were scanned at an integration time of 0.05 s/spectrum and pixel resolution was set to either 0.5 x 0.5 µm or 1 x 1 µm to generate the spectral maps. For in situ scanning of living pseudo-islets in suspension culture, an organ-on-chip device was used as described earlier [21]. Briefly, pseudo-islets were loaded in flow traps by means of hydrostatic pressure. By applying a constant flow rate of 50 µl/h the pseudo-islets were kept immobilized. For imaging, the inverted Raman setup with a 60x objective (Carl Zeiss GmbH, Jena, Germany) was employed. The green laser of 50 mW with an integration time of 0.5 s/spectrum with pixel resolutions of 2 x 2 µm was used. The spectral data pre-processing and analysis was conducted on the Project Five 5.2 software (WITec GmbH). The protocol is as follows: firstly, every spectrum was cropped from the range of 200 to 3000 cm^{-1} wavenumbers. Secondly, the artefacts caused by the cosmic rays were eliminated. Lastly, the graph background was then subtracted and the normalization of the area for each spectrum was performed. True component analysis (TCA) was utilized to generate the images with the signal intensity distribution representing specific components (DCN, ECM, ER). Principal component analysis (PCA) was applied to assess variations of molecular shifts as previously described [21]. PCA analysis was performed using the software Unscrambler X (CAMO Software AS, Oslo, Norway). PC scores and loadings plots were used to identify and interpret differences in the molecular composition of the three components.

Image analysis

Co-localization analysis was performed via a self-written macro in Microsoft Excel (Microsoft Corporation). Briefly, the pixels of the red channel displaying insulin were compared to the pixels of the green channel displaying ECM proteins. The pixels were counted as co-localized if both

pixels exceeded a defined threshold. Co-localization was normalized by the number of pixels of the ECM protein channel exceeding the threshold.

Blinded DCN-stained sections were counted by three independent unbiased observers. Cells were counted as DCN-positive if they expressed a clear DCN- and DAPI-positive staining. DCN-positive cells were categorized as periphery if they were present within the first two cell layers of the section viewed from outside to inside. All other DCN-positive cells were categorized as pseudo-islet core.

Semi-quantitative gray value intensity (GVI) analysis of IF-stained sections and Raman TCA components was performed using ImageJ V 1.52p. For IF images, the region of interest (ROI) was chosen to include all DAPI-positive cells and copied into the channel to analyze. The obtained GVI was normalized by the area of the ROI. For Raman images, ROI for semi-quantification was chosen to include all nuclei-spectrum-positive pixels of the Raman TCA signal and copied to the channel for the components of interest (ECM, DCN and ER). The obtained GVI was normalized by the area of the ROI.

DCN direct labeling

For conjugation and purification of DCN, the Fluoro-spin 490 protein labeling & purification kit (MK-D0125-Z010.0-001, emp BIOTECH GmbH, Berlin, Germany) with DYOMICS DY-490 Fluorophore was used according to the manufacturer's instructions. Briefly, the required dye volume was calculated using the given equation 2:

$$V_{dye} = \frac{(C_{protein,initial} * V_{protein} * 1000)}{C_{activated\ dye\ solution} * MW_{protein}} * MR \quad (2)$$

The activated dye was gently mixed with protein solution and incubated for 5 min at RT. For purification, the dye-protein-mixture was pipetted onto a washing gel and centrifuged at 1000 x g for 2 min. The purified protein conjugate was collected, and the absorbance was measured at 280 nm and 493 nm. To verify the degree of labeling and calculate the final concentration of the labeled DCN, equations (3), (4) and (5) were used.

$$\varepsilon = \frac{A_{280}}{C_{protein,initial} * b} \quad (3)$$

$$C_{protein,conjugated} = \frac{A_{280} - (A_{493} * K) * DF}{\varepsilon} * MW \quad (4)$$

$$D = \frac{A_{493} * DF}{6300 * C_{protein,conjugated}} * MW \quad (5)$$

The description of the values and all values used and calculated can be found in **Suppl. Table S2**.

Results

DCN co-localizes with insulin in human pancreatic islets

To identify potential ECM proteins as treatment candidates to support β-cell functionality post-transplantation, IF staining was used on native human pancreatic tissue focusing on basement membrane (BM) proteins such as laminins (LAM) and collagen type 4 (COL4), the fibrillar ECM proteins FN and COL1, as well as DCN (**Fig. 1 A-E**). Co-localization studies showed a significantly higher ratio of co-localized DCN-positive and insulin (INS)-positive pixels within the native pancreatic tissue when compared with the other ECM proteins (**Fig. 1 F**; LAM: 0.04 ± 0.04; COL4: 0.03 ± 0.02; FN: 0.36 ± 0.09; COL1: 0.19 ± 0.13 vs DCN: 0.91 ± 0.04; n ≥ 6, ****$p < 0.0001$). Further co-localization studies showed a significantly higher correlation of DCN with INS when compared with glucagon (GLU) (**Fig. 1 G, H**; **Fig 1 I**; GLU: 0.25 ± 0.15 vs INS: 0.79 ± 0.03; n = 4, ***$p < 0.001$), indicating a potentially important role of DCN in connection with the insulin-secreting β-cells within the islets of Langerhans.

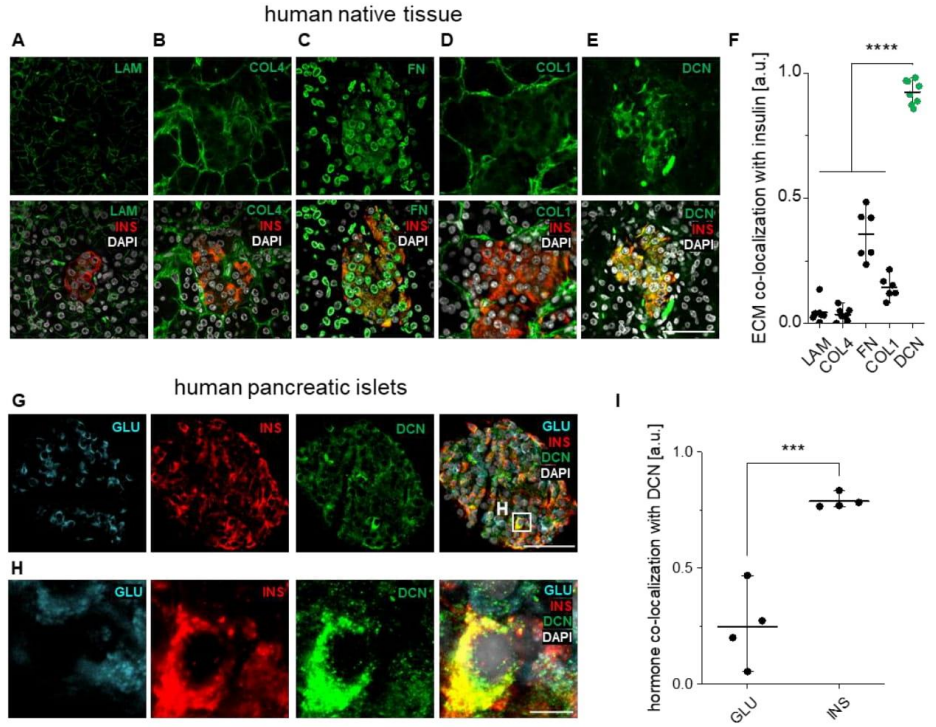

Fig. 1: DCN co-localizes with insulin-producing β-cells in vivo. Expression patterns of (**A**) LAM, (**B**) COL4, (**C**) FN, (**D**) COL1, and (E) DCN in native pancreatic tissue. (**F**) Co-localization study shows strong correlation between DCN and insulin-expressing β-cells in islets of Langerhans. 1-way ANOVA with Tukey's multiple comparison test (n ≥ 6) ****$p < 0.0001$. (**G, H**) Expression patterns of glucagon (GLU), insulin (INS), and DCN in isolated human pancreatic islets. (**I**) Co-localization study shows significantly higher correlation of DCN with INS compared to GLU. Unpaired t-test (n = 4) ***$p < 0.001$. Scale bars equal 50 µm (**A-E, G**) and 5 µm (**H**).

DCN binds to the β-cells in pseudo-islets and improves insulin secretion in suspension

To test the hypothesis that DCN has a potential impact on the functionality of β-cells in the human pancreas, the human β-cell line EndoC-βH3 was aggregated into pseudo-islets and treated with 50 µg/ml of in-house produced human recombinant full-length DCN (+DCN) [22]. Upon glucose stimulation, DCN-treated pseudo-islets (pseudo-islets +DCN) secreted significantly more insulin compared to the control (**Fig. 2 A**; 3.70 ± 0.98 mU/l control vs 5.83 ± 1.39 mU/l +DCN at 20 mM glucose; n ≥ 4, ****$p < 0.0001$), accompanied with a significant increase in the GSIS index (1.39 ± 0.12 control vs 2.03 ± 0.35 +DCN; n ≥ 4, *$p < 0.05$). IF staining for DCN of control pseudo-islets and pseudo-islets +DCN did not exhibit differences in GVI per pixel (**Fig. 2 B,** 1.84 ± 0.58 control vs 1.98 ± 1.07 +DCN; n = 8, $p = 0.76$); however, structural variances were seen. In control pseudo-islets, DCN was homogenously expressed throughout the entire pseudo-islet, while pseudo-islets +DCN showed DCN-positive cells in the outer layer of the pseudo-islets (**Fig. 2 B,** white arrows). This pattern was observed as early as 24 h after DCN-treatment (**Fig. 2 C, Suppl. Fig S1 A, B**). The interaction of DCN in the periphery of the pseudo-islet was further confirmed using directly labelled DCN (**Suppl. Fig. S1 C**). Live tracking of the pseudo-islets +DCN showed that DCN directly attaches to the periphery of the pseudo-islets as early as 3 h post-treatment. Further analysis of the ECM composition of control pseudo-islets and pseudo-islets +DCN revealed a significant decrease of both fibrillar ECM proteins FN (**Fig. 2 D**, 3.12 ± 0.72 control vs 1.76 ± 0.48 +DCN; n ≥ 4, *$p < 0.05$) and COL1 (**Fig. 2 E**, 7.66 ± 0.91 control vs 4.60 ± 1.44 +DCN; n = 8, ****$p < 0.0001$) after DCN-treatment. In contrast, DCN did not have a significant effect on the expression of E-cadherin (**Suppl. Fig. 2 A**, 3.05 ± 0.47 control vs 3.29 ± 0.46 +DCN; n ≥ 4, $p = 0.46$), INS (**Suppl. Fig. 2 B**, 3.55 ± 1.66 control vs 3.84 ± 0.81 +DCN; n ≥ 4, $p = 0.71$), or the BM proteins LAM (**Suppl. Fig. 2 C**, 2.02 ± 1.13 control vs 2.70 ± 0.46 +DCN; n = 7, $p = 0.52$) and COL4 (**Suppl. Fig. 2 D**, 3.08 ± 0.65 control vs 3.49 ± 1.06 +DCN; n = 8, $p = 0.18$). These results show for the first time the stimulatory effect of DCN-treatment on the insulin secretion of β-cells. Furthermore, DCN-treatment reduced the expression of fibrosis-affiliated ECM proteins under suspension culture conditions.

NGS reveals significant impact of DCN-treatment on mitochondria and ER

NGS was performed to investigate the effects of DCN-treatment on the overall gene expression of pseudo-islets upon the glucose challenge. RNA was isolated after 30 min of high-glucose treatment at 20 mM glucose. In total, DCN-treatment led to a total of 348 differentially expressed genes, 84 of which were associated with a KEGG pathway (**Fig. 3 A**). 51 of these 84 genes were β-cell-related and classified to pathway networks related to ER, calcium-signaling, cyclic guanosine monophosphate (cGMP), semaphorin, mitogen-activated protein kinase (MAPK), Type 2 DM, and oxidative phosphorylation (OxPhos) (**Fig. 3 B**). Of special interest were the genes related to OxPhos (**Fig. 3 C, D**) and ER (**Fig. 3 E, F**). In the OxPhos network, all genes that were differentially expressed were related to the electron transport chain and were significantly upregulated in pseudo-islets +DCN (**Fig. 3 D**). This indicates an increased mitochondrial activity in the DCN-treated cells after high-glucose treatment at 20 mM glucose. In the ER network, 8 of 10 genes were significantly upregulated after DCN-treatment (**Fig. 3 F**). Among other tasks, the ER in β-cells is responsible for the folding and transport or proteins, such as insulin. Detailed NGS results are available in the data repository.

Urbanczyk & Jeyagaran et al.
Decorin improves human pancreatic β-cell function and regulates ECM expression in vitro

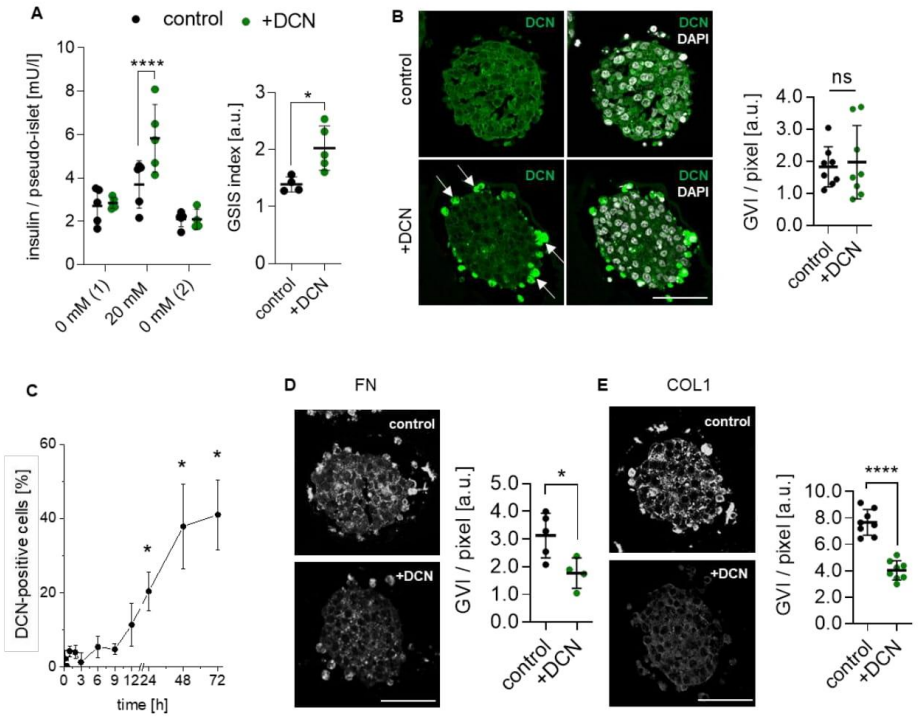

Fig. 2: DCN stimulates pseudo-islet functionality in suspension cultures and modulates ECM expression. (**A**) DCN treatment in vitro stimulates functionality of pseudo-islets. 1-way ANOVA with Tukey's multiple comparison test (n ≥ 4), ****$p < 0.0001$. Unpaired t-test (n ≥ 4), *$p < 0.05$. (**B**) DCN-treatment resulted in strong expression of DCN in cells on the outside of the pseudo-islets (white arrows) with no difference in overall GVI per pixel (n = 8). Unpaired t-test. (**C**) DCN-positive cells on the periphery of the pseudo-islets are seen as early as 24 h after DCN treatment. 1-way ANOVA with Tukey's multiple comparison (n ≥ 6), *$p < 0.05$. Quantification of (**D**) FN (n ≥ 4) and (**E**) COL1 (n = 8) IF staining shows a significant decrease for both ECM proteins upon DCN treatment. Unpaired t-test, *$p < 0.05$, ****$p < 0.0001$. Scale bars equal 50 µm.

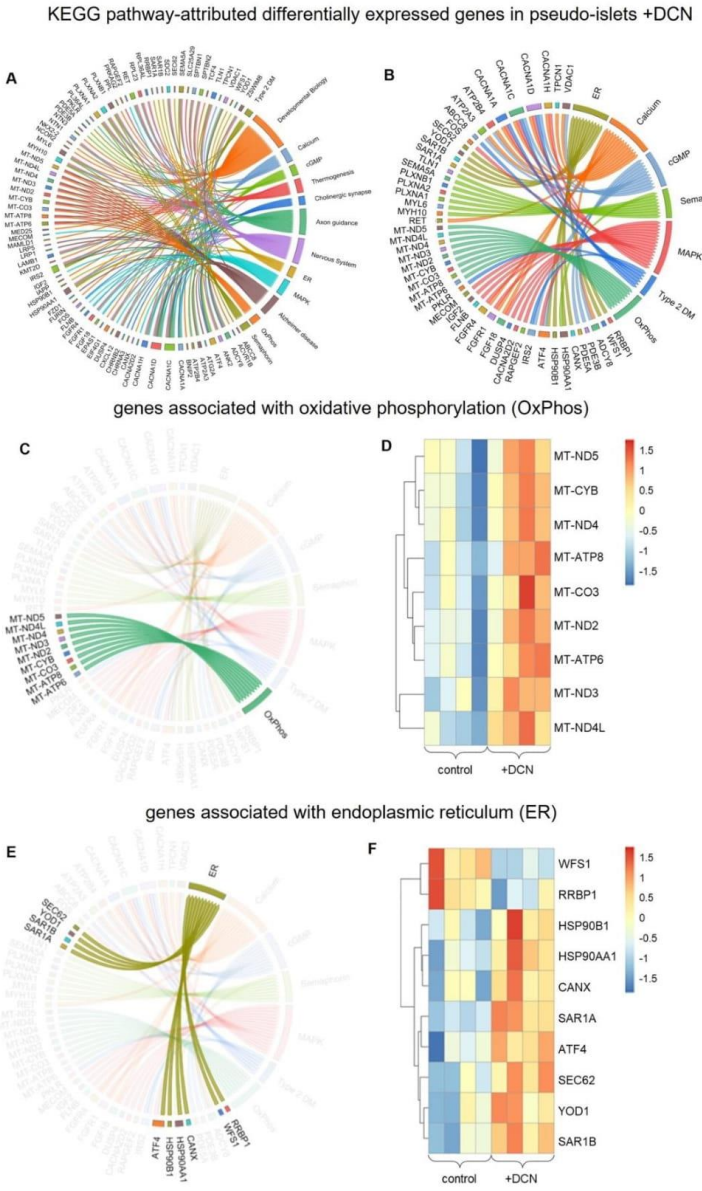

Fig. 3: NGS identifies differentially expressed genes in pseudo-islets +DCN. RNA was harvested immediately after high-glucose treatment of the pseudo-islets to identify genes affected by the DCN-treatment during insulin secretion (n = 4). (**A**) 84 differentially expressed genes were matched to specific pathways using the KEGG database after DCN treatment. (**B**) 51 of these 84 genes are β-cell-related genes that have roles in 7 different pathways and mechanisms. (**C**) 9 genes related to OxPhos were differentially expressed. (**D**) All of these 9 genes were upregulated after DCN-treatment. (**E**) 10 genes related to the endoplasmic reticulum were differentially expressed in pseudo-islets +DCN. (**F**) 8 of these 10 genes were upregulated after DCN-treatment. Genes were classified as differentially expressed with $p_{adjusted} < 0.05$.

386 *Raman imaging confirms changes in the endoplasmic reticulum of DCN-treated pseudo-islets*

387 Raman imaging was employed to further identify potential biochemical changes in the DCN-
388 treated pseudo-islets with special focus on the ER. The acquired Raman data were analyzed
389 using TCA as well as PCA. TCA is a quantitative Raman image analysis method that provides
390 unique insight into the spatial distribution of pixels with specific spectral characteristics, which
391 can be used to locate different components within a sample or tissue. In contrast, PCA is a
392 more qualitative analysis method that gives further insights in differences of the overall
393 molecular composition between samples and tissues [21]. TCA was performed to localize three
394 major components of interest within control pseudo-islets and pseudo-islets +DCN, namely the
395 general ECM component as well as the specific components for DCN and the ER (**Fig. 4 A, B**).
396 The spectrum for the general ECM component was obtained as described earlier [8]. The
397 spectra for the DCN and the ER components were obtained by measuring cellular areas
398 positively stained for DCN and ER, respectively (**Suppl. Fig. S3**). We defined the ER spectrum
399 by averaging Raman spectra obtained from pixels that stained positively for the ER tracker.
400 The resulting ER spectrum showed characteristic peaks (750, 1001, 1128, 1303, 1446 and
401 1606 cm^{-1} (**Suppl. Fig. S3 F**)) for protein-rich regions similar to those described by Prats Mateu
402 et al. [33]. It should be mentioned that especially the peak at 750 cm^{-1} is usually described for
403 cytochrome-c, a protein of the mitochondrial membrane, indicating contributions of other cell
404 organelles to this ER spectrum [34]. The TCA false color images of the three components did
405 not show any differences in GVI per pixel (**Suppl. Fig. S4, B** (ECM): 0.32 ± 0.05 control vs 0.38
406 ± 0.10 +DCN; n = 3, $p = 0.49$; **E** (DCN): 0.45 ± 0.15 control vs 0.33 ± 0.03 +DCN; n = 3, $p = 0.35$;
407 **H** (ER): 0.49 ± 0.05 control vs 0.43 ± 0.06 +DCN; n = 3, $p = 0.28$). Evaluation by component-
408 positive area (**Suppl. Fig. S4, C** (ECM): 65.55 ± 8.97 % control vs 70.04 ± 14.00 % +DCN; n =
409 3, $p = 0.72$; **F** (DCN-positive area): 45.47 ± 8.64 % control vs 45.45 ± 4.84 % +DCN; n = 3, $p =$
410 1.00; **I** (ER): 74.00 ± 1.62 % control vs 74.32 ± 8.60 % +DCN; n = 3, $p = 0.96$) between control
411 and DCN-treatment did not show any significant differences; however, PCA, which gives
412 insights about the biochemical composition of the ER component showed a separation between
413 control pseudo-islets and pseudo-islets +DCN (**Fig. 4 C**) with a significant difference between
414 the mean PC-2 loading scores (**Fig. 4 D**: -0.003 ± 0.0007 control vs 0.003 ± 0.003 +DCN; n = 3,
415 $*p < 0.05$). As the mean PC-2 loading score is positive for pseudo-islets +DCN (**Fig 4 D**), the
416 changes after DCN-treatment can be attributed to positive peaks in the PC-2 loading plot indicating
417 increase in phosphatidylinositol (PI) (415, 516, and 770 cm^{-1}) (**Fig 4 E**). In contrast, control
418 pseudo-islets with a negative mean PC-2 loading score (**Fig. 4 D**) were characterized by negative
419 peaks for triacylglycerol (TAG) (1252 and 1300 cm^{-1}) and cholesterol (1444 and 1659 cm^{-1}) (**Fig.**
420 **4 E**). Peak intensity analysis of the ER Raman spectra of control pseudo-islets and pseudo-islets
421 +DCN, which gives a quantitative result about the levels of the different components, indicated
422 significant differences between both groups (**Fig. 4 F-H**, **Suppl. Fig. S5 G**). While PI levels were
423 significantly upregulated upon DCN-treatment (**Fig. 4 F**), TAG and cholesterol levels were
424 significant downregulated upon DCN-treatment (**Fig. 4 G, H**). PCA of the ECM component (**Suppl.**
425 **Fig. S5 A-C, B** (PC-1): -0.0007 ± 0.003 control vs 0.001 ± 0.007 +DCN; n = 3, $p = 0.77$; **C** (PC-
426 2): 0.0006 ± 0.002 control vs 0.0007 ± 0.0009 +DCN; n = 3, $p = 0.47$) and the DCN component
427 (**Suppl. Fig. S5 D-F, E** (PC-1): -0.002 ± 0.003 control vs 0.003 ± 0.004 +DCN; n = 3, $p = 0.25$**; F**
428 (PC-2): 0.002 ± 0.002 control vs -0.002 ± 0.002 +DCN; n = 3, $p = 0.08$) did not show any significant
429 separation between both groups. A detailed description of the peaks and their assignments can
430 be found in **Suppl. Table S3**.

Urbanczyk & Jeyagaran et al.
Decorin improves human pancreatic β-cell function and regulates ECM expression in vitro

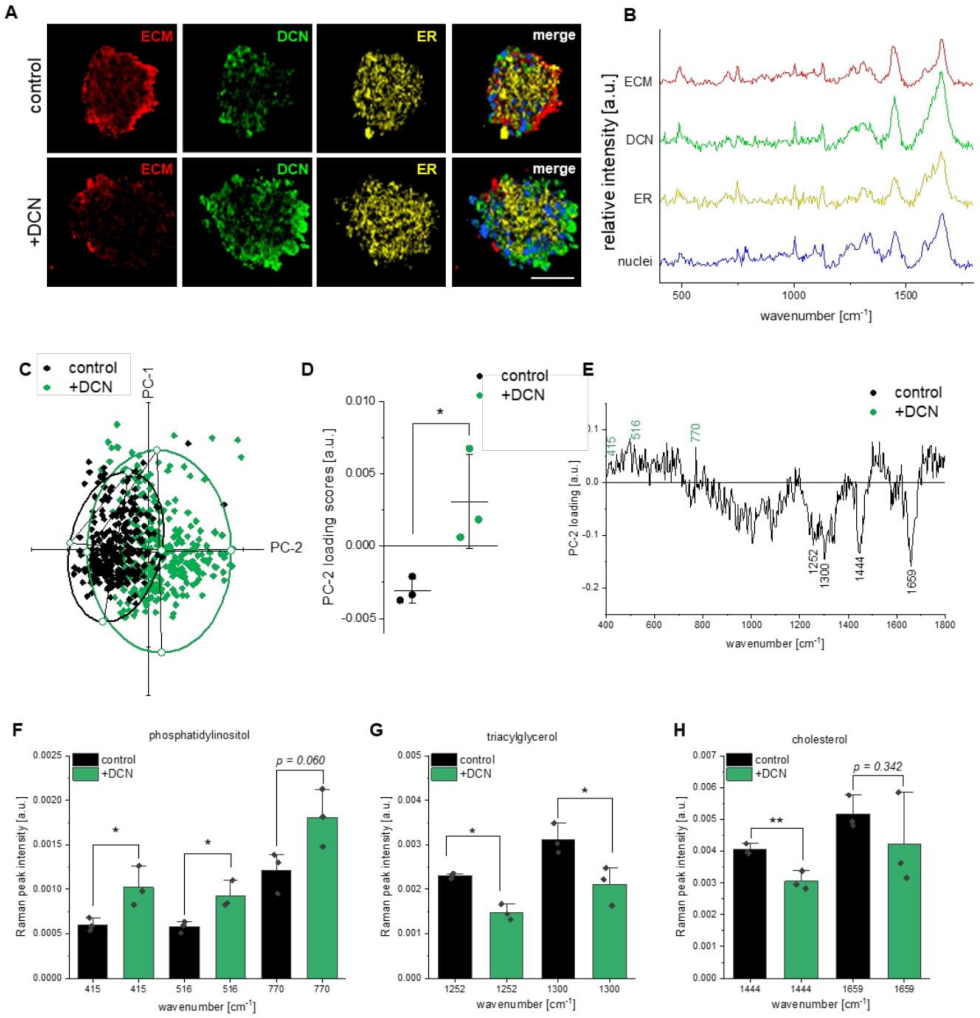

Fig. 4: Raman imaging of live pseudo-islets under 20 mM glucose. (**A**) Application of Raman spectra for ECM, DCN, and ER on live control pseudo-islets and pseudo-islets +DCN. Scale bar equals 50 µm. (**B**) Corresponding representative Raman spectra of ECM, DCN, ER, and nuclei. (**C**) PCA of the obtained ER component shows a separation via PC-2 between control pseudo-islets and pseudo-islets +DCN. (**D**) Comparing the PC-2 loading scores of 100 spectra shows a significant difference between control and pseudo-islets +DCN (n = 3). Unpaired t-test, $*p < 0.05$. (**E**) Loading of PC-2 indicates an increased expression of PI (peaks at 415, 516, and 770 cm^{-1}) in pseudo-islets +DCN compared with the control cultures while control pseudo-islets showed an increased presence of TAG (peaks at 1252 and 1300 cm^{-1}) and cholesterol (peaks at 1444 and 1659 cm^{-1}). Upon DCN-treatment, (**F**) PI levels are increased in pseudo-islets, whereas levels of (**G**) TAG and (**H**) cholesterol are decreased (n = 3). Unpaired t-tests, $*p < 0.05$, $**p < 0.01$.

GMP-grade COL1 and DCN mimic features of the native pancreatic environment in support of pseudo-islets in vitro

To determine whether DCN has similar effects in a biomaterial suitable for islet transplantation, pseudo-islets were encapsulated within a clinical grade, good manufacturing practice (GMP)-approved COL1 gel [23] as a carrier material and treated with DCN. To investigate the structural distribution of the native fibrillar collagen network within the islets of Langerhans in vivo, we performed IF staining of human native pancreatic tissue (**Fig. 5 A, B**). We were able to mimic the observed pattern by encapsulating our pseudo-islets in a COL1 hydrogel (**Fig. 5 C, D**). Evaluation of the stiffness of a pure COL1 gel and a COL1 gel with pseudo-islets showed a significant difference of the elastic modulus for both groups (**Fig. 5 E**, 3.1 ± 0.24 COL1 gel vs 4.1 ± 0.23 COL1 gel with pseudo-islets, n ≥ 4, ****p < 0.001*); however, both groups lied within the stiffness range of pancreatic tissue reported in the literature [35–37]. IF staining for DCN of control pseudo-islets and pseudo-islets +DCN in the COL1 gel showed that DCN in control pseudo-islets was homogeneously distributed, whereas DCN-treated pseudo-islets in the gel showed a DCN-positive layer of cells in the periphery of the pseudo-islets (**Fig. 5 F**, white arrows). Overall, there were no significant differences of GVI per pixel between both groups (1.84 ± 1.52 control vs 1.80 ± 0.88 +DCN, n ≥ 12, *p = 0.95*). This result is comparable to the results obtained in pseudo-islets treated with DCN in suspension. We further confirmed this observation by employing Raman imaging on fixed control pseudo-islets and fixed pseudo-islets +DCN in the COL1 gel (**Fig. 5 G, Suppl. Fig. S6 B**). We conducted TCA on the same three main components (ECM, DCN, and ER) and evaluated the component-positive area as described earlier for pseudo-islets in suspension. TCA false color images displayed a significant decrease of the component-positive area for ECM within pseudo-islets +DCN (**Fig. 5 H**, 69.16 ± 4.45 % control vs 11.77 ± 5.12 % +DCN, n = 3, ****p < 0.001*). The component-positive area for DCN was significantly higher in pseudo-islets +DCN compared to the control (**Fig 5 I**, 22.72 ± 1.48 % control vs 45.89 ± 7.07 % +DCN, n = 3, **p < 0.05*). The ER component showed no difference between both groups (**Fig. 5 J**, 60.38 ± 9.67 % control vs 23.11 ± 19.67 % +DCN, n = 3, *p = 0.07*). The GVI per pixel of the ECM component was significantly decreased in the DCN-treated pseudo-islets (**Suppl. Fig. S6 B, C,** 0.95 ± 0.04 control vs 0.83 ± 0.03 +DCN, n = 3, **p < 0.05*), confirming the results of the component-positive area evaluation. GVI per pixel of the DCN component (**Suppl. Fig. S6 D, E,** 0.56 ± 0.02 control vs 0.61 ± 0.03 +DCN, n = 3, *p = 0.09*) and the ER component (**Suppl. Fig. S6 G, H,** 0.40 ± 0.09 control vs 0.51 ± 0.17 +DCN, n = 3, *p = 0.45*) showed no significant difference between both groups; however, the numbers followed a similar trend as the component-positive area evaluation. PCA of the components ECM and DCN did not show any separation between both groups (**Suppl. Fig. S7 A-F, B** (ECM, PC-1), 0.0019 ± 0.0016 control vs -0.0019 ± 0.0015 +DCN, n = 3, *p = 0.07*; **C** (ECM, PC-2), -0.0001 ± 0.0014 control vs -0.0001 ± 0.000.0006 +DCN, n = 3, *p = 0.85*; **E** (DCN, PC-1), 0.0019 ± 0.0030 control vs -0.0019 ± 0.0032 +DCN, n = 3, *p = 0.29*; **F** (DCN, PC-2), 0.0011 ± 0.0016 control vs -0.0014 ± 0.0035 +DCN, n = 3, *p = 0.42*). Interestingly, PCA of the ER component (**Suppl. Fig. S7 G**) showed a significant difference between control pseudo-islets and pseudo-islets +DCN attributed to PC-1 (**Suppl. Fig S7 H**, 0.0043 ± 0.0016 control vs -0.0042 ± 0.0031 +DCN, n = 3, **p < 0.05*). Differences between both groups were attributed to cholesterol (1442 and 1602 cm^{-1}) as well as TAG (1249 and 1300 cm^{-1}) (**Suppl. Fig. S7 J, K**). After DCN-treatment, cholesterol peaks at 1442 cm^{-1} were significantly upregulated, whereas cholesterol peaks at 1662 cm^{-1} were significantly downregulated (**Suppl. Fig. S 7 L**), indicating structural differences of cholesterol, such as cis or Z-confirmation found in fatty acids, rather than quantitative differences [38]. Interestingly, the decrease in TAG due to the DCN-treatment were preserved in the COL1 gel represented by a significant decrease in the peak intensity at 1249 cm^{-1}. The peak at 1300 cm^{-1} did not show a statistically significant decrease (**Suppl. Fig. 7 M**). Overall, the observed effects of the DCN-treatment on β-cell-containing pseudo-islets in suspension could be recapitulated in an encapsulation environment, especially regarding the DCN-binding to the periphery of the pseudo-islets as well as the rearrangement of the expressed ECM. These results suggest the suitability of COL1 as a potential carrier material to use DCN in an islet transplantation environment.

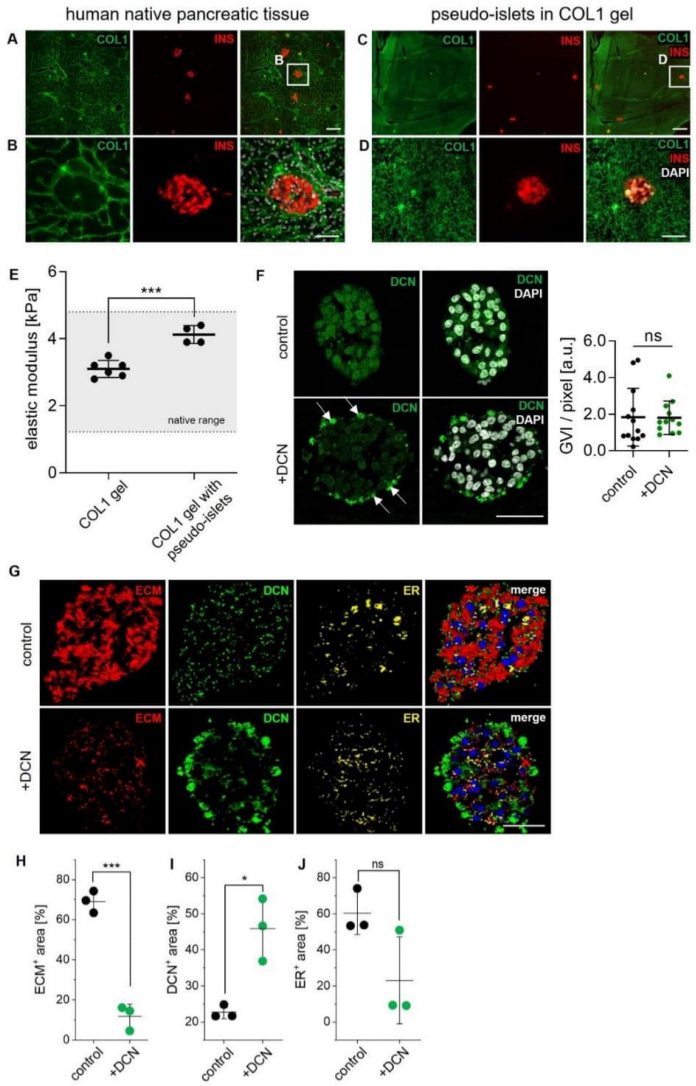

494

495 **Fig. 5: Structural evaluation of control pseudo-islets and pseudo-islets +DCN in COL1 gel.** (**A, B**) Distribution of islets of
496 Langerhans in native pancreatic tissue surrounded by a COL1 matrix. (**C, D**) Pseudo-islets in a COL1 gel recreates native distribution
497 of islets of Langerhans in vivo. Scale bars equal 200 µm (**A, C**) and 50 µm (**B, D**). (**E**) Evaluation of the elastic modulus of pure COL1
498 gel and COL1 gel loaded with pseudo-islets in comparison to the elastic modulus of the of native pancreatic tissue according to
499 literature shown in grey (n ≥ 4). (**F**) Pseudo-islets in COL1 gel +DCN show DCN-positive cells on the outside of the pseudo-islets with
500 no difference in overall GVI per pixel (n ≥ 12). (**G**) Raman images of unstained sections of control pseudo-islets and pseudo-islets
501 +DCN in COL1 gel presenting the components for ECM, DCN, ER, and the merged image including the nuclei component. Scale bar
502 equals 50 µm. Area percentage analysis of (**H**) ECM component (n = 3), (**I**) DCN component (n = 3) and (**J**) ER component (n = 3)
503 confirms the presence of DCN on the outside of the pseudo-islets and show an overall decrease in ECM content in pseudo-islets in
504 COL1 gel +DCN compared to control. Unpaired t-test, $*p < 0.05$, $***p < 0.001$.

505 *DCN improves insulin secretion and impacts ECM patterns of β-cell-containing pseudo-islets*
506 *embedded in a COL1 gel*

507 After confirming that the interaction of DCN and pseudo-islets in the COL1 gel were comparable
508 to the parameters observed in suspension, the effects of DCN on pseudo-islet function in the
509 COL1 gel were investigated. Upon glucose challenge, pseudo-islets +DCN secreted significantly
510 more insulin than the control group (**Fig. 6 A**, 50.19 ± 6.68 mU/l control vs 61.53 ± 24.15 mU/l
511 +DCN at 0 mM glucose; n ≥ 7, $p = 0.20$; 98.82 ± 12.86 mU/l control vs 119.41 ± 14.57 mU/l +DCN
512 at 20 mM glucose; n ≥ 8, $*p < 0.05$); however, the GSIS index was not affected (**Fig. 6 B**, 1.97 ±
513 0.09 control vs 1.94 ± 0.21 +DCN; n ≥ 7, $p = 0.75$). IF staining for both INS (**Fig. 6 C**, 3.88 ± 1.03
514 control vs 7.13 ± 3.17 +DCN; n ≥ 8, $**p < 0.01$) and E-cadherin (**Fig. 6 D**, 4.06 ± 0.99 control vs
515 6.75 ± 2.38 +DCN; n ≥ 8, $**p < 0.01$) showed a significant increase in pseudo-islets +DCN
516 compared to control, supporting the results from the GSIS assay. Evaluation of the impact of DCN
517 on the pseudo-islet ECM showed that DCN-treatment significantly decreased COL1 (**Fig. 6 E**,
518 2.27 ± 0.61 control vs 0.98 ± 2.38 +DCN; n ≥ 9, $****p < 0.0001$) and LAM contents (**Fig. 6 F**, 11.40
519 ± 1.77 control vs 5.78 ± 1.89 +DCN; n = 10, $****p < 0.0001$). In contrast, COL4 intensity was
520 significantly increased after DCN-treatment compared to the control (**Fig. 6 G**, 0.79 ± 0.57 control
521 vs 1.69 ± 0.67 +DCN; n ≥ 6, $*p < 0.05$). DCN-treatment of pseudo-islets in the COL1 gel did not
522 influence the expression intensity of FN (**Suppl. Fig S8**, 2.51 ± 1.11 control vs 2.66 ± 1.29 +DCN;
523 n ≥ 13, $p = 0.76$).

Urbanczyk & Jeyagaran et al.
Decorin improves human pancreatic β-cell function and regulates ECM expression in vitro

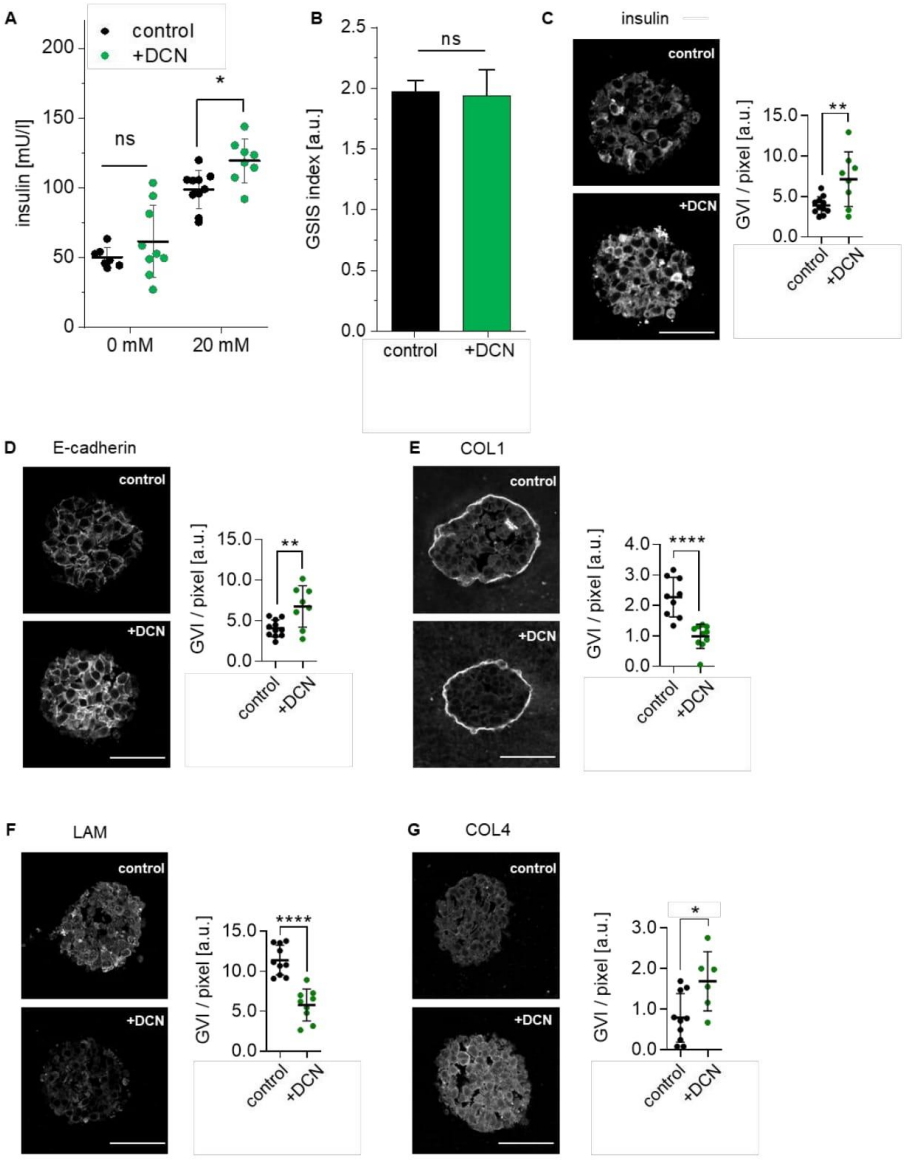

Fig. 6: Functionality and ECM assessment of control pseudo-islets and pseudo-islets +DCN in COL1 gel. (**A**) Pseudo-islets in COL1 gel +DCN show significantly increased insulin secretion after high-glucose treatment compared to the control (n ≥ 7). 1-way ANOVA with Fisher's multiple comparison, *$p < 0.05$. (**B**) GSIS index of pseudo-islets +DCN in COL1 gel shows no significant difference compared to the control. Pseudo-islets +DCN in COL1 gel show significantly increased expression of (**C**) INS (n ≥ 8), (**D**) E-cadherin (n ≥ 8), and the BM protein (**G**) COL4 (n ≥ 6). In contrast, DCN-treatment significantly decreases the expression of (**E**) COL1 (n ≥ 9) and (**F**) LAM (n ≥ 9). Unpaired t-test, **$p < 0.01$, ****$p < 0.0001$. Scale bars equal 50 µm.

Discussion

Research in the field of islet transplantation has progressed immensely over the last decade; however, clinical translation of the findings has been rather slow. The treatment and encapsulation of islets within materials based on native ECM proteins has been shown to support cell survival and function in a transplantation setting. In this study, we identified DCN to be highly co-localized with insulin-producing β-cells in human pancreatic tissues. We identified that DCN-treatment increased the glucose-responsiveness of our in vitro pseudo-islet model. DCN-treatment also reduced the expression of FN and COL1, ECM proteins affiliated with fibrosis. Further analysis using next-generation sequencing and Raman microspectroscopy identified changes in mitochondrial activity and ER because of the DCN-treatment. When the pseudo-islets were encapsulated within a clinically approved COL1 gel, the positive effects of DCN-treatment on glucose-responsiveness and ECM expression were maintained, suggesting that the advantages of DCN-treatment may be translatable to a transplantation setting.

DCN is a small leucine-rich proteoglycan involved in the regulation of multiple cellular processes including cell growth, proliferation, and migration. In particular, it has been investigated for its anti-tumorigenic effects through antagonizing key receptor tyrosine pathways involved in cancer progression and sequestering of growth factors within the ECM [39]. These properties were achieved through its role in preventing fibrillogenesis of fibrillar proteins such as COL1, as well as tumor-suppression via p53 signaling [40]. Within the pancreas, DCN was found to be most expressed by pancreatic pericytes forming the interstitial matrix and islet BM to support β-cells [41]. In the mouse model of insulinoma where there is an excess production of insulin by β-cells, DCN was found to be significantly downregulated [42]. In our study, DCN-treatment increased the glucose-responsiveness of the pseudo-islets. While little work has been done in understanding the role of this proteoglycan in the environment of a pancreatic islet, it is known that DCN plays a role in glucose tolerance. Mice lacking DCN had impaired glucose tolerance, which was associated with reduced ECM organization and increased activation of the complement cascades, promoting inflammation [43]. Interestingly, these effects of glucose intolerance and inflammation in DCN knockout mice could be attributed to the increased expression of histidase, a protein that degrades histidine. The amino acid histidine has been shown to ameliorate insulin resistance, inflammation, and oxidative stress when supplemented [44–46]. The protective effect of DCN in terms of modulating inflammation can be further advantageous in a transplantation setting. In response to a transplanted graft, the host's immune system attempts to repair the damaged tissue and limit the interaction with the foreign material at the transplant site. This results in the transplanted device becoming enclosed within a dense layer of inflammatory cells and connective tissue [47]. During this process, the ECM is remodeled to support the regeneration of the tissue resulting in the deposition of ECM proteins such as FN and the fibrillar COL1 [48], which ultimately isolates the transplanted device from the host's system, rendering the transplant ineffective. Interestingly, in our study, DCN-treatment significantly downregulated the presence of ECM proteins FN and COL1, in line with past research that identified DCN as a modulator of scar tissue formation and reduced inflammatory responses [49–51]. These observations were recapitulated in our in vitro model in which the pseudo-islets were encapsulated within a COL1 carrier gel. Similar to the effect seen in our suspension cultures, DCN treatment of the encapsulated pseudo-islets improved the glucose response and modulated the presence of the COL1. While FN was not significantly affected by the DCN treatment in the gel as it did in suspension, LAM were found to be significantly downregulated and COL4 was significantly upregulated upon DCN treatment. Taken together our functional data of the pseudo-islets and the regulation of ECM presence, DCN-treatment has the potential to support islet transplantation by improving islet functionality and supporting graft survival post-transplantation through modulation of fibrotic tissue formation.

To investigate potential cellular processes through which the DCN-treatment improves insulin secretion in β-cells, pseudo-islets challenged with a high glucose concentration were used for NGS analysis. In our DCN-treated pseudo-islets, NGS results identified genes associated with the

582 mitochondrial electron transport chain and the ER to be differentially expressed. The electron
583 transport chain is the final step of cellular respiration in the mitochondria for the production of ATP
584 through OxPhos [52], and is essential for the appropriate secretion of insulin by β-cells [53,54]. An
585 upregulation of genes involved in the protein complexes of the electron transport chain is seen in
586 the DCN-treated samples. This supports our observations of increased insulin secretion in the
587 DCN samples where greater levels of ATP are required for the highly metabolic process of insulin
588 production and secretion. Isolated mitochondria from β-cells revealed a significant decrease in
589 electron transport activity in the glucose-unresponsive cells when compared with glucose-
590 responsive cells [55]. Further, it has been shown that reduced electron transport chain activity,
591 expression, and mitochondrial DNA has been associated with increased insulin resistance and
592 Type 2 DM [56], supporting our finding of high metabolic activity of β-cells after DCN-treatment.

593 The ER is responsible for precise protein synthesis and trafficking to the necessary cellular
594 compartments. Cells undergo ER stress when there is an accumulation of misfolded proteins at
595 which point, they activate response pathways including ER-associated degradation (ERAD) and
596 the unfolded protein response (UPR). Through these pathways, they degrade misfolded proteins
597 and increase the presence of molecular chaperones required for proper protein folding. β-cells
598 experience high levels of ER stress due to the secretion of insulin upon glucose challenge [57–
599 60]. The increased amount of secretory proteins (in this case insulin) and proteins involved in the
600 trafficking of said proteins allows for a greater number of proteins that can be misfolded, increasing
601 ER stress [61]. It has been suggested that approximately 20% of proinsulin is misfolded [62–64],
602 at which point the protein is degraded. Studies have also shown that this high requirement of the
603 ER can also be the cause of β-cell dysfunction and loss, leading to the progression of Type 2 DM
604 [65–67]. Our NGS data showed that the ER proteins Wolframin ER transmembrane glycoprotein
605 (WFS1) and Ribosome Binding Protein 1 (RRBP1) were downregulated in the DCN-treated
606 samples. WFS1 is a calcium (Ca^{2+}) channel that allows Ca^{2+} to enter the ER [68], which is found
607 primarily within the β-cells of the pancreatic islets [69]. Ca^{2+} plays a key role in both protein folding
608 and insulin secretion, where ER stress is known to lead to a decrease in Ca^{2+} within the ER [70,71].
609 The reduced WFS1 at the ER can increase Ca^{2+} oscillations within the cytosol, increasing the
610 amount of Ca^{2+} being secreted as a result of the DCN-treatment. There have been conflicting
611 studies indicating the role of WFS1 in the cellular response to ER stress. Within the pancreatic
612 islet, WFS1 expression at the mRNA and protein levels were increased following drug-induced
613 ER stress [69]. It has also been shown that the loss of WFS1 can lead to ER stress and β-cell
614 dysfunction [72], where mutations in the WFS1 gene, associated with Wolfram syndrome, also
615 leads to the onset and progression of type 2 diabetes [73]. Additionally, we observed a
616 downregulation of RRBP1. RRBP1 is involved in the interaction of the ribosomes to the ER to
617 support protein translation and transport, where knockdown of this protein resulted in ER stress
618 [74]; however, a genomic and proteomic study in murine islets, showed that RRBP1 was
619 upregulated in mice with Type 2 DM, suggesting it may have a role in β-cell dysfunction [75].

620 NGS identified further genes associated with ER stress including heat shock proteins (HSPs),
621 ATF4, and YOD1 to be upregulated in the DCN-treated samples. HSP90A is an indicator of cellular
622 stress, particularly in response to inflammation [76], and is also associated with the onset of Type
623 1 DM [77]. ATF4 is a transcription factor that plays a key role in response to ER stress, through
624 activation of 4E-BP1 expression [58,78]. The upregulation of the HSPs and ATF4 in the DCN-
625 treated samples can be in response to the cellular stress caused by the increased demand for
626 protein production and trafficking within the ER to maintain homeostasis. YOD1 is a deubiquitinase
627 involved in ERAD for the degradation and removal of lysosomes [79]. Its upregulation in the DCN-
628 treated samples implies its necessity for both the processing of autophagocytosed DCN and
629 quality control of the increased amount of protein (insulin) produced and trafficked.

630 Interestingly, Raman spectroscopy also identified the ER component to be significantly affected
631 in the DCN-treated samples with emphasis on PI. PIs are the precursor to the many variations of

phosphoinositides that are involved in a variety of cellular processes including vesicular trafficking, engulfment, ion channel regulation, and intracellular signaling [80–82]. As such, the increased presence of PI can be attributed to the need for increased numbers of vesicles for insulin secretion. Past studies observing phospholipid presence during glucose-stimulated insulin secretion also identified an increase in PI when there is increased insulin secretion at high glucose concentrations [21,83]. Apart from an increase in PI, Raman microspectroscopy highlighted the decrease in TAG in DCN-treated samples. Sánchez-Archidona et al. identified TAGs as potential regulators of insulin secretion and insulin signaling pathways [84]. They found that reduced TAG content led to an increase in insulin secretion by increased K_{ATP}-channel expression. Furthermore, β-cells secrete lipase, a lipoprotein involved in the release of free fatty acids from TAG that increases basal insulin secretion [85]. The addition of DCN might shift the balance towards higher free fatty acid uptake by β-cells, resulting in increased insulin secretion and reduced levels of TAG in DCN-treated samples. One limitation of Raman imaging, especially for fixed pseudo-islets +DCN in COL1, is the previous embedding in paraffin. This embedding technique results in a strong Raman signal of the paraffin in the range from 1000 to 1500 cm^{-1}, which is an area of interest especially for lipids and proteins in our study. Hence, some features, especially regarding PI, TAG, and cholesterol that were observable during our in situ Raman imaging of living non-processed pseudo-islets, were potentially not identified in the COL1 gel samples in this study.

NGS analyses showed an upregulation of genes involved in protein and vesicular trafficking including CANX, SAR1A, SEC62, and SAR1B, potentially due to the increased release of insulin in secretory vesicles. CANX is a Ca^{2+}-binding protein involved in the processing and quality control of protein folding within the ER. SAR1A, SEC62, and SAR1B are involved in vesicular trafficking of proteins from the ER to the golgi apparatus in preparation for secretion. The upregulation of such genes is in line with our observations of increased insulin secretion in the DCN-treated samples. Impaired transport of (pro)insulin between the two organelles results in β-cell failure, lipotoxicity, and diabetes [86–89], where MIN6 cells, a murine pancreatic insulinoma β-cell line, mutant for Sar1A were unable to achieve proper folding of proinsulin, resulting in ER stress and β-cell failure [90,91]. The upregulation of SAR1A suggests DCN-treatment improves insulin secretion through upregulation of proteins that support the folding of insulin.

Conclusion

In this study, we demonstrated the beneficial effect of DCN on the insulin production of human β-cells. DCN-treatment improved glucose-stimulated insulin secretion of β-cells in pseudo-islets cultured in suspension, with an increased expression of genes involved in mitochondrial activity as well as protein folding and vesicle formation. Additionally, we showed that ECM expression patterns within pseudo-islets were significantly impacted by DCN treatment. Interestingly, expression of ECM proteins affiliated with the formation of fibrotic capsules were significantly downregulated in DCN-treated samples. Our findings have potential implications for the design of improved islet transplantation strategies since we showed that DCN-treatment can potentially address two major hurdles: (1) help to regenerate lost or inadequately expressed ECM of isolated islets of Langerhans [92], and (2) prevent the formation of a fibrotic capsule that commonly forms around an implant. Furthermore, increased insulin production and secretion in response to glucose is a burdensome process for the cell. DCN-treated samples were able to activate response pathways within the ER and mitochondria to cope with the increased cellular stress. Taken together, we propose that DCN-treatment of islet transplants can potentially support β-cell survival and increase function post-transplantation.

678 **Author Contributions**
679 M.U. and A.J. contributed equally to this work. M.U., A.J., A.Z., S.N., S.L.L. and K.S-L. designed
680 the experiments and wrote the manuscript. M.U., A.J., A.Z., C.L., S.N., S.L.L. and J.M. performed
681 experiments and analyzed data. L.K. analyzed data. G.D. gave conceptual advice. The main data
682 supporting the findings of this study are available within the article and its supplementary
683 information. The raw data generated in this study are available from the corresponding author
684 upon request.

685 **Declaration of competing interests**
686 The authors declare no competing financial interest.

687 **Acknowledgements**
688 We thank Prof. Peter Loskill (University Tübingen) for providing the organ-on-chip device, and
689 Mariella Bosch (University Tübingen) for her technical support. NGS methods were performed
690 with the support of the DFG-funded NGS Competence Center Tübingen (INST 37/1049-1).

691 **Funding sources**
692 This work was financially supported by the European Union (H2020-NMP10-2014-645991-2,
693 DRIVE; H2020-ITN 766181, DELIVER to G.P.D. and K.S.-L.), the International Foundation for
694 Ethical Research and the Swiss National Science Foundation (SNSF) (to A.Z.), the Ministry of
695 Science, Research and the Arts of Baden-Württemberg (33-729.55-3/214 and SI-BW 01222-91 to
696 K.S.-L.), the Deutsche Forschungsgemeinschaft (INST 2388/64-1 to K.S.-L.), and the Ministry
697 State Ministry of Baden-Wuerttemberg for Economic Affairs, Labour and Housing Construction (3-
698 4332.62-NMI/65 to K.S.-L.).

Appendix A. Supplementary figures

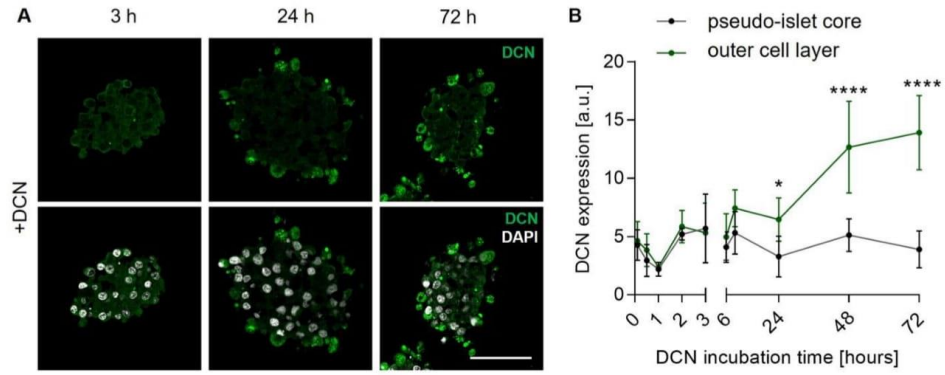

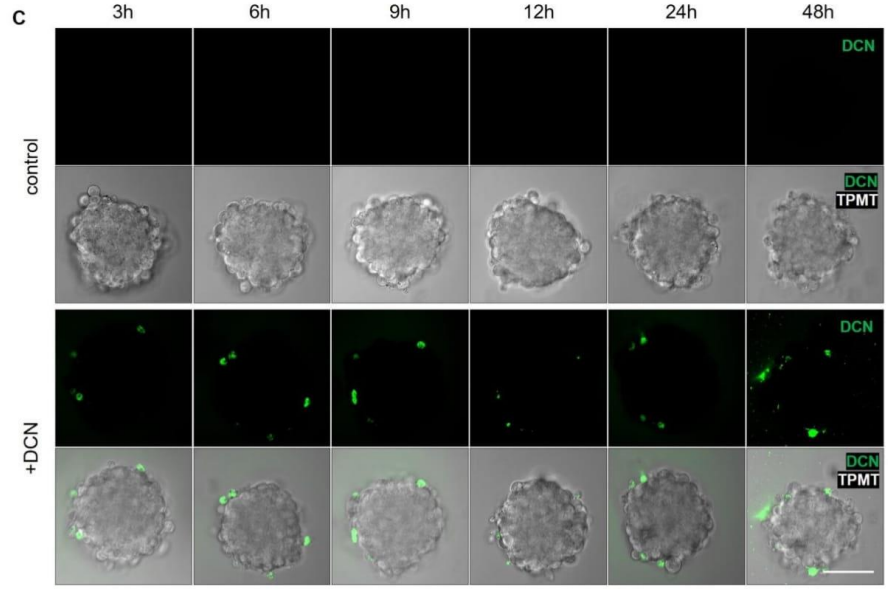

Suppl. Fig. S1: Timeseries of DCN binding to pseudo-islets via IF staining and direct protein labeling. (**A**) IF staining of DCN-treated pseudo-islets at different time points over 72h. (**B**) Quantification of DCN-positive cells in the outer layer of the pseudo-islets shows a significant increase after 24 h. (**C**) Detection of fluorescence-labeled DCN over 48 h shows DCN binding already after 3 h. Scale bars equal 50 µm.

Urbanczyk & Jeyagaran et al.
Decorin improves human pancreatic β-cell function and regulates ECM expression in vitro

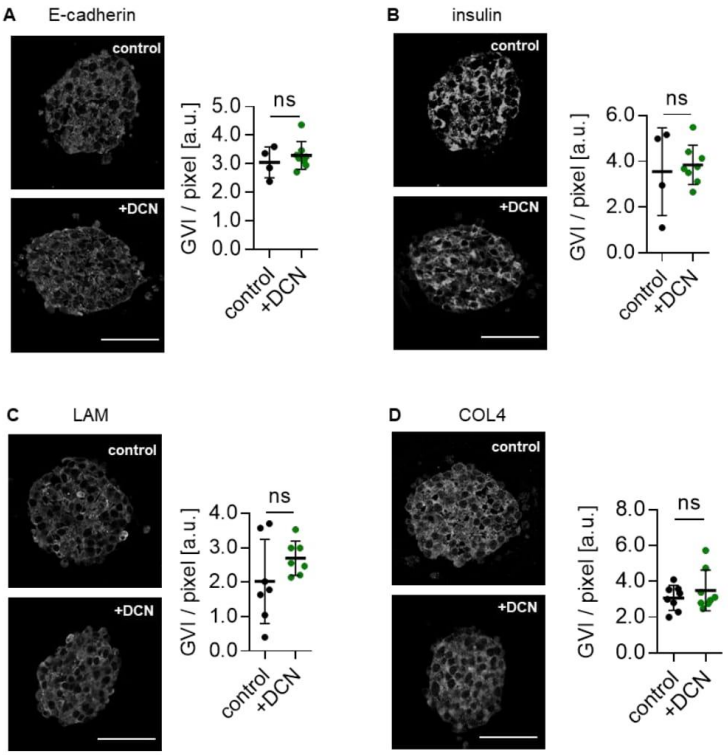

Suppl. Fig. S2: IF staining of pseudo-islets +DCN and control in suspension. Quantification of IF staining showed no significant difference between control pseudo-islets and pseudo-islets +DCN for (**A**) E-cadherin (n ≥ 4), (**B**) insulin (n ≥ 4), (**C**) LAM (n = 7) and (**D**) COL4 (n = 8). Unpaired t-test. Scale bars equal 50 µm.

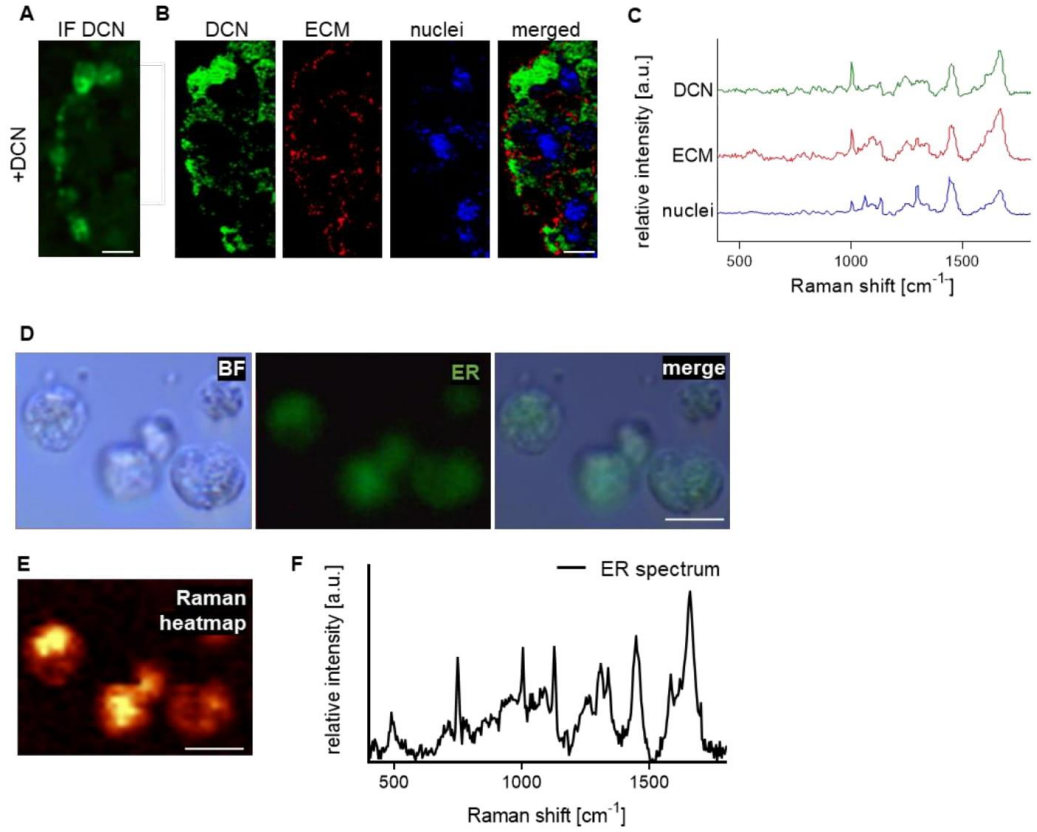

712

713 **Suppl. Fig. S3: Acquiring the Raman spectrum for DCN and ER in EndoC-βH3.** (**A**) IF staining of DCN on pseudo-islets in COL1
714 gel +DCN to establish the Raman DCN signature. Scale bar equals 10 µm. (**B**) Raman signatures attributed to DCN, ECM, and nuclei
715 with the (**C**) corresponding Raman spectrum. (**D**) Brightfield and fluorescence image of ER in the EndoC-βH3 cells stained with ER-
716 Tracker™ Green. (**D, E**) The Raman heatmap and the ER spectrum were acquired based on the detection of the fluorescence signal.
717 Scale bars equal 10 µm. (**F**) Corresponding Raman ER spectrum of pixels positively stained for ER tracker.

Urbanczyk & Jeyagaran et al.
Decorin improves human pancreatic β-cell function and regulates ECM expression in vitro

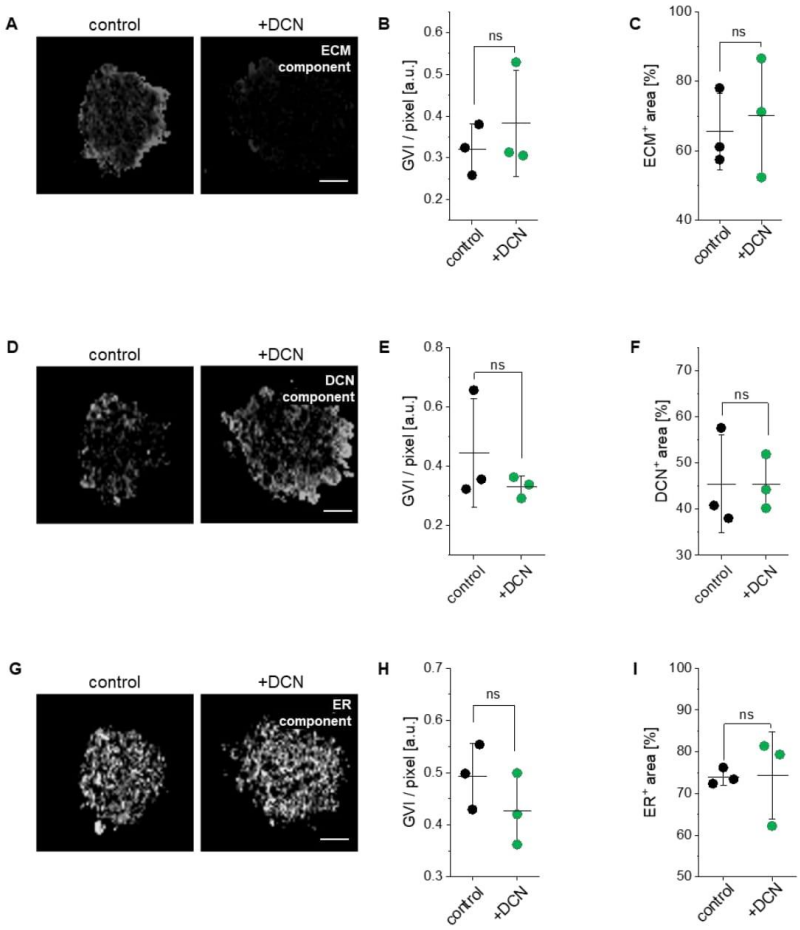

718

719 **Suppl. Fig. S4: Raman imaging and quantification of live pseudo-islets +DCN and controls.** Raman images of (**A**) ECM
720 component, (**D**) DCN component, and (**G**) ER component in live pseudo-islets +DCN and controls. Corresponding GVI and area
721 percentage analysis of (**B, C**) ECM component (n = 3), (**E, F**) DCN component (n = 3), and (**H, I**) ER component (n = 3). Unpaired t-
722 test. Scale bars equal 20 µm.

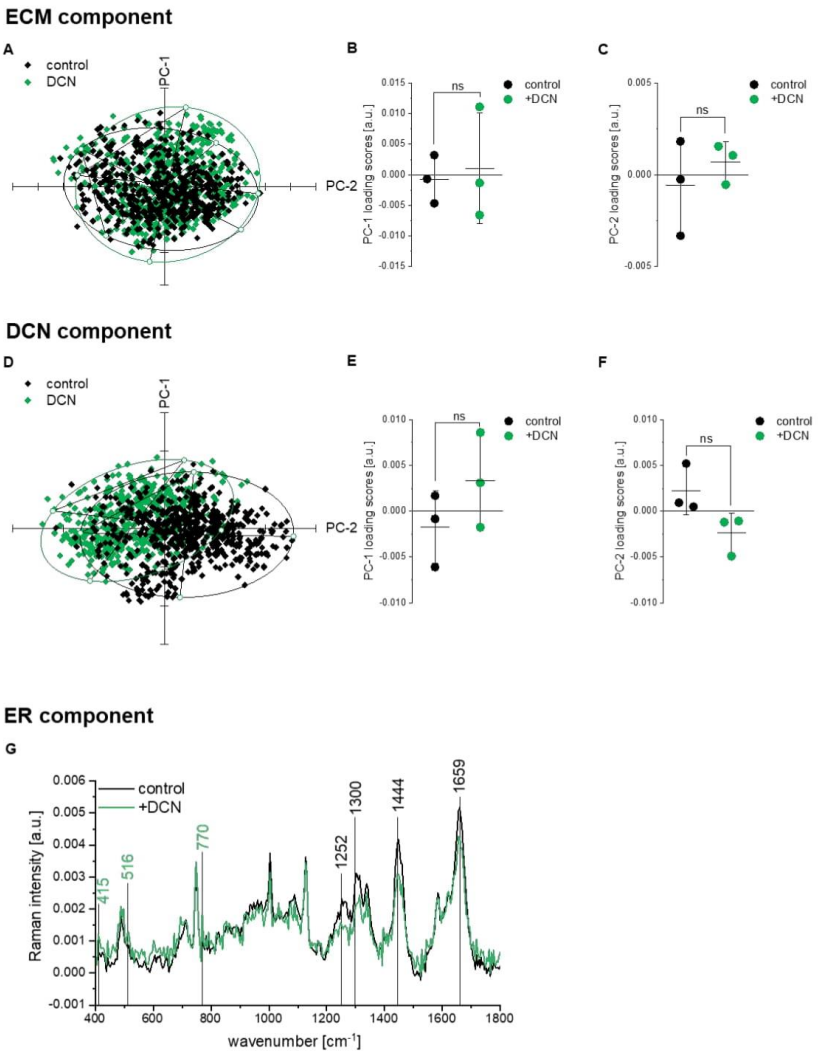

723

724 **Suppl. Fig. S5: PCA of ECM, DCN and ER components of live control pseudo-islets and pseudo-islets +DCN.** PCA of 200
725 spectra per sample (n = 3) of the obtained (**A-C**) ECM and (**D-F**) DCN component shows no separation between control and +DCN
726 pseudo-islets. (**G**) Mean ER spectrum of control pseudo-islets and pseudo-islets +DCN.

727

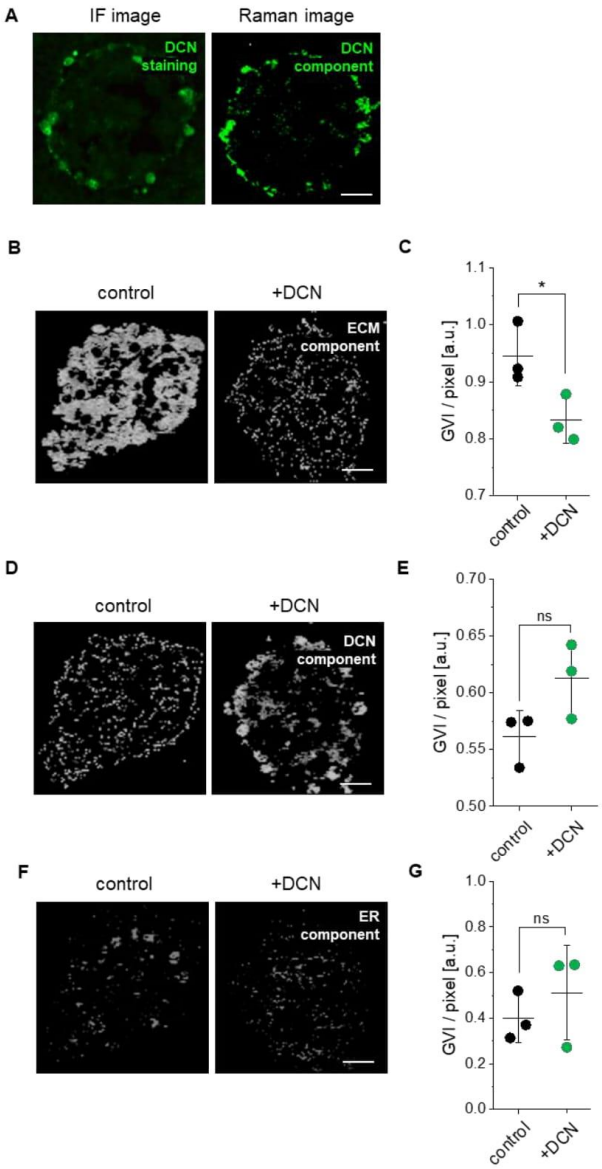

728

729 **Suppl. Fig. S6: IF staining and Raman imaging of fixed control pseudo-islets and pseudo-islets +DCN in COL1 gel.** (**A**) IF
730 staining for DCN and corresponding Raman image on unstained fixed pseudo-islets in COL1 gel +DCN. Raman image of (**B**) ECM
731 component, (**D**) DCN component and (**F**) ER component on fixed control pseudo-islets and pseudo-islets +DCN in COL1. (**C**) GVI
732 analysis of ECM signal intensity showed a significant difference between both groups (n = 3). (**E**) GVI analysis of DCN signal intensity
733 showed no significant difference between both groups (n = 3). (**G**) GVI analysis of ER signal intensity showed no significant difference
734 between both groups (n = 3). Unpaired t-tests, *$p < 0.05$. Scale bars equal 20 µm.

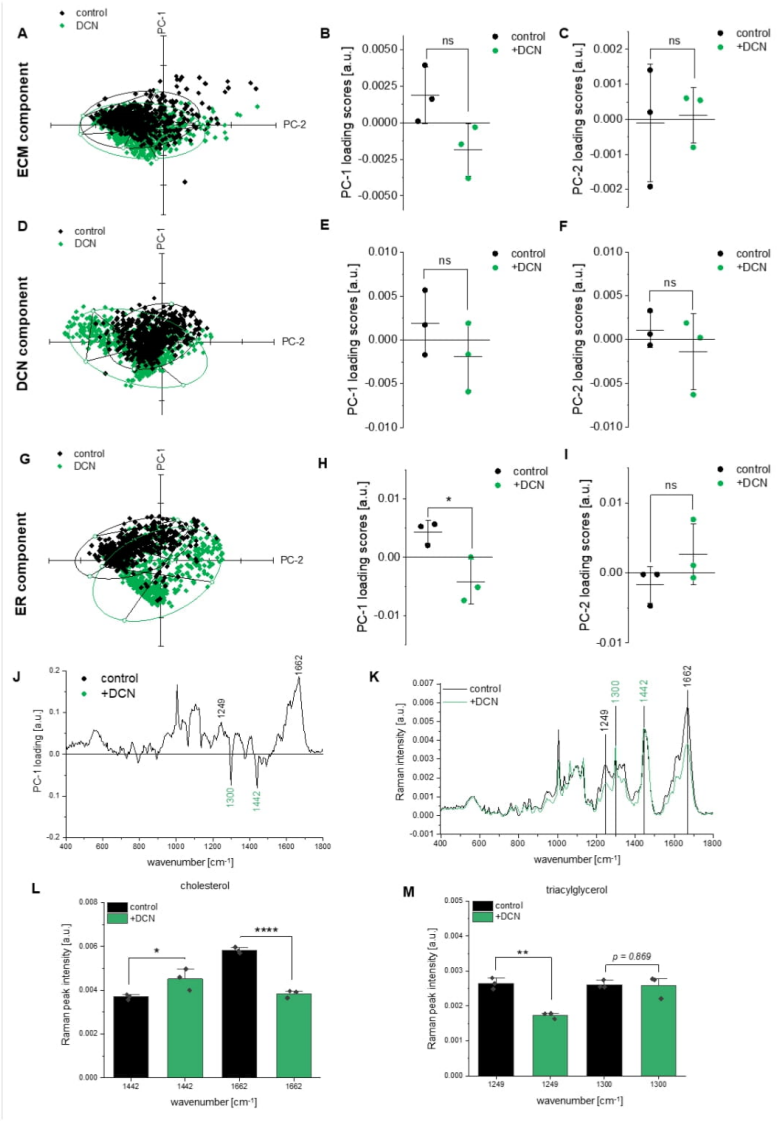

Suppl. Fig. S7: PCA of ECM, DCN and ER component of fixed control pseudo-islets and pseudo-islets +DCN in COL1 gel. PCA of 200 spectra per sample (n = 3) of the obtained (**A**) ECM, (**D**) DCN and (**G**) ER component of pseudo-islets in COL1 gel +DCN and the control. Loading scores of (**B, C**) ECM component and (**E, F**) DCN component show no significant difference. (**H**) Loading score of PC-1 of the ER component shows a significant difference between control pseudo-islets and pseudo-islets +DCN in COL1 gel. (**I**) PC-2 shows no significant difference. (**J**) Differences of PC-1 are characterized by cholesterol (1442 and 1662 cm^{-1}) and triacylglycerol (1249 and 1300 cm^{-1}) for control and +DCN in COL1 gel, respectively. (**K**) Mean ER spectrum of control pseudo-islets and pseudo-islets +DCN in COL1 gel. (**L**) Quantitative peak analysis shows an upregulation of cholesterol levels after DCN-treatment at 1442 cm^{-1}, while the peak at 1662 shows a significant downregulation (n = 3). (**M**) Quantitative peak analysis shows a downregulation of triacylglycerol levels after DCN-treatment at 1249 cm^{-1}, while the peak at 1300 cm^{-1} shows no significant difference (n = 3). Unpaired t-tests, *$p < 0.05$, **$p < 0.01$, ****$p < 0.0001$.

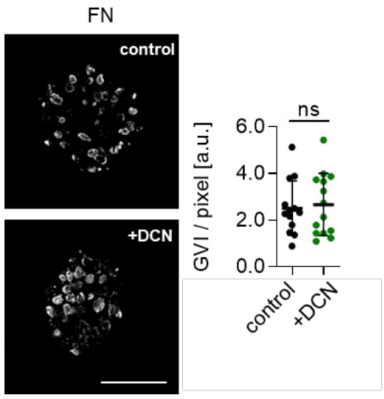

Suppl. Fig. S8: IF staining of pseudo-islets for FN in control COL1 gel (control) and COL1 gel +DCN (+DCN). IF staining for FN and quantification showed no significant difference between control pseudo-islets and pseudo-islets +DCN in COL1 gel (n = 13). Scale bar equals 50 µm. Unpaired t-test.

Appendix B. Supplementary Tables

Suppl. Table S1: List of antibodies and used antigen retrieval treatments for IF staining.

antibodies	antigen retrieval	0.1% Triton-X	dilution
primary antibodies			
Anti-Collagen 1 antibody (Acris R1038)	TRIS EDTA pH9, 8 min Citrate pH6, 8 min	-	1:250
Anti-Collagen 4 antibody (ab6586)	Citrate pH6, 8 min	-	1:250
Anti-Decorin antibody (sc-73896)	TRIS EDTA pH9, 8 min	-	1:200
Anti-Decorin antibody (GTX 101250)	TRIS EDTA pH9, 8 min Citrate pH6, 8 min	-	1:250
Anti-E-cadherin antibody (ab76055)	Citrate pH6, 8 min	15 min	1:250
Anti-Fibronectin-antibody (ab2413)	Citrate pH6, 8 min	-	1:100
Anti-Insulin-antibody (ab181547)	TRIS EDTA pH9, 8 min	15 min	1:200
Anti-Laminin-antibody (ab11575)	Citrate pH6, 8 min	-	1:50
secondary antibodies			
Alexa Fluor 488 anti-rabbit IgG(ab150077)	-	-	1:250
Alexa Fluor 488 anti-mouse IgG 1 (ab150117)	-	-	1:250
Alexa Fluor 594 anti-rabbit IgG(ab150080)	-	-	1:250

758 **Suppl. Table S2:** List variables and values used for direct labeling of DCN.

variable	explanation	value
V_{dye}	volume of dye	6.15 µl
$C_{protein,initial}$	initial concentration of the protein	2347.15 µg/ml
$V_{protein}$	volume of the protein	100 µl
$C_{activated\ dye\ solution}$	concentration of the activated dye solution	2 µMol/ml
$MW_{protein}$	molecular weight of the protein	100 kDa
MR	molar ration of the activated dye solution	5 a.u.
ε	molecular extinction coefficient	1.272 ml/(mg*cm)
A_{280}	average absorbance at 280 nm	0.15655 a.u.
b	path length of absorbance reader	0.05 cm
$C_{protein,conjugated}$	concentration of the protein after labeling	2072.47 µg/ml
A_{493}	average absorbance at 493 nm	0.058 a.u.
K	correction factor that compensates for absorbance at 280 nm	0.1 a.u.
DF	dilution factor	5 a.u.
D	degree of labeling	2.01 a.u.

759

760

761 **Suppl. Table S3**: Raman peak assignments.

peak [cm^{-1}]	assignment	reference
415	phosphatidylinositol	[93]
516	phosphatidylinositol	[94]
770	phosphatidylinositol	[93]
1252	triacylglycerol	[38]
1300	triacylglycerol	[38]
1444	cholesterol	[38]
1659	cholesterol	[38,95]

762

References

[1] E.J. Boyko, D.J. Magliano, S. Karuranga, L. Piemonti, P. Riley, P. Saeedi, H. Sun, eds., IDF Diabetes Atlas, 10th ed., 2021. https://diabetesatlas.org.

[2] B.J. Hering, W.R. Clarke, N.D. Bridges, T.L. Eggerman, R. Alejandro, M.D. Bellin, K. Chaloner, C.W. Czarniecki, J.S. Goldstein, L.G. Hunsicker, D.B. Kaufman, O. Korsgren, C.P. Larsen, X. Luo, J.F. Markmann, A. Naji, J. Oberholzer, A.M. Posselt, M.R. Rickels, C. Ricordi, M.A. Robien, P.A. Senior, A.M. James Shapiro, P.G. Stock, N.A. Turgeon, Phase 3 trial of transplantation of human islets in type 1 diabetes complicated by severe hypoglycemia, Diabetes Care. 39 (2016) 1230–1240. doi:10.2337/dc15-1988.

[3] Q. Zhou, D.A. Melton, Pancreas regeneration, Nature. 557 (2018) 351–358. doi:10.1038/s41586-018-0088-0.

[4] J. Shapiro, Islet Transplantation in Seven Patients with Type 1 Diabetes Mellitus Using a Glucocorticoid-free Immunosuppressive Regimen, N. Engl. J. Med. 343 (2000) 230–238.

[5] A. Del Toro-Arreola, A.K. Robles-Murillo, A. Daneri-Navarro, J.D. Rivas-Carrillo, The role of endothelial cells on islet function and revascularization after islet transplantation, Organogenesis. 12 (2016) 28–32. doi:10.1080/15476278.2016.1165378.

[6] M. Urbanczyk, S.L. Layland, K. Schenke-Layland, The role of extracellular matrix in biomechanics and its impact on bioengineering of cells and 3D tissues, Matrix Biol. 85–86 (2020) 1–14. doi:10.1016/j.matbio.2019.11.005.

[7] M. Urbanczyk, A. Zbinden, S.L. Layland, G. Duffy, K. Schenke-Layland, Controlled Heterotypic Pseudo-Islet Assembly of Human β-Cells and Human Umbilical Vein Endothelial Cells Using Magnetic Levitation, Tissue Eng. Part A. 26 (2020) 387–399. doi:10.1089/ten.tea.2019.0158.

[8] A. Zbinden, M. Urbanczyk, S.L. Layland, L. Becker, J. Marzi, M. Bosch, P. Loskill, G.P. Duffy, K. Schenke-Layland, Collagen and Endothelial Cell Coculture Improves β-Cell Functionality and Rescues Pancreatic Extracellular Matrix, Tissue Eng. Part A. (2020) ten.tea.2020.0250. doi:10.1089/ten.tea.2020.0250.

[9] C. Laporte, E. Tubbs, M. Pierron, A. Gallego, A. Moisan, F. Lamarche, T. Lozano, A. Hernandez, C. Cottet-Rousselle, A.-S. Gauchez, V. Persoons, F. Bottausci, C. Fontelaye, F. Boizot, S. Lablanche, F. Rivera, Improved human islets' viability and functionality with mesenchymal stem cells and arg-gly-asp tripeptides supplementation of alginate micro-encapsulated islets in vitro., Biochem. Biophys. Res. Commun. 528 (2020) 650–657. doi:10.1016/j.bbrc.2020.05.107.

[10] D.M. Salvay, C.B. Rives, X. Zhang, F. Chen, D.B. Kaufman, W.L. Lowe, L.D. Shea, Extracellular Matrix Protein-Coated Scaffolds Promote the Reversal of Diabetes After Extrahepatic Islet Transplantation, Transplantation. 85 (2008) 1456–1464. doi:10.1097/TP.0b013e31816fc0ea.

[11] T. Linn, K. Schneider, H.P. Hammes, K.T. Preissner, H. Brandhorst, E. Morgenstern, F. Kiefer, R.G. Bretzel, Angiogenic capacity of endothelial cells in islets of Langerhans, FASEB J. 17 (2003) 1–17. doi:10.1096/fj.02-0615fje.

[12] A. Gamble, R. Pawlick, A.R. Pepper, A. Bruni, A. Adesida, P.A. Senior, G.S. Korbutt, A.M.J. Shapiro, Improved islet recovery and efficacy through co-culture and co-transplantation of islets with human adipose-derived mesenchymal stem cells, PLoS One. 13 (2018) e0206449. doi:10.1371/journal.pone.0206449.

[13] M. Perez-Basterrechea, M.M. Esteban, M. Alvarez-Viejo, T. Fontanil, S. Cal, M. Sanchez Pitiot, J. Otero, A.J. Obaya, Fibroblasts accelerate islet revascularization and improve long-term graft survival in a mouse model of subcutaneous islet transplantation, PLoS One. 12 (2017) e0180695. doi:10.1371/journal.pone.0180695.

[14] A. Zbinden, S.L. Layland, M. Urbanczyk, D.A.C. Berrio, J. Marzi, M. Zauner, A. Hammerschmidt, E.M. Brauchle, K. Sudrow, S. Fink, M. Templin, S. Liebscher, G. Klein, A. Deb, G.P. Duffy, G.M. Crooks, J.A. Eble, H.K.A. Mikkola, A. Nsair, M. Seifert, Nidogen-1 Mitigates Ischemia and Promotes Tissue Survival and Regeneration, 2002500 (2020) 1–18. doi:10.1002/advs.202002500.

[15] J. Crisóstomo, A.M. Pereira, S.J. Bidarra, A.C. Gonçalves, P.L. Granja, J.F.J. Coelho, C.C. Barrias, R. Seiça, ECM-enriched alginate hydrogels for bioartificial pancreas: an ideal niche to improve insulin secretion and diabetic glucose profile, J. Appl. Biomater. Funct. Mater. 17 (2019). doi:10.1177/2280800019848923.

[16] J.Y.C. Cheng, M. Raghunath, J. Whitelock, L. Poole-Warren, Matrix Components and Scaffolds for Sustained Islet Function, Tissue Eng. Part B Rev. 17 (2011) 235–247. doi:10.1089/ten.teb.2011.0004.

[17] D. Brandhorst, H. Brandhorst, S. Acreman, Y. Kimura, S.L. Layland, K. Schenke-Layland, P.R.V. Johnson, Recombinant Nidogen-1 Significantly Improves Survival of Hypoxic Human Islets, J. Nuff. Dep. Surg. Sci. 1 (2020). doi:10.37707/jnds.v1i2.91.

[18] T.A. Wynn, T.R. Ramalingam, Mechanisms of fibrosis: therapeutic translation for fibrotic disease., Nat. Med. 18 (2012) 1028–40. doi:10.1038/nm.2807.

[19] S. Ricard-Blum, G. Baffet, N. Théret, Molecular and tissue alterations of collagens in fibrosis, Matrix Biol. 68–69 (2018) 122–149. doi:10.1016/j.matbio.2018.02.004.

[20] A. Menke, G. Adler, TGFbeta-induced Fibrogenesis of the Pancreas, Int. J. Gastrointest. Cancer. 31 (2002) 41–46.

817 doi:10.1385/IJGC:31:1-3:41.

818 [21] A. Zbinden, J. Marzi, K. Schlünder, C. Probst, M. Urbanczyk, S. Black, E.M. Brauchle, S.L. Layland, U. Kraushaar, G. Duffy,
819 K. Schenke-Layland, P. Loskill, Non-invasive marker-independent high content analysis of a microphysiological human
820 pancreas-on-a-chip model, Matrix Biol. 85–86 (2020) 205–220. doi:10.1016/j.matbio.2019.06.008.

821 [22] S. Hinderer, K. Sudrow, M. Schneider, M. Holeiter, S.L. Layland, M. Seifert, K. Schenke-Layland, Surface functionalization
822 of electrospun scaffolds using recombinant human decorin attracts circulating endothelial progenitor cells., Sci. Rep. 8
823 (2018) 110. doi:10.1038/s41598-017-18382-y.

824 [23] X. Xiong, R. Ghosh, E. Hiller, F. Drepper, B. Knapp, H. Brunner, S. Rupp, A new procedure for rapid, high yield purification
825 of Type I collagen for tissue engineering, Process Biochem. 44 (2009) 1200–1212. doi:10.1016/j.procbio.2009.06.010.

826 [24] S. Andrew, FastQC. A Quality Control Tool for High Throughput Sequence Data, (2010).

827 [25] F. Krueger, Trim Galore: A Wrapper Tool around Cutadapt and FastQC to Consistently Apply Quality and Adapter Trimming
828 to FastQ Files, with Some Extra Functionality for MspI-Digested RRBS-Type (Reduced Representation Bisufite-Seq)
829 Libraries, (2012).

830 [26] A. Dobin, C.A. Davis, F. Schlesinger, J. Drenkow, C. Zaleski, S. Jha, P. Batut, M. Chaisson, T.R. Gingeras, STAR: Ultrafast
831 universal RNA-seq aligner, Bioinformatics. 29 (2012) 15–21. doi:10.1093/bioinformatics/bts635.

832 [27] L. Wang, S. Wang, W. Li, RSeQC: Quality control of RNA-seq experiments, Bioinformatics. 28 (2012) 2184–2185.
833 doi:10.1093/bioinformatics/bts356.

834 [28] Y. Liao, G.K. Smyth, W. Shi, featureCounts: An efficient general purpose program for assigning sequence reads to genomic
835 features, Bioinformatics. 30 (2014) 923–930. doi:10.1093/bioinformatics/btt656.

836 [29] P. Ewels, M. Magnusson, S. Lundin, M. Kaeller, Summarize analysis results for multiple tools and samples in a single
837 report, Bioinformatics. 32 (2016) 3047–3048. doi:10.1093/bioinformatics/btw354.

838 [30] Y. Benjamini, Y. Hochberg, Controlling the False Discovery Rate: A Practical and Powerful Approach to Multiple Testing, J.
839 R. Stat. Scoeity Ser. B. 57 (1995) 289–300. doi:10.1111/j.2517-6161.1995.tb02031.x.

840 [31] M. Kanehisa, S. Goto, KEGG: kyoto encyclopedia of genes and genomes, Nucleic Acids Res. 28 (2000) 27–30.
841 doi:10.1093/nar/28.1.27.

842 [32] M. Gillespie, B. Jassal, R. Stephan, M. Milacic, K. Rothfels, A. Senff-Ribeiro, J. Griss, C. Sevilla, L. Matthews, C. Gong, C.
843 Deng, T. Varusai, E. Ragueneau, Y. Haider, B. May, V. Shamovsky, J. Weiser, T. Brunson, N. Sanati, L. Beckman, X.
844 Shao, A. Fabregat, K. Sidiropoulos, J. Murillo, G. Viteri, J. Cook, S. Shorser, G. Bader, E. Demir, C. Sander, R. Haw, G.
845 Wu, L. Stein, H. Hermjakob, P. D'Eustachio, The reactome pathway knowledgebase 2022, Nucleic Acids Res. 50 (2022)
846 D687–D692. doi:10.1093/nar/gkab1028.

847 [33] B. Prats Mateu, E. Harreither, M. Schosserer, V. Puxbaum, E. Gludovacz, N. Borth, N. Gierlinger, J. Grillari, Label-free live
848 cell imaging by Confocal Raman Microscopy identifies CHO host and producer cell lines, Biotechnol. J. 12 (2017) 1600037.
849 doi:10.1002/biot.201600037.

850 [34] T. Morimoto, L. Da Chiu, H. Kanda, H. Kawagoe, T. Ozawa, M. Nakamura, K. Nishida, K. Fujita, T. Fujikado, Using redox-
851 sensitive mitochondrial cytochrome Raman bands for label-free detection of mitochondrial dysfunction, Analyst. 144 (2019)
852 2531–2540. doi:10.1039/c8an02213e.

853 [35] K. Arda, N. Ciledag, E. Aktas, B.K. Aribas, K. Köse, Quantitative assessment of normal soft-tissue elasticity using shear-
854 wave ultrasound elastography., AJR. Am. J. Roentgenol. 197 (2011) 532–6. doi:10.2214/AJR.10.5449.

855 [36] Y. Shi, Y. Liu, F. Gao, Y. Liu, S. Tao, Y. Li, K.J. Glaser, R.L. Ehman, Q. Guo, Pancreatic stiffness quantified with MR
856 elastography: Relationship to postoperative pancreatic fistula after pancreaticoenteric anastomosis, Radiology. 288 (2018)
857 476–484. doi:10.1148/radiol.2018170450.

858 [37] M. Sugimoto, S. Takahashi, M. Kojima, N. Gotohda, Y. Kato, S. Kawano, A. Ochiai, M. Konishi, What is the nature of
859 pancreatic consistency? Assessment of the elastic modulus of the pancreas and comparison with tactile sensation,
860 histology, and occurrence of postoperative pancreatic fistula after pancreaticoduodenectomy., Surgery. 156 (2014) 1204–
861 11. doi:10.1016/j.surg.2014.05.015.

862 [38] K. Czamara, K. Majzner, M.Z. Pacia, K. Kochan, A. Kaczor, M. Baranska, Raman spectroscopy of lipids: a review, J.
863 Raman Spectrosc. 46 (2015) 4–20. doi:10.1002/jrs.4607.

864 [39] W. Zhang, Y. Ge, Q. Cheng, Q. Zhang, L. Fang, J. Zheng, Decorin is a pivotal effector in the extracellular matrix and tumour
865 microenvironment., Oncotarget. 9 (2018) 5480–5491. doi:10.18632/oncotarget.23869.

866 [40] T. Neill, L. Schaefer, R. V Iozzo, Decorin - A Guardian from the Matrix, Am. J. Pathol. 181 (2012) 380–387.
867 doi:10.1016/j.ajpath.2012.04.029.

868 [41] L. Sakhneny, A. Epshtein, L. Landsman, Pericytes contribute to the islet basement membranes to promote beta-cell gene
869 expression., Sci. Rep. 11 (2021) 2378. doi:10.1038/s41598-021-81774-8.

[42] A. Naba, K.R. Clauser, D.R. Mani, S.A. Carr, R.O. Hynes, Quantitative proteomic profiling of the extracellular matrix of pancreatic islets during the angiogenic switch and insulinoma progression., Sci. Rep. 7 (2017) 40495. doi:10.1038/srep40495.

[43] J. Svärd, T.H. Røst, C.E.N. Sommervoll, C. Haugen, O.A. Gudbrandsen, A.E. Mellgren, E. Rødahl, J. Fernø, S.N. Dankel, J. V. Sagen, G. Mellgren, Absence of the proteoglycan decorin reduces glucose tolerance in overfed male mice., Sci. Rep. 9 (2019) 4614. doi:10.1038/s41598-018-37501-x.

[44] R.N. Feng, Y.C. Niu, X.W. Sun, Q. Li, C. Zhao, C. Wang, F.C. Guo, C.H. Sun, Y. Li, Histidine supplementation improves insulin resistance through suppressed inflammation in obese women with the metabolic syndrome: A randomised controlled trial, Diabetologia. 56 (2013) 985–994. doi:10.1007/s00125-013-2839-7.

[45] Y.T. Lee, C.C. Hsu, M.H. Lin, K. Sen Liu, M.C. Yin, Histidine and carnosine delay diabetic deterioration in mice and protect human low density lipoprotein against oxidation and glycation, Eur. J. Pharmacol. 513 (2005) 145–150. doi:10.1016/j.ejphar.2005.02.010.

[46] X. Sun, R. Feng, Y. Li, S. Lin, W. Zhang, Y. Li, C. Sun, S. Li, Histidine supplementation alleviates inflammation in the adipose tissue of high-fat diet-induced obese rats via the NF-κB-and PPARγ-involved pathways, Br. J. Nutr. 112 (2014) 477–485. doi:10.1017/S0007114514001056.

[47] B. Rolfe, J. Mooney, B. Zhang, S. Jahnke, S.-J. Le, Y.-Q. Chau, Q. Huang, H. Wang, G. Campbell, J. Campbell, The Fibrotic Response to Implanted Biomaterials: Implications for Tissue Engineering, in: Regen. Med. Tissue Eng. - Cells Biomater., InTech, 2011. doi:10.5772/21790.

[48] T.N. Wight, S. Potter-Perigo, The extracellular matrix: an active or passive player in fibrosis?, Am. J. Physiol. Gastrointest. Liver Physiol. 301 (2011) G950-5. doi:10.1152/ajpgi.00132.2011.

[49] W.A. Border, N.A. Noble, T. Yamamoto, J.R. Harper, Y. u Yamaguchi, M.D. Pierschbacher, E. Ruoslahti, Natural inhibitor of transforming growth factor-beta protects against scarring in experimental kidney disease., Nature. 360 (1992) 361–4. doi:10.1038/360361a0.

[50] L. Schaefer, K. Macakova, I. Raslik, M. Micegova, H.-J. Gröne, E. Schönherr, H. Robenek, F.G. Echtermeyer, S. Grässel, P. Bruckner, R.M. Schaefer, R. V. Iozzo, H. Kresse, Absence of Decorin Adversely Influences Tubulointerstitial Fibrosis of the Obstructed Kidney by Enhanced Apoptosis and Increased Inflammatory Reaction, Am. J. Pathol. 160 (2002) 1181–1191. doi:10.1016/S0002-9440(10)64937-1.

[51] T.W.L. Groeneveld, M. Oroszlán, R.T. Owens, M.C. Faber-Krol, A.C. Bakker, G.J. Arlaud, D.J. McQuillan, U. Kishore, M.R. Daha, A. Roos, Interactions of the Extracellular Matrix Proteoglycans Decorin and Biglycan with C1q and Collectins, J. Immunol. 175 (2005) 4715–4723. doi:10.4049/jimmunol.175.7.4715.

[52] D. Nolfi-Donegan, A. Braganza, S. Shiva, Mitochondrial electron transport chain: Oxidative phosphorylation, oxidant production, and methods of measurement., Redox Biol. 37 (2020) 101674. doi:10.1016/j.redox.2020.101674.

[53] A. Wiederkehr, C.B. Wollheim, Minireview: implication of mitochondria in insulin secretion and action, Endocrinology. 147 (2006) 2643–2649. doi:10.1210/en.2006-0057.

[54] B.A. Kaufman, C. Li, S.A. Soleimanpour, Mitochondrial regulation of β-cell function: maintaining the momentum for insulin release, Mol Asp. Med. 42 (2015) 91–104. doi:10.1016/j.mam.2015.01.004.

[55] S. Malmgreh, D.G. Nicholls, J. Taneera, K. Bacos, T. Koeck, A. Tamaddon, R. Wibom, L. Groop, C. Ling, H. Mulder, V. V. Sharoyko, Tight coupling between glucose and mitochondrial metabolism in clonal β-cells is required for robust insulin secretion, J. Biol. Chem. 284 (2009) 32395–32404. doi:10.1074/jbc.M109.026708.

[56] V.B. Ritov, E. V. Menshikova, J. He, R.E. Ferrell, B.H. Goodpaster, D.E. Kelley, Deficiency of subsarcolemmal mitochondria in obesity and type 2 diabetes, Diabetes. 54 (2005) 8–14. doi:10.2337/diabetes.54.1.8.

[57] N. Shrestha, R.B. Reinert, L. Qi, Endoplasmic Reticulum Protein Quality Control in β Cells, Semin. Cell Dev. Biol. 103 (2020) 59–67. doi:10.1016/j.semcdb.2020.04.006.

[58] S. Yamaguchi, H. Ishihara, T. Yamada, A. Tamura, M. Usui, R. Tominaga, Y. Munakata, C. Satake, H. Katagiri, F. Tashiro, H. Aburatani, K. Tsukiyama-Kohara, J. Miyazaki, N. Sonenberg, Y. Oka, ATF4-Mediated Induction of 4E-BP1 Contributes to Pancreatic β Cell Survival under Endoplasmic Reticulum Stress, Cell Metab. 7 (2008) 269–276. doi:10.1016/j.cmet.2008.01.008.

[59] S.G. Fonseca, J. Gromada, F. Urano, Endoplasmic reticulum stress and pancreatic β-cell death, Trends Endocrinol. Metab. 22 (2011) 266–274. doi:10.1016/j.tem.2011.02.008.

[60] N. Rabhi, E. Salas, P. Froguel, J.S. Annicotte, Role of the unfolded protein response in β cell compensation and failure during diabetes, J. Diabetes Res. 2014 (2014). doi:10.1155/2014/795171.

[61] A. El Ouaamari, J.-Y. Zhou, C.W. Liew, J. Shirakawa, E. Dirice, N. Gedeon, S. Kahraman, D.F. De Jesus, S. Bhatt, J.-S. Kim, T.R.W. Clauss, D.G. Camp, R.D. Smith, W.-J. Qian, R.N. Kulkarni, Compensatory Islet Response to Insulin Resistance Revealed by Quantitative Proteomics, J. Proteome Res. 14 (2015) 3111–3122. doi:10.1021/acs.jproteome.5b00587.

[62] J. Wang, Y. Chen, Q. Yuan, W. Tang, X. Zhang, K. Osei, Control of Precursor Maturation and Disposal Is an Early Regulative Mechanism in the Normal Insulin Production of Pancreatic β-Cells, PLoS One. 6 (2011) e19446. doi:10.1371/journal.pone.0019446.

[63] J. Sun, J. Cui, Q. He, Z. Chen, P. Arvan, M. Liu, Proinsulin misfolding and endoplasmic reticulum stress during the development and progression of diabetes☆, Mol. Aspects Med. 42 (2015) 105–118. doi:10.1016/j.mam.2015.01.001.

[64] M. Liu, Y. Li, D. Cavener, P. Arvan, Proinsulin Disulfide Maturation and Misfolding in the Endoplasmic Reticulum, J. Biol. Chem. 280 (2005) 13209–13212. doi:10.1074/jbc.C400475200.

[65] N. Shrestha, E. De Franco, P. Arvan, M. Cnop, Pathological β-Cell Endoplasmic Reticulum Stress in Type 2 Diabetes: Current Evidence, Front. Endocrinol. (Lausanne). 12 (2021) 1–7. doi:10.3389/fendo.2021.650158.

[66] D.L. Eizirik, A.K. Cardozo, M. Cnop, The Role for Endoplasmic Reticulum Stress in Diabetes Mellitus, Endocr. Rev. 29 (2008) 42–61. doi:10.1210/er.2007-0015.

[67] S.Z. Hasnain, J.B. Prins, M.A. McGuckin, Oxidative and endoplasmic reticulum stress in β-cell dysfunction in diabetes, J. Mol. Endocrinol. 56 (2016) R33–R54. doi:10.1530/JME-15-0232.

[68] D. Takei, H. Ishihara, S. Yamaguchi, T. Yamada, A. Tamura, H. Katagiri, Y. Maruyama, Y. Oka, WFS1 protein modulates the free Ca 2+ concentration in the endoplasmic reticulum, FEBS Lett. 580 (2006) 5635–5640. doi:10.1016/j.febslet.2006.09.007.

[69] K. Ueda, J. Kawano, K. Takeda, T. Yujiri, K. Tanabe, T. Anno, M. Akiyama, J. Nozaki, T. Yoshinaga, A. Koizumi, K. Shinoda, Y. Oka, Y. Tanizawa, Endoplasmic reticulum stress induces Wfs1 gene expression in pancreatic β-cells via transcriptional activation, Eur. J. Endocrinol. 153 (2005) 167–176. doi:10.1530/eje.1.01945.

[70] I.X. Zhang, J. Ren, S. Vadrevu, M. Raghavan, L.S. Satin, ER stress increases store-operated Ca2+ entry (SOCE) and augments basal insulin secretion in pancreatic beta cells, J. Biol. Chem. 295 (2020) 5685–5700. doi:10.1074/jbc.RA120.012721.

[71] L.S. Satin, Localized calcium influx in pancreatic β-cells: Its significance for Ca2+-dependent insulin secretion from the islets of Langerhans, Endocrine. 13 (2000) 251–262. doi:10.1385/ENDO:13:3:251.

[72] S.G. Fonseca, M. Fukuma, K.L. Lipson, L.X. Nguyen, J.R. Allen, Y. Oka, F. Urano, WFS1 Is a Novel Component of the Unfolded Protein Response and Maintains Homeostasis of the Endoplasmic Reticulum in Pancreatic β-Cells, J. Biol. Chem. 280 (2005) 39609–39615. doi:10.1074/jbc.M507426200.

[73] H. Inoue, Y. Tanizawa, J. Wasson, P. Behn, K. Kalidas, E. Bernal-Mizrachi, M. Mueckler, H. Marshall, H. Donis-Keller, P. Crock, D. Rogers, M. Mikuni, H. Kumashiro, K. Higashi, G. Sobue, Y. Oka, M.A. Permutt, A gene encoding a transmembrane protein is mutated in patients with diabetes mellitus and optic atrophy (Wolfram syndrome), Nat. Genet. 20 (1998) 143–148. doi:10.1038/2441.

[74] H.-Y. Tsai, Y.-F. Yang, A.T. Wu, C.-J. Yang, Y.-P. Liu, Y.-H. Jan, C.-H. Lee, Y.-W. Hsiao, C.-T. Yeh, C.-N. Shen, P.-J. Lu, M.-S. Huang, M. Hsiao, Endoplasmic reticulum ribosome-binding protein 1 (RRBP1) overexpression is frequently found in lung cancer patients and alleviates intracellular stress-induced apoptosis through the enhancement of GRP78, Oncogene. 32 (2013) 4921–4931. doi:10.1038/onc.2012.514.

[75] H. Lu, Y. Yang, E.M. Allister, N. Wijesekara, M.B. Wheeler, The Identification of Potential Factors Associated with the Development of Type 2 Diabetes, Mol. Cell. Proteomics. 7 (2008) 1434–1451. doi:10.1074/mcp.M700478-MCP200.

[76] G.J. Ocaña, L. Pérez, L. Guindon, S.N. Deffit, C. Evans-Molina, D.C. Thurmond, J.S. Blum, Inflammatory stress of pancreatic beta cells drives release of extracellular heat-shock protein 90 α, Immunology. 151 (2017) 198–210. doi:10.1111/imm.12723.

[77] A.S.M. Moin, M. Nandakumar, A. Diane, M. Dehbi, A.E. Butler, The Role of Heat Shock Proteins in Type 1 Diabetes, Front. Immunol. 11 (2021) 1–11. doi:10.3389/fimmu.2020.612584.

[78] R.C. Wek, T.G. Anthony, EXtENDINg β cell survival by UPRegulating ATF4 translation, Cell Metab. 4 (2006) 333–334. doi:10.1016/j.cmet.2006.10.006.

[79] C. Papadopoulos, P. Kirchner, M. Bug, D. Grum, L. Koerver, N. Schulze, R. Poehler, A. Dressler, S. Fengler, K. Arhzaouy, V. Lux, M. Ehrmann, C.C. Weihl, H. Meyer, VCP /p97 cooperates with YOD 1, UBXD 1 and PLAA to drive clearance of ruptured lysosomes by autophagy , EMBO J. 36 (2017) 135–150. doi:10.15252/embj.201695148.

[80] S. Cockcroft, N. Carvou, Biochemical and biological functions of class I phosphatidylinositol transfer proteins, Biochim. Biophys. Acta - Mol. Cell Biol. Lipids. 1771 (2007) 677–691. doi:10.1016/j.bbalip.2007.03.009.

[81] N.J. Blunsom, S. Cockcroft, Phosphatidylinositol synthesis at the endoplasmic reticulum, Biochim. Biophys. Acta - Mol. Cell Biol. Lipids. 1865 (2020) 158471. doi:10.1016/j.bbalip.2019.05.015.

[82] P. Mayinger, Phosphoinositides and vesicular membrane traffic, Biochim. Biophys. Acta - Mol. Cell Biol. Lipids. 1821 (2012) 1104–1113. doi:10.1016/j.bbalip.2012.01.002.

[83] M.J. MacDonald, L. Ade, J.M. Ntambi, I.U.H. Ansari, S.W. Stoker, Characterization of phospholipids in insulin secretory granules and mitochondria in pancreatic beta cells and their changes with glucose stimulation, J. Biol. Chem. 290 (2015) 11075–11092. doi:10.1074/jbc.M114.628420.

[84] A.R. Sánchez-Archidona, C. Cruciani-Guglielmacci, C. Roujeau, L. Wigger, J. Lallement, J. Denom, M. Barovic, N. Kassis, F. Mehl, J. Weitz, M. Distler, C. Klose, K. Simons, M. Ibberson, M. Solimena, C. Magnan, B. Thorens, Plasma triacylglycerols are biomarkers of β-cell function in mice and humans, Mol. Metab. 54 (2021) 101355. doi:10.1016/j.molmet.2021.101355.

[85] K.L. Pappan, Z. Pan, G. Kwon, C.A. Marshall, T. Coleman, I.J. Goldberg, M.L. McDaniel, C.F. Semenkovich, Pancreatic β-Cell Lipoprotein Lipase Independently Regulates Islet Glucose Metabolism and Normal Insulin Secretion, J. Biol. Chem. 280 (2005) 9023–9029. doi:10.1074/jbc.M409706200.

[86] M. Bensellam, E.L. Maxwell, J.Y. Chan, J. Luzuriaga, P.K. West, J.C. Jonas, J.E. Gunton, D.R. Laybutt, Hypoxia reduces ER-to-Golgi protein trafficking and increases cell death by inhibiting the adaptive unfolded protein response in mouse beta cells, Diabetologia. 59 (2016) 1492–1502. doi:10.1007/s00125-016-3947-y.

[87] N. Hwang, M.Y. Kwon, J.B. Cha, S.W. Chung, J.M. Woo, Tunicamycin-induced Endoplasmic Reticulum Stress Upregulates the Expression of Pentraxin 3 in Human Retinal Pigment Epithelial Cells, Korean J. Ophthalmol. 30 (2016) 468–478. doi:10.3341/kjo.2016.30.6.468.

[88] H. Guo, Y. Xiong, P. Witkowski, J. Cui, L.J. Wang, J. Sun, R. Lara-Lemus, L. Haataja, K. Hutchison, S.O. Shan, P. Arvan, M. Liu, Inefficient translocation of preproinsulin contributes to pancreatic β cell failure and late-onset diabetes, J. Biol. Chem. 289 (2014) 16290–16302. doi:10.1074/jbc.M114.562355.

[89] Y. ho Lee, J. Kim, K. Park, M.S. Lee, β-cell autophagy: Mechanism and role in β-cell dysfunction, Mol. Metab. 27 (2019) S92–S103. doi:10.1016/j.molmet.2019.06.014.

[90] R. Zhu, X. Li, J. Xu, C. Barrabi, D. Kekulandara, J. Woods, X. Chen, M. Liu, Defective endoplasmic reticulum export causes proinsulin misfolding in pancreatic β cells, Mol. Cell. Endocrinol. 493 (2019) 110470. doi:10.1016/j.mce.2019.110470.

[91] J. Fang, M. Liu, X. Zhang, T. Sakamoto, D.J. Taatjes, B.P. Jena, F. Sun, J. Woods, T. Bryson, A. Kowluru, K. Zhang, X. Chen, COPII-Dependent ER Export: A Critical Component of Insulin Biogenesis and β-Cell ER Homeostasis., Mol. Endocrinol. 29 (2015) 1156–69. doi:10.1210/me.2015-1012.

[92] D. Brandhorst, H. Brandhorst, S. Acreman, Y. Kimura, S.L. Layland, K. Schenke-Layland, P.R.V. Johnson, Recombinant Nidogen-1 Significantly Improves Survival of Hypoxic Human Islets, J. Nuff. Dep. Surg. Sci. 1 (2020). doi:10.37707/jnds.v1i2.91.

[93] C. Krafft, L. Neudert, T. Simat, R. Salzer, Near infrared Raman spectra of human brain lipids, Spectrochim. Acta Part A Mol. Biomol. Spectrosc. 61 (2005) 1529–1535. doi:10.1016/j.saa.2004.11.017.

[94] R. Jyothi Lakshmi, V.B. Kartha, C. Murali Krishna, J.G. R Solomon, G. Ullas, P. Uma Devi, Tissue Raman spectroscopy for the study of radiation damage: brain irradiation of mice., Radiat. Res. 157 (2002) 175–82. doi:10.1667/0033-7587(2002)157[0175:trsfts]2.0.co;2.

[95] L. Silveira, S. Sathaiah, R.A. Zângaro, M.T.T. Pacheco, M.C. Chavantes, C.A.G. Pasqualucci, Correlation between near-infrared Raman spectroscopy and the histopathological analysis of atherosclerosis in human coronary arteries, Lasers Surg. Med. 30 (2002) 290–297. doi:10.1002/lsm.10053.

Appendix III

TISSUE ENGINEERING: Part A
Volume 26, Numbers 7 and 8, 2020
Mary Ann Liebert, Inc.
DOI: 10.1089/ten.tea.2019.0158

termis
Tissue Engineering
& Regenerative Medicine
International Society

ORIGINAL ARTICLE

Controlled Heterotypic Pseudo-Islet Assembly of Human β-Cells and Human Umbilical Vein Endothelial Cells Using Magnetic Levitation

Max Urbanczyk, MSc,[1] Aline Zbinden, MSc,[1] Shannon L. Layland, MBA,[1] Garry Duffy, BSc, PhD,[2] and Katja Schenke-Layland, MSc, PhD[1,3–5]

β-Cell functionality and survival are highly dependent on the cells' microenvironment and cell–cell interactions. Since the pancreas is a highly vascularized organ, the crosstalk between β-cells and endothelial cells (ECs) is vital to ensure proper function. To understand the interaction of pancreatic β-cells with vascular ECs, we sought to investigate the impact of the spatial distribution on the interaction of human cell line-based β-cells (EndoC-βH3) and human umbilical vein endothelial cells (HUVECs). We focused on the evaluation of three major spatial distributions, which can be found within human islets *in vivo*, in tissue-engineered heterotypic cell spheroids, so-called pseudo-islets, by controlling the aggregation process using magnetic levitation. We report that heterotypic spheroids formed by spontaneous aggregation cannot be maintained in culture due to HUVEC disassembly over time. In contrast, magnetic levitation allows the formation of stable heterotypic spheroids with defined spatial distribution and significantly facilitated HUVEC integration. To the best of our knowledge, this is the first study that introduces a human-only cell line-based *in vitro* test system composed of a coculture of β-cells and ECs with a successful stimulation of β-cell secretory function monitored by a glucose-stimulated insulin secretion assays. In addition, we systematically investigate the impact of the spatial distribution on cocultures of human β-cells and ECs, showing that the architecture of pseudo-islets significantly affects β-cell functionality.

Keywords: diabetes, islets, β-cells, insulin, endothelial cells, 3D

Impact Statement

Tissue engineering of coculture systems containing β-cells and endothelial cells (ECs) is a promising technique to stimulate β-cell functionality. In this study, we analyzed human pancreatic islet tissue and revealed three different native distributions of β-cells and ECs. We successfully recreated these distributions *in vitro* by employing magnetic levitation of human β-cells and ECs, forming controlled heterotypic pseudo-islets, which enabled us to identify a significant impact of the pseudo-islet architecture on insulin secretion.

Introduction

In 2018, 425 million people were known to suffer from diabetes mellitus (DM), with millions more remaining undiagnosed.[1,2] The number of DM patients is estimated to increase to >600 million by 2045.[1] DM is a chronic disease, where the physiological feedback loop of blood glucose regulation is impaired by either the reduction of β-cell mass and insulin production, type 1 DM (T1D), or by a defective response to insulin in tissues, type 2 DM.[3] The T1D incidence rate increases annually by 3% worldwide, similarly increasing the number of patients with various complications accompanied by T1D such

[1]Department of Women's Health, Research Institute for Women's Health, Eberhard Karls University Tübingen, Tübingen, Germany.
[2]Department of Anatomy, School of Medicine, College of Medicine, Nursing and Health Sciences, National University of Ireland Galway, Galway, Ireland.
[3]The Natural and Medical Sciences Institute (NMI) at the University of Tübingen, Reutlingen, Germany.
[4]Cluster of Excellence iFIT (EXC 2180) "Image-Guided and Functionally Instructed Tumor Therapies," Eberhard Karls University Tübingen, Tübingen, Germany.
[5]Department of Medicine/Cardiology, Cardiovascular Research Laboratories, University of California, Los Angeles, California.

as cardiovascular diseases, peripheral vascular diseases, or nephropathy. T1D patients rely on life-long medication and treatment, such as exogeneous insulin replacement or, in more severe cases, immunosuppression after pancreatic β-cell transplantation.[4,5,6] Attempts toward the long-term treatment of T1D by β-cell transplantation frequently fails due to an impaired graft survival as a result of lost extracellular matrix (ECM)[7,8] or lack of vascularization accompanied by hypoxia after islet isolation.[4,9,10]

The pancreas is a highly vascularized organ,[11] which is particularly true for the β-cell-containing islets of Langerhans, with a capillary density of 400 capillaries/mm^2.[12] During homeostasis, endothelial cells (ECs) within the pancreas are vital for the maintenance of the microenvironment of the insulin-producing β-cells by upregulation of ECM-associated genes[13] to secrete crucial basement membrane proteins.[14–17] β-cells and ECs share a natural proximity and are, by necessity, exposed to each other and each other's products.[9,18] The combination of pancreatic β-cells and ECs might be the key to stimulate β-cell survival and functionality and help to overcome the high transplant loss rate of ~60%.[5,19] However, understanding the interactions between β-cells and ECs is required to optimize those transplantable grafts.[19] Unfortunately, the availability of islets of Langerhans explants is limited.[20] Therefore, scientists rely on cell lines as an alternative model to mimic the functionality of islets of Langerhans *in vitro*. Current research on T1D focuses on the understanding of β-cell re-establishment by the investigation of complex cellular organoids, such as heterotypic cell aggregates from β-cells and ECs,[9,18] so-called pseudo-islets. Bioengineered prevascularized grafts combining β-cells and ECs *ex vivo* have been reported,[21–24] potentially reducing the required time to develop angiogenesis and revascularization *in vivo*, facilitating graft survival after transplantation.[13,25] Apart from the aspect of increased survival,[22] distinct groups have shown that β-cell and EC cocultures impact graft vascularization and increase β-cell functionality.[9,10,14,18,26] However, to the best of our knowledge, functional stimulation in cell line-based β-cell systems has only been shown in intraspecific cocultures of rodent cells[14] and interspecific cocultures of rodent β-cells and human ECs[18,26,27] *in vitro*. A human-based coculture *in vitro* test system using ECs that stimulate β-cell functionality has not been presented, since only rodent β-cell lines (e.g., INS-1E or MIN6) were shown to be glucose responsive, whereas the functionality of human β-cell lines was controversially discussed.[28] However, evaluation of rodent pancreatic islets revealed major differences in the spatial cell and ECM distribution[29] and in insulin secretion mechanisms,[30] emphasizing the need for a human cell line-based model.

Recently, the conditionally immortalized, nonproliferating and glucose-sensitive human β-cell line EndoC-βH3 was developed, enabling research on β-cells with a human genetic background without the need to use donor pancreas explants.[31,32] In this study, we investigated whether the spatial distribution of the EndoC-βH3 cells and human umbilical vein endothelial cells (HUVECs) has an impact on the insulin production within three-dimensional (3D) pseudo-islet cultures. The heterotypic spheroids were formed by spontaneous or controlled aggregation using magnetic levitation.[33] The procedure of magnetic levitation functionalizes cells on their surfaces using a combination of poly-L-lysine with gold and iron oxide nanoparticles. Afterward, cellular movement and aggregation can be guided using external magnetic fields (Fig. 1), enabling a controlled aggregation to form (multi-) cellular 3D spheroids with defined spatial distributions.[19]

Materials and Methods

Cell culture

If not stated otherwise, all cell types used in this study were cultured under standard humidified cell culture conditions (37°C, 5% carbon dioxide).

EndoC-βH3 cells (Univercell Biosolutions, Paris, France), a conditionally immortalized human pancreatic β-cell line, was cultured according to the manufacturer's instructions. In brief, cells were cultured in coated (βcoat®; Univercell Biosolutions) T25 flasks at a density of 70,000 cells/cm^2 in culture medium (OPTIβ1®; Univercell Biosolutions) supplemented with 10 μg/mL puromycin (ant-pr; InvivoGen, San Diego, CA) and passaged every 7 days. The immortalizing transgenes were removed by a 21-day treatment with 4-hydroxy tamoxifen (H7904; Sigma-Aldrich, Schnelldorf, Germany) to obtain nonproliferative β-cells that closely mimic human β-cells (Supplementary Fig. S1).

Vascular endothelial growth factor prescreened HUVECs (C-12205; PromoCell, Heidelberg, Germany) were cultured in EC growth medium (C-22010; PromoCell) in T25 flasks. Cells were passaged at a density of 80–90%. Medium was changed every 2–3 days. HUVECs were used between passages 2 and 6.

Rat insulinoma INS-1E cells (a kind gift of P. Maechler from the University of Geneva) were cultured in adjusted RPMI 1640 (12633012; Gibco, Thermo Fisher Scientific, Darmstadt, Germany) containing 10 mM HEPES (Gibco), 50 μM 2-mercapto-ethanol (Sigma-Aldrich), 1 mM pyruvate (Gibco), 5% fetal bovine serum (Sigma-Aldrich), 100 iU/mL penicillin, and 100 μg/mL streptomycin. The medium was changed every 2–3 days. The cells were passaged or seeded at a confluency of 80–90%.

Pseudo-islet assembly

For a controlled aggregation of cells within pseudo-islets, magnetic levitation was employed using the 96-well Bioprinting Kit (655840; Greiner Bio-One, Frickenhausen, Germany). In detail, β-cells and HUVECs were treated overnight with NanoShuttle™-PL at a concentration of 40 μL/mL in media according to the manufacturer's protocol. After the NanoShuttle-PL treatment, magnetized β-cells and HUVECs, as well as conventionally cultured β-cells and HUVECs were individually detached from their flasks using 0.25% Trypsin/EDTA. For coculture experiments, all cells were seeded at a density of 5000 cells/50 μL in corresponding cell culture media per well in a low adherence u-bottom 96-well plate (650970; Greiner Bio-One). We used three different conditions: (1) "1:1," where the same amount of HUVECs and β-cells were mixed before seeding to form pseudo-islets with a heterogeneous distribution of both cell types; (2) "ECs inside," where HUVECs were surrounded by β-cells; and (3) "β-cells inside," where β-cells were surrounded by HUVECs (Fig. 1). In detail, for the "1:1" condition, magnetized or conventionally cultured cells of both cell types were seeded for magnetic levitation or spontaneous aggregation at day 0, placed atop the

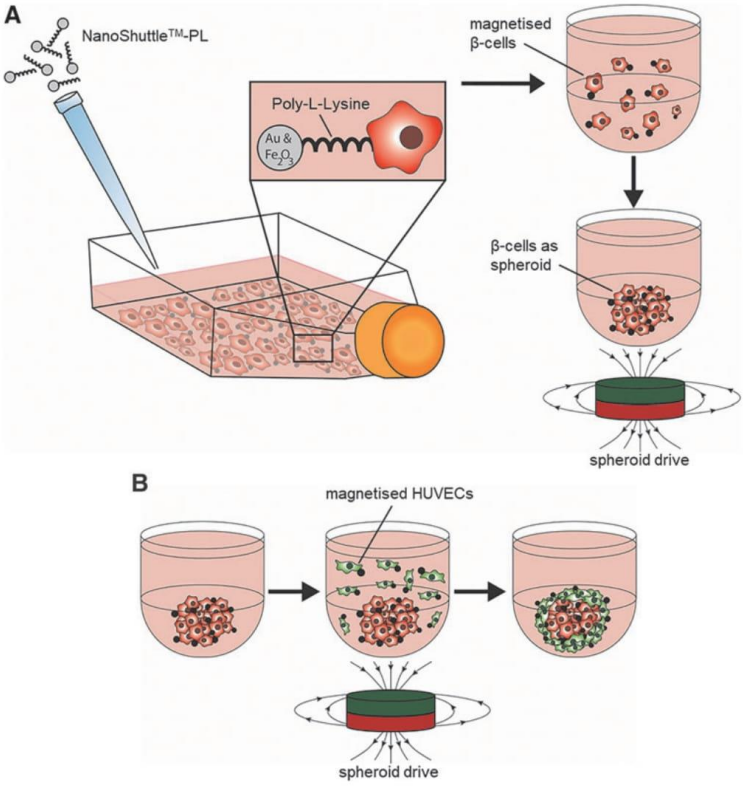

FIG. 1. Schematic of magnetic levitation to create two-layered heterotypic spheroids. **(A)** NanoShuttle™-PL is added to a T25 flask containing cells and incubated at 37°C overnight. After detaching, β-cells are added into a low adherence u-bottom 96-well plate and aggregated by applying external magnetic forces using the spheroid drive. **(B)** HUVECs are treated with NanoShuttle-PL overnight, and are added as single cell suspension to the already formed spheroids from step A. Applying a magnetic field through the spheroid drive forces the HUVECs to aggregate around the preformed β-cell-containing spheroids creating a two-layered pseudo-islet composed of β-cells and HUVECs. HUVECs, human umbilical vein endothelial cells.

spheroid drive (Greiner Bio-One) for 1 h for exposure to an external magnetic field, followed by culture under standard conditions for 5 days. For the ''ECs inside'' condition, magnetized HUVECs for magnetic levitation or standard HUVECs for spontaneous aggregation were seeded at day 0 and placed atop the spheroid drive for 1 h, followed by culture under standard conditions. At day 2 of the culture, magnetized β-cells or standard β-cells were added to the HUVEC spheroids formed by either magnetic levitation or spontaneous aggregation, placed atop the spheroid drive for 1 h, followed by culture under standard conditions for 5 days. For the ''β-cells inside'' condition, magnetized β-cells for magnetic levitation or standard β-cells for spontaneous aggregation were seeded at day 0, placed atop the spheroid drive for 1 h, followed by culture under standard conditions. After 2 days of culture, magnetized HUVECs or standard HUVECs were added to the β-cell spheroids formed by magnetic levitation or spontaneous aggregation, placed atop the spheroid drive for 1 h, followed by culture under standard conditions for additional 3 days. A graphical representation of the experimental timeline can be found in Figure 2. Spontaneous aggregation was not guided by the spheroid drive assembly. The cell ratio within the pseudo-islets was 5000 β-cells to 5000 HUVECs, and the cell culture medium was a 1:1 mixture of OPTIβ1 and EC growth medium throughout all experiments.

Terminal deoxynucleotidyl transferase-mediated nick-end labeling assay

Cell death analysis was performed using pseudo-islets composed of either magnetized β-cells and HUVECs or conventionally cultured β-cells. After culture, the pseudo-islets were fixed with 4% paraformaldehyde (Sigma-Aldrich) overnight at 4°C, embedded in paraffin, and cut into 3 μm thick sections. Terminal deoxynucleotidyl transferase-mediated nick-end labeling (TUNEL) staining was performed using the Click-iT TUNEL kit (C10245; Thermo Fisher Scientific). In brief, sections were deparaffinized in xylene and rehydrated through graded ethanol (100–50%) and vascular endothelial (VE)-water washes, and permeabilized using 0.25% Triton-X for 20 min. Terminal deoxynucleotidyl transferase reaction buffer was applied for 1 h at 60°C before slides were incubated with Click-iT reaction buffer for 30 min. Counterstaining was performed using a 4′,6-diamidino-2-phenylindole (DAPI; Sigma-Aldrich) solution with a concentration of 2 μg/mL for 10 min before mounting with ProLong® Gold antifade mounting medium (P36934; Invitrogen™, Darmstadt, Germany).

Glucose-stimulated insulin secretion assay

Before performing the glucose-stimulated insulin secretion (GSIS) assays, all pseudo-islets were cultured in starvation medium (OPTIβ2®; Univercell Biosolutions) for 24 h

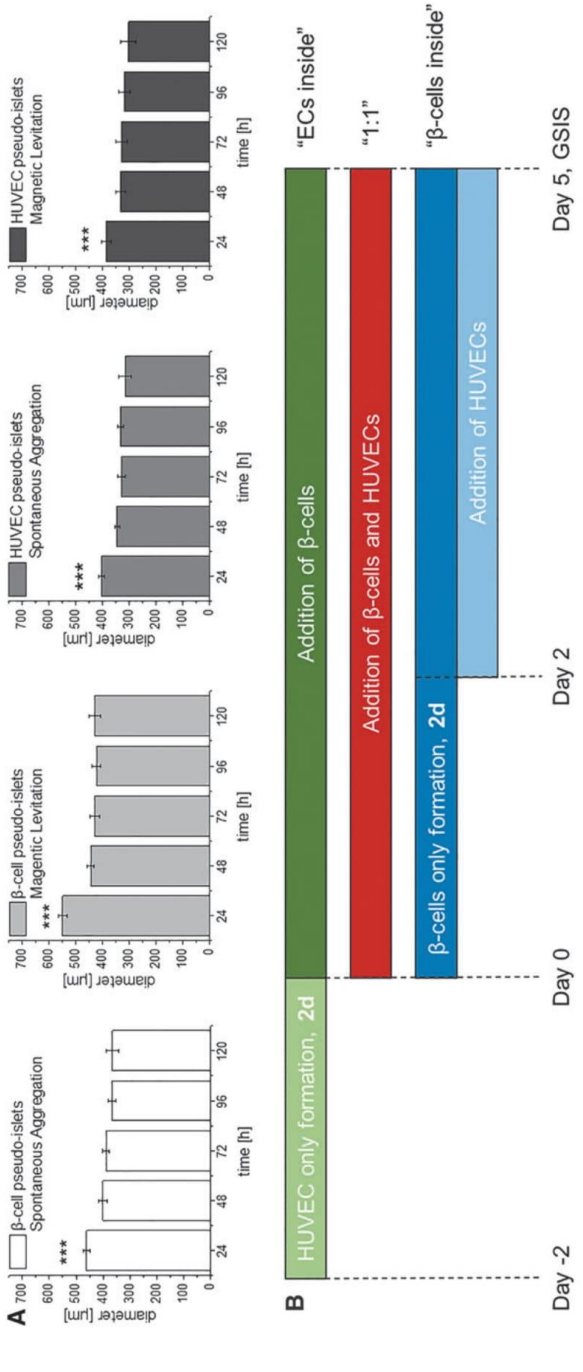

FIG. 2. Illustration of experimental timeline with regard to external constraints. (**A**) Pseudo-islets require 48 h of culture time to form stable aggregates independent from the culture method or cell type. (**B**) Experimental timeline required to form stable pseudo-islets, and β-cells are cultured for 5 days according to manufacturer's protocol before GSIS testing is performed. One-way ANOVA, $n = 10$, $^{***}p < 0.001$. ANOVA, analysis of variance; ECs, endothelial cells; GSIS, glucose-stimulated insulin secretion.

under standard conditions. Afterward, the pseudo-islets were washed twice with β-Krebs medium, consisting of KREBS-buffer (βKREBS®; Univercell Biosolutions) containing 10% bovine serum albumin (A-9576; Sigma-Aldrich), followed by an incubation for 1 h in β-Krebs medium for synchronization as previously described.[31] Subsequently, the pseudo-islets were alternatingly incubated in basal β-Krebs medium (Krebs 1), β-Krebs medium with 20 mmol/L D-glucose (20 mM glucose) (Gibco), and basal β-Krebs medium (Krebs 2) for 1 h under each condition. After each incubation, the supernatant was removed and stored at −20°C until further analysis. The insulin content of all supernatants was analyzed using an ultrasensitive human insulin enzyme-linked immunosorbent assay (10-1132-01; Mercodia, Uppsala, Sweden). Insulin content was normalized by number of pseudo-islets.

GSIS index

The GSIS index from Krebs 1 to 20 mM glucose was calculated using the formula: (insulin secretion of 20 mM glucose)/(insulin secretion of Krebs 1); the GSIS index from 20 mM glucose to Krebs 2 was calculated accordingly using the formula: (Insulin secretion of Krebs 2)/(insulin secretion of 20 mM glucose). The standard deviation was calculated using the formula for propagation of error.

Immunofluorescence staining and microscopy

Pseudo-islets were processed to 3 μm thick sections and deparaffinized as described earlier. Adult human pancreatic tissue sections were purchased from Novus Biologicals (NBP2-30191; Novus Biologicals, Bio-Techne GmbH, Wiesbaden, Germany). For all sections, heat-mediated antigen retrieval in TRIS-EDTA (pH = 9.0) and citrate (pH = 6.0) buffer was performed. All sections were blocked in 2% goat block serum. For immunofluorescence (IF) staining, the following primary antibodies and dilutions were used: platelet endothelial cell adhesion molecule-1 (CD31; sc-71872; Santa Cruz, USA, 1:50), insulin (A0564; DAKO, Frankfurt, Germany, 1:200), epithelial cadherin (E-cadherin) (ab76055; Abcam, 1:250), Ki67 (ab15880; Abcam, 1:1000). For IF staining of CD31 and insulin, the sections were pretreated with 0.1% Triton-X 100 for 10 min. The primary antibodies were incubated overnight at 4°C. The following secondary antibodies were used at a dilution of 1:250: Alexa Fluor® goat anti-mouse immunoglobulin G (IgG) 1 (488), goat anti-mouse IgG 2a (488) and goat anti-guinea pig (594) (all Invitrogen). Isotype controls were included. Counterstaining was performed using DAPI solution (Sigma-Aldrich) with a concentration of 2 μg/mL for 10 min before mounting with ProLong Gold antifade mounting medium (Thermo Fisher Scientific). IF staining and bright field (BF) images from pseudo-islets were captured at 10× or 20× magnification and 1.0× tube lens, IF staining images from pancreatic tissues were captured at 63× magnification and 1.0× tube lens using an Observer Z1 light microscope from Zeiss (Carl Zeiss, Jena, Germany). BF images of long-term stability were obtained with 10× magnification and 1.6× tube lens.

Image analysis

Blinded TUNEL images were quantified by two unbiased observers. Cells were identified as $TUNEL^+$ when exhibiting a clear green and blue double staining. The cell death ratio was calculated by quantifying $TUNEL^+$ cells, normalized to the DAPI count per pseudo-islet using the formula: normalized cell death ratio = ($TUNEL^+$ cells in pseudo-islet)/(DAPI count per pseudo-islet).

CD31 expression per insulin was quantified using IF images. Regions of interest (ROIs) were drawn focusing on the insulin staining, which was then overlaid onto the CD31 staining. Grey value intensities (GVI) were measured for both insulin and CD31. The CD31 ratio was calculated using the formula: ratio = (GVI of CD31 in ROI)/(GVI of insulin in ROI).

E-cadherin expression was measured by GVI analysis of $DAPI^+$ regions within pseudo-islets. All measurements were performed using ImageJ.

To assess the EC location within pseudo-islets of the ''β-cells inside'' distribution formed by magnetic levitation, the pseudo-islets were divided in two areas with the same size: A_{inside} and $A_{periphery}$, where A_{inside} had a radius of 0.707 days. The GVI of CD31 staining was measured in A_{inside} and multiplied by the area of A_{inside}, to obtain the total CD31 expression within the corresponding area. The same procedure was executed for $A_{periphery}$. The ratio of $CD31_{inside}$ and $CD31_{periphery}$ was calculated using the formula: ratio = (total $CD31_{inside}$)/(total $CD31_{periphery}$).

Blinded Ki67 IF images were quantified by two unbiased observers. Cells exhibiting a clear $Ki67^+$ and $DAPI^+$ staining were counted as proliferative. The proliferation rate was calculated using the formula: proliferation rate = ($Ki67^+$/$DAPI^+$ cells in pseudo-islet)/($DAPI^+$ cells in pseudo-islet).

Statistical analysis

Statistical analysis was performed using Origin 2018 (OriginLab, Northampton, MA). Results shown throughout the entire article are means ± standard deviations. All data sets were tested for normal distribution with Kolmogorov–Smirnov test. Outliers were identified with Grubb's test. Significance of the CD31/insulin ratio was analyzed using one-way analysis of variance (ANOVA) ($n \geq 6$). The statistical significances of the TUNEL assay were analyzed with Student's *t*-test and one-way ANOVA, respectively ($n = 10$). GSIS data were statistically analyzed using two-way ANOVA with Tukey's multiple comparison for the effect of aggregation process and spatial distribution ($n \geq 3$). The GSIS index from Krebs 1 to glucose and from glucose to Krebs 2 was statistically analyzed by one-way ANOVA with Tukey's multiple comparison ($n \geq 3$). Pseudo-quantification of E-cadherin was assessed using one-way ANOVA with Tukey's multiple comparison for the effect of spatial distribution ($n = 20$). The β-cell and HUVEC pseudo-islets formed by spontaneous aggregation or magnetic levitation were statistically analyzed using one-way ANOVA with Tukey's multiple comparison for the effect of time on pseudo-islet size ($n = 10$). GSIS data of functionality assessment were statistically analyzed by two-way ANOVA with Tukey's multiple comparison ($n = 10$). The corresponding GSIS index from Krebs 1 to glucose and from glucose to Krebs 2 was statistically analyzed by one-way ANOVA with Tukey's multiple comparison ($n = 10$). Area comparison and total $CD31^+$ content were statistically analyzed using Student's *t*-test ($n = 10$). Relative cell number during excision was statistically evaluated using one-way ANOVA ($n = 7$). The significance of proliferation rate was analyzed using Student's *t*-test ($n = 10$). Statistical significance was defined at $p < 0.05$.

Results

Magnetic levitation facilitates controlled aggregation of heterotypic pseudo-islets and HUVEC integration

In native pancreatic tissue (Fig. 3A, H, O), we identified three major naturally occurring spatial distributions of β-cells and ECs: (1) the heterogeneous distribution of both cell types (''1:1,'' Fig. 3A), (2) ECs surrounded by β-cells (''ECs inside,'' Fig. 3H), and (3) β-cells surrounded by ECs (''β-cells inside,'' Fig. 3O). Based on these findings, schematics were developed to model the distributions in heterotypic pseudo-islets that needed to be evaluated (Fig. 3B, I, P).

To mimic the three distribution patterns seen in native pancreatic tissue, and in addition to spontaneous aggregation, we utilized magnetic levitation for a controlled cellular movement and aggregation by employing external magnetic fields. To identify a potential impact of the NanoShuttle-PL treatment on cell survival, TUNEL assays were performed to evaluate DNA fragmentation within cells as an indication of the last step of cell apoptosis or necrosis.[34,35] TUNEL analysis revealed no significant differences in the number of cells exhibiting DNA fragmentation within the β-cell-containing pseudo-islet cultures after 48 h ($3.19 \pm 0.53\%$ spontaneous aggregation vs. $3.41 \pm 0.80\%$ magnetic levitation, $p = 0.922$) or 120 h ($5.97 \pm 1.01\%$ spontaneous aggregation vs. $5.71 \pm 0.58\%$ magnetic levitation, $p = 0.887$) (Fig. 4). Furthermore, glucose response of pseudo-islets after 120 h was maintained after NanoShuttle-treatment (Supplementary Fig. S2).

Spontaneous aggregation led in all three distribution types (''1:1,'' ''ECs inside'' and ''β-cells inside'') to the disassembly of HUVECs from the β-cell-composed pseudo-islets (Fig. 3C, D, J, K, Q, R). IF staining revealed that almost no $CD31^+$ HUVECs were present within the insulin-producing β-cell-composed pseudo-islets (Fig. 3C, J, Q).[36,37] In contrast, magnetic levitation resulted in the formation of intact heterotypic pseudo-islets with a promoted HUVEC integration (Fig. 3E, F, L, M, S, T). These heterotypic pseudo-islets were stable for up to 25 days (Fig. 5). IF staining revealed that $CD31^+$ HUVECs were heterogeneously distributed throughout the ''1:1'' pseudo-islets (Fig. 3F). The ''ECs inside'' condition produced pseudo-islets that showed a distinguishable $CD31^+$ HUVEC center (Fig. 3M). IF staining of the pseudo-islets formed based on the ''β-cells inside'' distribution pattern showed predominantly $CD31^+$ HUVECs in the periphery of the constructs (Fig. 3T; Supplementary Fig. S3).

According to these observations, quantification showed a statistically significant increase in $CD31^+$ HUVECs in all pseudo-islet distribution types formed by magnetic levitation when compared with pseudo-islets formed by spontaneous aggregation (''1:1'': 0.45 ± 0.23 vs. 0.18 ± 0.07, $^{**}p < 0.01$, Fig. 3G; ''ECs inside,'' 0.95 ± 0.20 vs. 0.23 ± 0.05, $^{***}p < 0.001$, Fig. 3N; ''β-cells inside,'' 0.47 ± 0.15 vs. 0.22 ± 0.08, $^{**}p < 0.01$, Fig. 3U).

Spatial distribution of heterotypic pseudo-islet cultures significantly influences insulin secretion upon glucose stimulation

We assessed the functionality of the pseudo-islet cultures by measuring the insulin secretion using serial GSIS assays (Fig. 6A, B). We identified that pseudo-islets composed of β-cells inside and HUVECs outside secreted significantly higher amounts of insulin upon glucose stimulation, independently of the aggregation method when compared with all other cell compositions or the control group, which is pseudo-islets composed of β-cells alone formed by spontaneous aggregation (''β-cells inside'' spontaneous aggregation: 49.37 ± 10 mU/L vs. ''β-cells inside'': magnetic levitation 55.09 ± 5.01 mU/L, $^{***}p < 0.001$, Fig. 6A). Interestingly, the pseudo-islets composed of β-cells inside and HUVECs outside formed by magnetic levitation produced significantly higher levels of insulin in the initial basal state after Krebs 1 medium treatment when compared with the control group (25.85 ± 3.80 mU/L vs. 10.59 ± 1.29 mU/L, $^{*}p < 0.05$, Fig. 6A). The ''β-cells inside'' condition formed by magnetic levitation also secreted significantly higher levels of insulin in the second basal state, after Krebs 2 medium treatment, when compared with any other condition and the control group ($^{**}p < 0.01$, Fig. 6A). Importantly, no relevant statistically significant differences in the GSIS indices calculated from the serial GSIS were observed (Fig. 6B), which indicates that the stimulable nature of β-cells is not altered in the ''β-cells inside'' distribution group, although the basal insulin levels are increased. Importantly, the observed differences in glucose response were not attributable to cell death, since TUNEL analyses of the three spatial distributions formed by magnetic levitation did not exhibit any significant differences in DNA fragmentation (''1:1'': $6.76 \pm 2.32\%$, ''ECs inside'': $7.99 \pm 2.44\%$, ''β-cells inside'': $7.40 \pm 2.10\%$, Fig. 6C–F).

In summary, we identified that heterotypic pseudo-islets with β-cells inside and HUVECs outside formed by magnetic levitation exhibited the highest insulin secretory function in every condition without a loss in stimulation capabilities from basal to high glucose and back to the basal state.

β-Cells surrounded by HUVECs express significantly more E-cadherin

E-cadherin is a cell surface adhesion protein that is associated with cell–cell interactions and has been proposed to promote insulin secretion through intra-islet communications.[38–40] In this study, we investigated the expression of E-cadherin in the heterotypic pseudo-islets formed by magnetic levitation (Fig. 6G–J). We identified that E-cadherin was distributed evenly throughout the ''1:1'' and ''β-cells inside'' heterotypic pseudo-islets (Fig. 6G, I). In contrast, pseudo-islets composed of ECs inside and β-cells outside did not express E-cadherin in the center (Fig. 6H). In general, we saw that only β-cells expressed E-cadherin. Interestingly, β-cells of the ''β-cells inside'' condition expressed significantly higher levels of E-cadherin per cell when compared with the other conditions (''β-cells inside'': 75.75 ± 15.15 compared with ''1:1'': 55.17 ± 5.93 and ''ECs inside'': 47.02 ± 6.39; $p < 0.001$, Fig. 6J).

Discussion

Pancreatic β-cells, which are naturally surrounded by a major capillary network that provides proper nutrition, oxygenation, cell–ECM, and cell–cell interactions, suffer from loss of this microenvironment after transplantation.[41]

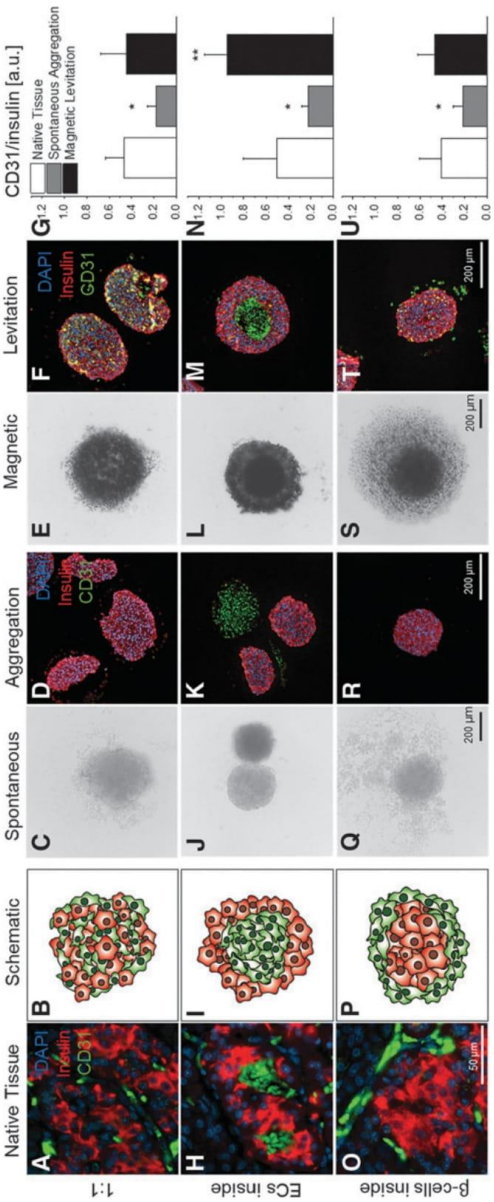

FIG. 3. Spatial distribution of β-cells and ECs in native pancreas tissue, representative BF and IF staining images of *in vitro*-formed heterotypic pseudo-islets with spontaneous aggregation or magnetic levitation as well as CD31/insulin analysis. Native tissue staining for CD31 as EC marker and insulin as β-cell marker revealed different spatial distributions of ECs and β-cells within the human pancreas (**A, H, O**). Spatial distributions are shown in the schematic depiction for 1:1 (**B**), ECs inside (**I**), and β-cells inside (**P**) (ECs in *green*, β-cells in *red*). BF images of heterotypic pseudo-islets in culture and IF images after histological preparation of heterotypic pseudo-islets formed by spontaneous aggregation (**C, D, J, K, Q, R**) showed no interaction and disassemble of HUVECs independent from the spatial distribution. BF and IF images of heterotypic pseudo-islets formed with magnetic levitation (**E, F, L, M, S, T**) showed improved interaction and controlled aggregation. HUVEC integration was significantly increased with magnetic levitation and comparable with native levels (**G, N, U**). Student's *t*-test, $n = 6$, $^{*}p < 0.01$, $^{**}p < 0.001$. BF, bright field; DAPI, 4′,6-diamidino-2-phenylindole; IF, immunofluorescence.

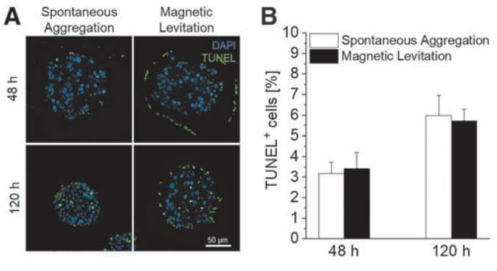

FIG. 4. Evaluation of influence of NanoShuttle™-PL treatment on DNA fragmentation of cells, indicating the final stage of apoptosis and necrosis. **(A)** TUNEL staining of pseudo-islets formed with spontaneous aggregation and magnetic levitation after 48 and 120 h. **(B)** Quantification of TUNEL$^+$ cells per DAPI. Student's *t*-test, $n = 10$. TUNEL, terminal deoxynucleotidyl transferase-mediated nick-end labeling.

Recreating the pancreatic niche by the combination of ECs and pancreatic β-cells may contribute to graft survival *in vitro*.[42] Apart from improved graft survival[13,22] and prevascularization,[43] the coculture of β-cells with ECs provides beneficial effects on β-cell functionality.[10,18,27] However, these stimulatory capabilities of ECs on β-cells have not been shown to exist in a human-only cell line-based *in vitro* model. In addition, the influence of the spatial distribution in such human heterotypic cell aggregates has not been clarified. Yet, both are requirements that need to be met to understand factors contributing to regulatory mechanisms in the crosstalk of β-cells and ECs in the human body.[44]

In this study, we identified three major spatial distributions of β-cells and ECs in native human pancreatic tissue: (1) the even distribution of both cell types, (2) ECs surrounded by β-cells, and (3) β-cells surrounded by ECs. We

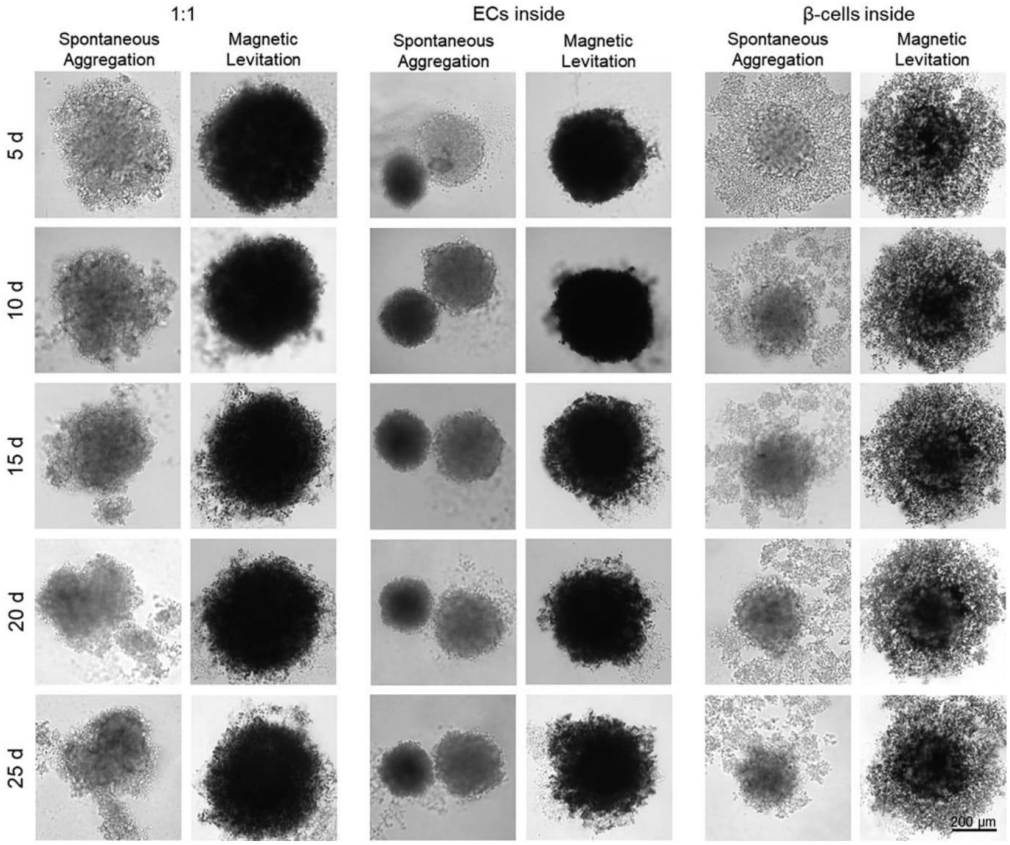

FIG. 5. Representative BF images of long-term stability tests of heterotypic pseudo-islets using spontaneous aggregation and magnetic levitation for up to 25 days with minor disassembly occurring after day 15. Heterotypic pseudo-islets formed with magnetic levitation were stable for up to 25 days independent from spatial distribution. Pseudo-islets formed with spontaneous aggregation show disaggregation starting at day 10 for ''1:1'' pseudo-islets, at day 5 for ''ECs inside'' pseudo-islets and at day 10 for ''β-cells inside'' pseudo-islets.

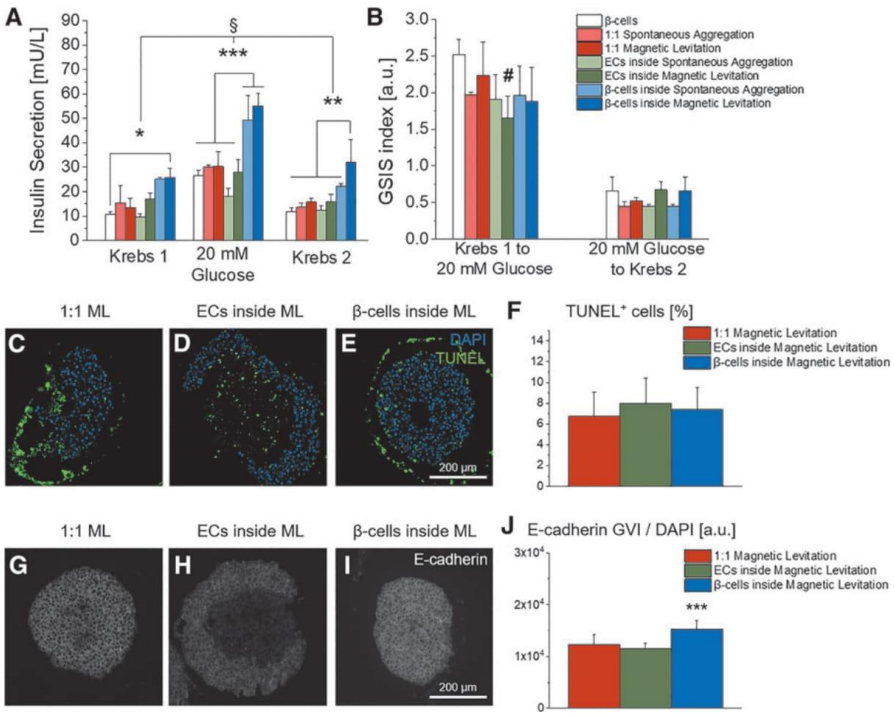

FIG. 6. Functionality assessment of heterotypic pseudo-islets formed with spontaneous aggregation and magnetic levitation. **(A)** ''β-cells inside'' secreted significantly more insulin upon glucose challenge. In addition, ''β-cells inside'' formed with magnetic levitation had significantly increased levels of basal insulin secretion; one-way ANOVA, $n \geq 3$. **(B)** The GSIS index for ''β-cells inside'' did not differ significantly showing comparable stimulation properties although basal insulin secretion is increased; one-way ANOVA, $n \geq 3$. **(C–E)** Representative images of TUNEL staining of heterotypic spheroids with the three different spatial distributions formed with magnetic levitation. **(F)** Quantification of TUNEL$^+$ cells per DAPI. One-way ANOVA, $n = 10$. **(G–I)** Representative images for GVI analysis of IF staining for E-cadherin and **(J)** pseudo-quantification of heterotypic pseudo-islets formed by magnetic levitation; one-way ANOVA, $n = 20$. $^{\S}p < 0.001$, $^{\#}p < 0.01$, $^{*}p < 0.05$, $^{**}p < 0.01$ $^{***}p < 0.001$. GVI, grey value intensities.

introduced an abstract classification (1–3) of the complex anatomy to recreate an *in vitro* system based of these naturally occurring distributions. Furthermore, investigation of the spatial distribution of the islets of Langerhans revealed that each β-cell in native islets is surrounded by at least one EC,[9,11,18] underlining the relevance of all three selected spatial distributions. To recapitulate those three distribution patterns, ''1:1,'' ''ECs inside'' and ''β-cells inside,'' heterotypic pseudo-islets consisting of human β-cells and HUVECs were formed *in vitro* by spontaneous aggregation. In contrast to previous studies showing natural aggregation of HUVECs with murine MIN6 cells,[18] in our hands, HUVECs did not interact with the human β-cells. Moreover, the HUVECs formed rather autonomous spheroids, and a formation of stable pseudo-islets with defined structural features was not possible. One limitation could be that HUVECs are not an ideal cell source to mimic vascular ECs in combination with the human β-cell line EndoC-βH3, although HUVECs have been widely used and established to model ECs behavior.[5,18,25,27,43,45–48] Dissimilarities upon cytotoxic reagents or in cytoarchitecture of islets have been previously described, underlining major differences between human and rodent pancreatic islets, which limits the possibility to extrapolate from results obtained in rodent systems to the human ones.[29,49]

Since β-cells rely on an highly specialized environment,[15] a human cell line-based *in vitro* test system might require particularly specialized ECs to properly model the interaction between β-cells and ECs, such as human pancreatic microvascular ECs or ductal epithelial cells (DECs). DECs, for instance, play an important role in pancreatic morphogenesis[50] as well as during initial islet differentiation.[51] Furthermore, it has been shown that insulin-producing β-cells can be derived from DECs[52,53] since both cell types originate from foregut endodermal progenitors,[51] hinting toward comparable specialized capabilities and properties. In addition, different groups found that DECs increase the viability and proliferation of mature β-cells by secretion of islet growth and regulatory factors such as insulin-like growth factor 2, thus naturally contributing to the maintenance of the β-cell population in the pancreas *in vivo*.[50,54]

To overcome the interactional problem between HUVECs and human β-cells, we used magnetic levitation to form heterotypic pseudo-islets. This technique uses positively charged poly-L-lysine amino chains to attach gold and iron oxide nanoparticles to the cell surface, which in turn enables a controlled cell aggregation by application of external magnetic fields.[55] By utilizing magnetic levitation, we created pseudo-islets in a controlled manner with defined internal architectures and improved HUVEC integration. Magnetic levitation helps, therefore, to overcome the inefficient incorporation of different cell types in heterotypic spheroids as seen when using spontaneous aggregation like in this study and as it was described previously by Kusamori *et al.*[14] This method is also improving the reproducibility of mixed heterotypic spheroids and addresses the limitation of conventional methods to control the size of multicellular spheroids.[14,56]

In our study, pseudo-islets were derived using 5000 cells/cell type per spheroid with magnetic levitation. TUNEL assays showed that the cell viability within the pseudo-islets was not impacted by the method. Structural and distributional differences can be easily monitored in bigger heterotypic spheroids, facilitating also the quantification of cell–cell and cell–matrix integrations. With the successful establishment of the human cell line-based *in vitro* model, further studies can now be conducted with smaller pseudo-islet sizes ranging in the native pancreatic islet size of ~150 μm, improving both functionality and survival of pseudo-islets.[57–60] A limitation of the current setup are the varying culture times of the three different coculture pseudo-islet types, which originated from external constraints: (1) pseudo-islets need 48 h to form stable aggregates, independent from cell type and culture method, and (2) the mandatory culture time for the β-cells of 5 days before GSIS according to manufacturer's protocol (Fig. 2).

We were further interested in the question of how multicellular spatial distributions, as seen in native human pancreas, may impact insulin secretion upon glucose stimulation within the *in vitro*-engineered pseudo-islets. The spatial influence of ECs during pancreatic development has been described before, showing that the dorsal aorta initiates the endocrine differentiation, which can be monitored by an increased insulin expression and by the formation of pancreatic bud-like structures that form from the endoderm.[61] When Lammert *et al.* removed the dorsal aorta in their study, no insulin gene expression was seen.[61] During development, the spatial distribution of ECs and blood vessels adapt as the pancreas forms from an adjacent distribution of ECs and endoderm to a dense meshwork of capillaries within the fully developed pancreas,[62] supporting the important role of ECs for endocrine functionality. In this study, we identified that only constructs with β-cells inside and HUVECs outside achieved a significant insulin secretion stimulation upon glucose challenge. Although both aggregation procedures, spontaneous aggregation and magnetic levitation, showed comparable amounts of secreted insulin, a significant stimulation in basal insulin secretion was solely identified for the "β-cells inside" constructs formed by magnetic levitation (Fig. 6A). Importantly, no significant alteration in any of both GSIS indices could be observed. Loss in GSIS index would be an epiphenomenon of impaired intracellular feedback loops and β-cell mis-sensing of extracellular levels of glucose and insulin,[63] undermining the validity of this *in vitro* test system.

In our hands, an increase in β-cell insulin secretion could only be achieved when HUVECs were added to preformed β-cell-composed pseudo-islets. Thus, spatial distribution is critical to enhance β-cell functionality. The "β-cell inside" distribution pattern has also been used by Ilieva *et al.*,[50] Ferrer *et al.*,[53] and Murray *et al.*[54] to stimulate insulin secretion, although not by design, since isolated pancreatic islets had been used in their setup, which are already solidly formed. In contrast, Kusamori *et al.*[14] reported spontaneous formation of the "ECs inside" distribution when adding murine ECs, fibroblasts and β-cells simultaneously to form heterotypic spheroids, which also led to an increased insulin secretion. This might be explained by optimal cell–cell interactions in this intraspecific rodent model consistent of mouse ECs, mouse fibroblasts, and mouse β-cells.[14] Although nearly no HUVECs were integrated when using spontaneous aggregation, also those conditions were able to be stimulated by coculture. This phenomenon has already been described by groups that used EC-conditioned media to upregulate β-cell functionality by introducing factors expressed by ECs into the β-cell culture.[9,50] Our results indicate that either the self-assembly of β-cells inside and HUVECs outside integrates a sufficient percentage of HUVECs to achieve β-cell stimulation, or that β-cells only require signalling molecules expressed by HUVECs to be stimulated.

Heterotypic pseudo-islets with β-cells inside and HUVECs outside expressed significantly higher levels of the cell–cell adhesion marker E-cadherin than in any other spatial distribution (Fig. 6G–J). E-cadherin has been shown to promote intracellular insulin secretion[38–40] by its binding properties to β-catenin, thus controlling actin skeleton remodeling through α-catenin,[64] which is known to regulate insulin secretion from β-cells.[65] In addition to cell–cell adhesion, E-cadherin functions as cell proliferation mediator within the islets through the Wnt pathway, contributing to β-cell mass stability.[40,66] Since HUVECs express only VE-cadherin and neuronal (N-) cadherin,[67] yet no E-Cadherin (Fig. 6H), the integration of HUVECs into the pseudo-islets possibly disturbed the β-cell communication in the "1:1" and "ECs inside" distributions, whereas the "β-cells inside" constructs were formed without any HUVEC intermission. Since both cadherins can bind p120, another cell adhesion protein related to β-catenin, VE-cadherin might interfere with E-cadherin and hence interrupt the cell–cell signalling between the β-cells, resulting in stimulated insulin secretion solely in the "β-cells inside" condition.[64,68–70] To summarize, the spatial distribution, which can be controlled by using magnetic levitation, is critical to stimulate the EndoC-βH3 cell functionality by HUVEC coculture. Only when cultured as "β-cells inside" distribution, β-cells exhibited an increased insulin secretory function, accompanied with elevated levels of E-cadherin, which is vital for cell–cell communication and insulin expression.

A pathway through which ECs might upregulate β-cell functionality is through interaction of CD31 with the integrin $\alpha_v\beta_3$, since CD31 expressed by ECs is a counter-receptor of $\alpha_v\beta_3$.[37,71,72] CD31 regulates angiogenesis, migration, proliferation, and cell–cell interaction by homophilic binding, but has also been shown to interact heterophilic.[71] An interaction

of CD31 with the $\alpha_v\beta_3$-integrin present on the cell surface of β-cells[73] might also promote β-cell functionality and survival. It has been described that the binding of $\alpha_v\beta_3$ activates the ERK1/2-pathway, which is known to increase an intercellular insulin response.[73–75] However, the activation of $\alpha_v\beta_3$ by CD31 alone cannot completely explain the increased β-cell functionality, since heterotypic spheroids with the ''ECs inside'' distribution revealed the highest CD31 ratio without a significantly increased insulin secretion, implying that other pathways take place in the stimulation process of β-cells.

Conclusion

In this study, we have established the first human cell line-based pseudo-islet *in vitro* test system to investigate coculture effects of human β-cells on human ECs. Magnetic levitation allowed the stable formation of heterotypic pseudo-islets with defined spatial distributions of β-cells and HUVECs. In addition, we showed that the stimulatory capabilities of ECs on β-cells were best utilized when a β-cell composed pseudo-islet is surrounded by an outer layer of ECs, emphasizing that the spatial distribution as well as cell–cell interactions are crucial for an increased insulin secretion and, therefore, β-cell functionality. Together, these promising results lay the foundation for upcoming study to further improve the *in vitro* test model and investigate coculture interactions of human β-cells and ECs en route to develop prevascularized transplantable islet grafts.

Acknowledgment

We thank Prof. P. Maechler for the kind donation of the rat insulinoma INS-1E cells.

Disclosure Statement

No competing financial interests exist.

Funding Information

This study was funded by the European Union's Horizon 2020 research and innovation programmes under the grant agreement number 645991, DRIVE, and 812865, DELIVER (both to G.D. and K.S.-L.), the Deutsche Forschungsgemeinschaft (INST 2388/34-1, SCHE701/14-1 and Germany's Excellence Strategy—EXC 2180-390900677 all to K.S.-L.) and the Ministry of Science, Research and the Arts of Baden-Württemberg (33-729.55-3/214 and SI-BW 01222-91 [both to K.S-L.]).

Supplementary Material

Supplementary Figure S1
Supplementary Figure S2
Supplementary Figure S3

References

1. IDF Diabetes Atlas 2017. IDF Diabetes Atlas, 8th edition. Brussels, Belgium: International Diabetes Federation, 2017.
2. Dankwa-Mullan, I., Rivo, M., Sepulveda, M., Park, Y., Snowdon, J., and Rhee, K. Transforming diabetes care through artificial intelligence: the future is here. Popul Health Manag **22,** 229, 2018.
3. Rogal, J., Zbinden, A., Schenke-layland, K., and Loskill, P. Stem-cell based organ-on-a-chip models for diabetes research. Adv Drug Deliv Rev **140,** 101, 2019.
4. Borchers, A.T., Uibo, R., and Gershwin, M.E. The geoepidemiology of type 1 diabetes. Autoimmun Rev J **9,** 355, 2010.
5. Vlahos, A.E., Cober, N., and Sefton, M.V. Modular tissue engineering for the vascularization of subcutaneously transplanted pancreatic islets. Proc Natl Acad Sci USA **114,** 201619216, 2017.
6. Cañibano-Hernández, A., Sáenz, L., and Espona-noguera, A. Current advanced therapy cell-based medicinal products for type-1-diabetes treatment. Int J Pharm **543,** 107, 2018.
7. Cross, S.E., Vaughan, R.H., Willcox, A.J., *et al.* Key matrix proteins within the pancreatic islet basement membrane are differentially digested during human islet isolation. Am J Transplant **17,** 451, 2017.
8. Hadavi, E., Leijten, J., Brinkmann, J., Jonkheijm, P., Karperien, M., and van Apeldoorn, A. Fibronectin and collagen IV microcontact printing improves insulin secretion by INS1E cells. Tissue Eng Part C Methods **24,** 628, 2018.
9. Johansson, Å., Lau, J., Sandberg, M., Borg, L.A.H., Magnusson, P.U., and Carlsson, P.O. Endothelial cell signalling supports pancreatic beta cell function in the rat. Diabetologia **52,** 2385, 2009.
10. Shin, J.-Y., Jeong, J.-H., Han, J., *et al.* Transplantation of heterospheroids of islet cells and mesenchymal stem cells for effective angiogenesis and antiapoptosis. Tissue Eng Part A **21,** 1024, 2014.
11. Olsson, R., and Carlsson, P. The pancreatic islet endothelial cell: emerging roles in islet function and disease. Int J Biochem Cell Biol **38,** 710, 2006.
12. Brissova, M., Shostak, A., Fligner, C.L., *et al.* Human islets have fewer blood vessels than mouse islets and the density of islet vascular structures is increased in type 2 diabetes. J Histochem Cytochem **63,** 637, 2015.
13. Kaufman-Francis, K., Koffler, J., Weinberg, N., Dor, Y., and Levenberg, S. Engineered vascular beds provide key signals to pancreatic hormone-producing cells. PLoS One **7,** 1, 2012.
14. Kusamori, K., Nishikawa, M., Mizuno, N., *et al.* Increased insulin secretion from insulin-secreting cells by construction of mixed multicellular spheroids. Pharm Res **33,** 247, 2016.
15. Stendahl, J.C., Kaufman, D.B., and Stupp, S.I. Review extracellular matrix in pancreatic islets: relevance to scaffold design and transplantation. Cell Transplant **18,** 1, 2009.
16. Zhu, H., Li, W., Liu, Z., *et al.* Selection of Implantation Sites for Transplantation of Encapsulated Pancreatic Islets. Tissue Eng Part B Rev **24,** 191, 2017.
17. Gaetani, R., Aude, S., DeMaddalena, L.L., *et al.* Evaluation of different decellularization protocols on the generation of pancreas-derived hydrogels. Tissue Eng Part C Methods **24,** 697, 2018.
18. Skrzypek, K., Barrera, Y.B., Groth, T., and Stamatialis, D. Endothelial and beta cell composite aggregates for improved function of a bioartificial pancreas encapsulation device. Int J Artif Organs **41,** 152, 2018.
19. Del Toro-Arreola, A., Robles-Murillo, A.K., Daneri-Navarro, A., and Rivas-Carrillo, J.D. The role of endothelial cells on islet function and revascularization after islet transplantation. Organogenesis **12,** 28, 2016.

20. Aloy-Reverté, C., Moreno-Amador, J.L., Nacher, M., Montanya, E., and Semino, C.E. Use of RGD-functionalized sandwich cultures to promote redifferentiation of human pancreatic beta cells after in vitro expansion. Tissue Eng Part A **24,** 394, 2017.
21. Citro, A., Moser, P.T., Dugnani, E., *et al.* Biofabrication of a vascularized islet organ for type 1 diabetes. Biomaterials **199,** 40, 2019.
22. Hospodiuk, M., Moncal, K.K., Ayan, B., *et al.* Sprouting angiogenesis in engineered pseudo islets. Biofabrication **10,** 035003, 2018.
23. Miyakoshi, J., Sakurai, T., Nagata, N., *et al.* The Efficient prevascularization induced by fibroblast growth factor 2 with a collagen-coated device improves the cell survival of a bioartificial pancreas. Pancreas **28,** e70, 2004.
24. Krawiec, J.T., Weinbaum, J.S., Liao, H.-T., *et al.* In vivo functional evaluation of tissue-engineered vascular grafts fabricated using human adipose-derived stem cells from high cardiovascular risk populations. Tissue Eng Part A **22,** 765, 2016.
25. Roux, B.M., Akar, B., Zhou, W., *et al.* Preformed vascular networks survive and enhance vascularization in critical sized cranial defects. Tissue Eng Part A **24,** 1603, 2018.
26. Sabra, G., and Vermette, P. A 3D cell culture system: separation distance between INS-1 cell and endothelial cell monolayers co-cultured in fibrin influences INS-1 cells insulin secretion. Biotechnol Bioeng **110,** 619, 2013.
27. Paget, M.B., Murray, H.E., Bailey, C.J., Flatt, P.R., and Downing, R. Rotational co-culture of clonal β-cells with endothelial cells: effect of PPAR-γ agonism in vitro on insulin and VEGF secretion. Diabetes Obes Metab **13,** 662, 2011.
28. Skelin, M., Rupnik, M., and Cencic, A. Pancreatic beta cell lines and their applications in diabetes mellitus research. ALTEX **27,** 105, 2010.
29. Cabrera, O., Berman, D.M., Kenyon, N.S., Ricordi, C., Berggren, P., and Caicedo, A. The unique cytoarchitecture of human pancreatic islets has implications for islet cell function. PNAS **103,** 2334, 2006.
30. MacDonald, M.J., Longacre, M.J., Stoker, S.W., *et al.* Differences between human and rodent pancreatic islets: low pyruvate carboxylase, ATP citrate lyase, and pyruvate carboxylation and high glucose-stimulated acetoacetate in human pancreatic islets. J Biol Chem **286,** 18383, 2011.
31. Benazra, M., Lecomte, M.J., Colace, C., *et al.* A human beta cell line with drug inducible excision of immortalizing transgenes. Mol Metab **4,** 916, 2015.
32. Zbinden, A., Marzi, J., Schlünder, K., *et al.* Non-invasive marker-independent high content analysis of a microphysiological human pancreas-on-a-chip model. Matrix Biol 2019. [Epub ahead of print]; DOI: 10.1016/j.matbio .2019.06.008.
33. Haisler, W.L., Timm, D.M., Gage, J.A., Tseng, H., Killian, T.C., and Souza, G.R. Three-dimensional cell culturing by magnetic levitation. Nat Protoc **8,** 1940, 2013.
34. Hurst, P.R., Mora, J.M., and Fenwick, M.A. Caspase-3, TUNEL and ultrastructural studies of small follicles in adult human ovarian biopsies. Hum Reprod **21,** 1974, 2006.
35. Segale, J., Espadamala, J., Mateu, E., Domingo, M., Chianini, F., and Nofrarı, M. Apoptosis in normal lymphoid organs from healthy normal, conventional pigs at different ages detected by TUNEL and cleaved caspase-3 immunohistochemistry in paraffin-embedded tissues. Vet Immunol Immunopathol **99,** 203, 2004.
36. Baeyens, L., De Breuck, S., Lardon, J., Mfopou, J.K., Rooman, I., and Bouwens, L. In vitro generation of insulin-producing beta cells from adult exocrine pancreatic cells. Diabetologia **48,** 49, 2005.
37. Newman, P.J. The biology of PECAM-1. J Clin Invest **99,** 3, 1997.
38. Lecomte, M., Pechberty, S., Machado, C., *et al.* Aggregation of engineered human β-cells into pseudoislets: insulin secretion and gene expression profile in normoxic and hypoxic milieu. Cell Med **8,** 99, 2016.
39. Bi, X., Pohl, N.M., Qian, Z., *et al.* Decorin-mediated inhibition of colorectal cancer growth and migration is associated with E-cadherin in vitro and in mice. Carcinogenesis **33,** 326, 2017.
40. Rogers, G.J., Hodgkin, M.N., and Squires, P.E. E-cadherin and cell adhesion: a role in architecture and function in the pancreatic islet. Cell Physiol Biochem **19,** 987, 2007.
41. Takahashi, Y., Sekine, K., Kin, T., Takebe, T., and Taniguchi, H. Self-condensation culture enables vascularization of tissue fragments for efficient therapeutic transplantation. Cell Rep **23,** 1620, 2018.
42. Hillebrands, J.-L., Van Schilfgaarde, R., De Vos, P., De Haan, B.J., and Strubbe, J.H. Efficacy of a prevascularized expanded polytetrafluoroethylene solid support system as a transplantation site for pancreatic islets1. Transplantation **63,** 824, 2003.
43. Skrzypek, K., Nibbelink, M.G., Karbaat, L.P., Karperien, M., van Apeldoorn, A., and Stamatialis, D. An important step towards a prevascularized islet macroencapsulation device—effect of micropatterned membranes on development of endothelial cell network. J Mater Sci Mater Med **29,** 91, 2018.
44. Narayanan, S., Loganathan, G., Dhanasekaran, M., *et al.* Intra-islet endothelial cell and β-cell crosstalk: implication for islet cell transplantation. World J Transplant **7,** 117, 2017.
45. Lam, G.C., and Sefton, M.V. Hypoxia-inducible factor drives vascularization of modularly assembled engineered tissue. Tissue Eng Part A **25,** 1127, 2019.
46. Kuehn, C., Dubiel, E.A., Sabra, G., and Vermette, P. Culturing INS-1 cells on CDPGYIGSR-, RGD- and fibronectin surfaces improves insulin secretion and cell proliferation. Acta Biomater **8,** 619, 2012.
47. Gillies, G.T., Broaddus, W.C., Fillmore, H.L., *et al.* In vitro angiogenesis by human umbilical vein endothelial cells (HUVEC) induced by three-dimensional co-culture with glioblastoma cells. J Neurooncol **92,** 121, 2009.
48. Bishop, E.T., Bell, G.T., Bloor, S., Broom, I.J., Hendry, N.F.K., and Wheatley, D.N. An in vitro model of angiogenesis: basic features. Angiogenesis **3,** 335, 1999.
49. Eizirik, D.L., Pipeleers, D.G., Ling, Z., Welsh, N., Hellerström, C., and Andersson, A. Major species differences between humans and rodents in the susceptibility to pancreatic beta-cell injury. Proc Natl Acad Sci U S A **91,** 9253, 1994.
50. Ilieva, A., Yuan, S., Wang, R.N., Agapitos, D., Hill, D.J., and Rosenberg, L. Pancreatic islet cell survival following islet isolation: the role of cellular interactions in the pancreas. J Endocrinol **161,** 357, 1999.
51. Murtaugh, L.C. Pancreas and beta-cell development: from the actual to the possible. Development **134,** 427, 2006.
52. Park, I.S., Bendayan, M., Kim, S.Y., *et al.* Clusterin induces differentiation of pancreatic duct cells into insulin-secreting cells. Diabetologia **49,** 311, 2006.

53. Ferrer, J., Solar, M., De Medts, N., *et al.* Pancreatic exocrine duct cells give rise to insulin-producing β cells during embryogenesis but not after birth. Dev Cell **17,** 849, 2009.
54. Murray, H.E., Paget, M.B., Bailey, C.J., and Downing, R. Sustained insulin secretory response in human islets cocultured with pancreatic duct-derived epithelial cells within a rotational cell culture system. Diabetologia **52,** 477, 2009.
55. Daquinag, A.C., Souza, G.R., and Kolonin, M.G. Adipose tissue engineering in three-dimensional levitation tissue culture system based on magnetic nanoparticles. Tissue Eng Part C Methods **19,** 336, 2013.
56. Lin, R.Z., and Chang, H.Y. Recent advances in three-dimensional multicellular spheroid culture for biomedical research. Biotechnol J **3,** 1172, 2008.
57. Hellman, B., and Angervall, L. The frequency distribution of the number and volume of the islets of Langerhans in man. Acta Pathol Microbiol Scand **53,** 230, 1961.
58. Hilderink, J., Spijker, S., Carlotti, F., *et al.* Controlled aggregation of primary human pancreatic islet cells leads to glucose-responsive pseudoislets comparable to native islets. J Cell Mol Med **19,** 1836, 2015.
59. Ichihara, Y., Utoh, R., Yamada, M., Shimizu, T., and Uchigata, Y. Size effect of engineered islets prepared using microfabricated wells on islet cell function and arrangement. Heliyon **2,** e00129, 2016.
60. Kim, H.J., Alam, Z., Hwang, J.W., *et al.* Optimal formation of genetically modified and functional pancreatic islet spheroids by using hanging-drop strategy. TPS **45,** 605, 2013.
61. Lammert, E., Cleaver, O., and Melton, D. Role of endothelial cells in early pancreas and liver development. Mech Dev **120,** 59, 2003.
62. Cleaver, O., and Dor, Y. Vascular instruction of pancreas development. Development **139,** 2833, 2012.
63. Röder, P.V., Wu, B., Liu, Y., and Han, W. Pancreatic regulation of glucose homeostasis. Exp Mol Med **48,** e219, 2016.
64. Nollet, F., Kools, P., and Van Roy, F. Phylogenetic analysis of the cadherin superfamily allows identification of six major subfamilies besides several solitary members. J Mol Biol **299,** 551, 2000.
65. Kalwat, M.A., and Thurmond, D.C. Signaling mechanisms of glucose-induced F-actin remodeling in pancreatic islet β cells. Exp Mol Med **45,** e37, 2013.
66. Sell, H., Näther, C., and Herges, R. Amino-substituted diazocines as pincer-type photochromic switches. Beilstein J Org Chem **9,** 1, 2013.
67. Ferreri, D.M., Minnear, F.L., Yin, T., Kowalczyk, A.P., and Peter, A. N-cadherin levels in endothelial cells are regulated by monolayer maturity and p120 availability. Cell Commun Adhes **15,** 333, 2009.
68. Angst, B.D., Marcozzi, C., and Magee, A.I. The cadherin superfamily: diversity in form and function. J Cell Sci **114,** 629, 2001.
69. Wheelock, M.J., and Johnson, K.R. Cadherins as modulators of cellular phenotype. Annu Rev Cell Dev Biol **19,** 207, 2003.
70. Dejana, E., Bazzoni, G., and Lampugnani, M.G. Vascular endothelial (VE)-cadherin: Only an intercellular glue? Exp Cell Res **252,** 13, 1999.
71. Piali, L., Hammel, P., Uherek, C., Bachmann, F., Gisler, R.H., and Dunon, D. CD31/PECAM-1 is a ligand for otv133 integrin involved in adhesion of leukocytes to endothelium. J Cell Biol **130,** 451, 1995.
72. Hadavi, E., Leijten, J., Engelse, M., *et al.* Microwell scaffolds using collagen-IV and laminin-111 lead to improved insulin secretion of human islets. Tissue Eng Part C Methods **25,** 71, 2019.
73. Riopel, M., Stuart, W., and Wang, R. Fibrin improves beta (INS-1) cell function, proliferation and survival through integrin αvβ3. Acta Biomater **9,** 8140, 2013.
74. Itakura, J., Ishiwata, T., Shen, B., Kornmann, M., and Korc, M. Concomitant over-expression of vascular endothelial growth. Int J Cancer **34,** 27, 2000.
75. Zhang, W., Thompson, B.J., Hietakangas, V., and Cohen, S.M. MAPK/ERK signaling regulates insulin sensitivity to control glucose metabolism in Drosophila. PLoS Genet **7,** 1, 2011.

Address correspondence to:
Katja Schenke-Layland, MSc, PhD
Department of Women's Health
Research Institute for Women's Health
Eberhard Karls University Tübingen
Silcherstr. 7/1
Tübingen 72076
Germany

E-mail: katja.schenke-layland@med.uni-tuebingen.de,
katja.schenke-layland@nmi.de

Received: June 13, 2019
Accepted: October 4, 2019
Online Publication Date: December 23, 2019

Supplementary Data

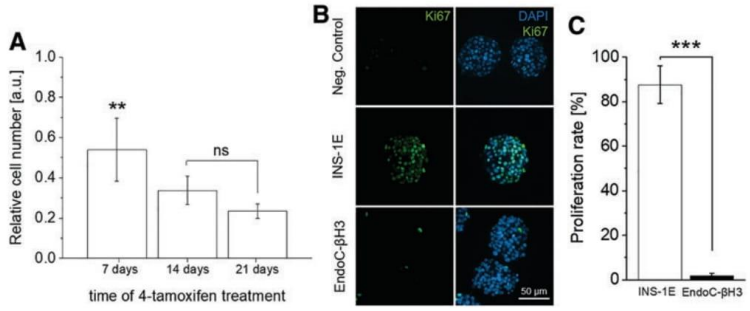

SUPPLEMENTARY FIG. S1. Demonstration of successful removal of proliferation gene of EndoC-βH3 cells by 4-tamoxifen treatment during excision. **(A)** Reduction of proliferation rate during treatment time. One-way ANOVA, $n=7$, $^{**}p<0.01$. **(B)** Ki67 staining of rat insulinoma cells (INS-1E) pseudo-islets as positive control for proliferation and EndoC-βH3 pseudo-islets. **(C)** Percentage of proliferating cells in INS-1E and EndoC-βH3 pseudo-islets. Student's *t*-test, $n=10$, $^{***}p<0.001$. ANOVA, analysis of variance; DAPI, 4′,6-diamidino-2-phenylindole; ns, not statistically significant.

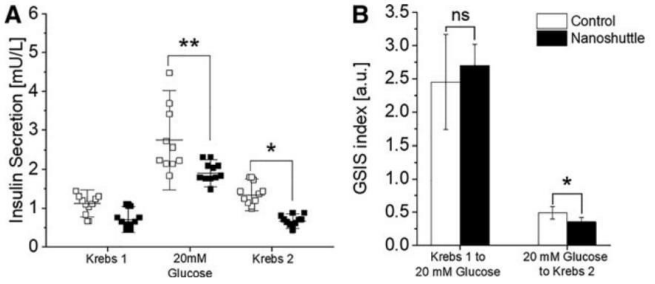

SUPPLEMENTARY FIG. S2. Functionality assessment in three-dimensional after treatment with NanoShuttle™. **(A)** Insulin secretion after serial GSIS assay of pure β-cell pseudo-islets with 1000 cells/pseudo-islets after 5 days in culture. Two-way ANOVA, $n=10$, $^{*}p<0.05$, $^{**}p<0.01$. **(B)** GSIS index of serial GSIS assay showing no relevant differences in functionality after treatment with NanoShuttle™. Student's *t*-test, $n=10$, $^{*}p<0.05$. GSIS, glucose-stimulated insulin secretion.

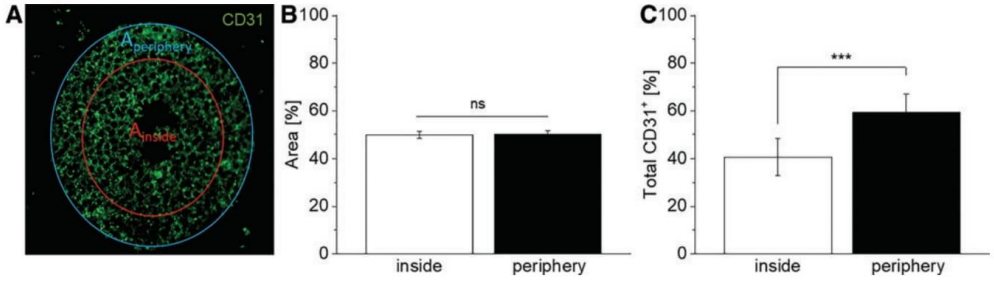

SUPPLEMENTARY FIG. S3. Analysis of the distribution of endothelial cells in ''β-cells inside'' formed with magnetic levitation. **(A)** Schematic of the area of interest that was evaluated as ''inside'' and ''periphery.'' **(B)** Area ratio of ''inside'' and ''periphery.'' Student's *t*-test, $n=10$. **(C)** Total $CD31^+$ staining within areas ''inside'' and ''periphery'' showing that $CD31^+$ cells are mainly located in the periphery of ''β-cells-inside'' formed with magnetic levitation. Student's *t*-test, $n=10$, $^{***}p<0.001$.

Appendix IV

TISSUE ENGINEERING: Part A
Volume 27, Numbers 13 and 14, 2021
Mary Ann Liebert, Inc.
DOI: 10.1089/ten.tea.2020.0250

termis
Tissue Engineering
& Regenerative Medicine
International Society

ORIGINAL ARTICLE

Collagen and Endothelial Cell Coculture Improves β-Cell Functionality and Rescues Pancreatic Extracellular Matrix

Aline Zbinden, MSc,[1,2,*] Max Urbanczyk, MSc,[1,2,*] Shannon L. Layland, MBA,[1,2]
Lucas Becker, MSc,[1–3] Julia Marzi, PhD,[1–4] Mariella Bosch, BSc,[1,2] Peter Loskill, PhD,[1,2,5]
Garry P. Duffy, PhD,[6] and Katja Schenke-Layland, MSc, PhD[1–4,6,7]

The use of biomaterials and biomaterial functionalization is a promising approach to support pancreatic islet viability posttransplantation in an effort to reduce insulin dependence for patients afflicted with diabetes mellitus type 1. Extracellular matrix (ECM) proteins are known to impact numerous reparative functions in the body. Assessing how endogenously expressed pancreatic ECM proteins are affected by posttransplant-like hypoxic conditions may provide significant insights toward the development of tissue-engineered therapeutic strategies to positively influence β-cell survival, proliferation, and functionality. Here, we investigated the expression of three relevant groups of pancreatic ECM proteins in human native tissue, including basement membrane (BM) proteins (collagen type 4 [COL4], laminins [LAM]), proteoglycans (decorin [DCN], nidogen-1 [NID1]), and fibril-forming proteins (fibronectin [FN], collagen type 1 [COL1]). In an *in vitro* hypoxia model, we identified that ECM proteins were differently affected by hypoxic conditions, contributing to an overall loss of β-cell functionality. The use of a COL1 hydrogel as carrier material demonstrated a protective effect on β-cells mitigating the effect of hypoxia on proteoglycans as well as fibril-forming protein expression, supporting β-cell functionality in hypoxia. We further showed that providing endothelial cells (ECs) into the COL1 hydrogel improves β-cell response as well as the expression of relevant BM proteins. Our data show that β-cells benefit from a microenvironment composed of structure-providing COL1 with the incorporation of ECs to withstand the harsh conditions of hypoxia. Such hydrogels support β-cell survival and can serve as an initial source of ECM proteins to allow cell engraftment while preserving cell functionality posttransplantation.

Keywords: β-cells, diabetes, hypoxia, extracellular matrix, collagen type I

Impact Statement

Expression analysis identifies hypoxia-induced pathological changes in extracellular matrix (ECM) homeostasis as potential targets to support β-cell transplants by encapsulation in biomaterials for the treatment of diabetes mellitus. A collagen-1 hydrogel is shown to attenuate the effect of hypoxia on β-cells and their ECM expression. The functionalization of the hydrogel with endothelial cells increases the β-cell response to glucose and rescues essential basement membrane proteins.

[1]Department of Bioengineering, Eberhard Karls University Tübingen, Tübingen, Germany.
[2]Department of Women's Health, Research Institute for Women's Health, Eberhard Karls University Tübingen, Tübingen, Germany.
[3]Cluster of Excellence iFIT (EXC 2180) "Image-Guided and Functionally Instructed Tumor Therapies," Eberhard Karls University Tübingen, Tübingen, Germany.
[4]NMI Natural and Medical Sciences Institute at the University of Tübingen, Reutlingen, Germany.
[5]Fraunhofer IGB, Stuttgart, Germany.
[6]Anatomy & Regenerative Medicine Institute, School of Medicine, College of Medicine Nursing and Health Sciences, National University of Ireland Galway, Galway, Ireland.
[7]Cardiovascular Research Laboratories, Department of Medicine/Cardiology, David Geffen School of Medicine at UCLA, Los Angeles, California, USA.
*These two authors contributed equally to this work.

Introduction

THE EXTRACELLULAR MATRIX (ECM) physically and biochemically supports tissues and organs. It consists of large fibrillar proteins, glycoproteins, and proteoglycans, as well as water, growth factors, enzymes, and other biomolecules.[1] The ECM is vital for cell survival and function as it provides biological, chemical, and mechanical cues to cells, which in turn, remodel the ECM to control tissue homeostasis.[1]

Alterations and disruptions of the ECM homeostatic state adversely affect cells resulting in structural tissue damages, diseases, and potentially organ failure.[2] Mechanical disruption of the ECM that occurs during injury or is induced during transplant surgery can severely compromise cell survival and function, ultimately hindering cell engraftment.[1] This is a major issue in cell and tissue transplantation due to a number of underlying factors, including the hypoxic environment at the transplant site, the implant/transplant-triggered immune response, and pathological ECM remodeling posttransplantation.

The transplantation of Islets of Langerhans or isolated pancreatic β-cells is a promising therapy to treat type 1 diabetes mellitus. However, poor engraftment combined with hypoxic conditions of posttransplantation are responsible for the loss of more than 60% of the transplanted cells within 1 month, leading to the loss of insulin-independency and severe hypoglycemic events.[3,4] Therefore, strategies to improve transplant survival and efficacy should include tissue-engineered methods to support the transplants' survival under hypoxic conditions and improve the ECM homeostasis of the transplant itself.

The isolation of the Islets of Langerhans from donor pancreases severs the vasculature connection between the islets and pancreas. During this process, collagenases are infused into the tissues, disrupting the interstitial matrix of fibrillar proteins, such as collagen type 1 (COL1).[4–6] The process partially digests the double basement membrane (BM) surrounding the islets, which is composed of collagen type 4 (COL4), laminins (LAM), fibronectin (FN), and proteoglycans.[6,7] BM proteins were reported to be differentially affected by the isolation procedure; perlecan and laminin α5 are completely lost, while COL4 and other LAM are still present after the process.[7] The resulting loss in ECM structure has been previously shown to negatively impact islet survival and function of posttransplantation.[8]

Endothelial cells (ECs) are the main source of BM proteins in the native pancreas.[9] Most transplantation sites lack ECs. The reestablishment of EC presence via revascularization requires several days of posttransplantation.[10] During that time, β-cells experience severe hypoxic conditions leading to improper ECM remodeling. Hence, β-cells initially rely on their intrinsic ECM protein expression to survive in a hypoxic posttransplantation environment or on external support, for example, carrier materials such as collagen-based hydrogels.[11,12]

Although many studies have shown the importance of the ECM and how it affects β-cell function, there have been very few investigations on how hypoxia regulates the expression and homeostasis of endogenous ECM in pancreatic islets.[13] Therefore, we developed an *in vitro* hypoxia model to investigate the ECM expression of β-cell composed of pseudoislets and to monitor pathological ECM changes under hypoxic conditions (Supplementary Fig. S1). We showed that hypoxia differentially affects the expression of BM proteins, proteoglycans, and fibril-forming ECM proteins. The use of a clinically approved COL1 hydrogel as carrier material allowed the rescue of the proteoglycans and fibril-forming ECM proteins. Coculturing ECs with β-cell pseudoislets in the COL1 hydrogel improved the endogenous expression of BM proteins. The combination of biological cues together with ECs is a promising strategy to prevent or reduce hypoxia-related apoptosis and loss of β-cell functionality.

Materials and Methods

INS1E cell culture and pseudoislet assembly

The insulin producing rat insulinoma cell line INS1E was a kind gift from Prof. Maechler from the University of Geneva, Switzerland. INS1E cells were cultured in adapted RPMI 1640 (Gibco) containing 10 mM HEPES (Gibco), 50 μM 2-mercapto-ethanol (Sigma-Aldrich), 1 mM pyruvate (Gibco), 5% fetal bovine serum (Sigma-Aldrich), 100 iU/mL penicillin, and 100 μg/mL streptomycin, under standard humidified normoxic conditions (37°C, 5% CO_2, 20% O_2), and passaged at 80% confluency. To assemble pseudoislets, nonadherent 96-well U-bottom plates (Thermo Fisher Scientific) were used at a density ranging from 500 to 10,000 cells per well in a working volume of 100 μL/well and placed under normoxic conditions for 48 h before any experiment. Hypoxia experiments were performed under the following conditions: 37°C, 5% CO_2 and 1% O_2, which were chosen according to literature.[14–16] In detail, pseudoislets were seeded in overnight preincubated hypoxia medium. Media was changed every other day. Every 24 h, images of the pseudoislets were obtained using a brightfield microscope (Zeiss), and the pseudoislet size was analyzed using ImageJ V 1.52p. The growth speed was assessed by applying a linear regression curve for each pseudoislet size from day 2 to 8, resulting in the average growth in micrometers per day.

Viability assay

Fluorescein diacetate (FDA)/propidium iodide (PI) (Sigma-Aldrich) staining was performed according to the manufacturer's protocol. In brief, pseudoislets were washed once with phosphate-buffered saline (PBS), incubated with 33 μL FDA and 300 μL PI per 1 mL RPMI 1640 for 15 min at normoxic conditions. After incubation, pseudoislets were washed three times with PBS before recording the fluorescence using a laser scanning microscope 710 (Zeiss). The fluorescence was recorded in the z-stack mode using maximum intensity projection. Images were evaluated by Zen Blue (Zeiss) and ImageJ V 1.52p software. The number of PI^+ cells was normalized by the diameter of each pseudoislet.

Human umbilical vein endothelial cell culture and coculture pseudoislet assembly

Human umbilical vein endothelial cell (HUVEC) culture and coculture pseudoislet assembly was performed as recently reported.[17] The magnetizing of HUVEC and INS1E allows the proper and reproducible aggregation of pseudoislets by placing the HUVECs around the INS1E β-cells. In brief, HUVECs (PromoCell) were cultured in corresponding

EC growth medium (PromoCell), passaged at a confluency between 80% and 90%, and used between passage 2 and 6. For coculture pseudoislets assembly, INS1E cells and HUVECs were magnetized overnight before seeding, using NanoShuttle™-PL (Greiner) at a concentration of 40 μL/mL according to the manufacturer's protocol. To obtain optimal glucose-stimulated insulin secretion (GSIS) functionality of the cocultured pseudoislets, INS1E cells were seeded first at a density of 500 cells per well in 50 μL INS1E media to ensure proper pseudoislet formation. HUVECs were added 24 h later at a density of 500 cells per well in 50 μL HUVEC media, resulting in a media ratio of 1:1, and placed atop the magnetic levitation plate for 30 min under standard culture conditions for another 24 h.

COL1 pseudoislet encapsulation

An average number of 48 pseudoislets or coculture pseudoislets were encapsulated in COL1 with a concentration of 6.0 mg/mL with a total volume of 250 μL following the manufacturer's instructions (Fraunhofer IGB, Stuttgart[18]).

GSIS assay

Ninety-six hours after seeding, pseudoislets with 500 and 1000 cells per pseudoislet were grouped by 4 per well in 50 μL medium. Pseudoislets were washed twice using KREBS 1×buffer containing 0.1% bovine serum albumin (Sigma-Aldrich) and 25 mM HEPES (Gibco). Then, pseudoislets were incubated for 30 min in KREBS 1×buffer under normoxic conditions. Subsequently, KREBS 1×buffer containing 3.3 mM glucose (Gibco) was added and the pseudoislets were incubated for 1.5 h. The pseudoislets were washed again twice and incubated with KREBS 1×buffer containing 16.7 mM glucose for another 1.5 h. The supernatants were collected and stored at −20°C for further insulin detection using enzyme-linked immunosorbent assay (Mercodia). The GSIS index represents the fold increase in insulin secretion from 3.3 to 16.7 mM glucose. For the GSIS assay in COL1 hydrogel, all incubation times were doubled with regard to diffusion properties.

Histological analysis

Pseudoislets were washed with PBS (Gibco), fixed with 4% paraformaldehyde, embedded in HistoGel® (Thermo Fisher Scientific), and processed for paraffin embedding using a Shandon Citadel 1000 (Thermo Fisher Scientific) according to the manufacturer's protocol. Sections were cut with a thickness of 3 μm (Microtome RM2145; Leica), deparaffinized using xylene, and rehydrated by graded ethanol (100–50%) in VE-water. Adult human pancreatic tissues were commercially obtained from Novus biologicals (NBP2-30191; Novus Biological, Bio-Techne GmbH, Wiesbaden, Germany).

Immunofluorescence staining

TRIS-EDTA (pH9) and citrate (pH6) buffer were used for antigen retrieval. The antibodies were used according to the manufacturer's specifications and are shown in Supplementary Table S1. Sections were incubated for 10 min with 4′,6-diamidino-2-phenylindole (DAPI, 2 μg/mL in PBS; Sigma-Aldrich) prior mounting with Molecular Probes ProLong Gold Antifade solution (Invitrogen). Immunofluorescence (IF) staining images of pseudoislets and pancreatic tissues were obtained using an Axio Observer Z1 microscope (Zeiss) as well as laser scanning microscopes 710 (Zeiss) and 780 (Zeiss). The images were analyzed using Zeiss Zen Blue software and ImageJ V1.52p.

Terminal deoxynucleotidyl transferase-mediated nick-end labeling assay

Click-iT TUNEL Alexa Fluor Imaging Assay Kit (Thermo Fisher Scientific) was used according to the manufacturer's specifications and used as previously described.[17] In brief, the sections were deparaffinized and permeabilized with 0.25% Triton-X for 20 min. Terminal deoxynucleotidyl transferase reaction buffer was added to the slides for 60 min at 60°C. Subsequently, sections were incubated with Click-iT reaction buffer for 30 min at room temperature. The counterstaining was performed using DAPI.

Image analysis

PI^+ cells were counted using an automated macro in ImageJ V 1.52p and normalized by the size of the pseudoislet. Blinded terminal deoxynucleotidyl transferase-mediated nick-end labeling (TUNEL)- and Ki67-stained images were quantified by two independent, unbiased observers. Cells were counted as $TUNEL^+$ and $Ki67^+$ when exhibiting a green (TUNEL or Ki67) and blue (DAPI) double staining. Ratios of $TUNEL^+$ and $Ki67^+$ cells were calculated by dividing the number of $TUNEL^+$ and $Ki67^+$ cells, respectively, by the number of total $DAPI^+$ cells. Staining intensities were evaluated via the mean gray value (MGV) per pixel within the region of interest (ROI). Pseudoislet ROI was selected as $DAPI^+$ area and for human pancreatic sections as $insulin^+$ region. Fold changes were calculated by dividing the MGV of the hypoxia samples by the MGV of the normoxia samples. The standard deviation was calculated using the formula for the propagation of error.

Nuclear expression of FN was quantified by a custom-written macro using Microsoft Excel (Microsoft Corporation, 2018). The program validates, whether the single pixel values of the blue channel (DAPI) and the green channel (FN) exceed a set threshold value. If both thresholds were exceeded, this pixel was counted as nuclear FN expression. The pixel was counted as nonnuclear FN expression only when the green threshold was exceeded. The percentage of nuclear FN expression was calculated using the following formula: percentage of nuclear fibronectin expression = (number of pixels with nuclear fibronectin expression)/(number of pixels with nuclear fibronectin expression + number of pixels with nonnuclear fibronectin expression).

Overall fold changes for ECM protein expression between normoxic COL1 hydrogel and hypoxic COL1 hydrogel+HUVECs were calculated by multiplying the fold changes of (hypoxic COL1 hydrogel/normoxic COL1 hydrogel)*(hypoxic COL1 hydrogel + HUVECs/hypoxic COL1 hydrogel).

Raman imaging of pseudoislets

INS1E pseudoislets were prepared for Raman imaging as previously described.[19] In brief, hypoxic and control

pseudoislets were placed in a microfluidic chip for noninvasive *in situ* Raman imaging. The microfluidic device stabilizes the pseudoislets during measurements, while supplementing nutrients via media perfusion. Spectral mapping was performed on a customized inverted WITec alpha300 R Raman system (WITec GmbH) equipped with a green laser (532 nm) and a CCD spectrograph with a grating of 600 g/mm. An incubation chamber (Okolab S.R.L.) was integrated in the setup to keep the pseudoislets constantly at 37°C. Images were acquired as triplicates at a laser power of 58 mW, an integration time per spectrum of 0.5 s and a pixel resolution of 1×1 μm.

Multivariate data analysis

Image analysis of the spectral map was performed with the Project Five 5.2 software (WITec GmbH). Raman data were pretreated whereby each scan was subjected to cosmic ray removal, polynomial baseline correction (to remove the glass background), and intensity normalization. True component analysis (TCA) was performed at the spectral range of 600–1800 cm^{-1}. In brief, TCA is a nonnegative matrix factorization-based multivariate data analysis tool elaborating spectral components, which predominantly occur in the data set allowing to identify the localization of these components by false color intensity distribution heatmaps. Gray value intensities per pixel (MGV) were determined in ImageJ V 1.52p to semiquantify the distribution of the spectral components in normoxic and hypoxic conditions. Furthermore, TCA allowed to preselect ROI with similar spectral information representing nuclei, ECM, and mitochondria, which was extracted for further in-depth analysis of the molecular composition by principal component analysis (PCA) using Unscrambler X10.5 (Camo). PCA is a multivariate data analysis tool reducing the dimensionality of a set of spectral data on a vector-based approach. Each vector, the so-called principal component (PC), describes a variation in the spectra. Plotting PC values against each other visualizes a correlation or separation of two or more data sets.

Statistical analysis

Statistical analysis was performed using Origin 2019b (OriginLab) and GraphPad Prism version 6.00 for Windows (GraphPad Software). Results are shown throughout the entire article as mean ± standard deviation. All data sets are tested for normal distribution using Kolmogorov–Smirnov test; outliers were removed using Grubb's test with a confidence interval of 0.05. All *n*-numbers, applied tests, and corresponding significances for each result are listed in the figure legends.

Results

Assembly of pancreatic β-cells into glucose-responsive pseudoislets

To assess the ECM-related changes induced by hypoxic conditions on pancreatic islets, we established an *in vitro* model composed of INS1E β-cells that were assembled into pseudoislets to mimic the insulin-secreting endocrine function of the native Islets of Langerhans. The native pancreatic islets range is from 50 to 400 μm in diameter with an average size of 150 μm.[20,21] Therefore, pseudoislets were formed by spontaneous aggregation with 500 to 10,000 cells per pseudoislets (Fig. 1). The proliferative nature of the INS1E β-cells lead to an overall increase in their size over time, monitored for a period of 8 days (Fig. 1A). The growth speed was impacted by the number of initially seeded cells: pseudoislets of 2000 (2k), 4000 (4k), and 10,000 (10k) cells per pseudoislet grew significantly faster than pseudoislets of 500 (0.5k) and 1000 (1k) cells per pseudoislet (Fig. 1B).

Diffusion of nutrients and oxygen are essential for the survival and physiological function of three-dimensional (3D) cell constructs.[22,23] The lack of diffusion that occurs in large cell aggregates results in the formation of a hypoxic core.[24] Therefore, we assessed the influence of pseudoislet size on pseudoislet viability (Fig. 1C). We observed a hypoxic core depicted by PI-stained cells in large pseudoislets (4k and 10k pseudoislets) after 8 days in culture, which was not observed in smaller pseudoislets (0.5k, 1k, and 2k pseudoislets). The quantification of PI^+ cells in 0.5k, 1k, and 2k pseudoislets showed a significantly higher dead cell ratio in 2k pseudoislets compared with 0.5k and 1k pseudoislets after 3 and 8 days (0.5k: 0.038 ± 0.026 [3 days] vs. 0.082 ± 0.04 [8 days], $p < 0.0001$; 1k: 0.0656 ± 0.024 [3 days] vs. 0.163 ± 0.006 [8 days], $p < 0.01$; 2k: 0.163 ± 0.022 [3 days] vs. 0.0164 ± 0.040, $p < 0.0001$). These data suggest that 0.5k and 1k pseudoislets allowed for proper nutrient and oxygen diffusion overtime, which is in line with previous studies showing that pseudoislets above 1000 cells per islet lead to an unstable aggregation (Fig. 1D).[24,25]

The major function of β-cells is to secrete insulin in response to glucose, which is also influenced by the pseudoislet size.[26,27] Therefore, GSIS assays were performed to assess potential functional differences between 0.5k and 1k pseudoislets (Fig. 1E, F). The GSIS index revealed that 0.5k pseudoislets had a significantly higher glucose response compared with the 1k pseudoislets (Fig. 1E; 0.5k GSIS of 2.024 ± 0.51 compared with 1k GSIS 1.232 ± 0.340; $p < 0.05$). We showed that 0.5k pseudoislets were highly viable and glucose-responsive with an average basal insulin secretion of 0.0427 ± 0.0077 and 0.0839 ± 0.0134 μg/L per islet when stimulated with 16.7 mM glucose (Fig. 1F). The 0.5k pseudoislets were chosen for all further experiments, as they offer high reproducibility and stability over time to study the effects of hypoxia on endogenous β-cell ECM expression.

Hypoxia induces apoptosis and impairs pseudoislet functionality in vitro

Pseudoislets were subjected for a period of 48 h to hypoxic conditions (1% oxygen). B-cell death, proliferation, and functionality were evaluated to validate the hypoxic effect in the *in vitro* model (Fig. 2). The expression of caspase-3, which is a downstream activator of the apoptotic pathway, significantly increased under hypoxic conditions (Fig. 2A).[28] To verify that the activation of caspase-3 signaled to its final target, we looked at the number of cells positive for TUNEL, which identifies DNA fragmentation in nuclei that occurs during late-stage apoptosis.[28] We identified a significant increase of $TUNEL^+$ cells in the hypoxia *in vitro* model (Fig. 2B; 0.54% ± 0.76% normoxia vs. 10.45% ± 0.764% hypoxia; $p < 0.0001$), confirming the completion of apoptotic pathways. The proliferative

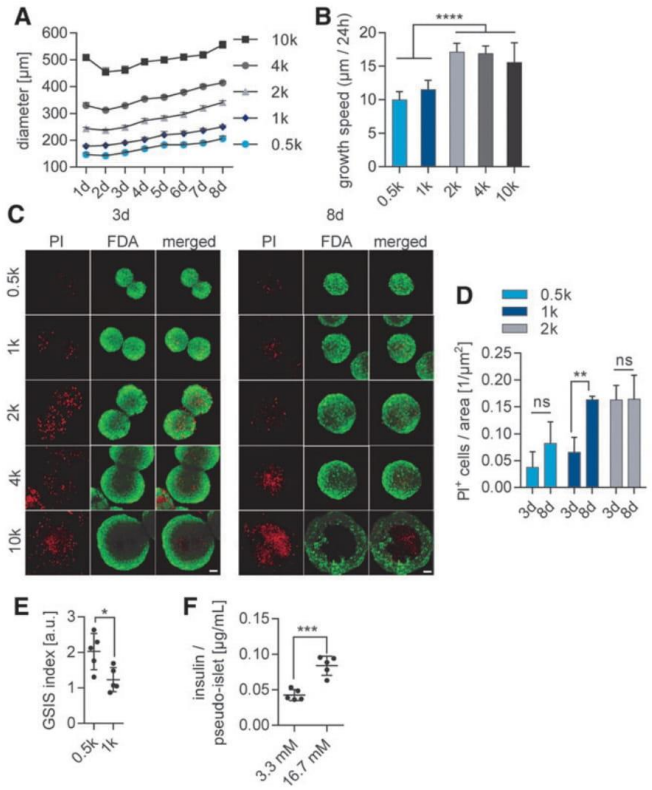

FIG. 1. Pseudoislet size affects survival, growth, and functionality *in vitro*. **(A)** Pseudoislet size assessment over a period of 8 days. Different cell concentrations were tested: 10,000 cells per pseudoislet (10k), 4000 cells per pseudoislet (4k), 2000 cells per pseudoislet (2k), 1000 cells per pseudoislet (1k), and 500 cells per pseudoislets. **(B)** Evaluation of growth speed of pseudoislets depending on the initial number of seeded cells. **(C)** Cell viability at 3 days after seeding and 8 days after seeding. FDA indicates live cells (*green*) and PI indicates dead cells (*red*). **(D)** Quantification of FDA/PI ratio of 0.5k, 1k, and 2k pseudoislets after 3 and 8 days, $n \geq 3$, two-way ANOVA with Tukey's multiple comparisons test. **(E)** GSIS index of 0.5k pseudoislets compared to 1k pseudoislets, $n = 5$, unpaired *t*-test. **(F)** Insulin secretion of 0.5k pseudoislets under 3.3 mM glucose and 16.7 mM glucose, $n = 5$, unpaired *t*-test. $^{*}p < 0.05$, $^{**}p < 0.01$, $^{***}p < 0.001$, $^{****}p < 0.0001$. Scale bars = 50 µm. FDA, fluorescein diacetate; GSIS, glucose-stimulated insulin secretion; PI, propidium iodide.

capacity of INS1E β-cells was impaired by the hypoxic culture condition, demonstrated by a significant loss of Ki67 expression (Fig. 2C; 79.27% ± 7.89% normoxia vs. 43.3% ± 11.34% hypoxia; $p < 0.001$).

We assessed GSIS, insulin expression, and E-cadherin expression, which is an important cell–cell contact protein contributing to pseudoislet integrity and functionality under hypoxic conditions.[29] We showed that pseudoislets cultured under hypoxic conditions expressed significantly lower amounts of E-cadherin (Fig. 2D; 6321 ± 1086 gray value intensities (GVI)/pixel normoxia vs. 1940 ± 209 GVI/pixel hypoxia; $p < 0.0001$) and also expressed significantly less insulin (Fig. 2E; 14223 ± 2491 GVI/pixel normoxia vs. 4583 ± 1204 GVI/pixel hypoxia; $p < 0.0001$), contributing to a lack of response when stimulated by glucose (Fig. 2F).

To identify hypoxia-specific biochemical changes *in situ* within the living cells and cell-derived ECM in pseudoislets, Raman microspectroscopy and Raman imaging were used as noninvasive marker-independent techniques on living pseudoislets (Fig. 2G–K).[19] Raman imaging and TCA identified three main components in the pseudoislets that were previously assigned to nuclei, mitochondria, and ECM (Fig. 2G, H). Major peaks related to nuclei were identified as 785 cm^{-1} (DNA) and 826 and 1090 cm^{-1} (PO_2 backbone). Mitochondria TCA was defined by intense peaks located at 747, 1125, and 1583 cm^{-1} describing heme vibrations in cytochrome C complexes.[30,31] The ECM TCA was highly impacted by changes in collagens (1173, 1310, and 1340 cm^{-1}).[30,32,33] TCA quantification further revealed a significant decrease in the distribution of the nuclei component, indicating changes and/or loss of the nuclear biochemical spectral fingerprint, while there was no impact on the mitochondrial component (Fig. 2I).

For in-depth analysis of the TCA patterns within the mitochondrial component, Raman spectra were subjected to PCA. The multivariate data analysis of single spectra showed a separation according to the first principal component (PC1) (Fig. 2J). The loading of PC1 revealed that the major molecular differences responsible for the separation were 751 and 1125 cm^{-1}, indicating that mitochondria of pseudoislets are more active under normoxic conditions (Fig. 2K). The negative range showed an overall higher protein signal in hypoxic pseudoislets, which may be the results of mitochondrial damage followed by the infiltration of cytoplasmic proteins.

Raman TCA quantification identified a significant alteration of the ECM proteins in hypoxic pseudoislets. This impact on crucial pancreatic ECM structures most likely contributes to the loss of β-cell function, as it has been previously shown that intraislet ECM interactions can modulate β-cell proliferation and survival.[34]

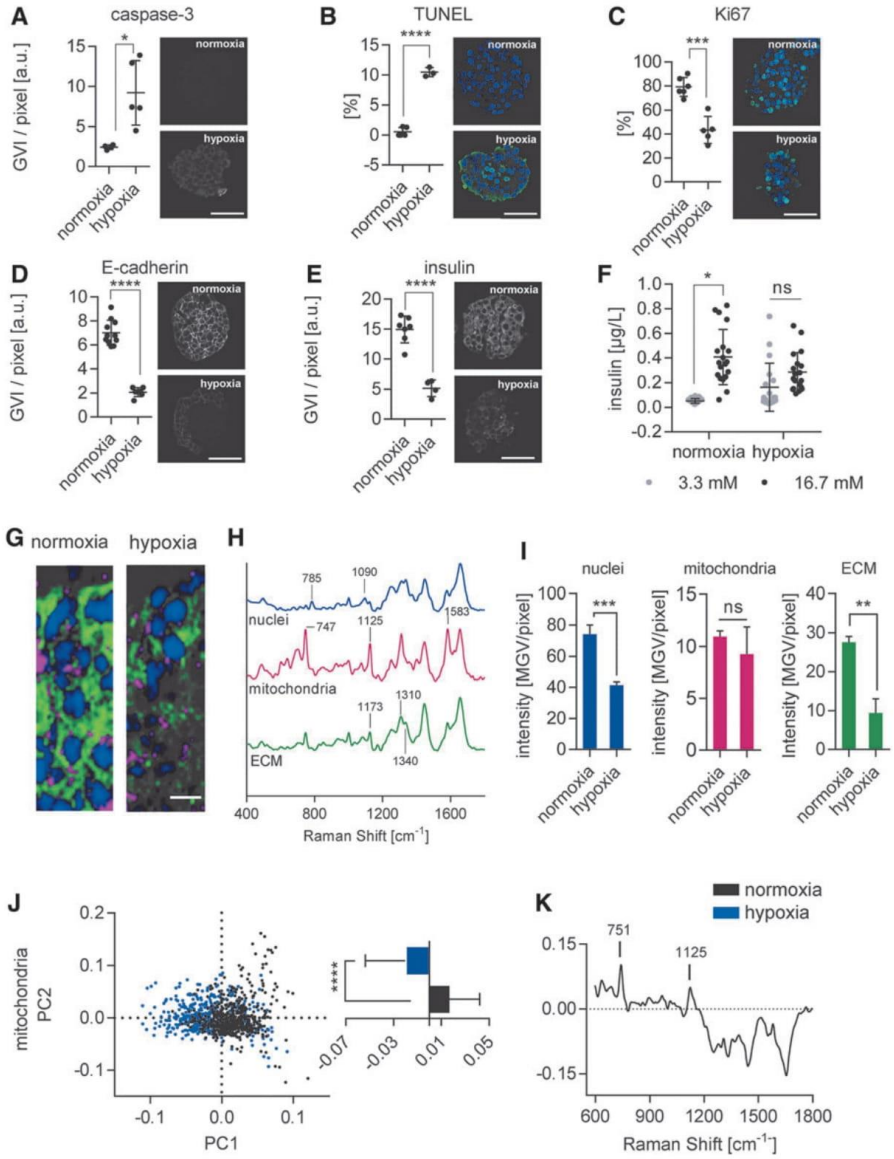

FIG. 2. Hypoxia induces apoptosis and impairs pseudoislet functionality *in vitro*. **(A, B)** Cell death assessment under normoxic and hypoxic conditions is quantified via **(A)** expression of cleaved caspase-3 ($n \geq 4$) and **(B)** number of TUNEL$^+$ cells ($n \geq 3$) (TUNEL$^+$ in *green*, DAPI in *blue*), **(C)** Ki67 ($n \geq 5$) (Ki67$^+$ in *green*, DAPI in *blue*), **(D)** E-cadherin expression ($n \geq 6$), **(E)** insulin expression ($n \geq 6$); unpaired *t*-test. Scale bars = 50 µm. **(F)** GSIS response of pseudoislets ($n = 19$); two-way ANOVA with Tukey's multiple comparisons test. **(G–K)** *In situ* characterization of hypoxic pseudoislets by Raman imaging. **(G)** Identification and location of the three major components: nuclei (*blue*), mitochondria (*pink*), and ECM (*green*). Scale bar = 10 µm. **(H)** Corresponding Raman spectra of the three major TCA components. **(I)** Semiquantification of component intensities ($n \geq 3$); unpaired *t*-tests. **(J)** Separation of normoxic and hypoxic samples by mitochondrial spectra component by PCA and difference of spectral mean values ($n = 600$); unpaired *t*-test. **(K)** Loadings plot of PC1 with peak marking responsible for sample separation. *$p < 0.05$, **$p < 0.01$, ***$p < 0.001$, ****$p < 0.0001$. DAPI, 4′,6-diamidino-2-phenylindole; ECM, extracellular matrix; PC, principal component; PCA, principal component analysis; TCA, true component analysis; TUNEL, terminal deoxynucleotidyl transferase-mediated nick-end labeling.

Hypoxia differentially impairs the ECM protein expression in pseudoislets

To assess the effects of hypoxia on endogenous ECM expression in β-cells, we focused on three different groups of ECM proteins: BM proteins (LAM and COL4), the proteoglycans decorin (DCN) and nidogen-1 (NID1), and the fibril-forming proteins FN and COL1 (Fig. 3 and Supplementary Fig. S2). Comparative immunofluorescence staining verified the presence of the selected ECM proteins in both native human pancreatic tissue and pseudoislets cultured under normoxic conditions. However, semiquantification showed that hypoxia differentially regulated ECM expression. The expression of BM proteins LAM (Fig. 3A, B) and COL4 (Fig. 3C, D) was homogenous throughout pseudoislets cultured under normoxic conditions and significantly decreased in the hypoxia *in vitro* model (LAM: 12259 ± 985 GVI/pixel normoxia vs. 7628 ± 1241 GVI/pixel hypoxia, $p < 0.001$; COL4: 5980 ± 336 GVI/pixel normoxia vs. 3928 ± 900.97 hypoxia, $p < 0.001$).

Similar to the BM proteins, the expression patterns of DCN (Fig. 3E, F; 8619 ± 436 GVI/pixel normoxia vs. 5464 ± 504 GVI/pixel hypoxia; $p < 0.001$) and NID1 (Fig. 3G, H; 12267 ± 1656 GVI/pixel normoxia vs. 7568 ± 1675 GVI/pixel hypoxia; $p < 0.01$) were homogeneous under normoxic conditions, but significantly decreased in the hypoxia *in vitro* model.

In contrast to BM proteins and proteoglycans, the expression levels of fibril-forming proteins (Fig. 3I–M) were not significantly impacted (FN: 7820 ± 2499 GVI/pixel normoxic conditions vs. 8454 ± 1840 GVI/pixel hypoxic conditions, $p = 0.68$; COL1: 5527 ± 1353 GVI/pixel normoxia vs. 5915 ± 1617 GVI/pixel hypoxia, $p = 0.70$). Although FN expression did not significantly decrease ($p = 0.68$), its cellular location shifted from cytoplasmic to nuclear after being subjected to hypoxia (Fig. 3I).

Changes in ECM composition have been described to promote transcriptional changes in the nucleus, potentially hinting toward cellular stress.[35] Therefore, we investigated whether cytoplasmic and nuclear expression of FN was present under hypoxic conditions (Fig. 3K). When normalized to the normoxia pseudoislet controls (1.0 ± 0.26), native human tissue did not show a significant fold change (0.91 ± 0.19, $p = 0.75$). In contrast, under hypoxic conditions, pseudoislets expressed significantly more nuclear FN (1.0 ± 0.26 normoxia vs. 1.46 ± 0.29 hypoxia; $p < 0.01$), reflecting increased cellular stress under hypoxic conditions.

Our data show that β-cells have the ability to express relevant pancreatic ECM proteins under normoxic conditions.[34,36] However, hypoxia significantly impacted pancreatic BM proteins, glycoproteins, and FN, while COL1 expression remained stable.

COL1 hydrogel mimics native pancreatic tissue and attenuates hypoxic impact on pseudoislet functionality

To prevent ECM loss with concomitant loss of functionality under hypoxic conditions, we investigated the effect of encapsulating the pseudoislets in a COL1 hydrogel that is commercially available as an FDA-approved GMP-product and has been used to support β-cell function in normoxic conditions.[37,38] Pseudoislets were encapsulated in a COL1 hydrogel, exhibiting similar COL1 expression patterns to native human adult pancreatic tissue (Fig. 4).

The impact of COL1 hydrogel on pseudoislets under hypoxic conditions was investigated by comparing changes in apoptosis, proliferative capacity, basic β-cell functionality and ECM protein expression patterns with pseudoislets cultured in suspension under hypoxic conditions (Fig. 5A–F). The expression of the hypoxia-induced apoptosis marker caspase-3 (Fig. 5A; 4.41 ± 1.44 suspension vs. 1.77 ± 0.68 COL1 hydrogel; $p < 0.05$) as well as the number of $TUNEL^+$ cells (Fig. 5B; 5.88 ± 1.67 suspension vs. 3.27 ± 0.76 COL1 hydrogel; $p < 0.05$) were significantly decreased in pseudoislets cultured in the 3D COL1 hydrogel when compared with pseudoislets grown in suspension cultures. Although the proliferative capacity between pseudoislets in suspension and COL1 hydrogel was comparable (Fig. 5C; 0.55 ± 0.14 suspension vs. 0.49 ± 0.15 COL1 hydrogel; $p = 0.55$), the expression of E-cadherin (0.31 ± 0.06 suspension vs. 0.75 ± 0.25 COL1 hydrogel; $p < 0.01$) and insulin (0.32 ± 0.09 suspension vs. 0.59 ± 0.12 COL1 hydrogel; $p < 0.01$) was significantly higher in pseudoislets in COL1 hydrogel (Fig. 5D, E). While hypoxia significantly decreased the overall insulin content of the pseudoislets in COL1 hydrogel, E-cadherin did not change significantly (Supplementary Fig. S3). Pseudoislets in COL1 hydrogel under normoxic and hypoxic conditions secreted significantly more insulin with 16.7 mM glucose stimulation than in the basal state (3.3 mM) (Fig. 5F; normoxia: 0.08 ± 0.03 basal state vs. 0.144 ± 0.04 16.7 mM glucose, $p < 0.05$; hypoxia: 0.09 ± 0.02 basal state vs. 0.16 ± 0.06 16.7 mM glucose, $p < 0.05$). These data demonstrate the beneficial effect of the COL1 hydrogel on pseudoislet functionality when comparing glucose diffusion and insulin release under hypoxic conditions.

Exogenous biomechanical cues are known to impact cellular behavior.[1] Therefore, we investigated whether providing an external COL1 hydrogel changes the ECM protein secretion patterns in the pseudoislet cultures (Fig. 5G–M). Interestingly, only the secretion of LAM (6577 ± 1360 GVI/pixel normoxia vs. 4007 ± 594 hypoxia; $p < 0.05$) and COL4 (8553 ± 223 GVI/pixel normoxia vs. 7306 ± 708 GVI/pixel hypoxia; $p < 0.05$) significantly decreased, whereas the expression of DCN (9117 ± 2877 GVI/pixel normoxia vs. 6418 ± 1824 GVI/pixel hypoxia; $p = 0.14$) and NID1 (4451 ± 1488 GVI/pixel normoxia vs. 3996 ± 96 GVI/pixel hypoxia; $p = 0.60$), as well as fibril-associated (FN: 6655 ± 936 GVI/pixel normoxia vs. 7129 ± 1360 GVI/pixel hypoxia; $p = 0.58$) and fibrillar proteins (COL1: 9396 ± 2297 GVI/pixel normoxia vs. 6751 ± 2022 GVI/pixel hypoxia; $p = 0.18$) were not significantly impaired. In contrast to pseudoislets cultured in suspension, no change in nuclear FN expression was observed under hypoxia in pseudoislets encapsulated in the 3D COL1 hydrogel (Fig. 5L; 1.0 ± 0.09 normoxia vs. 0.90 ± 0.24 hypoxia; $p = 0.46$).

COL1 hydrogel functionalized with HUVECs supports endogenous pseudoislet BM protein expression

The encapsulation of pseudoislets in a COL1 hydrogel attenuated the hypoxic effect and preserved the expression of the glycoproteins DCN and NID1. However, the expression of BM proteins LAM and COL4 remained impaired. ECs are an important producers of BM protein in the pancreas.[9] Therefore, we established a co-culture of 1000 INS1E β-cells with 1000 HUVECs using magnetic levitation with HUVECs surrounding the β-cells as previously described.[17] After culturing control β-cell only pseudoislets and coculture pseudoislets in a

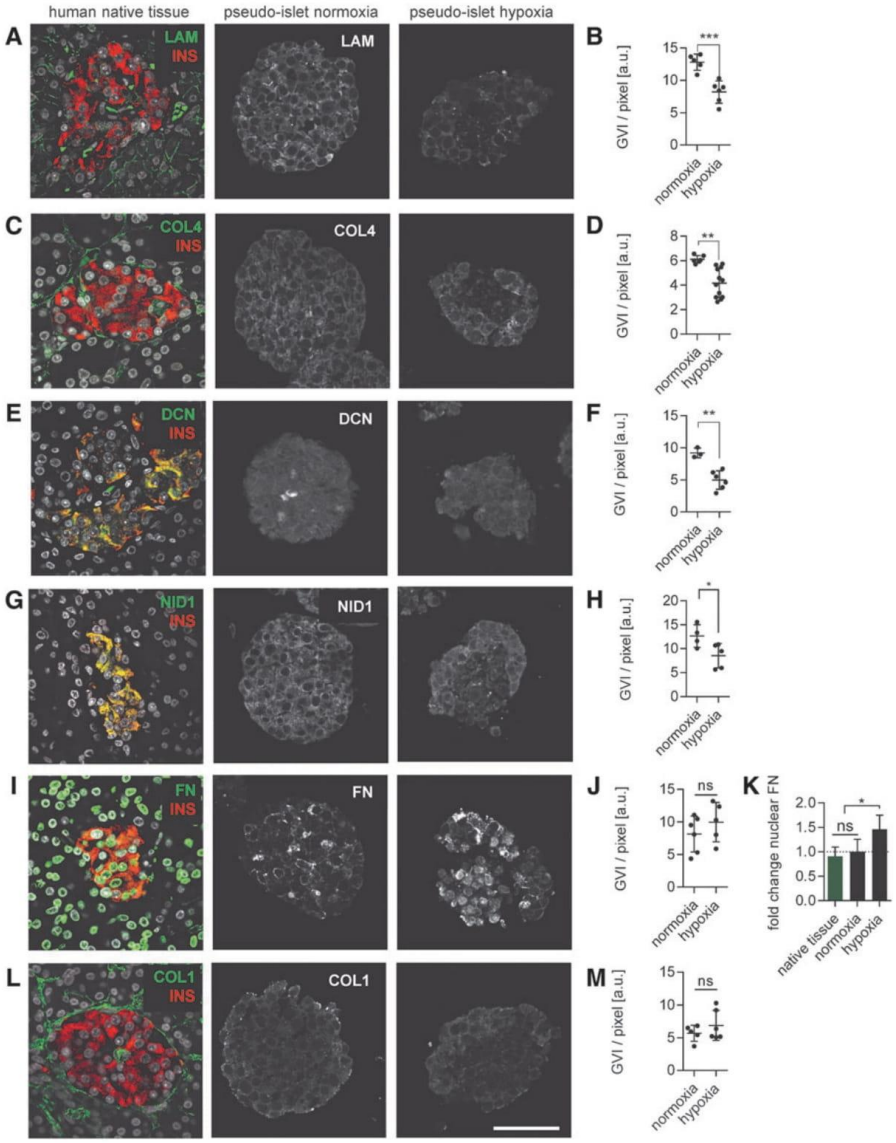

FIG. 3. Hypoxia differentially impacts the expression patterns of BM proteins, glycoproteins, fibrillar, and fibril-associated ECM proteins. IF staining and quantification of different ECM proteins in human native tissue and in pseudoislets under normoxic and hypoxic culture conditions. **(A–D)** BM proteins are represented by **(A, B)** LAM ($n \geq 5$) and **(C, D)** COL4 ($n \geq 6$). **(E–H)** Glycoproteins are represented by **(E, F)** DCN ($n \geq 3$) and **(G, H)** NID1 ($n \geq 4$). **(I–M)** Fibril-associated and fibrillar ECM proteins are represented by **(I, J)** FN ($n \geq 5$) and **(L, M)** COL1 ($n \geq 5$). **(K)** Quantification of nuclear FN in native pancreatic tissue, and in pseudoislets cultured under normoxic and hypoxic conditions ($n \geq 5$); one-way ANOVA. Unpaired *t*-test. $*p < 0.05$, $**p < 0.01$, $***p < 0.001$. Scale bar = 50 µm. BM, basement membrane; COL1, collagen type 1; COL4, collagen type 4; DCN, decorin; FN, fibronectin; IF, immunofluorescence; LAM, laminins; NID1, nidogen-1.

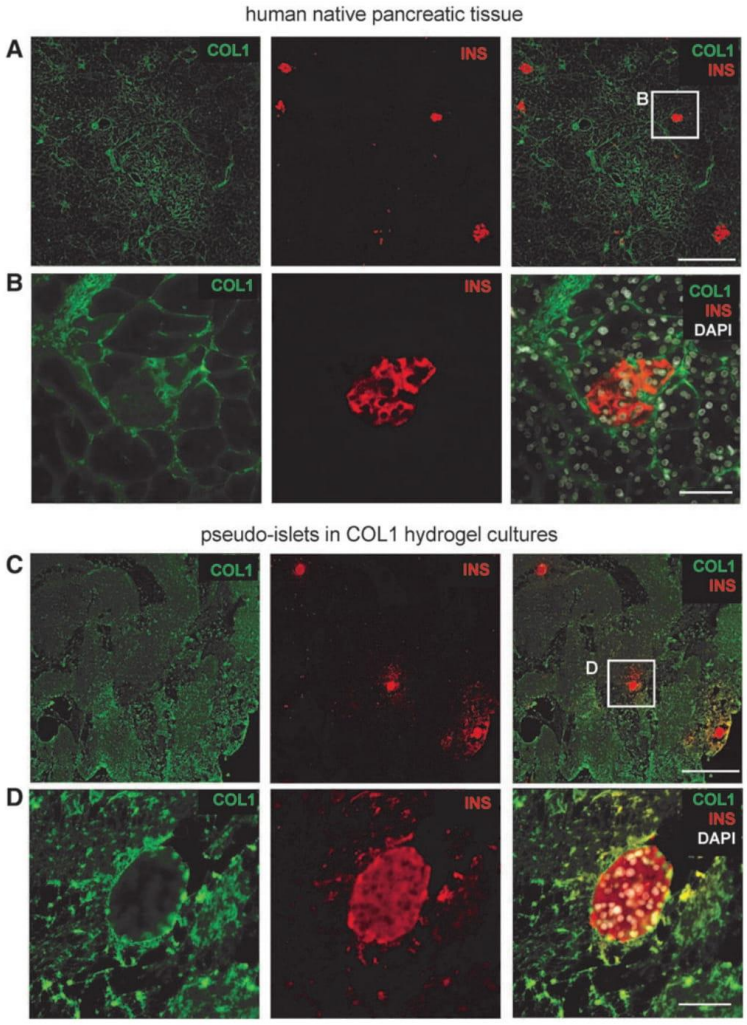

FIG. 4. COL1 hydrogel mimics native pancreatic tissue. **(A, B)** IF staining of adult pancreatic tissue showing COL1 (*green*), insulin (*red*), and nuclei (DAPI, *white*). Scale bars equal **(A)** 200 μm and **(B)** 50 μm. **(C, D)** IF staining of COL1-encapsulated pseudoislets with COL1 (*green*), insulin (*red*), and nuclei (DAPI, *white*). Scale bars equal **(C)** 200 μm and **(D)** 50 μm.

COL1 hydrogel for 48h under hypoxic conditions, functionality, and ECM protein expression were assessed (Fig. 6). Coculture pseudoislets grown in the COL1 hydrogel were glucose responsive after 48h in hypoxia (Fig. 6A) and secreted significantly more insulin upon glucose stimulation compared with only β-cell-containing pseudoislets in COL1 hydrogels (Fig. 6B; 0.16 ± 0.06 COL1 hydrogel vs. 0.36 ± 0.24 COL1 hydrogel+HUVECs; $p < 0.05$), while the GSIS was not significantly changed (Supplementary Fig. S4A). Furthermore, evaluation of caspase-3, TUNEL, Ki67, E-cadherin, and insulin expression using IF staining did not show significant differences between the two groups (Supplementary

FIG. 5. COL1 hydrogel improved pseudoislet functionality and minimized ECM changes due to hypoxia. **(A–F)** Relative fold change in expression due to hypoxic conditions of pseudoislets in suspension or encapsulated in COL1 gel; **(A)** cleaved caspase-3 ($n \geq 3$), **(B)** number of TUNEL$^+$ cells ($n \geq 3$), **(C)** Ki67, ($n \geq 4$), **(D)** E-cadherin ($n \geq 5$) and **(E)** insulin ($n \geq 4$), unpaired *t*-tests. **(F)** GSIS response of encapsulated normoxic and hypoxic pseudoislets ($n = 7$); two-way ANOVA with Tukey's multiple comparisons test. **(G–M)** Quantification of the expression under normoxic or hypoxic conditions of relevant pancreatic ECM proteins, including **(G)** LAM ($n = 4$), **(H)** COL4 ($n \geq 3$), **(I)** DCN ($n \geq 3$), **(J)** NID1 ($n \geq 4$), **(K)** FN ($n \geq 4$), and **(M)** COL1 ($n = 4$). **(L)** Quantification of nuclear FN in encapsulated normoxic and hypoxic pseudoislets ($n = 4$) with corresponding representative IF images are shown on the *right*. Unpaired *t*-tests. **(A–E, G–K, M)** Scale bars = 50 μm. **(L)** Scale bar = 5 μm $^*p < 0.05$, $^{**}p < 0.01$.

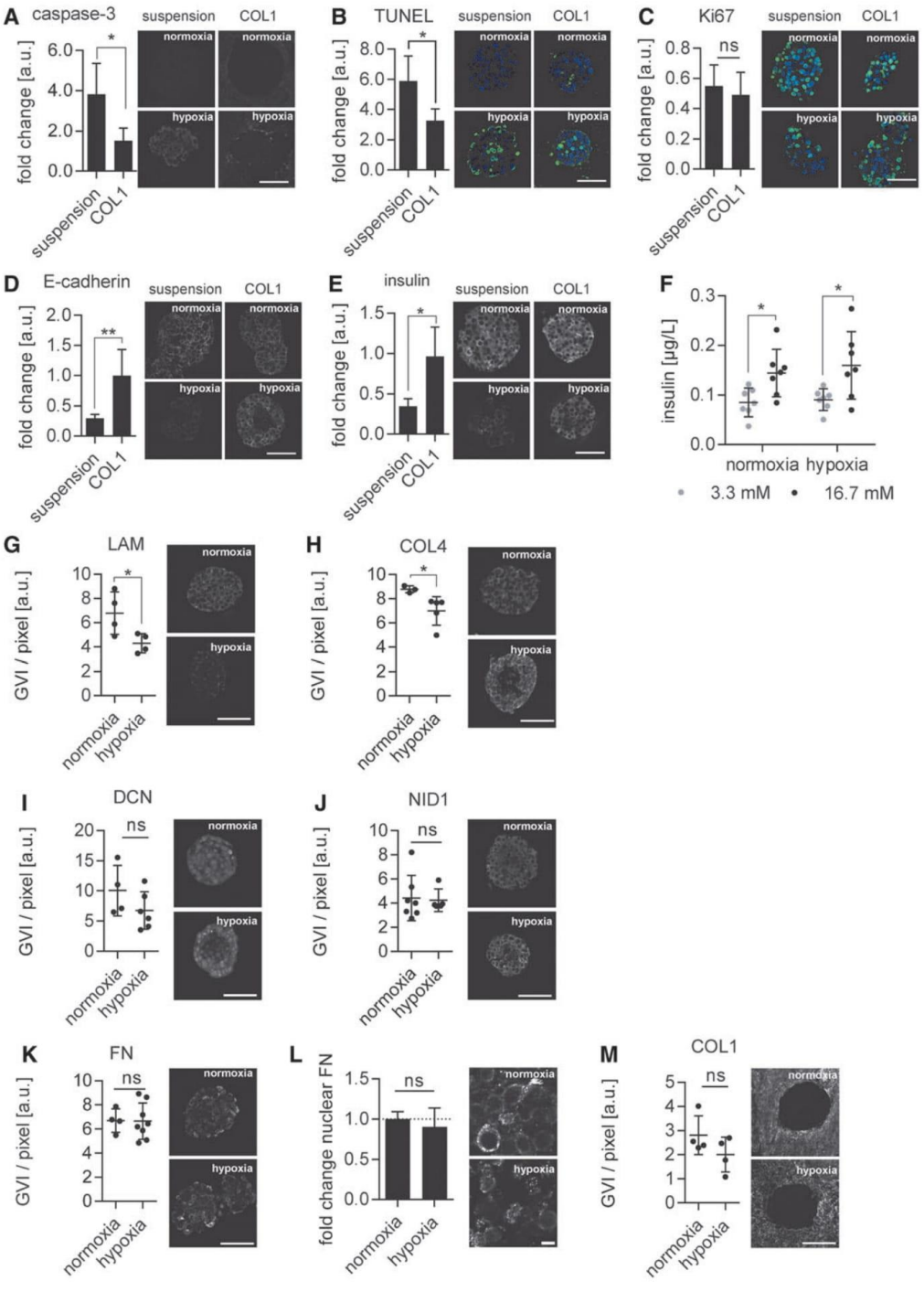
A caspase-3
suspension
COL1
normoxia
hypoxia
fold change [a.u.]
B TUNEL
C Ki67
ns
D E-cadherin
E insulin
F
insulin [µg/L]
3.3 mM
16.7 mM
G LAM
H COL4
GVI / pixel [a.u.]
I DCN
J NID1
K FN
L
fold change nuclear FN
M COL1

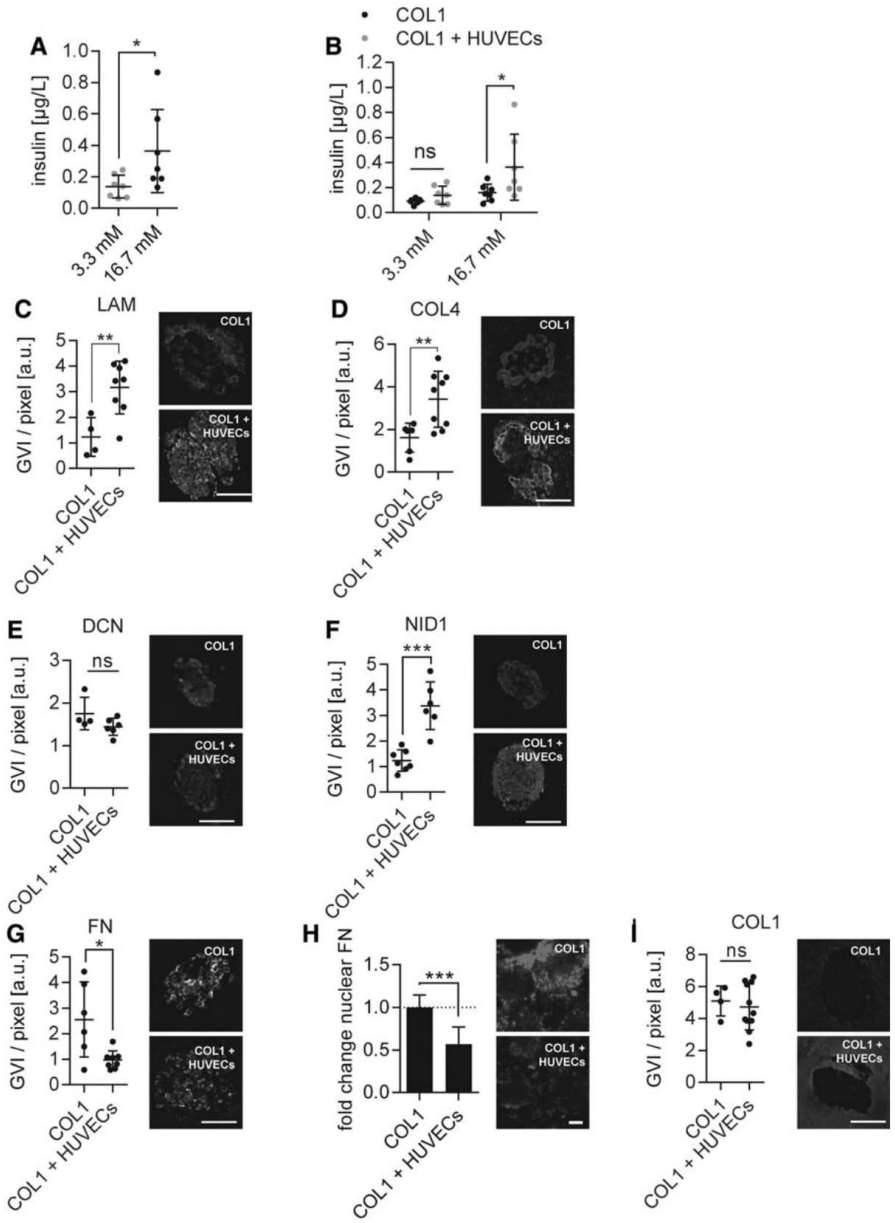

FIG. 6. COL1 hydrogel with incorporated HUVECs stimulates insulin and BM protein secretion in β-cell-containing pseudoislets. **(A)** Insulin expression in β-cells encapsulated in COL1 hydrogel with HUVECs ($n=7$). **(B)** β-cell-containing pseudoislets in COL1 hydrogel with HUVECs secrete significantly more insulin upon glucose stimulation compared with β-cell-containing pseudoislets cultured in COL1 hydrogels alone ($n=7$); two-way ANOVA with Sidak's multiple comparisons test. **(C–I)** Quantification of pancreatic ECM protein expression under hypoxic conditions in cultures with or without incorporation of HUVECs: **(C)** LAM ($n\geq4$), **(D)** COL4 ($n\geq6$), **(E)** DCN ($n\geq4$), **(F)** NID1 ($n\geq6$), **(G)** FN ($n\geq6$), and **(I)** COL1 ($n\geq4$). **(H)** Quantification of nuclear FN in pseudoislets with or without HUVECs ($n\geq6$). Unpaired *t*-tests. **(C–G, I)** Scale bars = 50 µm. **(H)** Scale bar = 5 µm. $^{*}p<0.05$, $^{**}p<0.01$, $^{***}p<0.001$. HUVEC, human umbilical vein endothelial cell.

Fig. S4B–F). The successful integration of HUVECs into the hydrogel was shown by significantly more $CD31^+$ cells (Supplementary Fig. S4G; 0.07 ± 0.03 GVI/pixel COL1 hydrogel vs. 0.26 ± 0.11 GVI/pixel COL1 hydrogel+HUVECS; $p < 0.01$). The evaluation of the ECM protein expression in β-cell only pseudoislets and coculture pseudoislets in the COL1 hydrogel after 48h (Fig. 6C–I) revealed a significant increase in both LAM (1.24 ± 0.66 GVI/pixel COL1 hydrogel vs. 3.16 ± 0.96 GVI/pixel COL1 hydrogel+HUVECs; $p < 0.01$) and COL4 (1.62 ± 0.62 GVI/pixel COL1 hydrogel vs. 3.42 ± 1.24 GVI/pixel COL1 hydrogel+HUVECs; $p < 0.01$) as well as NID1 (1.23 ± 0.39 GVI/pixel COL1 hydrogel vs. 3.38 ± 0.85 GVI/pixel COL1 hydrogel+HUVECs; $p < 0.001$). Interestingly, both the overall expression of FN (2.55 ± 1.34 GVI/pixel COL1 hydrogel vs. 0.97 ± 0.33 GVI/pixel COL1 hydrogel+HUVECs; $p < 0.05$) and the normalized nuclear expression of FN (1.0 ± 0.15 COL1 hydrogel vs. 0.57 ± 0.20 COL1 hydrogel+HUVEC; $p < 0.001$) decreased significantly, while DCN (1.75 ± 0.33 GVI/pixel COL1 hydrogel vs. 1.44 ± 0.18 COL1 hydrogel+HUVECs; $p = 0.12$) and COL1 (5.10 ± 0.81 GVI/pixel COL1 hydrogel vs. 4.72 ± 1.37 GVI/pixel COL1 hydrogel+HUVECs; $p = 0.64$) were not affected by the HUVEC coculture. These data demonstrate the stimulative capacity of HUVECs on β-cells regarding functionality, BM protein expression, and decrease in hypoxia-induced cellular stress markers.

Discussion

In healthy native pancreatic tissue, pancreatic β-cell functionality is supported by a highly specialized composition of ECM proteins produced by various cell types, including fibroblasts and ECs.[9,39] A dense vascularization of the pancreas further ensures highly oxygenated blood and nutrient delivery.[40] Using current protocols, during the Islets of Langerhans isolation procedure, the majority of the ECM and vascular access are destroyed, resulting in decreased islet survival and functionality.[8,41] Posttransplantation, the Islets of Langerhans are subjected to an ischemic period leading to severe hypoxia, with a partial oxygen pressure ranging from 5 to 10 mmHg, corresponding to 1% oxygen.[42] The removal of the pancreatic ECM, which is accelerated by hypoxic conditions, accentuates the importance for β-cells to produce their own microenvironment. However, the role of β-cell ECM production in hypoxia had not been investigated yet.

In this study, we asked whether β-cells have the ability to secrete ECM proteins and how their production is impacted by a hypoxic environment that mimics the initial phase posttransplantation where no vascularization is present. We developed a functional rat-based model to successfully mimic hypoxic conditions to study the direct effect of hypoxia on β-cells. In line with previously reported studies, β-cell glucose responsiveness was lost under hypoxic conditions accompanied by increased apoptosis and necrosis markers, especially in the core region of the islets.[16,43] Here, marker-free Raman imaging on living pseudoislets identified a significant hypoxia-induced alteration in ECM homeostasis. This impact on pancreatic ECM structures may contribute to the loss of β-cell function, as it had been previously shown that intraislet ECM interactions can modulate β-cell proliferation and survival.[34] The overall decrease in ECM signal within pseudoislets supports our hypothesis that hypoxia negatively impacts the ECM expression of β-cells.

The specific roles of the different types of ECM regarding Islets of Langerhans transplant survival and function are not fully understood.[44] Hence, we assessed the hypoxia-induced disruption of ECM homeostasis on six different ECM proteins. DCN is an important binding partner of collagens (mainly types I and III) that regulates collagen fibrillogenesis. The loss of DCN can lead to uncontrolled collagen fiber formation, which then results in pathological ECM development such as fibrosis and ultimately graft failure.[45] The hypoxia-induced decrease of DCN in the pseudoislets after 48 h expression can be a driver for early graft failure as a controlled fibrillogenesis of COL1 and COL3 may be impaired. Furthermore, DCN has been shown to positively affect angiogenesis and modulate the immune response,[46,47] which are both highly important processes to achieve proper transplant engraftment.

The main purpose of COL1 and other parts of the exocrine interstitial matrix is the preservation of structural stability[48] as well as assuring β-cell survival and insulin expression by stimulating a variety of surface receptors.[49] Although COL1 overall expression remained stable, the quality or maturity of COL1 fibers might be impaired by the decreased DCN expression. Immature COL1 has not been described yet to act via the same integrins as fully formed COL1, potentially contributing to the loss of glucose responsiveness.[50]

FN is another component of the interstitial matrix.[51] The impact of FN on β-cells is currently controversially discussed. Freshly isolated human Islets of Langerhans showed an improved glucose response on surfaces coated with FN.[37] Hadavi *et al.* recently published the positive effect of FN in combination with COL4 and LAM to stimulate β-cell functionality *in vitro*.[52] In contrast, Navarro-Alvarez *et al.* demonstrated that isolated human Islets of Langerhans, which were attached to FN-coated dishes, showed a clear tendency toward disintegration and loss of spherical structure.[53] Here, FN expression patterns exhibited a hypoxia-induced shift from cytoplasmic to nuclear expression, especially in the central region of the pseudoislets. Since FN is present in tissues to repair damaged cells, the increase in nuclear FN expression may be the first indicator for a hypoxia-induced cell damage.[54] Nuclear FN has been shown to be present in some tumor cells; however, the precise role of nuclear FN remains unclear.[55]

In contrast to proteins of the interstitial matrix, the expression of ECM proteins associated with the BM were highly affected by hypoxic conditions. In the pancreas, Islets of Langerhans are located in the BM, a dense network of copolymerized LAM and COL4. These proteins are connected by NID1, which acts as key bridging protein between LAM and COL4 in native tissues.[56] Laminin α5 and COL4 have been reported to modulate β-cell differentiation and maturation from stem cells into mature β-cells and stimulate insulin expression in pseudoislet systems,[57,58] highlighting the relevance of BM proteins for β-functionality *in vitro*. Since the expression of all proteins of the BM was reduced in our study under hypoxic conditions, this lack of BM proteins may be associated with functionality loss. Hence, the rescue of BM proteins may support β-cell function under hypoxic conditions posttransplantation.[59,60]

One approach to reduce hypoxia-induced damage and altered ECM expression is to provide exogenous ECM to the cellular transplant. The addition of a protective COL1 hydrogel surrounding the β-cell pseudoislets significantly

Table 1. Overview of Extracellular Matrix Protein Expression Changes in Collagen Type 1 Hydrogel of β-Cell Pseudoislets and Coculture Pseudoislets After 48 h Under Hypoxic Culture Conditions (Normalization to Pseudoislets Cultured Under Normoxic Culture Conditions)

ECM protein	*LAM*	*COL4*	*DCN*	*NID1*	*FN*	*COL1*
COL1 gel normoxia	1	1	1	1	1	1
COL1 gel hypoxia	0.63 ↓	0.80 ↓	n.s.	n.s.	n.s.	n.s.
COL1 gel+HUVECs hypoxia	1.61 ↑	1.69 ↑	n.s.	2.63 ↑	0.38 ↓	n.s.

The *up arrow* indicates significant upregulation ($p < 0.05$) and the *down arrow* indicates significant downregulation ($p < 0.05$).
COL1, collagen type 1; COL4, collagen type 4; DCN, decorin; EC, endothelial cell; ECM, extracellular matrix; FN, fibronectin; HUVECs, human umbilical vein endothelial cells; LAM, laminins; NID1, nidogen-1; n.s., not significant.

reduced the negative impact of hypoxia. While apoptotic and necrotic cell numbers decreased, functionality markers increased, and glucose responsiveness was restored. The results of previous studies on the effect of COL1 as well as the reduced number of apoptotic markers and dead cells in this study point toward a combination of biological and mechanophysical support by the COL1 hydrogel.[61–63]

Assessment of the endogenously expressed ECM proteins showed that DCN and NID1 could be restored. DCN binds COL1 via the leucine-rich repeats five to six to regulate its assembly, structure, and biomechanical properties.[64] The rescue of DCN might therefore be facilitated by the supply of the COL1 hydrogel, which offers possible binding sites. However, an interaction between COL1 and NID1 has not been reported yet. Interestingly, the translocation of FN into the nucleus was prevented, supporting the observation that the COL1 hydrogel attenuates the cellular stress levels of the hypoxic environment.

Although the levels of NID1 could be restored, the LAM and COL4 did not show any signs of rescue. The persistent lack of BM proteins suggests that providing β-cells with only COL1 is not enough for a long-term restoration of glucose-responsiveness. Therefore, we hypothesized that stimulation of β-cells by ECs might enhance the expression of BM proteins, as ECs are the main producers of BM proteins in pancreatic tissues.[9] We encapsulated both β-cells and HUVECs into the pseudoislets and cultured them in COL1 hydrogels. We identified that upon encapsulation of β-cells together with HUVECs, we could both stimulate functionality of β-cells as well as rescue BM protein expression of LAM, COL4, and the linker protein NID1 (Table 1). In addition, overall FN expression was reduced, which might be precipitated by the highly significant decrease in nuclear FN, an indicator for reduced hypoxia-induced cellular stress.[29] Furthermore, FN regulates the fibrotic response along with COL1,[49] which is unfavorable for engraftment of the transplant. Consequently, a drop in FN content may have a beneficial long-term effect.

In summary, our data demonstrate the supportive effect of the COL1 hydrogel protecting β-cell-composed pseudoislets under hypoxic conditions by reducing apoptotic effects and cell death, attenuating a loss of ECM protein secretion while rescuing the glucose responsiveness. We further showed how the combination of biological cues from ECs in a coculture system with COL1 hydrogel rescued BM protein expression and improved the glucose responsiveness. Importantly, COL1 is a bioactive base hydrogel that can be further modified and functionalized using growth factors, other ECM proteins or cell types to meet specific requirements, for example to improve transplant function,[5,24,37,61–63,65] or to create a more robust *in vitro* model. Future studies could include the addition of α and δ cells into the pseudoislets. Also, the investigation of reoxygenation posthypoxia would be of interest as it may elucidate key biomolecules influencing the transplantation and healing process; however, it may be difficult to mimic the exact time response and oxygen percentages *in vitro* that are found during the healing processes *in vivo*. In addition, the addition of immune cells would be of high interest as the foreign body response to islet transplantation is a major issue requiring the use of immune suppressants posttransplantation. Many groups are working on the addition of immune cells into *in vitro* test systems in general, which has been difficult in the past due to the complexity of the immune system. Any addition to *in vitro* model complexity must be weighed against its increase in cost and the ability to determine valid readouts that can answer the scientific question being asked.

Conclusion

In this study, we developed an *in vitro* model mimicking the hypoxic posttransplantation environment of pancreatic islets for the purpose of investigating and mitigating the pathological effects of hypoxia on ECM homeostasis with a functionalized material. We identified a significantly reduced production of important ECM proteins such as COL4, LAM, DCN, and NID1 within β-cells accompanied with increased cellular death and loss in functionality. Furthermore, we evaluated a clinically approved COL1 hydrogel and demonstrated its protective effect on β-cells in hypoxia. We further functionalized the hydrogel with HUVECs, which prevented ECM loss and stimulated β-cell functionality. By establishing a COL1 hydrogel, including ECs, we created a carrier matrix that attenuates the hypoxia-induced disruption of ECM homeostasis in β-cells to support them during the first phase of ECM reestablishment of posttransplantation and therefore potentially increase the efficacy of the Edmonton protocol for diabetic patients.

Disclosure Statement

No competing financial interests exist.

Funding Information

This work was financially supported by the European Union (H2020-NMP10-2014-645991-2, DRIVE to Katja Schenke-Layland and Garry Duffy), the International Foundation for Ethical Research (to Aline Zbinden), Germany's Excellence Strategy (EXC 2180-390900677 to Katja Schenke-Layland), as well as the Ministry of Science,

Research and the Arts of Baden-Württemberg (33-729.55-3/214 and SI-BW 01222-91 to Katja Schenke-Layland), and the Deutsche Forschungsgemeinschaft (INST 2388/33-1 and GRK 2543/1 to Katja Schenke-Layland).

Supplementary Material

Supplementary Table S1
Supplementary Figure S1
Supplementary Figure S2
Supplementary Figure S3
Supplementary Figure S4

References

1. Urbanczyk, M., Layland, S.L., and Schenke-Layland, K. The role of extracellular matrix in biomechanics and its impact on bioengineering of cells and 3D tissues. Matrix Biol **85–86,** 1, 2020.
2. Lukashev, M. ECM signalling: orchestrating cell behaviour and misbehaviour. Trends Cell Biol **8,** 437, 1998.
3. Thomas, F.T., Contreras, J.L., Bilbao, G., Ricordi, C., Curiel, D., and Thomas, J.M. Anoikis, extracellular matrix, and apoptosis factors in isolated cell transplantation. Surgery **126,** 299, 1999.
4. Shapiro, A.M.J., Lakey, J.R.T., Ryan, E.A., *et al.* Islet transplantation in seven patients with type 1 diabetes mellitus using a glucocorticoid-free immunosuppressive regimen. N Engl J Med **343,** 230, 2000.
5. Weber, L.M., and Anseth, K.S. Hydrogel encapsulation environments functionalized with extracellular matrix interactions increase islet insulin secretion. Matrix Biol **27,** 667, 2008.
6. Spiers, R.M., Marzi, J., Brauchle, E.M., *et al.* Donor age significantly influences the Raman spectroscopic biomolecular fingerprint of human pancreatic extracellular matrix proteins following collagenase-based digestion. Acta Biomater **99,** 269, 2019.
7. Cross, S.E., Vaughan, R.H., Willcox, A.J., *et al.* Key matrix proteins within the pancreatic islet basement membrane are differentially digested during human islet isolation. Am J Transplant **17,** 451, 2017.
8. Delaune, V., Berney, T., Lacotte, S., and Toso, C. Intraportal islet transplantation: the impact of the liver microenvironment. Transpl Int **30,** 227, 2017.
9. Nikolova, G., Strilic, B., and Lammert, E. The vascular niche and its basement membrane. Trends Cell Biol **17,** 19, 2007.
10. Rambøl, M.H., Han, E., and Niklason, L.E. Microvessel network formation and interactions with pancreatic islets in three-dimensional chip cultures. Tissue Eng Part A **26,** 556, 2020.
11. Cen, L., Liu, W.E.I., Cui, L.E.I., *et al.* Collagen tissue engineering: development of novel biomaterials. Pediatr Res **63,** 492, 2008.
12. Zhu, H., Li, W., Liu, Z., *et al.* Selection of implantation sites for transplantation of encapsulated pancreatic islets. Tissue Eng Part B Rev **24,** 191, 2017.
13. Irving-Rodgers, H.F., Choong, F.J., Hummitzsch, K., Parish, C.R., Rodgers, R.J., and Simeonovic, C.J. Pancreatic islet basement membrane loss and remodeling after mouse islet isolation and transplantation: impact for allograft rejection. Cell Transplant **23,** 59, 2014.
14. Mouré, A., Bacou, E., Bosch, S., *et al.* Extracellular hemoglobin combined with an O_2-generating material overcomes O_2 limitation in the bioartificial pancreas. Biotechnol Bioeng **116,** 1176, 2019.
15. Emamaullee, J.A., Shapiro, A.M.J., Rajotte R V., Korbutt, G., and Elliott, J.F. Neonatal porcine islets exhibit natural resistance to hypoxia-induced apoptosis. Transplantation **82,** 945, 2006.
16. Lehmann, R., Zuellig, R.A., Kugelmeier, P., *et al.* Superiority of small islets in human islet transplantation. Diabetes **56,** 594, 2007.
17. Urbanczyk, M., Zbinden, A., Layland, S.L., Duffy, G., and Schenke-Layland, K. Controlled heterotypic pseudo-islet assembly of human β-cells and human umbilical vein endothelial cells using magnetic levitation. Tissue Eng Part A **26,** 387, 2020.
18. Xiong, X., Ghosh, R., Hiller, E., *et al.* A new procedure for rapid, high yield purification of Type I collagen for tissue engineering. Process Biochem **44,** 1200, 2009.
19. Zbinden, A., Marzi, J., Schlünder, K., *et al.* Non-invasive marker-independent high content analysis of a microphysiological human pancreas-on-a-chip model. Matrix Biol **85–86,** 205, 2020.
20. Vlahos, A.E., Kinney, S.M., Kingston, B.R., *et al.* Endothelialized collagen based pseudo-islets enables tuneable subcutaneous diabetes therapy. Biomaterials **232,** 119710, 2020.
21. Hellman, B., and Angervall, L. The frequency distribution of the number and volume of the Islets of Langerhans in man. Acta Pathol Microbiol Scand **53,** 230, 2009.
22. Jun, Y., Lee, J., Choi, S., *et al.* In vivo–mimicking microfluidic perfusion culture of pancreatic islet spheroids. Sci Adv **5,** eaax4520, 2019.
23. Yuan, Q., Arkudas, A., Horch, R.E., *et al.* Vascularization of the arteriovenous loop in a rat isolation chamber model—quantification of hypoxia and evaluation of its effects. Tissue Eng Part A **24,** 719, 2018.
24. Ichihara, Y., Utoh, R., Yamada, M., Shimizu, T., and Uchigata, Y. Size effect of engineered islets prepared using microfabricated wells on islet cell function and arrangement. Heliyon **2,** e00129, 2016.
25. Hilderink, J., Spijker, S., Carlotti, F., *et al.* Controlled aggregation of primary human pancreatic islet cells leads to glucose-responsive pseudoislets comparable to native islets. J Cell Mol Med **19,** 1836, 2015.
26. Chen, Z., Wang, J., Sun, W., *et al.* Synthetic beta cells for fusion-mediated dynamic insulin secretion. Nat Chem Biol **14,** 86, 2018.
27. Rogal, J., Zbinden, A., Schenke-Layland, K., and Loskill, P. Stem-cell based organ-on-a-chip models for diabetes research. Adv Drug Deliv Rev **140,** 101, 2019.
28. Majtnerová, P., and Roušar, T. An overview of apoptosis assays detecting DNA fragmentation. Mol Biol Rep **45,** 1469, 2018.
29. Stendahl, J.C., Kaufman, D.B., and Stupp, S.I. Extracellular matrix in pancreatic islets: relevance to scaffold design and transplantation. Cell Transplant **18,** 1, 2009.
30. Dukor, R.K. Vibrational spectroscopy in the detection of cancer. In: Griffiths, P.R., edr. Handbook of Vibrational Spectroscopy. Chichester, UK: John Wiley & Sons, Ltd., 2006.
31. Brazhe, N.A., Treiman, M., Brazhe, A.R., Find, N.L., Maksimov, G.V., and Sosnovtseva, O.V. Mapping of redox state of mitochondrial cytochromes in live cardiomyocytes using raman microspectroscopy. PLoS One **7,** e41990, 2012.
32. Zhang, X., Yu, F., Li, J., *et al.* Investigation on the cancer invasion and metastasis of skin squamous cell carcinoma by Raman spectroscopy. Molecules **24,** 2059, 2019.
33. Cheng, W-T., Liu, M-T., Liu, H-N., and Lin, S-Y. Micro-Raman spectroscopy used to identify and grade human skin pilomatrixoma. Microsc Res Tech **68,** 75, 2005.

34. Townsend, S.E., and Gannon, M. Extracellular matrix–associated factors play critical roles in regulating pancreatic β-cell proliferation and survival. Endocrinology **160,** 1885, 2019.
35. Spencer, V.A., Xu, R., and Bissell, M.J. Extracellular matrix, nuclear and chromatin structure, and gene expression in normal tissues and malignant tumors: a work in progress. Adv Cancer Res **97,** 275, 2007.
36. Smink, A.M., and de Vos, P. Therapeutic strategies for modulating the extracellular matrix to improve pancreatic islet function and survival after transplantation. Curr Diab Rep **18,** 39, 2018.
37. Daoud, J., Petropavlovskaia, M., Rosenberg, L., and Tabrizian, M. The effect of extracellular matrix components on the preservation of human islet function in vitro. Biomaterials **31,** 1676, 2010.
38. Wang, Z.Z., and Sakiyama-Elbert, S.E. Matrices, scaffolds & carriers for cell delivery in nerve regeneration. Exp Neurol **319,** 1, 2019.
39. Topalovski, M., and Brekken, R.A. Matrix control of pancreatic cancer: new insights into fibronectin signaling. Cancer Lett **381,** 252, 2016.
40. Emamaullee, J.A., Rajotte R V, Liston, P., *et al.* XIAP overexpression in human islets prevents early post-transplant apoptosis and reduces the islet mass needed to treat diabetes. Diabetes **54,** 2541, 2005.
41. Dionne, K.E., Colton, C.K., and Yarmush, M.L. Effect of hypoxia on insulin secretion by isolated rat and canine islets of Langerhans. Diabetes **42,** 12, 1993.
42. Wu, H., Panakanti, R., Li, F., and Mahato, R.I. XIAP gene expression protects β-cells and human islets from apoptotic cell death. Mol Pharm **7,** 1655, 2010.
43. Zheng, X., Zheng, X., Wang, X., *et al.* Acute hypoxia induces apoptosis of pancreatic β-cell by activation of the unfolded protein response and upregulation of CHOP. Cell Death Dis **3,** 1, 2012.
44. Llacua, L.A., Faas, M.M., and de Vos, P. Extracellular matrix molecules and their potential contribution to the function of transplanted pancreatic islets. Diabetologia **61,** 1261, 2018.
45. Gubbiotti, M.A., Vallet, S.D., Ricard-Blum, S., and Iozzo R V. Decorin interacting network: a comprehensive analysis of decorin-binding partners and their versatile functions. Matrix Biol **55,** 7, 2016.
46. Järveläinen, H., Sainio, A., and Wight, T.N. Pivotal role for decorin in angiogenesis. Matrix Biol **43,** 15, 2015.
47. Hildebrand, A., Romaris, M., Rasmussen, M., *et al.* Interaction of the small interstitial proteoglycans biglycan, decorin and fibromodulin with transforming growth factor β. Biochem J **302(Pt 2),** 527, 1994.
48. Nagata, N., Iwanaga, A., Inoue, K., and Tabata, Y. Co-culture of extracellular matrix suppresses the cell death of rat pancreatic islets. J Biomater Sci Polym Ed **13,** 579, 2002.
49. Mouw, J.K., Ou, G., and Weaver, V.M. Extracellular matrix assembly: a multiscale deconstruction. Nat Rev Mol Cell Biol **15,** 771, 2014.
50. Boraschi-Diaz, I., Wang, J., Mort, J.S., and Komarova, S.V. Collagen type I as a ligand for receptor-mediated signaling. Front Phys **5,** 12, 2017.
51. Ignotzs, R.A., and Massague, J. Transforming growth factor-β stimulates the expression of fibronectin and collagen and their incorporation into the extracellular matrix. J Biol Chem **261,** 4337, 1986.
52. Hadavi, E., Leijten, J., Engelse, M., *et al.* Microwell scaffolds using collagen-IV and laminin-111 lead to improved insulin secretion of human islets. Tissue Eng Part C Methods **25,** 71, 2019.
53. Navarro-Alvarez, N., Rivas-Carrillo, J.D., Soto-gutierrez A, and Yuasa, T. Reestablishment of microenvironment is necessary to maintain in vitro and in vivo human islet function. Cell Transplant **17,** 111, 2016.
54. To, W.S., and Midwood, K.S. Plasma and cellular fibronectin: distinct and independent functions during tissue repair. Fibrogenesis Tissue Repair **4,** 1, 2011.
55. Zerlauth, G., Wesierska-Gadek, J., and Sauermann, G. Fibronectin observed in the nuclear matrix of HeLa tumour cells. J Cell Sci **89 (Pt 3),** 415, 1988.
56. Jiang, F., Naselli, G., and Harrison, L.C. Distinct distribution of laminin and its integrin receptors in the pancreas. J Histochem Cytochem **50,** 1625, 2002.
57. Spenlé, C., Simon-Assmann, P., Orend, G., and Miner, J.H. Laminin α5 guides tissue patterning and organogenesis. Cell Adh Migr **7,** 90, 2013.
58. Maillard, E., Sencier M-C, Langlois, A., *et al.* Extracellular matrix proteins involved in pseudoislets formation. Islets **1,** 232, 2009.
59. Mokkapati, S., Nischt, R., Smyth, N., Ho, M.S.P., and Bo, K. Nidogens—extracellular matrix linker molecules **395,** 387, 2008.
60. Kaido, T., Yebra, M., Cirulli, V., and Montgomery, A.M. Regulation of human β-cell adhesion, motility, and insulin secretion by collagen IV and its receptor α1β1. J Biol Chem **279,** 53762, 2004.
61. Bernhardt, A., Österreich, V., and Gelinsky, M. Three-dimensional co-culture of primary human osteocytes and mature human osteoclasts in collagen gels. Tissue Eng Part A **26,** 647, 2020.
62. Schuh, C.M.A.P., Day, A.G.E., Redl, H., and Phillips, J. An optimized collagen-fibrin blend engineered neural tissue promotes peripheral nerve repair. Tissue Eng Part A **24,** 1332, 2018.
63. Aloy-Reverté, C., Moreno-Amador, J.L., Nacher, M., Montanya, E., and Semino, C.E. Use of RGD-functionalized sandwich cultures to promote redifferentiation of human pancreatic beta cells after in vitro expansion. Tissue Eng Part A **24,** 394, 2017.
64. Kalamajski, S., Aspberg, A., and Oldberg, Å. The decorin sequence SYIRIADTNIT binds collagen type I. J Biol Chem **282,** 16062, 2007.
65. Riopel, M., and Wang, R. Collagen matrix support of pancreatic islet survival and function. Front Biosci **19,** 77, 2014.

Address correspondence to:
Katja Schenke-Layland, MSc, PhD
Department of Women's Health
Research Institute for Women's Health
Eberhard Karls University Tübingen
Silcherstr. 7/1
Tübingen 72076
Germany

E-mail: katja.schenke-layland@uni-tuebingen.de;
katja.schenke-layland@nmi.de

Received: August 26, 2020
Accepted: September 22, 2020
Online Publication Date: November 6, 2020

1 **Supplemental data**

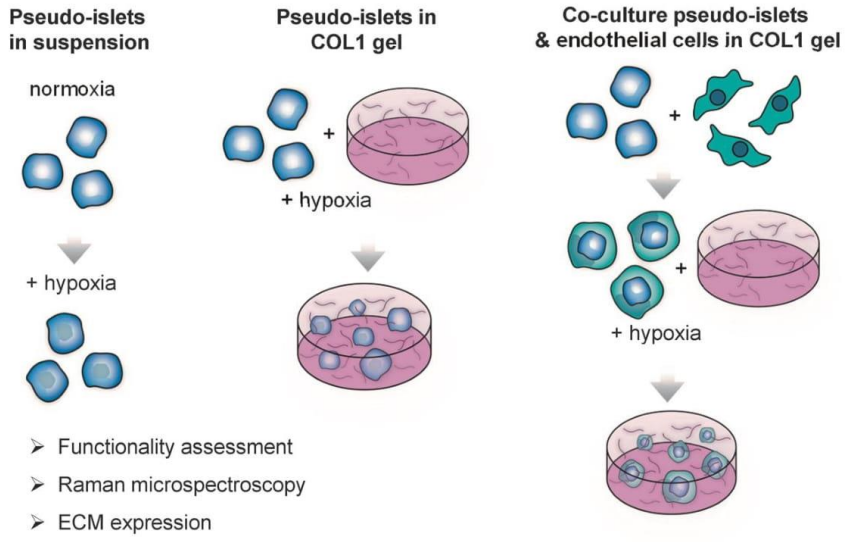

2

3 **Figure S1:** Illustration of the experimental set-up using pseudo-islets, pseudo-islets encapsulated into

4 a COL1 gel, and co-culture pseudo-islets with endothelial cells encapsulated into a COL1 gel.

5

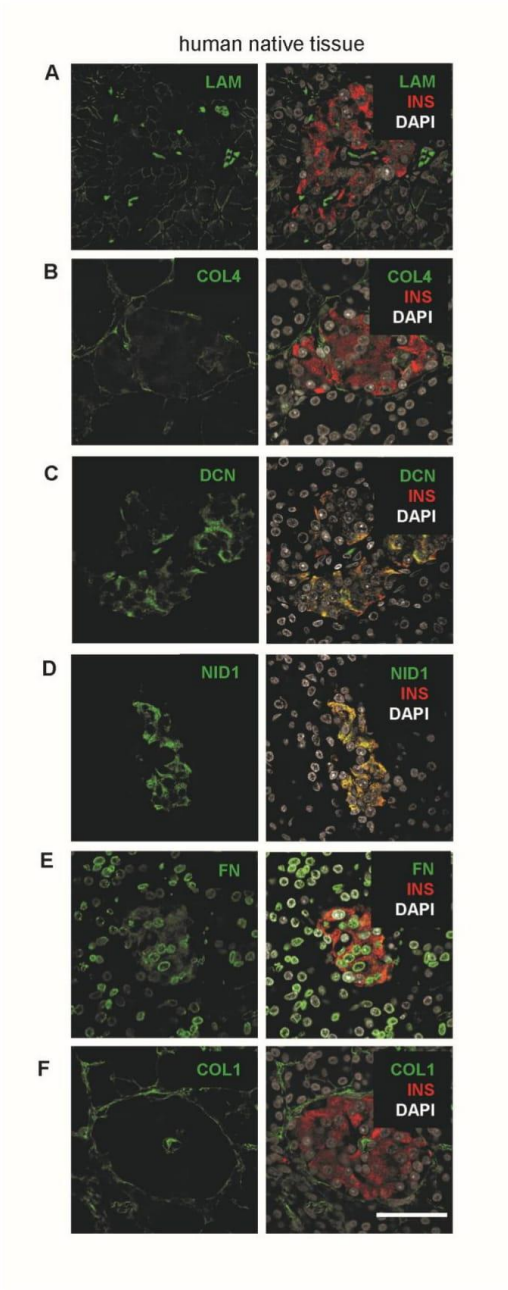

Figure S2: Immunofluorescence staining expression patterns of relevant ECM proteins (in green) in adult human pancreatic tissue. **(A)** LAM, **(B)** COL4, **(C)** DCN, **(D)** NID1, **(E)** FN and **(F)** COL1 with insulin (INS) in red and nuclei (DAPI) in white. Scale bar equals 50 µm.

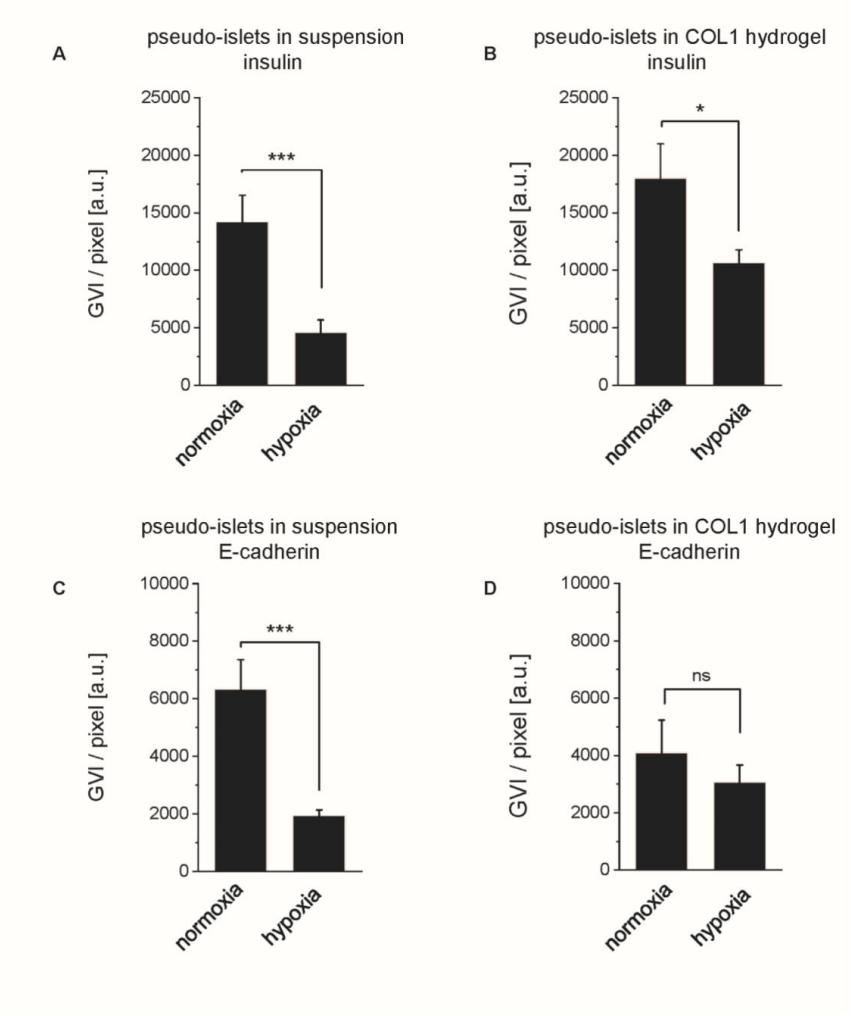

Figure S3: Expression of E-cadherin and insulin in suspension and COL1 hydrogel cultures under normoxic and hypoxic conditions. (**A,B**) Semi-quantification of IF staining of insulin in (**A**) suspension ($n \geq 6$) and (**B**) COL1 hydrogel cultures ($n \geq 4$) shows a significant decrease in insulin expression under hypoxic conditions. (**C,D**) E-cadherin staining in pseudo-islets in (**C**) suspension ($n \geq 6$) and (**D**) COL-1 hydrogel ($n \geq 5$). Unpaired t-test, *$p<0.05$, ***$p<0.001$.

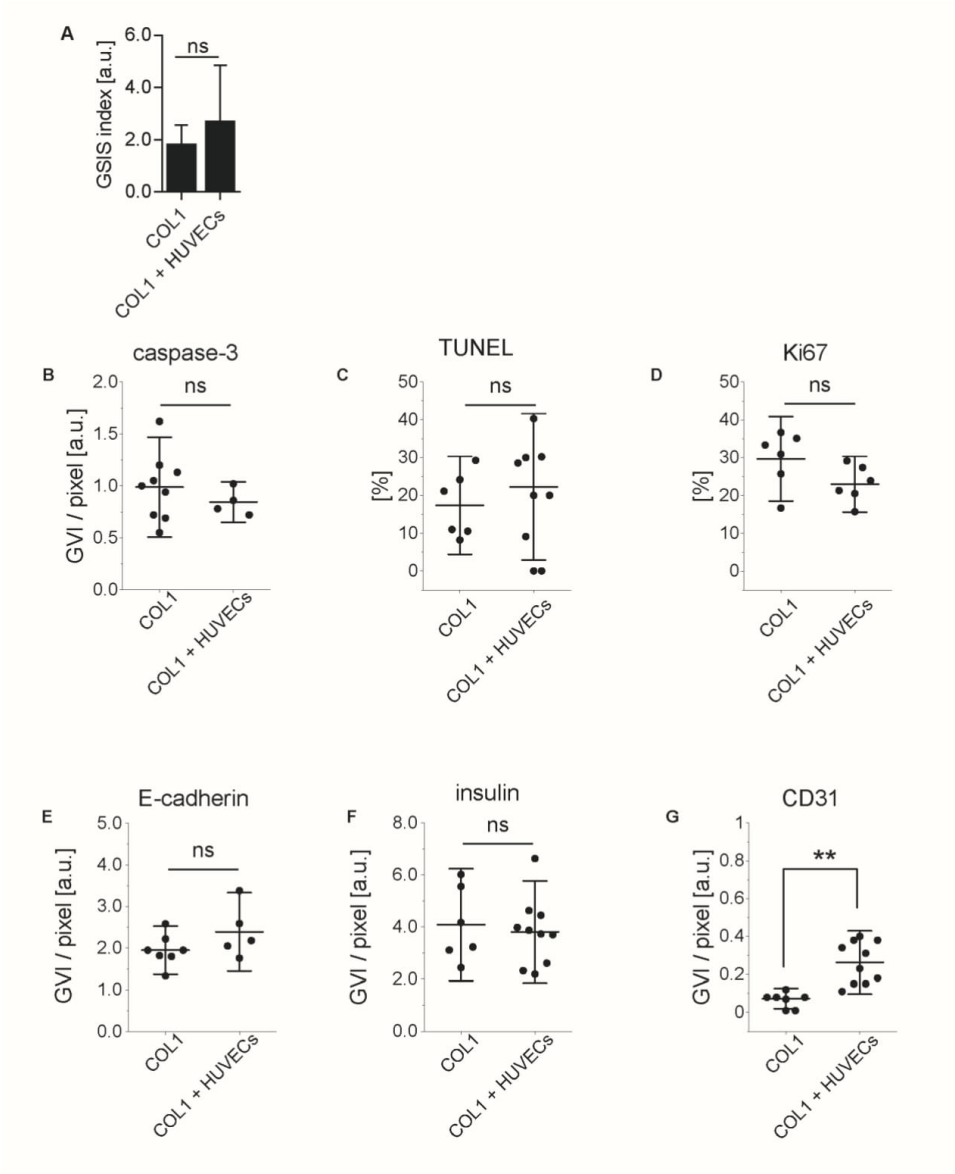

Figure S4: Comparison of β-cell pseudo-islets and co-culture β-cell pseudo-islets with HUVECs in COL1 hydrogel under hypoxic conditions for 48h. (**A**) No difference in GSIS response was observed. No differences were seen in the expression of (**B**) caspase-3 ($n \geq 4$), (**C**) TUNEL$^+$ cells ($n \geq 6$), (**D**) KI67 ($n = 6$), (**E**) E-cadherin ($n \geq 5$) and (**F**) insulin ($n \geq 6$). (**G**) Co-culture β-cell pseudo-islets express significantly more CD31 ($n \geq 6$). Unpaired t-test, **$p<0.01$.

Table S1: List of primary and secondary antibodies used for immunofluorescence staining

antibodies	0.1% Triton-X treatment	dilution
primary antibodies		
caspase-3 (ab13847)	30 min	1:100
collagen type 1 (ab138492)		1:75
collagen type 1 (R1038)		1:250
collagen type 4 (ab6586)		1:250
decorin (sc-73896)		1:200
E-cadherin (ab76055)		1:250
fibronectin (ab2413)		1:100
insulin (ab181547)	30 min	1:200
KI67 (ab15580)	30 min	1:1000
laminin (ab11575)		1:50
nidogen-1 (sc-33141)		1:100
secondary antibodies		
Alexa Fluor 488 anti-rabbit IgG(ab150077)		1:250
Alexa Fluor 488 anti-mouse IgG 1 (ab150117)		1:250
Alexa Fluor 594 anti-rabbit IgG(ab150080)		1:250